UNIVERSITY OF OKLAHOMA

GRADUATE COLLEGE

APPLICATION OF RAPID-SETTING BELITIC CALCIUM SULFOALUMINATE CEMENTS IN PRETENSIONED, PRESTRESSED CONCRETE

A DISSERTATION

SUBMITTED TO THE GRADUATE FACULTY

in partial fulfillment of the requirements for the

Degree of

DOCTOR OF PHILOSOPHY

By

STEPHEN JOSIAH ROSWURM
Norman, Oklahoma
2023

Downloaded from SHAREOK. Persistent Handle URL: https://hdl.handle.net/11244/337148

APPLICATION OF RAPID-SETTING BELITIC CALCIUM SULFOALUMINATE CEMENTS IN PRETENSIONED, PRESTRESSED CONCRETE

A DISSERTATION APPROVED FOR THE SCHOOL OF CIVIL ENGINEERING AND ENVIRONMENTAL SCIENCE

BY THE COMMITTEE CONSISTING OF

Dr. Royce W. Floyd, Chair

Dr. Jeffery S. Volz

Dr. Christopher C.E. Ramseyer

Dr. Kianoosh Hatami

Dr. J. David Baldwin

© Copyright by STEPHEN JOSIAH ROSWURM 2023

All Rights Reserved.

And I heard a loud voice from the throne saying, “Look! God’s dwelling place is now among the people, and he will dwell with them. They will be his people, and God himself will be with them and be their God. He will wipe every tear from their eyes. There will be no more death or mourning or crying or pain, for the old order of things has passed away.”

He who was seated on the throne said, “I am making everything new!” Then he said, “Write this down, for these words are trustworthy and true.”

He said to me: “It is done. I am the Alpha and the Omega, the Beginning and the End. To the thirsty I will give water without cost from the spring of the water of life. Those who are victorious will inherit all this, and I will be their God and they will be my children.”

Revelation 21: 3 - 7

Acknowledgements

To even begin to fully thank and properly recognize every individual who is responsible for helping me to achieve the completion of my doctoral degree is truly a daunting task! I will, however, give it the best try that I possibly can. First and foremost, I owe all my love and adoration to my Lord and Savior Jesus Christ, who has held me in His loving hands and empowered my every step and breath on this journey. Without Him, I am nothing, and my life exists to bring Him the utmost glory and honor.

My dear and precious family must be specifically thanked for their endless support, love, encouragement, and physical assistance. My dad and mom, Scot and Jenni Roswurm, are the most amazing parents I could ask for; their kindness and uplifting reassurances have been especially important to me. Mom and dad, I will never forget every kind word, every proud moment, and every beautiful evening lounging at the Mont and shooting the breeze. I want to specifically call out all my loving siblings and their families who have been a constant source of encouragement to me. Katie and Isaac; Jake and Ame; Seth and Bree; Jess and Amy; and Sam and Kate – each one of you all holds a unique place in my heart, and my heart feels full when I consider all the big and special ways you each have helped me reach this point. Katie helped me take beam strain measurements; Jake, Seth, Mom, Dad, and Katie showed up the night before a pour to help me shovel aggregates and cement; walks on campus, football games, hot dinners and showers crashing at your houses after long days at the lab. I'll never forget the light in the eyes of my nephews Marcus and Justin when they got to come watch the slab pour for the Fears Lab extension in 2020. I also want to thank my dear friends (basically brothers) Dakota and Connor who have been part of my journey at OU and running buddies in research for years. I could go on and on. You guys literally mean the world to me.

I owe a deep debt of gratitude to Dr. Royce Floyd, my doctoral advisor, and a man who I profoundly respect and admire. Dr. Floyd, you are the kindest and most patient man I have ever met, much less had the privilege of working for. Your steady and consistent guidance coupled with a willingness to let me fail, learn, rebound, and grow without ever feeling diminished has made me a better man and a more skilled engineer. I treasure the relationship that the Lord has fostered between me and your family, and I feel privileged that my doctoral chair and boss for the last 4-5 years I can truly call my friend. I pray that God blesses you, Molly, and the kids!

Many thanks also belong to all the members of my doctoral committee. Thank you to Dr. Jeff Volz, Dr. Kianoosh Hatami, Dr. James Baldwin, and Dr. Chris Ramseyer for taking time out of your busy schedules to serve in this capacity. Special thanks are owed to Dr. Volz and Dr. Ramseyer, who both graciously provided critical resources, supplies, and testing equipment that were vital to executing this research in Fears Lab. Dr. Ramseyer provided cement for early stage test mixes, spare vibrating wire strain gages and dataloggers for data acquisition, and various materials for small and large scale concrete formwork. Dr. Volz provided long-term usage of his self-reacting load frames for my creep testing and his semi-adiabatic calorimetry equipment for my concrete setting-time testing. Although all these resources were critical (and likely do not enumerate all that was provided to me), the provisions of the dataloggers and the creep frames in particular saved thousands upon thousands of dollars, significant fabrication efforts in the shop, and weeks to months of potential delays in my testing. I will always be grateful for these provisions! Finally, a special shoutout to Dr. Ramseyer – congratulations on your retirement; you've earned every minute of relaxation you choose to enjoy. I consider you a mentor and a true friend, and I'll always value our relationship. Here's to your service on the committee of every graduate degree that me and my brothers have earned!

I would be remiss if I failed to attempt to enumerate all of the staff and students who have been the lifeblood and the backbone of Fears Lab (and the CEES department) and helped me shoulder the physical load of my research and testing. First, thank you to Molly Smith and Laura Swan in the CEES office who keep everything running smoothly. Your efficiency in keeping everything running and kindness to always help us out is a massive lifeline. And a big shout out to Molly; like Dr. Ramseyer, you have been a part of the journey for me, Jake, Seth, and Jesse. You're a rockstar!

Thanks beyond words go out to Mike Schmitz, who served as lab supervisor at Fears Lab for my whole undergraduate and Master's programs and halfway up through my doctoral program. Mike, I will forever be deeply grateful for the time we got to work together, for the things you taught me, for your great stories, and most of all your unending patience. Needless to say, I was green and clueless when I started in the lab as a 16 year old kid in 2013 and I credit you with vastly improving my self confidence and determination. You taught me to take the bull by the horns, think outside the box, mess up, fix it, try again, and never ever stop learning. You have been greatly missed, and I wish you and your family all the best!

I cannot fully express my gratitude to John Bullock, Fears Lab supervisor since 2021, a genuine jack of all trades, Bang drinker extraordinaire, and my good friend. John came at a critical time for me personally when my research was really starting to ramp up. Your all-in, can do attitude gave me just the spark I needed; you always made me laugh; and early mornings or late nights breaking our backs just felt like extended coffee breaks because of your infectious good spirits! Getting to know you and Paula as friends has been a true pleasure and I feel like I've known ya'll forever. Your skill, work ethic, attention to detail, problem solving mind, and

drive for cleanliness and safety make Fears Lab a better place every single day! Every student now and in the future is lucky to learn from you.

To the students of Dr. Floyd's research group and the greater Fears Lab gang, I owe a tremendous amount of thanks. From Dr. Floyd's group, I want to thank Mujtaba Ahmadi, Omar Yadak, Zach Tiry, Cade Harris, Cole Walker, Dip Banik, and Jacob Starks. Multiple phases of my research were extremely labor intensive and I could not have done them alone. Cole was instrumental in helping with my early test mixes and material testing. Zach, Omar, and Mujtaba were absolute workhorses throughout my beam fabrication, helping batch materials, tie reinforcement and set forms, mix and cast, clear the beds, and so much more. In addition, I want to recognize that during these intense months of beam construction and testing, Dr. Floyd and John Bullock worked hard alongside me and the other students, going well above and beyond their respective job duties.

Other researchers and students in the lab were invaluable during my work. Jackson Milner also deserves an individual recognition; despite belonging to Dr. Volz's research group, Jackson was a vital asset in the execution of significant aspects of my work. Jackson showed up at 6 AM repeatedly for my pours, and regularly stayed longer than anyone else in the lab helping me. We routinely pulled 10, 12, and 14 hour days working together, as he generously gave of his time and labor to help with my work. Students from multiple research groups including Johnathan Martin, Jake Choate, and Abdirahman Haibe stepped in to help at times as well.

I want to specifically thank Dr. Trevor Looney for his assistance in my journey. Trevor was my T.A. in undergraduate classes, but we got the opportunity to work together extensively during our respective PhD research. It is crazy to think about how much I learned from Trevor. From our LabView class together, to long road trips to the panhandle on site visits, data

acquisition struggles in the lab, and numerous long work days when we were between lab supervisors, I am thankful for your friendship and the time we spent together. Even early mornings at the gym with Trevor taught me a whole lot. I'll always be struck by how different we are, but thankful that when there are shared goals and vision and work ethic, very different people can work together and share a great friendship! I wish you and Krista all the very, very best!

I also would like to thank CTS Cement Manufacturing Corporation for providing the BCSA cement that was utilized in this research. Specifically, I want to thank Chris Davis for consistently making himself available to provide valuable advice and insight about CTS products and Eric Bescher for his help in arranging CTS's donation of the BCSA cement. Thank you to Dolese Bros. Co. for generously donating to Fears Lab the fine and coarse aggregates and superplasticizer used throughout the experimental testing. Special thanks also go to Schwarz Ready Mix (SRM) of Norman, Oklahoma for their ready and willing cooperation on pouring the blocks for strand bond testing. SRM provided a truck and crew free of charge and spent a day on site at Fears Lab to mix and cast the rapid-setting concrete for this testing. Brian and Keith Schwarz and Jason Halter made the entire process smooth and were a great help in coordinating and executing the strand block pour.

Finally, thanks also to my church family (Tabernacle of the Congregation, formerly Norman Christian Fellowship) who have been part of my journey my entire life and always held me up in prayer and encouragement. I am quite sure that I have failed to properly recognize every individual who has contributed to the successful completion of my doctoral research and dissertation; so, for one last time, I offer up a heart overflowing with gratitude for all those who helped me attain this accomplishment.

Table of Contents

Acknowledgements v
List of Figures xiii
List of Tables xix
Abstract xxi
1. Introduction 1
1.0 Background and Overview 1
1.1 Motivation 2
1.2 Objectives 3
1.3 Goals 3
2. Literature Review 5
2.1 CSA Cement 5
2.1.1 History 5
2.1.2 Chemistry and Composition 6
2.1.3 Properties 9
2.1.4 Challenges 10
2.1.5 Applications 11
2.2 Prestressed Strand Bond 12
2.2.1 Strand Bond Theory 12
2.2.2 Estimation of Strand Bond 13
2.2.3 Strand Bond Testing 16
2.2.4 Accuracy and Limitations of Strand Bond Models 24
2.3 Loss of Prestress 27
2.3.1 Immediate Prestress Losses 27
2.3.2 Time-Dependent Losses 28
2.3.3 Estimating Prestress Losses 30
2.4 BCSA Cement in Prestressed Concrete 37
2.4.1 BCSA Cement Concrete – Non-Prestressed Beam Behavior 38
2.4.1 BCSA Cement Concrete –Prestressed Beam Behavior 40
2.5 Research Needs 47
2.5.1 SCC Mix Design and Fresh Properties 47
2.5.2 Bond Performance Characterization 48

2.5.3 Prestress Loss Prediction and Modeling 48
2.5.4 Creep and Shrinkage Relationships 48
3. Materials Testing 50
3.0 Introduction 50
3.1 Mix Design Development 51
3.1.1 Constituent Materials 52
3.1.2 Mixing Procedure 54
3.1.3 Fresh Concrete Property Testing 57
3.1.4 Test Batches and Results 58
3.1.5 Final Mix Proportions 65
3.2 Setting Time 66
3.2.1 Procedures 66
3.2.2 Results 71
3.3 Flexural Strength (Modulus of Rupture) 78
3.3.1 Procedures 78
3.3.2 Results 79
3.4 Modulus of Elasticity 84
3.4.1 Procedures 85
3.4.2 Results 87
3.5 Creep and Shrinkage 98
3.5.1 Creep Testing Procedures 98
3.5.2 Shrinkage Testing Procedures 110
3.5.3 Results 111
4. Structural Testing 124
4.0 Introduction 124
4.1 Direct Pullout Testing 124
4.1.1 Half-Scale Trial LBPT 126
4.1.2 Full-Scale LBPT 135
4.1.3 Results 146
4.2 Beam Specimen Design and Construction 154
4.2.1 Beam Design 154
4.2.2 Beam Fabrication Procedures 158

4.2.3 Trial Beams 170
4.2.4 Beam Production Data 185
4.3 Development Length Testing 193
4.3.1 Beam Testing 193
4.3.2 Results – Early (3 hr) Prestress Release 199
4.3.3 Results – Standard (24 hr) Prestress Release 225
4.3.4 Results – Development Length Summary 250
4.4 Transfer Length Testing 254
4.4.1 Instrumentation 254
4.4.2 Results 266
5. Prestress Losses: Measurement and Analysis 281
5.0 Introduction 281
5.1 Prestress Loss Measurement 281
5.1.1 Typical (24 hour) Prestress Release 283
5.1.2 Early (3 hour) Prestress Release 291
5.2 Elastic Shortening (ES) 297
5.3 Time-Dependent Losses 299
5.4 Time-Step Integration Model for Prestress Losses 302
5.4.1 Model Development and Experimental Verification 302
5.4.2 Model Validation with Data from Literature 313
5.5 Shrinkage and Creep Modelling for Prestress Loss Estimation 321
5.5.1 Shrinkage Modelling 323
5.5.2 Creep Modelling 327
6. Conclusions and Recommendations 332
6.0 Introduction 332
6.1 Conclusions – Material Testing 332
6.2 Conclusions – Structural Testing 335
6.3 Conclusions – Prestress Losses 339
6.4 Summary and General Conclusions 342
6.5 Recommendations for Future Work 346
References 350
Appendix A: Heat Evolution Plots from Calorimetry 357

Appendix B: Mix Quantities and Fresh Concrete Data 365
Appendix C: Detailed Pretensioning Records 380

List of Figures

Figure 1: Calcium sulfate contents of CSA cements (Bescher et al., 2018). 8
Figure 2: Dicalcium silicate (belite) contents of CSA cements (Bescher et al., 2018)..... 8
Figure 3: Transfer and development lengths in a pretensioned concrete member (Dang et al., 2016 after ACI 318) 15
Figure 4: Components of the ECADA test setup (Marti-Vargas et al., 2006b)..... 19
Figure 5: Stages of the ECADA test (Marti-Vargas et al., 2006b) 20
Figure 6: Tensioned pullout testing frames, before and after casting concrete (Stumps, 2016)... 22
Figure 7: Free end (top) and anchored end (bottom) of tensioned pullout testing frames (Stumps, 2016) 22
Figure 8: End slip measurements at transfer for tensioned pullout tests (Stumps, 2016)..... 23
Figure 9: Prestress losses and gains throughout the life of a pretensioned concrete girder (Tadros, et al., 2003). 29
Figure 10: Cross section of BCSA prestressed beam (Murray et al., 2019). 41
Figure 11: Reinforcement layout for BCSA bond tests with 0.6" strand (Bowser et al., 2020)... 43
Figure 12: Girder design utilized by Markosian et al. (2021) - (a) Profile and (b) Section 45
Figure 13: Small 1 ft^3 capacity rotating drum mixer (left) and medium 6 ft^3 capacity rotating drum mixer (right) – [listed capacities are maximum mix volumes not rated capacities]..... 55
Figure 14: Insulated container used for conditioning aggregates for setting time mixes 68
Figure 15: Calmetrix® Semi-Adiabatic Calorimeter..... 70
Figure 16: Correlation of calorimeter data with setting-time penetrometer 71
Figure 17: Calorimetry temperature curves for 70 ˚F mix series..... 72
Figure 18: Setting-time data from calorimeter with operating ranges highlighted..... 73
Figure 19: Calorimeter setting time data plotted with penetrometer setting time data for validation..... 75
Figure 20: Calorimeter setting-time data plotted against CTS workability time data 76
Figure 21: MOR Testing with Forney at Fears Lab..... 79
Figure 22: MOR data from RS Mix 2A..... 80
Figure 23: MOR data from RS Mix 2A normalized by square root of compressive strength..... 80
Figure 24: Compressive strength data from RS Mix 2A 81
Figure 25: MOR data from LBPT RS Mix 82
Figure 26: MOR data from LBPT RS Mix normalized by square root of compressive strength . 82
Figure 27: Compressive strength data from LBPT RS Mix 83
Figure 28: MOE test on Forney 1 (left) with compression test on Forney 2 (right)..... 86
Figure 29: MOE data from RS Mix 2C 88
Figure 30: Compressive strength data from RS Mix 2C..... 89
Figure 31: MOE data from RS Mix 2C normalized by square root of compressive strength 90
Figure 32: MOE data from RS Mix 2C normalized by compressive strength..... 91

Figure 33: MOE stress-strain data variation with time from RS Mix 2C 92
Figure 34: Best fit simple linear regression analysis to model/predict MOE using square root of compressive strength 93
Figure 35: MOE data from RS HI AGG Mix (round #2 high coarse aggregate) 95
Figure 36: Round #2 MOE compressive strength data (high coarse aggregate) 96
Figure 37: Best fit simple linear regression analysis to model/predict MOE using square root of compressive strength for Round #2 MOE with 0.82 C/F aggregate ratio 97
Figure 38: Creep measurement testing configuration (adapted from ASTM C512) 99
Figure 39: Creep specimen molds prepared for placement of the VWSG 100
Figure 40: Creep specimen VWSG installation 101
Figure 41: Typical metal stud after stripping forms (left) and DEMEC point glued to stud (right) 103
Figure 42: Setting reaction plates to load creep specimens 105
Figure 43: Levelling reaction plates to load creep frames 106
Figure 44: Creep frame with safety cage for stressing creep specimen in place 107
Figure 45: Creep specimens in final configuration, after load application, with instrumentation set and loading apparatus removed 108
Figure 46: DEMEC gage being used to take creep strain measurements 109
Figure 47: Raw VWSG data from creep testing (time measured from casting) 112
Figure 48: Raw VWSG data from creep testing (time measured from loading) 113
Figure 49: Compressive creep VWSG data with ES and shrinkage removed (from loading time) 114
Figure 50: Comparison of total strain measurements from VWSG and DEMEC 115
Figure 51: Comparison of creep and shrinkage strain measured with VWSG with DEMEC (ES removed from total) 116
Figure 52: Strains measured for creep test shrinkage companion specimens over time 121
Figure 53: Unrestrained drying shrinkage of RS Mix 2D measured using ASTM C157 122
Figure 54: LBPT specimen configuration (Arezoumandi et al., 2020 - after Logan, 1997) 125
Figure 55: Reinforcement cage for half-scale trial LBPT specimen 127
Figure 56: Formwork for half-scale trial LBPT specimen 128
Figure 57: Strands tied in place for half-scale trial LBPT specimen 129
Figure 58: Praschak®/MIX Mixer Systems® 21 ft^3 horizontal shaft concrete mixer at Fears Lab (model no. 21 DD RH) 130
Figure 59: Placing RS-SCC with hopper and overhead crane 131
Figure 60: RS-SCC filling half-scale LBPT specimen formwork 132
Figure 61: Half-scale LBPT specimen and compressive strength cylinders after casting 133
Figure 62: Testing setup for direct strand pullout with load and slip measurement used for the LBPT 134
Figure 63: Full-scale LBPT specimen formwork, reinforcing bar cage, and tied strands (clockwise from top left) 136
Figure 64: ASTM C33 fine aggregate (Dover sand) storage at Schwarz Ready Mix facility 137
Figure 65: Dolese 5/8" #3 cover coarse aggregate storage at Schwarz Ready Mix facility 138
Figure 66: 10 yd^3 concrete truck at Schwarz Ready Mix facility 139

Figure 67: Charging concrete truck with BCSA cement at Fears lab using construction forklift and two separate hoppers 140
Figure 68: Dispensing small portion of LBPT mix to measure the slump flow 141
Figure 69: Slump flow measurement for full-scale LBPT pour (clockwise from top left) 142
Figure 70: Positioning the mixer truck chute, filling the formwork, finishing the LBPT specimen surface, and a finished specimen (clockwise from top left)..... 143
Figure 71: Completed LBPT specimen (left) with MOR beams, compressive cylinders, and setting time test in progress, covered with green lid (right) 144
Figure 72: Hydraulic ram, load cell, and LVDT for strand pullout measurements 145
Figure 73: Compressive strength over time for the LBPT mix 147
Figure 74: LBPT strand pullout load results..... 148
Figure 75: LBPT strand bond strength results 151
Figure 76: LBPT strand bond strengths normalized by concrete compressive strength at time of testing..... 152
Figure 77: LBPT strand bond strengths normalized by square root of concrete compressive strength at time of testing..... 153
Figure 78: Section and elevation views for proposed beam design..... 155
Figure 79: Prestressing bed and abutment configuration in Fears Lab..... 159
Figure 80: Prestressing bed prepared for form panel placement, looking toward live end abutment..... 160
Figure 81: Prestressing bed with beam formwork in place, looking toward live end abutment. 161
Figure 82: Close-up view of beam reinforcement placed for casting..... 162
Figure 83: Beam formwork with strand, mild steel top bars, and WWR in place for casting.... 163
Figure 84: Filling beam formwork with concrete using a hopper and overhead crane 164
Figure 85: Strands chucked behind static bearing plate on dead end abutment (top) and strands chucked behind tensioning bulkhead on live end abutment with load cell (bottom)..... 165
Figure 86: Live end prestressing abutment configuration with hydraulic rams behind tensioning bulkhead and threaded bar/nut assembly to lock bulkhead in place after tensioning..... 167
Figure 87: Data acquisition hardware connected to load cell on live end abutment to measure stresses for strand jacking and prestress release (DAQ area protected with safety cage) 168
Figure 88: Trial beam B1 in the formwork after casting 172
Figure 89: View of trial beam B1 from the end after prestress release and cutting of the strands 173
Figure 90: Profile view of trial beam B1 after formwork removal..... 174
Figure 91: Rate of slump flow loss comparison for equivalent starting temperatures at 0.12 lb/cwt citric acid dosages with citric acid added after cement (FR1) and before and after cement (FR2) 176
Figure 92: 20-minute slump comparisons for mixes FR1 (conventional slump, left – 0 in.) and FR2 (slump flow, right – 16 in.) 177
Figure 93: Rate of slump flow loss comparison for comparable starting temperatures at 0.24 lb/cwt citric acid dosages with citric acid added after cement (FR3) and before and after cement (FR4) 179

Figure 94: 60-minute slump comparison for mixes FR3 (conventional slump, left – 0") and FR4 (slump flow, right – 15") 180
Figure 95: Conventional slump test of FR4 at 75 minutes (7.5 in.)..... 181
Figure 96: Trial beam B2 immediately after casting 183
Figure 97: Trial beam B2 being removed from the prestressing bed after forms are stripped and prestress released at 3.5 hours of age..... 184
Figure 98: Close-up view of Trial beam B2 showing smooth beam surface free of bug holes.. 185
Figure 99: Time history of apparent change in strand stress between strand tensioning and prestress release as indicated by load cell located between chuck and live end abutment..... 190
Figure 100: Span and support configuration for development length bending tests 194
Figure 101: Development length beam testing apparatus with instruments..... 196
Figure 102: LVDT's mounted to strands with block clamps to measure strand slip..... 198
Figure 103: Trial beam B2 load-deflection and load-slip response (3 ft - 4 in. dead end embedment and 6 ft - 9 in. live end embedment) 200
Figure 104: Trial beam B2 dead end after failure showing flexural cracking and top crushing 201
Figure 105: Trial beam B2 live end after failure showing flexural cracking and top crushing.. 202
Figure 106: Beam B9-3DV load-deflection and load-slip response (6 ft embedment) 203
Figure 107: Cracking pattern at failure for B9-3DV with 6 ft embedment (dead end) 205
Figure 108: Compression block crushing and flexural cracking in beam B9-3DV..... 206
Figure 109: Beam B6-3DV load-deflection and load-slip response (4 ft embedment) 207
Figure 110: Cracking pattern at failure for B6-3DV with 4 ft embedment (live end)..... 209
Figure 111: Compression block crushing and flexural cracking in beam B6-3DV (dead end).. 210
Figure 112: Beam B10-3DV load-deflection and load-slip response (3.5 ft embedment)..... 211
Figure 113: Cracking pattern at failure for B10-3DV with 3.5 ft embedment (dead end) 213
Figure 114: Compression block crushing and flexural cracking in B10-3DV (live end)..... 214
Figure 115: Beam B7-3DV load-deflection and load-slip response (3 ft embedment) 215
Figure 116: Cracking pattern at failure for B7-3DV with 3 ft embedment (dead end) 217
Figure 117: Comparison of cracking pattern at failure for B7-3DV with 3 ft embedment - live end (top) and dead end (bottom)..... 218
Figure 118: WWR failure modes from beam shear - welded junction failure (left) and rupture of gross section (right)..... 219
Figure 119: Beam B8-3DV load-deflection and load-slip response (2.5 ft embedment)..... 221
Figure 120: Cracking pattern at failure for B8-3DV with 2.5 ft embedment (live end)..... 223
Figure 121: Vertical and diagonal cracking near support location in beam B8-3DV (dead end) 225
Figure 122: Beam B16-24DV load-deflection and load-slip response (6 ft embedment)..... 226
Figure 123: Cracking pattern at failure for B16-24DV with 6' embedment (with crack progression through the test, clockwise from top left – dead end)..... 228
Figure 124: Compression block crushing and flexural cracking in B16-24DV (dead end) 229
Figure 125: Beam B15-24DV load-deflection and load-slip response (4 ft embedment)..... 230
Figure 126: Cracking pattern at failure for B15-24DV with 4 ft embedment (live end)..... 232
Figure 127: Compression block crushing and flexural cracking in B15-24DV (dead end) 233
Figure 128: Beam B12-24DV load-deflection and load-slip response (3.5 ft embedment)..... 234

Figure 129: Cracking pattern at failure for B12-24DV with 3.5 ft embedment (dead end) 236
Figure 130: Compression block crushing and flexural cracking in B12-24DV (live end) 237
Figure 131: Beam B13-24DV load-deflection and load-slip response (3 ft embedment) 238
Figure 132: Cracking pattern at failure for B13-24DV with 3 ft embedment (live end) 240
Figure 133: Cracking pattern at failure for B13-24DV with 3 ft embedment (dead end) 242
Figure 134: WWR damage from shear failure on test B13-24DV 243
Figure 135: Beam B14-24DV load-deflection and load-slip response (2.5 ft embedment) 245
Figure 136: Cracking pattern at failure for B14-24DV with 2.5 ft embedment (live end) 247
Figure 137: WWR failure mode from shear failure in beam B14-24DV – tensile yielding of gross section 248
Figure 138: Magnified view of tensile yielding in WWR after beam B14-24DV shear failure. 249
Figure 139: Failure moment versus strand embedment to identify development length for early (3 hr) prestress release 251
Figure 140: Failure moment versus strand embedment to identify development length for typical (24 hr) prestress release 253
Figure 141: Mounting technique for VWSG instrumentation 255
Figure 142: VWSG instrumentation schematic for long-term strain monitoring (TR series beams) 257
Figure 143: Longitudinal distribution of VWSG (interior DEMEC studs also visible on each formwork side) 258
Figure 144: Longitudinal distribution of DEMEC instrumentation for surface strain profile measurement 261
Figure 145: Typical DEMEC strain gage measurement for TR series beam 263
Figure 146: Typical strand draw-in measurement using a depth micrometer for TR series beam 265
Figure 147: Internal strain profiles from VWSG data at prestress release and 56 days 266
Figure 148: Internal strain profiles from VWSG data at 56 days and 120 days 268
Figure 149: External strain profiles determined from DEMEC data at prestress release (VWSG strain profiles shown for comparison) 269
Figure 150: 95% AMS method applied to a typical beam end strain profile (B5-24TR, live end, west side) 271
Figure 151: Average transfer length results at prestress release and at 56 days for 3 hour and 24 hour prestress release 277
Figure 152: Beams in storage for long-term prestress loss measurement in Fears Lab high bay 282
Figure 153: Early-age changes in midspan strain for Beam B3-24TR: (A) casting and setting, (B) shrinkage and thermal strains, (C) elastic shortening at prestress release, (D) time-dependent deformation (primarily creep and shrinkage), and (E) moving beam from prestressing bed to long-term supports 284
Figure 154: Time-dependent changes in midspan strain for Beam B3-24TR 286
Figure 155: Midspan time-dependent strain comparison for 24 hour release beams 287
Figure 156: Non-prestressed companion beam for shrinkage measurements 289
Figure 157: Shrinkage of non-prestressed companion beam for B3-24TR 290

Figure 158: Early-age changes in midspan strain for B4-3TR: (A)+(B) casting, setting, and shrinkage/thermal strains; (C) elastic shortening at prestress release; (D) time-dependent deformation (primarily creep and shrinkage); and (E) moving beam from prestressing bed to long-term supports 292
Figure 159: Time-dependent changes in strain at midspan for beam B4-3TR 294
Figure 160: Midspan time-dependent strain comparison for 3 hour release beams 295
Figure 161: Shrinkage of non-prestressed companion beam for B4-3TR 296
Figure 162: Comparison of measured and theoretical ES prestress loss values 298
Figure 163: Time-dependent (primarily creep and shrinkage) losses for TR series prestressed beams 300
Figure 164: Itemized breakdown for sources of measured long-term (240 day) prestress losses 301
Figure 165: Comparison of measured time-dependent prestress losses with time-step integration model results 308
Figure 166: Comparison of long-term prestress loss estimation approaches for beam B4-3TR, 3 hour release (*Denotes 1.2 ksi lump sum addition for strand relaxation) 310
Figure 167: Comparison of long-term prestress loss estimation approaches for beam B3–24TR, 24 hour release (*Denotes 1.2 ksi lump sum addition for strand relaxation) 312
Figure 168: Validating time-step model with BCSA cement concrete prestress loss data from Bowser (2016) and comparing with existing AASHTO LRFD (7th edition) and ACI (Zia et al., 1979) models 314
Figure 169: Average measured time-dependent prestress losses from Floyd and Ramseyer (2013) compared with multiple estimation techniques, using creep data loaded at 24 hrs under initial stress ratio of $0.48f'_c$ for material models 317
Figure 170: Average measured time-dependent prestress losses from Floyd and Ramseyer (2013) compared with multiple estimation techniques, using creep data loaded at 28 days under initial stress ratio of $0.40f'_c$ for material models 319
Figure 171: Average measured time-dependent prestress losses from Floyd and Ramseyer (2013) compared with time-step model and adjusted AASHTO refined method using creep data loaded at 28 days and at 24 hr age 320
Figure 172: Comparison of measured RS-SCC shrinkage with modelled values for ASTM C157 testing without adjustment to models 324
Figure 173: Comparison of measured RS-SCC shrinkage with modelled values for ASTM C157 testing with models adjusted for ultimate shrinkage strain of RS-SCC 325
Figure 174: Comparison of measured RS-SCC creep with modelled values for creep specimens loaded at 3 hour age 328
Figure 175: Comparison of measured RS-SCC creep with modelled values for creep specimens loaded at 1 day age 329
Figure 176: Comparison of measured RS-SCC creep with modelled values for creep specimens loaded at 28 day age 330
Figure 177: Calorimetry temperature curve for Mix T3, 50 $^{\circ}$F, 0 lb/cwt citric acid 357
Figure 178: Calorimetry temperature curve for Mix T0, 50 $^{\circ}$F, 0.1 lb/cwt citric acid 358
Figure 179: Calorimetry temperature curve for Mix T1, 50 $^{\circ}$F, 0.2 lb/cwt citric acid 358

Figure 180: Calorimetry temperature curve for Mix T2, 50 °F, 0.3 lb/cwt citric acid 359
Figure 181: Calorimetry temperature curve for Mix T4, 70 °F, 0 lb/cwt citric acid 359
Figure 182: Calorimetry temperature curve for Mix T5, 70 °F, 0.1 lb/cwt citric acid 360
Figure 183: Calorimetry temperature curve for Mix T6, 70 °F, 0.2 lb/cwt citric acid 360
Figure 184: Calorimetry temperature curve for Mix T7, 70 °F, 0.3 lb/cwt citric acid 361
Figure 185: Calorimetry temperature curve for Mix T8, 70 °F, 0.4 lb/cwt citric acid 361
Figure 186: Calorimetry temperature curve for Mix T9, 80 °F, 0.1 lb/cwt citric acid 362
Figure 187: Calorimetry temperature curve for Mix T10, 80 °F, 0.2 lb/cwt citric acid 362
Figure 188: Calorimetry temperature curve for Mix T11, 80 °F, 0.3 lb/cwt citric acid 363
Figure 189: Calorimetry temperature curve for Mix T12, 80 °F, 0.4 lb/cwt citric acid 363
Figure 190: Calorimetry temperature curve for Mix T13, 80 °F, 0.5 lb/cwt citric acid 364

List of Tables

Table 1: Chemical compositions of a function-based CSA cement classification (Bescher et al., 2018). 7
Table 2: Measured and estimated prestress losses from NCHRP 496 (Tadros et al., 2003) 33
Table 3: Comparison of predicted prestress losses with external research to verify accuracy of proposed models in NCHRP 496 (Tadros et al., 2003) 34
Table 4: Mix design proportions for BCSA and PC concrete (G. Cook, 2018). 38
Table 5: Mixture proportions for BCSA concrete (Murray et al., 2019). 41
Table 6: Mix designs and concrete properties for BCSA bond tests with 0.6" strand (Bowser et al., 2020). 44
Table 7: Batch Designation Overview with Key Tests (*Indicates Cement Lot #2 was Compromised) 51
Table 8: Targeted Performance Specifications for RS-SCC 52
Table 9: Aggregate Properties for RS-SCC 54
Table 10: Test Batches for Mix Development (No Fly Ash) 60
Table 11: Test Batch Results (No Fly Ash) 61
Table 12: Test Batches for Mix Development (with Fly Ash) 63
Table 13: Test Batch Results (with Fly Ash) 64
Table 14: Mix Design Proportions for RS-SCC 66
Table 15: Testing Matrix with Citric Acid Dosages used to Characterize Setting Time/Temperature Relationships 69
Table 16: VWSG Summary of Instantaneous Strains, Creep Strains, and Creep Coefficients .. 118
Table 17: Comparison of Calculated Elastic Strains and those Measured using VWSG and DEMEC Strain Gages 120
Table 18: Summary of Beam Design Properties 156
Table 19: Prestressed Beam Testing Matrix and Key Concrete Properties (f'_{ci}=concrete compressive strength at release, f'_c= concrete compressive strength at 28 days, except as noted * at 35 days, + at 21 days) 186
Table 20: Pretensioning Data for Early (3 hr) Release Beams 187
Table 21: Pretensioning Data for Typical (24 hr) Release Beams 188
Table 22: Development Length Test Summary for Early (3 hr) Prestress Release Beams 250

Table 23: Development Length Test Summary for Typical (24 hr) Prestress Release Beams... 250
Table 24: VWSG Instrumentation Layout for Long-Term Strain Monitoring (TR Series Beams) 257
Table 25: DEMEC Instrumentation Layout for Long-Term Strain Monitoring (TR Series Beams) 260
Table 26: Strand Draw-In at Release for all Prestressed Beams 272
Table 27: Comparison of Transfer Length Measurement Techniques at Release 274
Table 28: Comparison of Transfer Length Measurement Techniques at 56 Days 275
Table 29: Measured and Theoretical Elastic Shortening Prestress Losses with Relative Difference 298
Table 30: Mix Data for Beam B2 - Trial Pour 365
Table 31: Mix Data for Beam B3 – 24 Hour Transfer Length Testing 366
Table 32: Mix Data for Beam B4 – 3 Hour Transfer Length Testing 367
Table 33: Mix Data for Beam B5 – 24 Hour Transfer Length Testing 368
Table 34: Mix Data for Beam B6 – 3 Hour Development Length Testing 369
Table 35: Mix Data for Beam B7 – 3 Hour Development Length Testing 370
Table 36: Mix Data for Beam B8 – 3 Hour Development Length Testing 371
Table 37: Mix Data for Beam B9 – 3 Hour Development Length Testing 372
Table 38: Mix Data for Beam B10 – 3 Hour Development Length Testing 373
Table 39: Mix Data for Beam B11 – 3 Hour Transfer Length Testing 374
Table 40: Mix Data for Beam B12 – 24 Hour Development Length Testing 375
Table 41: Mix Data for Beam B13 – 24 Hour Development Length Testing 376
Table 42: Mix Data for Beam B14 – 24 Hour Development Length Testing 377
Table 43: Mix Data for Beam B15 – 24 Hour Development Length Testing 378
Table 44: Mix Data for Beam B16 – 24 Hour Development Length Testing 379
Table 45: Prestress Data for Beam B2 - Trial Pour 380
Table 46: Prestress Data for Beam B4 – 3TR 381
Table 47: Prestress Data for Beam B6 – 3DV 382
Table 48: Prestress Data for Beam B7 – 3DV 383
Table 49: Prestress Data for Beam B8 – 3DV 384
Table 50: Prestress Data for Beam B9 – 3DV 385
Table 51: Prestress Data for Beam B10 – 3DV 386
Table 52: Prestress Data for Beam B11 – 3TR 387
Table 53: Prestress Data for Beam B3 – 24TR 388
Table 54: Prestress Data for Beam B5 – 24TR 389
Table 55: Prestress Data for Beam B12 – 24DV 390
Table 56: Prestress Data for Beam B13 – 24DV 391
Table 57: Prestress Data for Beam B14 – 24DV 392
Table 58: Prestress Data for Beam B15 – 24DV 393
Table 59: Prestress Data for Beam B16 – 24DV 394

Abstract

In recent years, urgency for adopting sustainable materials has come to the forefront of the cement and concrete industries. Belitic calcium sulfoaluminate (BCSA) cement is an alternative cement which has a production energy demand of up to 60% less than portland cement and emits 30-50% less CO2. Although BCSA cement has been used in the U.S. for pavements, bridge decks, floors, and tanks, information on characteristics relevant to prestressed concrete is lacking. The purpose of this research was to establish strand bond, prestress loss, and time-dependent performance characteristics for BCSA cement concrete to increase production efficiency and member performance for precast, prestressed concrete. BCSA cement-based concrete can reach minimum strength for prestress transfer much sooner than portland cement concrete due to inherent rapid hardening properties. These time savings could allow precasters to clear stressing beds more quickly and streamline productivity, but the impact of early loading on long-term behavior is unknown. Mix designs for self-consolidating BCSA cement concrete were developed to provide sufficient workable time at various temperatures while reaching compressive strength required for prestress release in 2-3 hours. Material properties including flexural strength, elastic modulus, creep, and shrinkage were established. Untensioned large block pullout tests were used to characterize bond performance with age and fifteen 20 ft long prestress girders were fabricated and tested for strand transfer length, development length, and long-term prestress losses. Measured strand bond strengths were adequate and transfer and development lengths were shorter than code predictions. The measured material properties were used to model prestress losses which were compared with the values measured from the girder tests. Measured prestress losses were significantly lower than existing equations indicated, while models developed from material property data produced more accurate estimates.

1. Introduction

1.0 Background and Overview

Calcium sulfoaluminate (CSA) cements are a special class of hydraulic cementitious materials which can either be used in a concrete mixture as the primary binder to entirely replace conventional portland cement (PC), or as an additive in proportion with PC, depending on the type of CSA cement used and the desired concrete properties (Bescher et al., 2018). CSA cements vary from PC based upon their respective chemical constituents and reaction processes. Whereas portland cement concrete (PCC) gains strength based on the hydration of belite (dicalcium silicates, C_2S) and alite (tricalcium silicates, C_3S), CSA cement gains strength primarily through the hydration of calcium sulfoaluminates (tetracalcium trialuminosulfates, $C_4A_3\bar{S}$). One class of commercially available CSA cements utilizes belite in conjunction with calcium sulfoaluminates to work together in separate reaction phases and is known as belitic calcium sulfoaluminate (BCSA) cement (Bescher et al., 2018). When used as the binder in place of PC, BCSA cement results in rapid-setting concrete with very high early strength compared to PCC (D. Frank, 2011; T. Bowser, 2016; J. Roswurm, 2018). Concrete mixtures utilizing BCSA cement typically have excellent mechanical properties, including high strength, low shrinkage, and good durability (Bescher et al., 2012). In addition to high mechanical performance, BCSA cements offer increased sustainability, because the production of these cements is less energy and carbon dioxide intensive compared to PC (Hicks et al., 2015).

The chemical composition and mechanical properties of BCSA cements lend significant appeal to utilizing them in the precast, prestressed concrete industry. BCSA cement could be particularly advantageous for precast concrete, because its rapid setting time and very high early strength could provide for forms to be stripped and strands to be released sooner so that beams

can be moved to free up prestressing beds more quickly (Thomas et al., 2018). In addition, techniques like steam curing, used to accelerate strength gain, would not be necessary. These advantages could make BCSA cement a means for precasters to greatly increase production and eliminate costly inefficiencies in the production of pretensioned, prestressed concrete elements.

Since rapid-setting BCSA cements have not been widely applied to prestressed concrete in the United States, many critical research topics must be addressed in order to ensure that these materials can be safely and effectively used in the prestressed concrete industry on a large scale. The focus of this research is to investigate the bond performance and prestress loss behavior of pretensioned, prestressed BCSA cement concrete; to compare these behaviors to the requirements and predictions of current design codes; and to develop improved bond and prestress loss prediction models specifically for BCSA cement concrete.

1.1 Motivation

The primary motivation for conducting this research pertains to the significant potential for RS BCSA cement concrete to increase production efficiency and long-term performance of precast, prestressed elements. The rapid set and high early strength of BCSA cement concrete will allow for forms to be stripped and strands released sooner, freeing up stressing beds more quickly. In addition to the potential of increased production efficiency, preliminary studies have indicated BCSA cement may exhibit excellent bonding performance and low prestress losses, which could lead to improved performance throughout the lifespan of the member.

The nature of this material makes the research well suited to a doctoral dissertation, because the concept of applying RS BSCA cement in pretensioned, prestressed concrete has not been widely implemented or studied in the United States; only a few known studies in the U.S. have approached the issue. As discussed later, these studies were preliminary in nature and were

only intended to serve as proof of the concept and to gain an initial understanding of the material behavior in a prestressing application. Therefore, this dissertation topic is well-suited to both make a broad impact in the field of structural design of prestressed concrete and to fulfill the educational mission of investigating seminal and rigorous subject matter.

1.2 Objectives

- Determine whether RS BCSA cement can be used to develop a SCC concrete mix with reasonably consistent slump flows (herein referred to as RS-SCC).
- Expand existing understanding of the impact that retarding and super plasticizing admixtures have on the setting time of RS-SCC at a range of temperatures.
- Characterize the strand bond capability of RS-SCC applied to pretensioned, prestressed concrete.
- Investigate whether the age of loading affects the mechanical properties of RS-SCC in either the immediate or long-term sense.
- Investigate prestress losses for RS-SCC pretensioned, precast beams with both experimental and analytical approaches.
- Accumulate existing data regarding the creep and shrinkage behavior of BCSA cement concrete, and fill gaps where such data is limited or unavailable.

1.3 Goals

- Show that a RS-SCC with BCSA cement can be successfully utilized in casting pretensioned, prestressed concrete specimens.

- Develop quantitative mix design recommendations for RS-SCC that could guide precasters in compensating for ambient temperature changes and achieving acceptable working time before set.
- Determine whether current design standards for transfer and development length in pretensioned, prestressed concrete are conservative with respect to RS-SCC.
- Directly compare the pullout strength of strand embedded in RS-SCC at multiple progressive ages to investigate maturity effects on strand bond.
- Compare prestress losses for RS-SCC to estimates from current design standards for PCC.
- Develop prestress loss models specifically for RS-SCC so that designers can accurately estimate cambers, deflections, and service stresses.
- Utilize accumulated data to develop creep and shrinkage models for RS-SCC, which can be used to make predictions about the long-term behavior of prestressed elements made with this material.

2. Literature Review

2.1 CSA Cement

2.1.1 History

The development of early CSA cements dates back as far as the early 1890's, when the French researcher Candlot discovered that tricalcium aluminates in aqueous solution with calcium sulfate would produce "hydrated salts of calcium sulfoaluminate" which contained a unique expansive reaction product that is now known as ettringite (Klein et al., 1961). In the 1930's, Lerch, Ashton, and Bogue showed these calcium sulfoaluminate hydrates could come with differing levels of sulfates, with the low sulfate varieties not contributing to expansive behavior like those with higher sulfate levels (Klein et al., 1961). By the late 1940's, the French engineer H. Lossier had made major advances in utilizing CSA based reaction products to form expansive concrete; although these expansive concretes were not entirely perfected, other researchers followed suit in investigating similar materials (Klein et al., 1961 and Lin et al., 1963). This very early research laid the groundwork for the development of modern CSA cement in the United States around 45 years ago. In 1975, a patent was filed for a rapid-setting cement which was designed to use calcium sulfoaluminates in conjunction with dicalcium silicates (belite) to work together in separate reaction phases (Bescher et al., 2018). This early BCSA cement patent was largely based on research performed in the early 1960's at California Berkeley by Alexander Klein, who was pivotal in early expansive CSA cement in the U.S. (Klein et al., 1961; Lin et al., 1963; Bescher et al., 2018). In fact, the primary reactant in modern CSA/BCSA cements, known as ye'elimite as a naturally occurring mineral, has been named "Klein's compound" in his honor (Bescher et al., 2012). Since that time, modern CSA and BCSA cements with both rapid-setting and expansive properties have become readily commercially available in the U.S.

2.1.2 Chemistry and Composition

CSA cements undergo significantly different hydration reactions than PC because of their unique chemical composition. Unlike PC, CSA cement contains no alite, and therefore does not gain any of its early setting or strength properties from the production of CSH gel. Instead, calcium sulfoaluminates are hydrated together with calcium sulfate (gypsum) and free lime, according to a number of possible hydration reactions, which all result in rapid ettringite production. It is this formation of ettringite that results in the desirable mechanical properties of CSA cement-based concrete at early ages. Equations (1) and (2) present two chemical reactions that represent generalizations of the many hydration reactions that CSA cements may undergo (Bescher et al., 2018):

$$C_4A_3\bar{S} + 8C\bar{S} + 6C + 96H \rightarrow 3C_6A\bar{S}_3H_{32} \quad (1)$$

$$C_4A_3\bar{S} + 2C\bar{S} + 38H \rightarrow C_6A\bar{S}_3H_{32} + 2AH_3 \quad (2)$$

Note that the primary reaction product in either case is ettringite ($C_6A\bar{S}_3H_{32}$). In Equations (1) and (2), the proportion of calcium sulfoaluminates ($C_4A_3\bar{S}$), relative to calcium sulfates or gypsum ($C\bar{S}$), has a profound impact on both the hydration kinetics and the resulting mechanical behavior of the concrete. In fact, it is this proportion, coupled with the presence of belite in the cement, if any, which partially dictates whether the concrete will behave in an expansive manner or exhibit rapid-setting properties with high early strength (Bescher et al., 2018). Importantly, for BCSA cements, the presence of belite in the cement means that hydration reactions similar to those in PC will occur slowly over time; As a result, with proper curing, some of the long-term strength gain of BCSA cement is due to CSH gel production (Murray et al., 2019).

Since CSA cements encompass such a diverse array of mechanical properties based upon their chemical composition, a function-based classification system has been proposed in the literature. This classification system is similar to that used by ASTM C 150 to divide PC into 5 distinct types, based upon their behavior and suitable applications. Such a classification system was suggested by Bescher et.al. in 2018 and is presented here in Table 1.

Table 1: Chemical compositions of a function-based CSA cement classification (Bescher et al., 2018).

	Calcium Sulfoaluminate	Dicalcium Silicate	Calcium Sulfate	Other
Type A - Accelerating Additive	35 - 45%	0 - 20%	10 - 30%	5 - 55%
Type B - Belitic Calcium Sulfoaluminate Cement	20 - 30%	40 - 60%	5 - 25%	0 - 35%
Type C - Expansive Additive	10 - 20%	10 - 30%	40 - 60%	0 - 40%
Type K - Shrinkage Compensating Cement	1 - 10%	30 - 50%	1 - 20%	20 - 70%

Additionally, graphs showing how the proportions of CSA, calcium sulfate (gypsum), and belite affect the cement classifications are shown in Figures 1 and 2. Table 1, as well as Figures 1 and 2, show that expansive CSA cements are richer in calcium sulfate than the other types. This mirrors the early observations of Lerch, Ashton, and Bogue concerning the effect of sulfate levels on the behavior of CSA cements (Klein et al., 1961). Figure 2 shows that “Type B CSA” cements are richer in dicalcium silicate (belite) than the other types; this is the defining feature of a BCSA cement according to this classification. Also note, however, that all 4 types contain belite in some proportion, which is typically the case for modern, commercially available CSA cements in the U.S. Also note in Figures 1 and 2 that each class of cement contains some proportion of “other” constituents. For CSA and BCSA cements, these “other” constituents are often proprietary information. Hereafter, any CSA cements that are mentioned will be of the

Type B class as shown in Table 1, Figure 1, and Figure 2, and will be referred to as BCSA cement. Concrete produced with this material will be referred to as BCSA cement concrete.

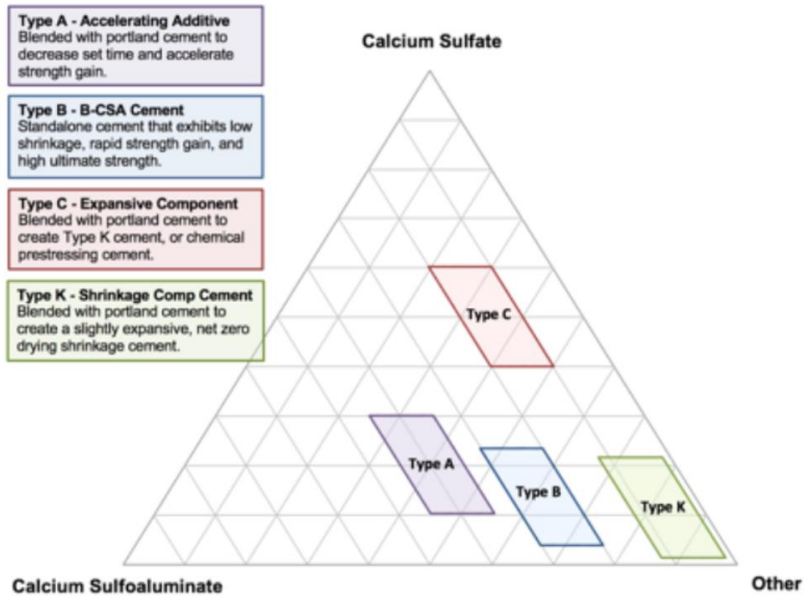

Figure 1: Calcium sulfate contents of CSA cements (Bescher et al., 2018).

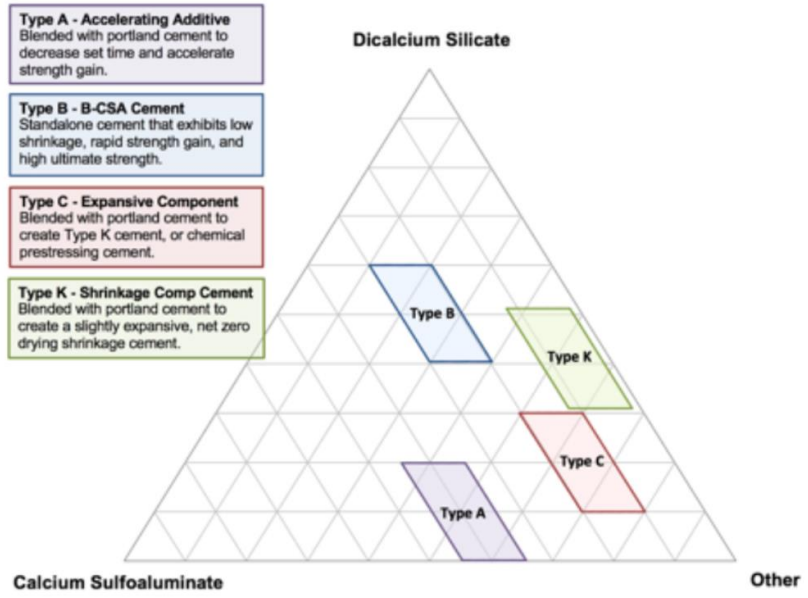

Figure 2: Dicalcium silicate (belite) contents of CSA cements (Bescher et al., 2018).

2.1.3 Properties

First, BCSA cement concrete provides high strength at very early ages; compressive strengths exceeding 3-4 ksi can be obtained at an age of 1-3 hours (D. Frank, 2011; T. Bowser, 2016; J. Roswurm, 2018). BCSA cement-based concretes also exhibit extremely low shrinkage, with ultimate shrinkage strains sometimes less than 200-300 microstrains (J. Roswurm, 2018; S. Tanksley, 2018; Afroughsabet et al., 2019). Although very little research has approached directly measuring creep in BCSA cement concrete, very low prestress loss measurements in precast, pretensioned concrete beams indicate that these materials experience reduced creep compared to PCC (Murray et al., 2019 and Bowser et al., 2020). In addition, research has shown that concrete made with BCSA cement exhibits excellent durability, particularly against freeze-thaw damage and sulfate attack (Bescher et al., 2016 and de Bruyn et al., 2017). While some have expressed concern over carbonation of BCSA cement-based concrete being a durability concern (Moffatt and Thomas, 2018), data has shown that if ordinary CSA cement contains adequate calcium sulfate and the concrete is mixed with a sufficiently low w/c ratio, carbonation is of little concern (Hargis et al., 2017 and Winnefeld et al., 2018). Field studies and laboratory testing have also indicated that BCSA cement concrete exhibits high flexural strength and fatigue performance, even after many years in service (Bescher and Ramseyer, 2013). Finally, BCSA cements also come with the added benefit of decreased environmental impact compared to PC. Due to the presence of gypsum and other miscellaneous, often proprietary, materials, BCSA cements require less limestone, leading to fewer carbon dioxide emissions during clinker production; they are kilned at temperatures around 250 degrees Celsius lower than PC, resulting in less required energy to heat the kilns; and they are believed to be incrementally easier to grind than PC cement clinkers, which reduces electricity demands during production (Bescher et al., 2012; Imbabi et al., 2012; Hicks et al., 2015; Bescher et al., 2018). Overall, BCSA cement production has a

reduced energy demand of up to 60% compared to PC and emits 30-50% less carbon dioxide (Thomas et al., 2018).

2.1.4 Challenges

One challenge with BCSA cement-based concrete is its short setting time, which is also one of its primary benefits. Set can occur in as little as 15 minutes for BCSA cement concrete, without use of retarding admixtures. This is because all CSA cements produce ettringite when they are hydrated, and the reaction kinetics of ettringite production are much faster than early CSH production in PCC. While this property makes BCSA cements desirable for high early strength applications, a side effect of these rapid setting times is that BCSA cement concretes experience a high rate of slump loss. This can be dealt with by using retarders, such as citric acid in granular or liquid form, and high-range water reducing admixtures (HRWRA), although more research is needed to characterize the admixture requirements of BCSA mix designs at various temperatures (Bowser, et al., 2020).

Another challenge concerning BCSA cements is their cost, which is around 4 times more than PC right now (Thomas et al., 2018). Several considerations affect this cost, however. First, BCSA cements create high strength concrete, and oftentimes less material is required to achieve a given strength when compared to PC. Additionally, the increased durability of BCSA concretes can result in lower overall life cycle costs. Researchers also expect that as the market share of BCSA's continues to grow, increased production of these materials will begin to drive the costs down (Thomas et al., 2018).

A final concern which has been raised about CSA and BCSA cement concrete pertains to suggestions that these materials could have a reduced corrosion resistance and increased porosity and permeability compared to conventional concrete (Alapati et al., 2022 and Ley, 2022). The

researchers raising these concerns have suggested that applying commercially available polymer based inhibitors may satisfactorily address the issue. Although formal durability testing is beyond the scope of this dissertation, it is reasonable to assume that since the dimensional stability of CSA/BCSA cement concrete is so high and its cracking potential generally so low that its effective in-service durability performance might be better than small-scale laboratory tests could indicate. This hypothesis is supported by a lack of corrosion and permeability complaints concerning CSA and BCSA cement concrete in the field.

2.1.5 Applications

Concrete mixtures utilizing CSA or BCSA based cements as the primary binder have been used for many applications in the last 40-45 years in the United States. Additionally, these cements have been used extensively in China since the 1970's (Thomas et al., 2018); however, this discussion is limited only to case studies where CSA and BCSA cements have been applied domestically. Although CSA and BCSA materials in the U.S. were seen as specialty or niche products in years past, their outstanding properties and widespread success have begun to drive more interest in mainstream, high-profile applications.

The California Department of Transportation (Caltrans) has successfully used rapid-setting BCSA cement concrete to replace more than 70,000 individual concrete highway pavement panels since the early 1990's, constituting over 200 lane miles of repairs and replacement (Ramseyer and Perez, 2009). Rapid-setting BCSA cements and Type K shrinkage compensating CSA cement have been used to perform runway and taxiway repairs and extensions at the Seattle-Tacoma and Rockford, IL airports respectively, and these repairs and additions have shown tremendous durability and longevity over the course of more than 20 years (Bescher and Ramseyer, 2013; CMT Inc., 1995; Herrin and Naughton, 2003; M. Chusid, 2006).

CSA based concrete has been applied to bridge related applications, primarily for cast in place (CIP) decks. The Ohio Turnpike Commission (OTC) has reported tremendous success using Type K CSA cement for shrinkage compensating concrete bridge decks (Phillips et al., 1997), and experimental studies using scaled bridge decks have also reported positive findings (Richardson et al., 2014). Additionally, rapid-setting BCSA cement was used on a rehabilitation project for a conventionally reinforced concrete box-girder bridge in San Francisco, CA. The repair of this heavily trafficked bridge was performed on time with an aggressive schedule, made possible by the excellent performance and high early strength gain of the BCSA cement concrete (P. Fimrite, 2014 and Maggenti et al., 2015).

2.2 Prestressed Strand Bond

Modern prestressing strand typically consists of 7 individual high strength steel wires, 6 of which are wrapped in a helical manner around a central "king" wire. For pretensioned applications, the strands are typically tensioned to 75% of their ultimate strength, before concrete is cast around the strand and into its forms. Once the concrete gains sufficient strength, the tension in the strand is released; at this time, bond strength between the strand and the concrete matrix is solely responsible for ensuring that the prestress force is transmitted into the member. Therefore, the strand bond behavior affects most important properties of the member, including flexure and shear strength, camber and deflection, and time-dependent prestress losses.

2.2.1 Strand Bond Theory

Strand bond performance in prestressed concrete is affected by numerous variables, including but not limited to, strand size and effective prestress (ACI 318, 2014 and AASHTO, 2017), strand spacing and arrangement (Dang et al., 2016), concrete strength (Ramirez and Russell, 2008), and strand surface condition (Logan, 1997 and Dang et al., 2014). There are three primary mechanisms which each are theorized to contribute to the total strand bond for a

pretensioned member. These mechanisms include adhesion, Hoyer's effect, and mechanical interlock (Janney, 1954 and Dang et al., 2014). Adhesion is the chemical bond that forms between the paste and the strand; adhesion is eliminated if any strand slip occurs. Hoyer's effect is fundamentally related to the friction force between the strand and the surrounding paste. A friction force is generated when a normal force acts between two surfaces that have a mutual coefficient of friction between them. In pretensioned concrete, the strand and concrete characteristics determine the coefficient of friction. The normal force between them is generated by pressure exerted on the concrete matrix due to lateral expansion of the strand when tension is released and/or the strand slips, according to Poisson's effect. Lastly, mechanical interlock is formed by concrete paste grabbing onto the perimeter of the helical prestressing strand through a mechanism which is analogous to interlock between concrete and ordinary deformed bar reinforcing steel (Janney, 1954 and Dang et al., 2014). Whereas mechanical interlock for conventionally reinforced concrete utilizes bonding action with the macroscopic surface profile of steel rebar, the individual wires of a prestressing strand are relatively smooth to the naked eye. Nevertheless, mechanical interlock with prestressing strand still exists. The entire strand experiences mechanical interlock as a unit, because the concrete matrix provides rotational resistance against the helical strand twisting as it slips. Mechanical interlock is also established at a smaller scale, because microscopic surface irregularities and slight manufactured slits or indentations on the individual wires that constitute the strand as a whole are also engaged.

2.2.2 Estimation of Strand Bond

2.2.2.1 Direct Pullout

There are several ways that the quality of strand bond can be assessed or quantified. One way of determining strand bond performance is to directly measure the force required to pull a strand out of a concrete element, and to correlate this result to the true bond strength. Direct

pullout tests for individual strand specimens were sequentially developed by several organizations, including the PTI (Post-Tensioning Institute) bond test, the NASP (North American Strand Producers) bond test, and the STSB (Standard Test for Strand Bond). Each of these tests shared a similar basis of directly pulling an untensioned strand out of a cylindrical specimen. The STSB has been accepted by ASTM International, and ASTM A1081 is now the standard test method for single-strand direct pullout testing (ASTM A1081). In addition to these single strand pullout tests, the Moustafa or Large Block Pullout Test (LBPT) offers an alternative direct pullout bond test but utilizes a geometry which allows many strands to be individually pulled from the same specimen. Researchers have reported pros and cons of both the ASTM A1081 and the LBPT/Moustafa pullout tests. The main drawback of these direct pullout tests is that they are performed on strands without tension, meaning that they may not accurately measure the full bond strength of the strand due to the omission of frictional bond from Hoyer's effect.

2.2.2.2 Transfer and Development Length

A more indirect means of estimating the strand bond quality is to measure the length of embedded strand required to fully transfer the prestress force into the concrete element, or to measure the length of embedded strand required to fully develop the strand at the ultimate capacity of the member. These embedded lengths are referred to as the transfer length (Lt) and the development length (Ld) respectively. Although they are less direct measures of the bond strength, the transfer and development lengths are of interest in studying strand bond because Lt and Ld must be sufficient in order for an engineer to design a pretensioned, prestressed beam. Figure 3 illustrates the transfer and development lengths for a pretensioned concrete beam.

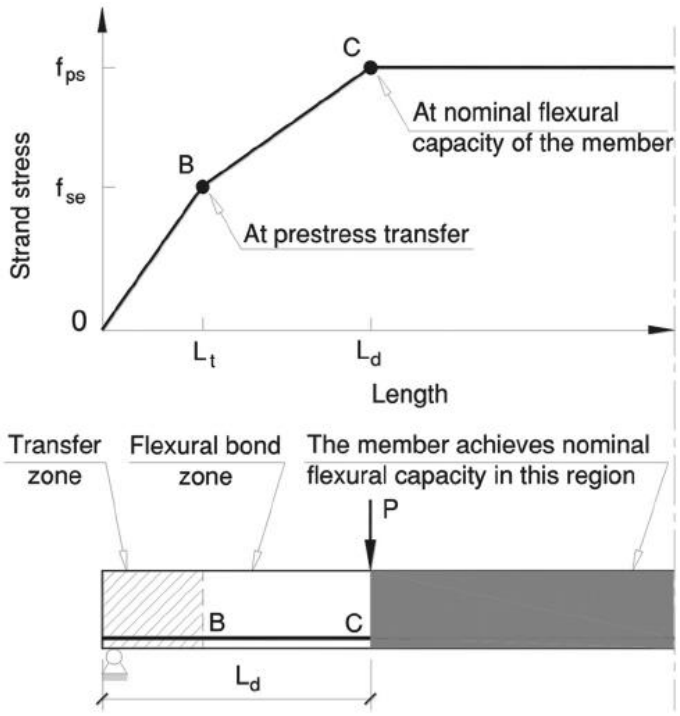

Figure 3: Transfer and development lengths in a pretensioned concrete member (Dang et al., 2016 after ACI 318)

Both ACI 318 and the AASHTO LRFD Bridge Design Specifications have design equations intended to accurately estimate transfer and development length for pretensioned, prestressed concrete beams (ACI 318-14, AASHTO 2017). These very similar equations only consider the stress level and strand size as variables in the bond capacity of the strand. The ACI equations for transfer and development length are shown in Equations (3) and (4) (ACI 318-14):

$$L_t = \frac{1}{3000} f_{se} d_b \tag{3}$$

$$L_d = \frac{1}{3000} f_{se} d_b + \frac{(f_{ps} - f_{se})}{1000} d_b \tag{4}$$

where f_{ps} and f_{se} are the strand stress at the ultimate nominal moment capacity of the beam and the effective prestress in psi, respectively, and d_b is the strand diameter in inches. Although ACI 318-14 does not explicitly separate the expressions for transfer and development length, the

commentary clearly indicates that the first term of Equation 4 represents the transfer length (ACI 318-14). The AASHTO equations are omitted here because they are identical except for a multiplier to account for shear in deep sections, and f_{ps} and f_{se} are input in ksi instead of psi. Since transfer length is always shorter than development length, it is conventional to consider L_d to be the sum of L_t and the so-called flexural bond length, which is the additional embedment beyond the transfer length required to reach the stress at ultimate flexural capacity. In addition to Equation (3), ACI allows the transfer length to be taken as $50d_b$, while AASHTO specifies $60d_b$, when designing for shear in girder end regions (ACI 318-14, AASHTO 2017). These estimates for transfer and development length do not include allowances for compressive strength, strand surface condition, and other factors that affect bond, and are intended to provide an average representation for strand bond performance in pretensioned concrete elements (Tabatabai and Dickson, 1993).

2.2.3 Strand Bond Testing

Strand bond performance can be tested experimentally through a number of different means. The direct pullout tests such as the ASTM 1081 and LBPT are primarily used to qualify the bonding capacity of strand samples or make parametric comparisons between materials and mixes. In addition, however, even though these tests do not utilize tensioned strands, some researchers have utilized direct pullout strengths to create correlations with transfer and development lengths (Ramirez and Russell, 2008).

2.2.3.1 Transfer Length

Transfer lengths can also be measured more directly by taking strain measurements at the level of the prestressing strands in a pretensioned concrete beam. This can be done using conventional strain gages applied directly to the strand, vibrating wire strain gages (VWSG) embedded alongside the strands (Bowser et al., 2020; Murray et al., 2019), fiber-optic sensors

along the strand (Floyd et al., 2018 & 2020), DEMEC measurements of surface strains (Burns and Russell, 1997), or laser imaging to obtain surface strains (Zhao et al., 2012). In any case, this strain data is collected at given intervals along the length of the beam and is plotted to create a strain profile. This strain profile can then be used along with the 95% Average Maximum Strain (AMS) method in order to estimate the transfer length (Burns and Russell, 1997). Alternatively, transfer length can be estimated by taking measurements of the strand end-slip. Integration along the length of the strand can be used to develop a simple equation which uses a bond stress distribution coefficient to relate the end-slip measurements to the transfer length (FIP, 1982; Dang et al., 2014 & 2016).

2.2.3.2 Development Length

Estimation of development length is typically performed by directly testing a beam in flexure and identifying the resulting mode of failure. The length of embedded strand between the free end of the beam and a concentrated load can be varied in order to identify the minimum length of strand required to achieve a stress in the strand equal to f_{ps}. If the mode of failure results in a flexural failure without strand slip, then it is assumed that f_{ps} has been reached, and the embedment length can be steadily decreased for other identical members until a bond-slip failure is observed. The embedment length where this crossover occurs would be the theoretical development length (Buckner, 1995; Dang et al., 2016). Alternatively, quality assurance tests have been developed, which use standardized sections and concentrated loads applied at set embedment lengths, in order to verify the strand bond capacity of a given concrete mixture design or strand sample (Peterman, 2009).

2.2.3.3 ECADA Test

Because of concerns about the repeatability and practicality of casting series of prestressed beam specimens and testing them to failure in flexure as a means of estimating the development length, researchers have developed alternative tests for measuring strand bond capacity. One such test was developed by researchers at the Polytechnic University of Valencia, and is referred to by its Spanish acronym ECADA, which translates in English to "Test to Characterize the Bond by Release and Pull Out" (Marti-Vargas et al., 2006a). The development of the ECADA test set out to resolve a quandary faced by researchers who wished to accurately estimate both the transfer and development lengths for the same specimen. Transfer and development length, sometimes referred to as transmission and anchorage lengths respectively outside the U.S., can both be determined experimentally, but conventionally by totally separate tests (Marti-Vargas et al., 2006b). Whereas transfer length can be determined by monitoring strain along the precompressed zone of the specimen or the slip at the free ends, these tests offer no information about development length. In turn, development length can be estimated using either direct pullout tests or by sequential flexural beam tests. But these development length tests do not offer any insights concerning transfer length. Additionally, direct pullout tests are limited by not accounting for Hoyer's effect due to tensioned strand, and flexural beam tests are innately limited by their size, cost, and fabrication requirements (Marti-Vargas et al., 2006b). The ECADA test offers the advantage of sequentially performing pretensioning and prestress transfer, followed by a pull-out operation on the opposite end of the same specimen, in an attempt to more accurately reflect the tensioned strand bond behavior. In this manner, the ECADA test can be used to glean data concerning both the transfer length (Marti-Vargas et al., 2007) and the development length (Marti-Vargas et al., 2006a) of a concentrically prestressed specimen, using a single experimental protocol. Figure 4 shows the components of the ECADA

test setup, and Figure 5 shows the sequencing utilized to transfer the prestress and pull-out of the strand.

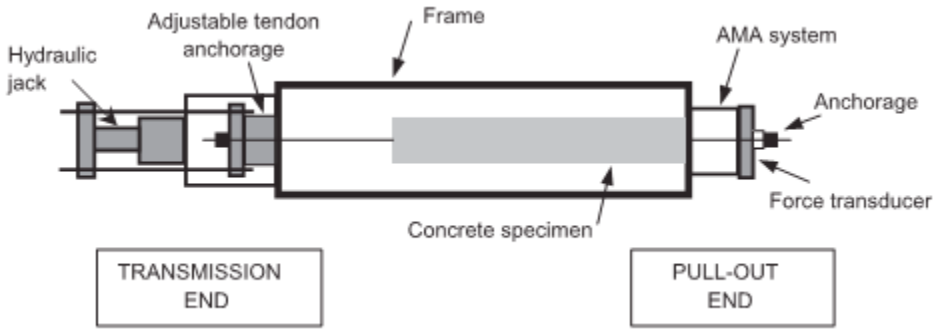

Figure 4: Components of the ECADA test setup (Marti-Vargas et al., 2006b)

The frame shown in Figure 4 consists of hollow steel tubes, with thick steel plates placed at each end. The prestressing strand passes through holes in the plates at either end of the frame, such that the strand can be anchored at one end and tensioned at the other end. A hydraulic jack is used to tension the strand from the so-called "transmission" end, and the AMA (anchorage measurement access) apparatus is used to anchor the strand at the "pull-out" end. The AMA apparatus also provides a space for a hollow load cell to be inserted, whereby prestress transfer force can be measured and it must be compatible with the hydraulic jack, so that the pull-out procedure can be performed after prestress transfer. The longitudinal stiffness of the frame is designed to slightly exceed the expected longitudinal stiffness of the concrete test specimen, so that the measured transfer lengths will not be unconservative (Marti-Vargas et al., 2007).

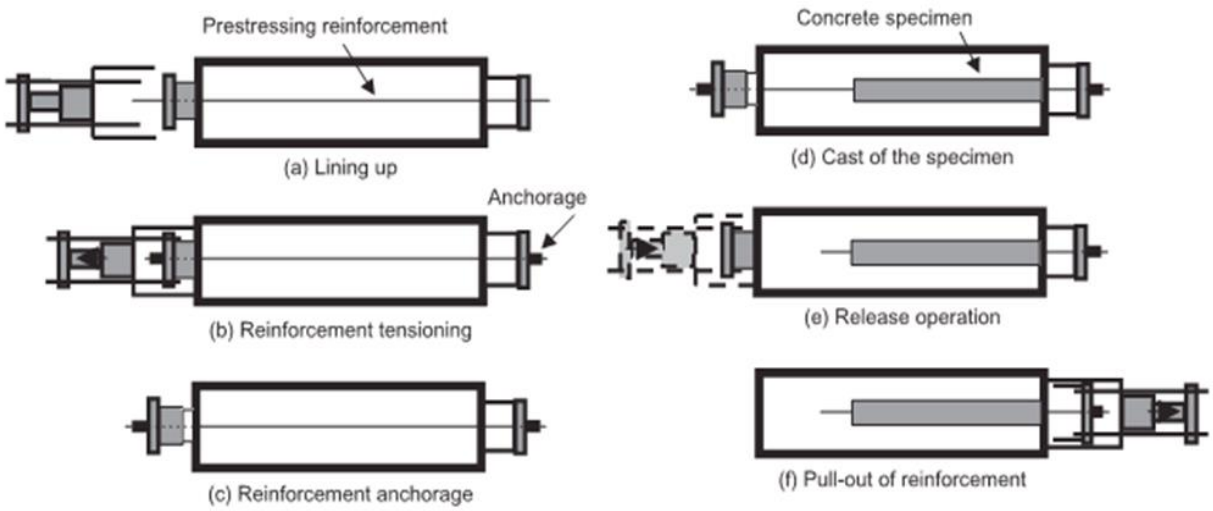

Figure 5: Stages of the ECADA test (Marti-Vargas et al., 2006b)

The first step in performing the ECADA test is to thread the prestressing strand through the frame and AMA, line up the components, and chuck the anchored end (Fig. 5a). Next, the hydraulic jack is used to pull the strand to the desired tension, often 75% of the ultimate strand strength (Fig. 5b). Then a chuck is added at the transmission end to lock in the strand force, and the hydraulic jack is removed (Fig. 5c) before casting the concrete specimen concentrically around the tensioned strand such that it abuts the anchorage end of the frame (Fig. 5d). The test has often been performed with a 4 in. square concrete cross-section (Marti-Vargas et al., 2007) and the specimen length is dictated by the desired embedment length. After the concrete is placed, finished, and has gained adequate strength, the prestress is gradually released using the hydraulic jack at the transmission end, while a hollow load cell on the strand at the AMA end records the reduction in strand stress during and after release (Fig. 5e). By repeating the steps in Fig. 5a-e for varying embedment lengths with otherwise identical variables, the change in prestress force can be plotted against embedment length, and the transfer length can be identified as the least embedment length required to achieve the effective prestress force (initial prestress less elastic shortening losses) in the strand (Marti-Vargas et al., 2006a). Alternatively, because

the restraint frame is incrementally stiffer than the test specimen, some strand end slip occurs at transfer at the anchored end, not just at the free end. Therefore, theoretically, strand slip at either end could also be plotted against embedment length, and the transfer length identified by the embedment length at which the strand end slip decreases drastically or is nearly eliminated. Due to large scatter, the researchers found the free end slip to be a somewhat unreliable indicator, but measuring the anchored end slip resulted in transfer length estimates that agreed well with those estimated using strand force measurements (Marti-Vargas et al., 2007). Finally, in Fig. 5f, the hydraulic jack can be reversed and placed on the AMA end of the specimen, and force applied to the strand to pull it out of the concrete specimen. Since the strand was tensioned, this pull-out test should more accurately comprehend all 3 major bonding actions compared to conventional pull-out tests. Similarly to the transfer length, the measured pull-out force can be plotted against the embedded strand length for a sequence of tests to identify the minimum embedded length required to reach a stress corresponding to full strand development (Marti-Vargas et al., 2006a).

Tensioned strand pull-out tests patterned after the ECADA philosophy have been performed at the University of Oklahoma (Stumps, 2016). Steel frames with end plates and anchorage systems similar to those described by Marti-Vargas et al. were constructed and a sequence of 5 tests at varied embedment lengths were performed for conventional PC concrete specimens with 4 in. square cross-sections. A primary deviation from the ECADA protocol was that linear variable differential transducers (LVDT's) were used to measure strand slip at either end at transfer instead of utilizing hollow or "donut" style load cells on the strand in the AMA mechanism (Stumps, 2016). Figure 6 shows the ECADA style testing frames which were fabricated at Fears Lab.

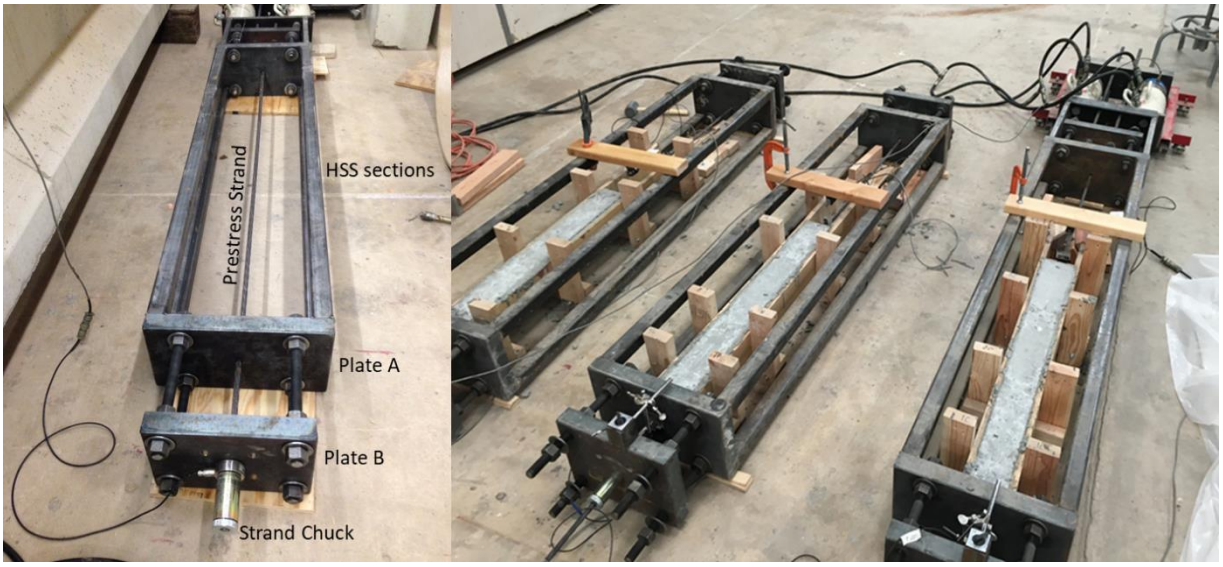

Figure 6: Tensioned pullout testing frames, before and after casting concrete (Stumps, 2016)

Figure 7 shows more detailed views of the free and anchored ends of the tensioned pullout testing frames.

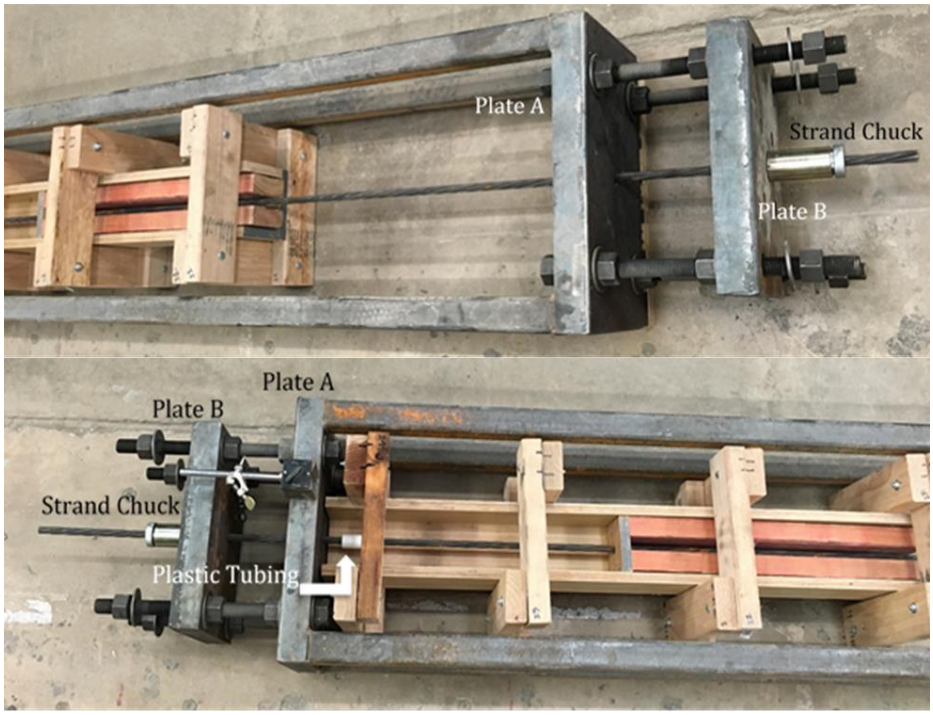

Figure 7: Free end (top) and anchored end (bottom) of tensioned pullout testing frames (Stumps, 2016)

In this experiment, a sequence of 5 tests were performed at embedment lengths of 26, 30, 34, 38, and 42 in., using 0.5" special 7-wire prestressing strands and an Oklahoma Department of Transportation (ODOT) standard PC concrete mix (Stumps, 2016). Strands were tensioned to approximately 75% of their 270 ksi ultimate strength before casting the specimens, which were mixed in one batch for consistency. Once the specimens had cured and reached a minimum compressive strength of 4 ksi, prestress force was released gradually, while LVDT's monitored the strand slip at both the free and anchored ends. This process was repeated for specimens with all 5 embedment lengths, and the maximum slip at each end was recorded in Figure 8.

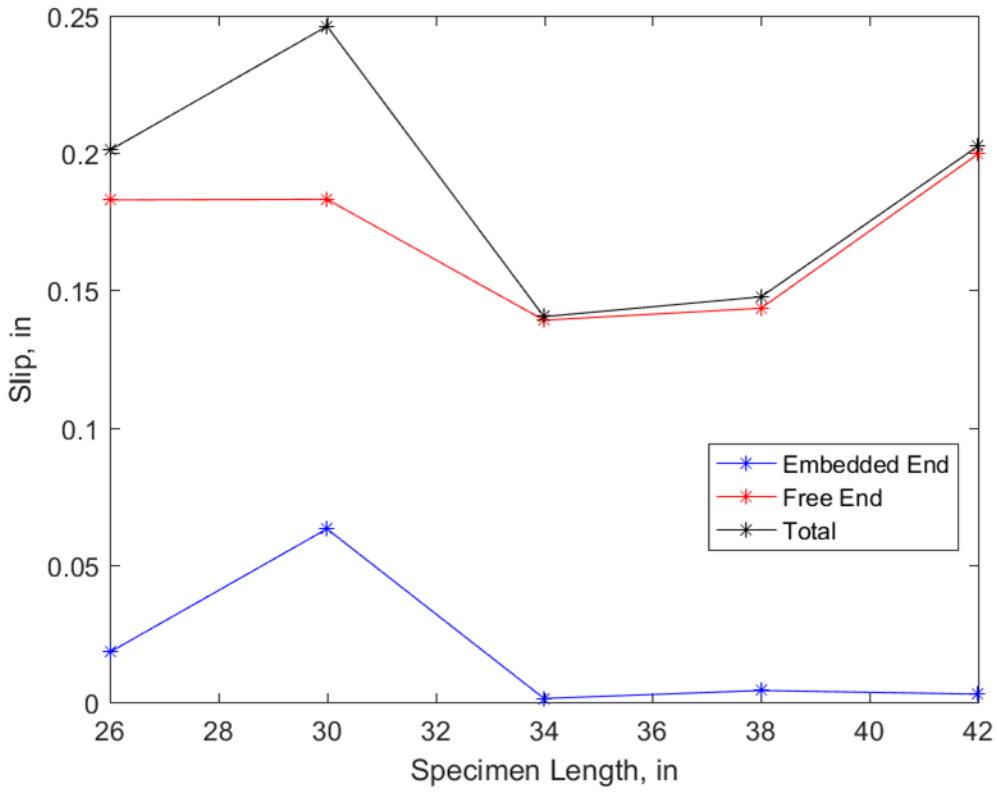

Figure 8: End slip measurements at transfer for tensioned pullout tests (Stumps, 2016)

Although this testing did not include subsequent direct pullout of the strands to analyze development length, Figure 8 clearly displays trends relevant to prestress transfer length.

According to engineering mechanics and the work of Marti-Vargas et al., the transfer length would coincide with the least embedment length which results in a drastic reduction in strand end slip to a small and uniform value. At the anchored end, this value should be close to zero, while at the free end, this value should be relatively constant but non-zero, because of accumulation of slippage through the transfer zone. Figure 8 shows that the anchored end slip decreases significantly between an embedment length of 30 and 34 in. and remains nearly constant at longer embedment lengths. The free end slip showed more variability and was less conclusive with regard to transfer length analysis. Based on the anchored end slip results, it was concluded that the prestress transfer length was at least 30 in. and at most 34 in; this result correlated reasonably well with the transfer length estimate from ACI 318, which predicted a value of 35.1 in. (Stumps, 2016). Similarly, to Marti-Vargas et al., this research concluded that using the ECADA test method with anchored end slip provides a meaningful, repeatable means of estimating transfer length, while the free end slip is a more unreliable or potentially inconclusive metric (Stumps, 2016).

2.2.4 Accuracy and Limitations of Strand Bond Models

2.2.4.1 Code Equations

The strand bond behavior predicted by the ACI and AASHTO transfer and development length equations are intended to provide an average representation for a wide array of variables that may impact bonding action (Tabatabai and Dickson, 1993). A significant limitation of these code equations is that they do not consider the material properties of the concrete that bonds to the strands, meaning that they may not accurately depict the bond behavior of an alternative cementitious material like BCSA cement concrete. The original derivation of the current code requirements, adopted first by ACI in the 1960's and later by AASHTO, assumed a uniform transfer bond stress of 400 psi, regardless of concrete strength or strand condition, and was based

on testing data which utilized 250 ksi, stress relieved strand which is no longer used in today's prestressing applications (Tabatabai and Dickson, 1993). As low relaxation, 270 ksi strand became standard in the industry, along with larger diameter strands up to 0.6 in. diameter, concerns were raised that the existing ACI and AASHTO bond estimates were obsolete and potentially unconservative in some cases (Buckner, 1995), leading the Federal Highway Administration (FHWA) to issue a memorandum in 1988 which restricted the use of larger diameter strands and added a 60% increase to the development lengths required by AASHTO (FHWA, 1988). Since that time, much research has been devoted to developing improved or modified transfer and development length estimates for modern strands and concrete, but the current ACI and AASHTO equations are still based on the original testing data from Hanson and Kaar in 1959.

Although these original formulations which are still codified were not explicitly intended to be conservative, research has shown that ACI and AASHTO estimates have conservatively overestimated required development length for self-consolidating and high strength concrete beams (Larson, 2006; Floyd et al., 2011).

2.2.4.2 Direct Pullout

The ASTM A1081 (formerly the STSB) and the LBPT direct pullout tests have several limitations. The LBPT in particular tends to be conservative, in that it has been known to not qualify strands that otherwise exhibit acceptable transfer and development lengths in a beam (Larson, 2006; Ramirez and Russell, 2008; Arezoumandi et al., 2020). This could be at least partially because with no tension on the strands, the full bonding capacity of the strands is not utilized. It has also been reported that the LBPT has difficulty in producing repeatable results (Ramirez and Russell, 2008). The ASTM A1081 bond test has been found to yield more repeatable results (Ramirez and Russell, 2008), but the main limitation of this test is its difficulty. The ASTM A1081 bond test requires a mortar instead of concrete, has stringent compressive strength limitations, and utilizes an uncommon steel pipe size for the sample forms (ASTM A1081; Dang et al., 2014).

2.2.4.3 Alternative Bond Models

Transfer and development length equations other than the ACI and AASHTO equations, as well as modifications to those equations, have been proposed with the purpose of accounting for important strand bond factors beyond strand diameter and strand stress. One such proposed equation has used STSB data to formulate a multiplier for the ACI transfer length estimate which accounts for the role of strand surface quality in bonding capacity (Dang et al., 2014). Others have sought to incorporate factors which account for the effects of concrete compressive strength (Ramirez and Russell, 2008; Ramirez-Garcia, 2015 & 2016). These equations tend to agree better with experimental data, especially for higher strength concrete (Floyd et al., 2011). Although no such models or equation modifications exist for BCSA cement concrete, it is reasonable to believe that their transfer and development lengths may vary due to their unique composition. At the very least, BCSA cements tend to create high strength concrete, making it

plausible that models which account for concrete compressive strength may be a better fit than current ACI or AASHTO equations for these materials. Further testing would be required to make this determination, however. Transfer and development length testing, either by tensioned pullout testing like the ECADA test, or by more conventional methods previously addressed, will be necessary to characterize a bond model specifically for BCSA cement concrete.

2.3 Loss of Prestress

When tension is released from the prestressing strands of a pretensioned, prestressed concrete member, several effects result in a reduction of the effective prestress. Some of these effects are immediate, and others occur over time throughout the design life of the member.

2.3.1 Immediate Prestress Losses

2.3.1.1 Anchorage Losses

The first immediate loss of prestress is due to anchorage seating and adjustment, as slippage in the chucks and prestressing equipment causes a reduction in tensile strain in the strand after the strand is tensioned, but before the concrete is cast. In other words, these losses represent the difference between the tensile stress applied by the jacking equipment and the actual tension in the strand. This type of prestress loss is generally compensated by overstressing the strand slightly, so that the net tension in the strand will be correct after the losses occur (PCI, 2010).

2.3.1.2 Elastic Shortening

The second source of immediate prestress loss is elastic shortening of the concrete member. When the concrete has cured, and the strands are released, the prestress force is carried into the concrete member through bond between the strand and concrete. The resulting compressive force on the concrete member causes it to shorten proportionately, according to fundamental engineering mechanics. As a result, since the strands have fully bonded to the

surrounding concrete outside the transfer zone, they are forced to shorten by the same amount (PCI, 2010). Factors which impact elastic shortening include the magnitude of the initial prestress and the modulus of the concrete, which is often taken as a function of the concrete compressive strength.

2.3.2 Time-Dependent Losses

Prestress losses that continue over time include shrinkage and creep of the concrete and relaxation of the prestressing strand.

2.3.2.1 Shrinkage

Shrinkage is the volumetric decrease of the concrete, a large portion of which is the result of the concrete drying as it cures (Wight, 2016). Like elastic shortening, bonding action carries the strain caused by shrinkage into the strand, reducing the prestress force. Shrinkage occurs from the time the concrete is cast and continues throughout the life of the concrete, although the bulk of this shrinkage occurs within around 28 days of the end of curing. Important factors that impact the magnitude of shrinkage, and therefore the magnitude of prestress losses due to shrinkage, include concrete properties such as w/cm ratio, paste content, cement type, and the surface area to volume (SA/V) ratio of the finished member, as well as environmental factors such as ambient temperature and relative humidity (Wight, 2016).

2.3.2.2 Creep and Strand Relaxation

Creep is the long-term increase in tensile or compressive strain of a material under a sustained load (Nawy, 2010). For pretensioned, prestressed concrete, creep strains are accumulated in compression due to the prestress force, resulting in incremental shortening of the concrete element, a decrease in the strand stress, and a corresponding reduction in prestress. It is important to note that creep strain is defined as the strain under sustained load, which is in addition to the elastic strain caused when the load is initially applied (Nawy, 2010). Those elastic

strains are already accounted for by elastic shortening losses. Therefore, concrete with a lower modulus, which accordingly experiences higher elastic shortening losses, may experience lower overall creep losses. This has been found to occur especially for sand lightweight concrete (ACI 423, 2016). In addition to concrete creep, tensioned prestressing strand relaxes over time; since the rate of relaxation is dependent on the strand stress, the rate of relaxation losses changes in response to other losses. For modern low-relaxation strand, however, relaxation losses are minor compared to other time-dependent losses (ACI 423, 2016).

Figure 9 shows a schematic that summarizes the various sources of prestress loss, as well as the chronology of their occurrence during the lifespan of a pretensioned concrete girder. Superimposed loads which increase the strand stress are also shown.

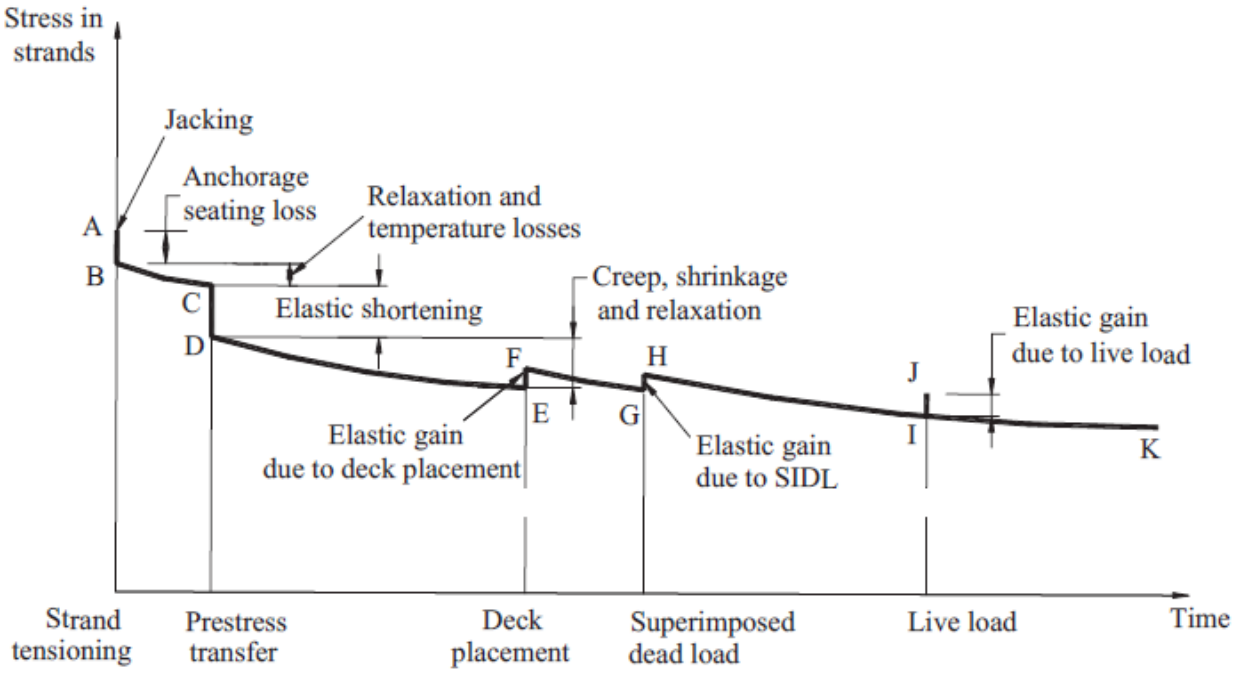

Figure 9: Prestress losses and gains throughout the life of a pretensioned concrete girder (Tadros, et al., 2003).

2.3.3 Estimating Prestress Losses

Many different theoretical and empirical methods and models exist to aid engineers in accurately estimating total prestress losses. Although prestress losses have little to no effect on the ultimate flexural strength of a pretensioned girder, they have a direct impact on service level considerations such as deflection, camber, and concrete stresses (ACI 423, 2016; PCI, 2010; Tadros et al., 2003). Significantly underestimating or exaggerating prestress losses can result in girders that sag or hog excessively and present serviceability issues over the girder's lifespan.

2.3.3.1 Lump-Sum Estimates

Historically, prestress losses were accounted for using a single lump-sum estimate. Early ACI and FHWA recommendations for prestressed concrete specified lump sum values of around 35 ksi for pretensioned members, and researchers proposed ranges of 25 to 40 ksi (ACI 423, 2016). Prior to the advent of low-relaxation strand in the 1970's, lump sum estimates were as high as 52-57 ksi (ACI 423, 2016). Although the 2011 ACI code referred to lump sum methods as "obsolete" (ACI 423, 2016), their use is not explicitly forbidden by ACI and they are considered viable for lightly prestressed applications with standard conditions and materials, or for preliminary design. With modern low-relaxation strand, PCI specifies total prestress loss between 25-50 ksi for normal weight concrete and 30-55 ksi for lightweight concrete, assuming standard conditions and applications (PCI, 2010).

2.3.3.2 AASHTO Methods

AASHTO offers both an approximate and a detailed method for estimating loss of prestress, depending on the desired level of refinement. The AASHTO approximate method (AASHTO 2017, Section 5.9.3.3) uses an equation that essentially estimates each time-dependent loss as an individual lumped value, and then sums them up. Like other lump-sum estimates, the AASHTO approximate method utilizes a bevy of qualifying assumptions to ensure

its applicability. The method is only applicable to normal weight concrete (NWC) which is moist cured or steam cured, uses low-relaxation steel, and is not exposed to unusual environmental conditions. In addition, the method is only intended for beams with composite deck elements, and it may not be used for sections with unusual geometries, defined as those with V/SA ratios that vary significantly from 3.5 in. Relaxation losses are taken as a constant 2.4 ksi for low-relaxation strand. Importantly, the approximate method does not account for elastic shortening losses, which must be added onto the sum of the time-dependent losses. The approximate method was calibrated by the refined method, which is discussed below (AASHTO, 2017)

The AASHTO refined method (AASHTO 2017, Section 5.9.3.4) is substantially more detailed, and accounts for each time-dependent loss individually by incorporating creep and shrinkage relationships. The AASHTO refined method was based on research performed under NCHRP Report 496, and it was designed to extend the loss prediction specifications to high-strength concrete bridge girders (Tadros et al., 2003). The AASHTO refined method divides the computation of time-dependent losses into shrinkage, creep, and relaxation, for both the time between prestress transfer and deck placement and the time between deck placement and the final time. An important attribute of the refined method is that it accounts for the interdependence of shrinkage, creep, and relaxation losses. As concrete shrinks, prestress loss occurs, which in turn reduces the compressive force on the concrete. This reduces the rate of creep compared to a constant compression force, and as the strand stress is reduced due to shrinkage and creep, the strand in turn relaxes less than it would under sustained constant stress (Tadros et al., 2003). This complex interaction is at least partially addressed in the AASHTO refined method by including the final girder creep coefficient in the transformed section coefficient which is used to compute shrinkage losses prior to deck placement. As would be

expected, the creep coefficient is inversely proportional to the shrinkage losses for a given shrinkage strain magnitude, which is reflective of the fact that increased shrinkage losses should result in decreased creep effects. Relaxation losses for the refined method may be calculated as a function of strand stress at transfer, intrinsic strand properties, and the magnitude of losses due to shrinkage and creep. However, an allowance is also made to still consider them as a lump-sum of 1.2 ksi for low-relaxation strand both before and after deck placement, for a total of up to 2.4 ksi (AASHTO, 2017).

2.3.3.3 AASHTO Methods – Accuracy and Limitations

NCHRP Report 496 gives data which compares losses measured for high-strength concrete girders of various types to losses predicted by the detailed method which became the basis of the AASHTO refined method. These comparisons include data from both the NCHRP 496 experiments and from similar tests reported in the literature. Table 2 shows the comparisons between prediction models for the girders studied in the NCHRP tests. Note that the AASHTO refined method shown in the table represents the 1998 code, before the proposed NCHRP detailed method was accepted by AASHTO.

Table 2: Measured and estimated prestress losses from NCHRP 496 (Tadros et al., 2003)

Girder	Measured[1]	PCI-BDM		AASHTO-LRFD Specifications				Proposed approximate method		Proposed detailed method (using estimated properties)		Proposed detailed method (using measured properties)	
				Refined		Lump-sum							
	Loss	Loss	Ratio*	Loss	Ratio*	Loss	Ratio*	Loss	Ratio*	Loss	Ratio*	Loss	Ratio*
Nebraska G1	31.96	36.85	1.15	52.24	1.63	50.29	1.57	40.18	1.26	38.42	1.20	40.68	1.27
Nebraska G2	35.65	38.27	1.07	52.24	1.47	50.29	1.41	40.18	1.13	40.00	1.12	40.68	1.14
New Hampshire G3	43.51	39.84	0.92	54.26	1.25	50.51	1.16	41.50	0.95	41.39	0.95	36.51	0.84
New Hampshire G4	42.33	39.84	0.94	54.26	1.28	50.51	1.19	41.50	0.98	41.39	0.98	36.51	0.86
Texas G7	25.35	32.11	1.27	52.52	2.07	48.83	1.93	34.20	1.35	27.67	1.09	25.46	1.00
Washington G18	42.06	40.33	0.96	66.86	1.59	52.69	1.25	38.07	0.91	35.85	0.85	38.47	0.91
Washington G19	39.98	40.33	1.01	66.86	1.67	52.69	1.32	38.07	0.95	35.85	0.90	38.47	0.96
Average	---	---	1.05	---	1.57	---	1.41	---	1.07	---	1.01	---	1.00
Standard deviation	---	---	0.12	---	0.26	---	0.25	---	0.16	---	0.12	---	0.15

[1] Modified for time infinity.
* Ratio to measured losses.

Table 2 shows that the NCHRP models for high-strength concrete clearly exhibit the closest alignment with this experimental data; this is expected, however, because the data in Table 2 from bridge girders located in Nebraska, New Hampshire, Texas, and Washington was used to calibrate the methods proposed in NCHRP 496. Therefore, to ensure the applicability and accuracy of the proposed prestress loss models, their performance was also compared to measured prestress losses from a variety of bridge girders reported in other research literature (Tadros et al., 2003). Table 3 shows the comparisons between prediction models for the girders reported in the tests of researchers external to NCHRP 496.

Table 3: Comparison of predicted prestress losses with external research to verify accuracy of proposed models in NCHRP 496 (Tadros et al., 2003)

Project		Measured[1]	PCI-BDM	AASHTO-LRFD Specifications		Proposed approx.	Proposed detailed
				Refined	Lump-sum		
No.	Reference						
1	Greuel et al. (*37*)	37.74	34.16	46.31	32.03	35.81	37.83
2	Pessiki et al. (*38*)	36.46	42.48	47.45	50.15	34.69	33.74
		36.64	42.99	47.64	50.98	36.27	35.56
3	Mossiossian et al. (*39*)	32.54	34.07	45.87	52.05	36.72	35.20
		35.11	34.07	45.87	52.05	36.72	35.20
4	Kebraei et al. (*40*)	17.92	23.68	36.61	38.93	23.92	23.71
		36.77	23.68	36.61	38.93	23.92	23.71
5	Shenoy et al. (*41*)	25.18	37.32	31.66	32.92	32.25	36.67
6	Stanton et al. (*42*)	34.17	25.76	34.72	41.29	26.71	31.62
		34.00	27.52	34.72	41.29	26.71	31.62
		65.62	40.14	63.35	54.31	38.45	39.06
		55.06	40.14	63.35	54.31	38.45	39.06
		69.29	40.14	63.35	54.31	38.45	39.06
7	Seguirant et al. (*43*)	36.11	43.33	50.05	51.25	35.16	41.66
		41.65	44.00	50.28	51.69	37.05	46.63
		35.03	46.06	50.39	53.40	37.91	47.98
8	Gross et al. (*35*)	35.68	37.98	61.76	48.21	38.50	33.91
		30.30	40.24	65.73	49.91	39.50	30.03
		32.51	38.41	60.95	47.59	38.01	34.64
		26.02	34.00	55.57	46.35	35.89	30.52
9	Gross et al. (*35*)	43.69	48.63	92.35	58.42	53.29	43.60
		50.80	48.87	92.60	58.42	53.43	43.85
		43.99	49.29	95.13	57.94	57.10	45.51
		44.68	49.81	95.07	58.20	56.40	44.84
		49.93	41.68	80.53	53.46	49.51	39.25
		50.80	48.90	95.43	59.05	56.46	44.88
		48.46	50.45	96.94	59.11	57.47	46.16
10	Gross et al. (*35*)	28.24	34.18	48.92	47.50	38.81	31.24
		27.95	34.18	48.92	47.50	38.81	31.24
		26.25	34.18	48.92	47.50	38.81	31.24
		23.96	30.64	46.36	47.48	36.76	27.72
Ave. Estimated/Measured Ratio			1.06	1.60	1.37	1.08	1.00

[1]Modified for time infinity.

Table 3 shows that even for an assortment of prestress loss data measured by other researchers, the proposed detailed method in NCHRP 496 shows excellent agreement, and the proposed approximate method also produces reasonable results. It is also worthwhile to note that in both Tables 2 and 3, the PCI-BDM approach produces reasonably close agreement with measured losses, while the previous 1998 AASHTO specifications significantly over-predict losses because they were not designed for high-strength concretes. It can be concluded, therefore, that the current AASHTO refined method (AASHTO, 2017), which is based upon the NCHRP

496 high-strength concrete model (Tadros et al., 2003), correlates well to experimental data. Since BCSA cement concretes are typically high-strength, the current AASHTO refined method might be a reasonable starting point for estimating prestress losses for these materials. Although the AASHTO refined method is limited by the fact that it was developed for conventional PC high strength concrete, its flexibility may allow relatively few factors to be changed regarding concrete modulus, creep, and shrinkage relationships in order to yield accurate results for BCSA cement concretes.

2.3.3.4 ACI Methods

Historically, ACI has not stipulated firm requirements for the estimation of prestress losses. Instead, they have given general recommendations on how to approach the issue, including use of lump-sum estimates in older codes, starting with ACI 318-63. In the ACI 318-83 code, the commentary was changed to recommend that lump-sum values were obsolete, although their use was not explicitly forbidden (ACI 423, 2016).

In 1979, Zia et. al. performed a study sponsored by ACI-ASCE Joint Committee 423 to investigate the development of a reasonably accurate and simple set of equations for estimating prestress loss, without resorting to lump-sum values (Zia et al., 1979). This study was referenced by ACI 318 as a means for estimating prestress loss until ACI 318-19, which now references ACI 423.10R-16, which serves as ACI's guide for estimation of prestress losses. ACI 423.10R-16 presents both a simplified method and a detailed method for estimating time-dependent losses; the simplified method in ACI 423 follows the method originally proposed by Zia in 1979. These simplified equations use basic engineering mechanics to compute stresses needed to estimate elastic shortening and creep losses based on the initial prestress, along with basic environmental and geometry data to estimate shrinkage losses. Relaxation losses are computed

based on strand properties, with the losses from all other sources deducted from the strand stress (Zia et al., 1979).

ACI 423.10R-16 also provides more detailed methods for estimating long-term prestress loss. First, the concept of age-adjusted effective modulus is introduced, which is the foundation of the AASHTO refined method. Chapter 6 of ACI 423 goes on to explain in great detail how the AASHTO refined method equations were derived and how they relate to the age-adjusted modulus and general mechanics of materials concepts (ACI 423, 2016). A more general and comprehensive age-adjusted modulus approach is also presented. This method utilizes internal equilibrium along with compatibility and constitutive equations to solve either 6 or 11 equations in as many unknowns, depending on whether the beam is cast with a composite deck. Additionally, detailed explanation is provided concerning how to approach using an incremental time step method to iterate through the varying load history in order to compute theoretical loss quantities. Finally, ACI 423 also references that some commercial software programs exist, which are suitable for approaching prestress loss estimation (ACI 423, 2016).

2.3.3.5 ACI Methods – Accuracy and Limitations

The ACI simplified procedure is very limited in applicability. The original procedure by Zia states that the equations were developed for prestressed members with a maximum compressive stress in the precompressed tensile zone under full dead load of 350-1750 psi. Also, the equations were based on concrete with a minimum strength of 4 ksi and minimum unit weight of 115 pcf (Zia et al., 1979). Therefore, the simplified procedure is not applicable to high strength concrete, and it is not applicable to lightweight concrete unless appropriate adjustment factors are applied. As stated in the original publication, a more detailed analysis is likely

appropriate to estimate prestress losses in an alternative material, such as BCSA cement concretes (Zia et al., 1979).

The ACI detailed methods include the AASHTO refined method and give increased insight into the formulation of the AASHTO approaches. Any of the ACI detailed methods would seem to be suitable for predicting the loss behavior of BCSA cement prestressed concrete members, because these methods are mostly very general and rely on case-specific data. As long as accurate creep, shrinkage, and elastic modulus data were obtained for a given concrete type under consideration, the ACI detailed methods would be applicable. One complication specifically concerning BCSA cement concrete might be that the very high early age strength might not directly correlate to maturity and/or stiffness. As a result, BCSA cement concretes may be vulnerable to early loading age disproportionately affecting long-term strain behavior. This cannot be known with certainty, however, without testing the material at various loading ages to determine its long-term response.

2.4 BCSA Cement in Prestressed Concrete

The composition and resulting properties of BCSA cements that have been described lend significant appeal to utilizing them in the precast, prestressed concrete industry. BCSA cement could be particularly advantageous because of its rapid setting time, very high early strength, and low shrinkage. With faster strength gain and set time, forms can be stripped sooner, strands can be released sooner, and beams can be moved to free up prestressing beds more quickly. In addition, techniques like steam curing, used to accelerate strength gain, would not be necessary (Thomas et al., 2018). Using BCSA cement in precast applications could present challenges, mainly related to the possibility of very short set times hindering concrete workability and the increased cost of the material. Researchers have pointed out, however, that precast manufacturers may be the best equipped of any concrete operations to deal with short set times, since they mix

their concrete on site (Thomas et al., 2018) and can carefully control admixture dosage and mix proportions. Additionally, decreased labor costs and increased production efficiency could help defray the added cost of the BCSA cement.

2.4.1 BCSA Cement Concrete – Non-Prestressed Beam Behavior

In order to describe the behavior of BCSA cement concrete in a pretensioned, prestressed application, it is important to understand how a BCSA cement concrete beam behaves with conventional, non-prestressed reinforcement. At this time, there is only one study concerning the behavior of BCSA cement concrete for reinforced, non-prestressed beams, to the best knowledge of this author. This study was completed at the University of Arkansas in 2018, and it involved characterizing the mechanical behavior of concrete beams made with rapid-setting BCSA cement, particularly with respect to flexural performance (G. Cook, 2018).

The experimental program for this study involved casting a total of 12 reinforced concrete beams, 4 with normal PCC from a local ready mix supplier and 8 with rapid-setting BCSA cement concrete, which were mixed in the laboratory. A commercially available BCSA cement was used which constituted the entire binder and was not blended with any PC (G. Cook, 2018). Table 4 below shows the mix designs utilized in this study.

Table 4: Mix design proportions for BCSA and PC concrete (G. Cook, 2018).

	BCSA	Portland Cement	
Cement	658	660	**lbs/CY**
Coarse Aggregate	1782	1775	**lbs/CY**
Fine Aggregate	1156	1340	**lbs/CY**
Water Reducer	18*	4	**oz/cwt**
Citric Acid	9	-	**oz/cwt**
W/C Ratio	0.48	0.40	

**The first BCSA mix (BCSA TD1) used 12 oz/cwt of HRWR*

These mixes were designed to be similar but varied slightly by necessity; because BCSA cement has a higher minimum water requirement to fully hydrate, the BCSA mix design used a higher w/c ratio. Additionally, citric acid, a commonly used retarding admixture for BCSA cement concrete, was used to delay set time and a higher dosage of water reducer was required to maintain workability compared to the PC mix.

The beams cast were 12 ft. long, with a 6 in. x 12 in. cross section, and the reinforcement layout was detailed to include both tension-controlled and over-reinforced behavior, with shear stirrups to eliminate any shear failures. The PC beams were tested at an age of 35 days, but the BCSA beams were broken into two groups, which were tested at 2-5 hours and 1 day respectively. The testing schedule was set this way in order to perceive any differences in behavior of the BSCA cement concrete at very early ages. The results of the third point loaded flexural tests showed that the cracking pattern experienced by the beams was very similar between the PC and BCSA specimens. Load-deflection data showed that despite the differences in testing age, cement type, and concrete compressive strength, all tension-controlled beams yielded within 10% of the same load and reached ultimate capacity within 12% of the same load. It is important to note that the compressive strength at testing for the PC beam concrete was approximately 6.6 ksi, while the compressive strength for the BCSA cement concrete beams ranged from around 3.8 ksi for the early age tests to between 6 and 8 ksi for the 1 day tests. For the over-reinforced (compression-controlled) beams, the BCSA beams tested at an age of a few hours showed a 20% reduction in ultimate strength compared to those tested at 1 day, indicating that the maturity and strength of the BCSA concrete has greater impact on capacity for an over-reinforced beam. Additionally, the 1 day compression-controlled BCSA beams had capacities 11% higher than the compression-controlled PC beams tested at over a month of age, even

though the BCSA compressive strength at the time of testing was lower. This finding raises the possibility that BCSA concrete may provide higher ultimate capacity for a given compressive strength than PC. Some additional findings included (G. Cook, 2018):

- The ACI modulus of rupture (MOR) equation of $7.5\sqrt{f'c}$ matched the cracking moment of the PC beams, but underestimated the cracking moment of the BCSA beams
- The nominal moment capacities for the beams computed by ACI 318, Section 22.3 were conservative for all tension-controlled beams, including the BCSA beams
- The calculated nominal moment capacities for the over-reinforced beams were exceeded by all specimens, but the BCSA beams, including those tested at 2-5 hours, outperformed their estimated capacities by almost 20% more than the PC beams
- The ductility index of the BCSA beams was higher than the PC beams, and in turn, the BCSA 1 day tests had a higher ductility index than the 2-5 hour BCSA beam tests

In summary, the existing ACI flexural strength procedures were found to be adequate as well as conservative for BCSA cement concrete conventionally reinforced beams. In addition, the hypothesis was proposed that the higher compression-controlled beams capacities for the BCSA concrete at lower compressive strengths may indicate that this concrete can achieve maximum compressive strains exceeding the 0.003 value recommended by ACI for normal PCC.

2.4.1 BCSA Cement Concrete –Prestressed Beam Behavior

There are currently 3 published articles in the U.S. concerning pretensioned, prestressed concrete using rapid-setting (RS) BCSA cement, to the best knowledge of this author. Two of these research projects were conducted by researchers at the University of Oklahoma. The first project set out to serve as a proof of concept for safely using BCSA cement in pretensioned, prestressed concrete beams, and to characterize the bond behavior, prestress loss, and ultimate

capacity in shear and flexure (Murray et al., 2019). The specimens consisted of 4 concentrically prestressed BCSA concrete beams, each 25 ft. long with the cross section shown in Figure 10.

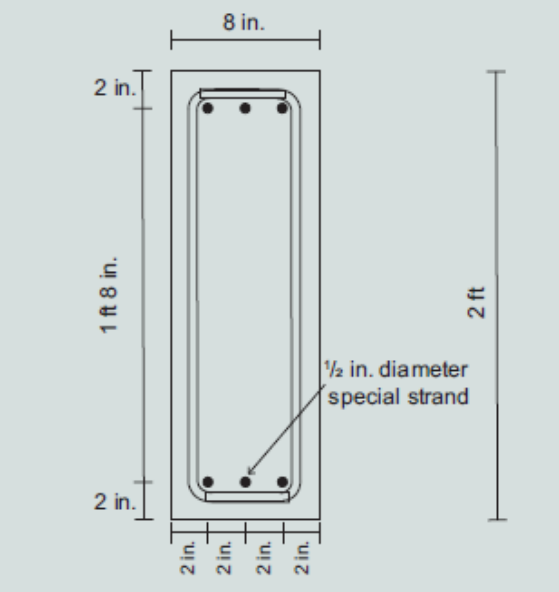

Figure 10: Cross section of BCSA prestressed beam (Murray et al., 2019).

The BCSA concrete mix design targeted a compressive strength of 3.5 ksi at prestress release and a slump flow of 24-28 in. Table 5 shows the mix design that was utilized for these beams.

Table 5: Mixture proportions for BCSA concrete (Murray et al., 2019).

Material	Quantity
Belitic calcium sulfoaluminate cement, lb/yd³	658
⅜ in. limestone, lb/yd³	1782
Sand, lb/yd³	1188
Water, lb/yd³	316
High-range water-reducing admixture, oz/100 lb cement	24
Water-cement ratio	0.48
Note: 1 in. = 25.4 mm; 1 lb/yd³ = 0.5926 kg/m³; 1 oz/100 lb = 1 mL/1.5352 kg.	

In addition to the materials shown in Table 5, citric acid was added as a retarder at a rate of between 0.25% and 0.35% of the weight of BCSA cement. The 4 beams, which were cast in 2 mixes on consecutive days, both exceed 3.5 ksi at release. Beams 1 and 2 reached 4.5 ksi by 2 hours and 10 minutes, and beams 3 and 4 reached 3.9 ksi by 1 hour and 32 minutes. Importantly, although SCC with a high slump flow of 24-28 in. was targeted, the actual slump flow attained by the mix was only 16.5 in. The beams were instrumented with vibrating wire strain gauges (VWSG) along the length of the beam at the level of the prestressing strands, to measure strain from the time of casting, out to long-term. This data was used to estimate transfer length and prestress losses. End-slip measurements were also taken to estimate transfer length. Finally, the beams were tested to failure in bending at approximate ages of 1-3 years in order to investigate the development length of the prestressing strands. The results of this study showed the following:

- The transfer lengths measured using the VWSG were comparable to estimated transfer lengths based on ACI and AASHTO recommendations (ACI 318, 2014 and AASHTO, 2017)
- Measured elastic shortening losses matched up well with estimates, but time-dependent losses were greatly overestimated by AASHTO equations (AASHTO, 2017)
- VWSG are an accurate means of measuring prestress loss and transfer length
- Development length bending tests indicated fair agreement with predicted strengths, but the results were somewhat inconclusive because a lack of transverse shear reinforcement resulted in shear cracks entering the transfer zone and disrupting the bond behavior

The second known research project concerning prestressed RS BCSA cement concrete, which was also performed at OU, was published Bowser et al. in 2020. This work focused on the

bond behavior of BCSA concrete with 0.6” prestressing strand. In this study, 12 prestressed concrete beams were cast, 4 with PC and 8 with BCSA cement. The prestress was released at 24 hours for the PC beams and either 2 hours or 24 hours for the BCSA beams. The layout of the reinforcement used in this study is shown in Figure 11.

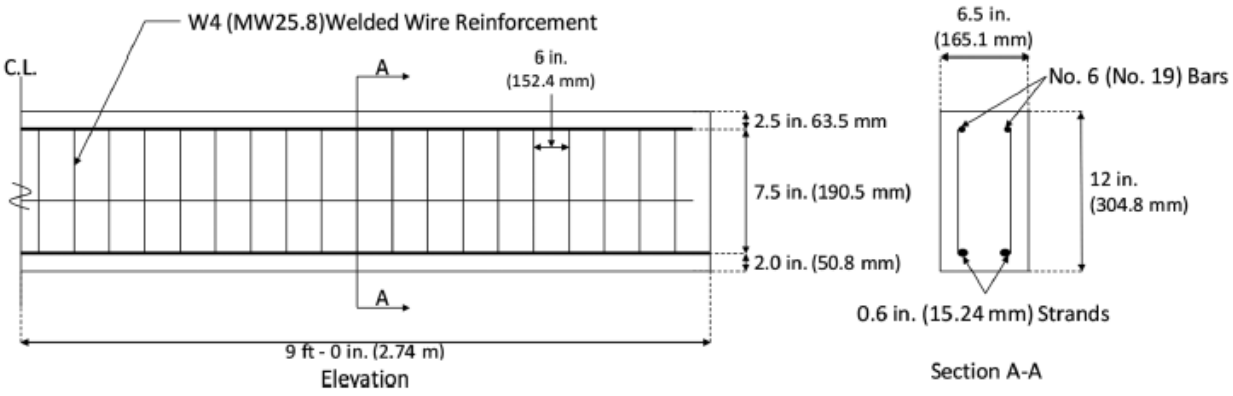

Figure 11: Reinforcement layout for BCSA bond tests with 0.6" strand (Bowser et al., 2020).

Before casting the prestressed beams, strand bond testing was performed in accordance with ASTM A1081, in order to qualify the strand and ensure it was suitable for use in further bond testing with the BCSA cement concrete. The pullout values from these tests met recommended minimums based upon studies sponsored by both NCHRP (Ramirez and Russell, 2008) and PCI (Riding et al., 2016). Table 6 shows the mix designs and concrete properties that were targeted in this study.

Table 6: Mix designs and concrete properties for BCSA bond tests with 0.6" strand (Bowser et al., 2020).

Specimens	PC	RS
Cement, lb/yd^3 (kg/m^3)	851 (505)	658 (390)
Coarse aggregate, lb/yd^3 (kg/m^3)	1372 (814)	1560 (926)
Fine aggregate, lb/yd^3 (kg/m^3)	1459 (866)	1188 (705)
Water, lb/yd^3 (kg/m^3)	315 (187)	329 (195)
w/c	0.37	0.50
HRWR, fl oz./100 lb (mL/100 kg)	6.5 (425)	6.0 (390)
Citric acid, wt./wt. cement	N/A	0.001
Targeted slump, in. (mm)	9 to 11 (229 to 279)	
Targeted compressive strength at release, psi (MPa)	3500 (24.1)	

Transfer lengths were measured using both DEMEC targets at the level of the prestressing strand and by end-slip estimates for all 12 beams. Prestress losses were measured using VWSG for 4 of the RS BCSA beams, 2 released at 2 hours, and 2 released at 24 hours. All 12 beams were tested to failure in flexure at 28 days of age, at a lower-bound strand embedment length based upon the estimated development length per ACI 318-14. Results showed that the transfer lengths of the BCSA beams were roughly equivalent to those of the PC beams, and that the governing ACI and AASHTO estimates for transfer length were adequate for all the mix designs and release times that were studied. The study also determined that currently accepted prestress loss prediction models were not accurate for the BCSA beams, overestimating the measured losses by 79-169%, depending on the method used. Lastly, the flexural tests showed that every BCSA specimen reach its full nominal flexural capacity when tested at an embedment length equal to the ACI development length. This indicates that the BCSA cement concrete has adequate bond performance relative to ACI requirements, and further testing at variable embedment lengths may show that BCSA cements can exhibit bond performance that exceeds ACI requirements (Bowser et al., 2020).

The last research project concerning the application BCSA cement for prestressed concrete was published in 2021 by researchers from Utah and Nebraska (Markosian et al., 2021). This research involved the analysis of a scale prestressed bridge girder patterned after a full-scale Utah bridge girder design. This girder was instrumented and tested for camber, transfer length, prestress losses, and ultimate strength. Figure 12 shows the girder design utilized in this study.

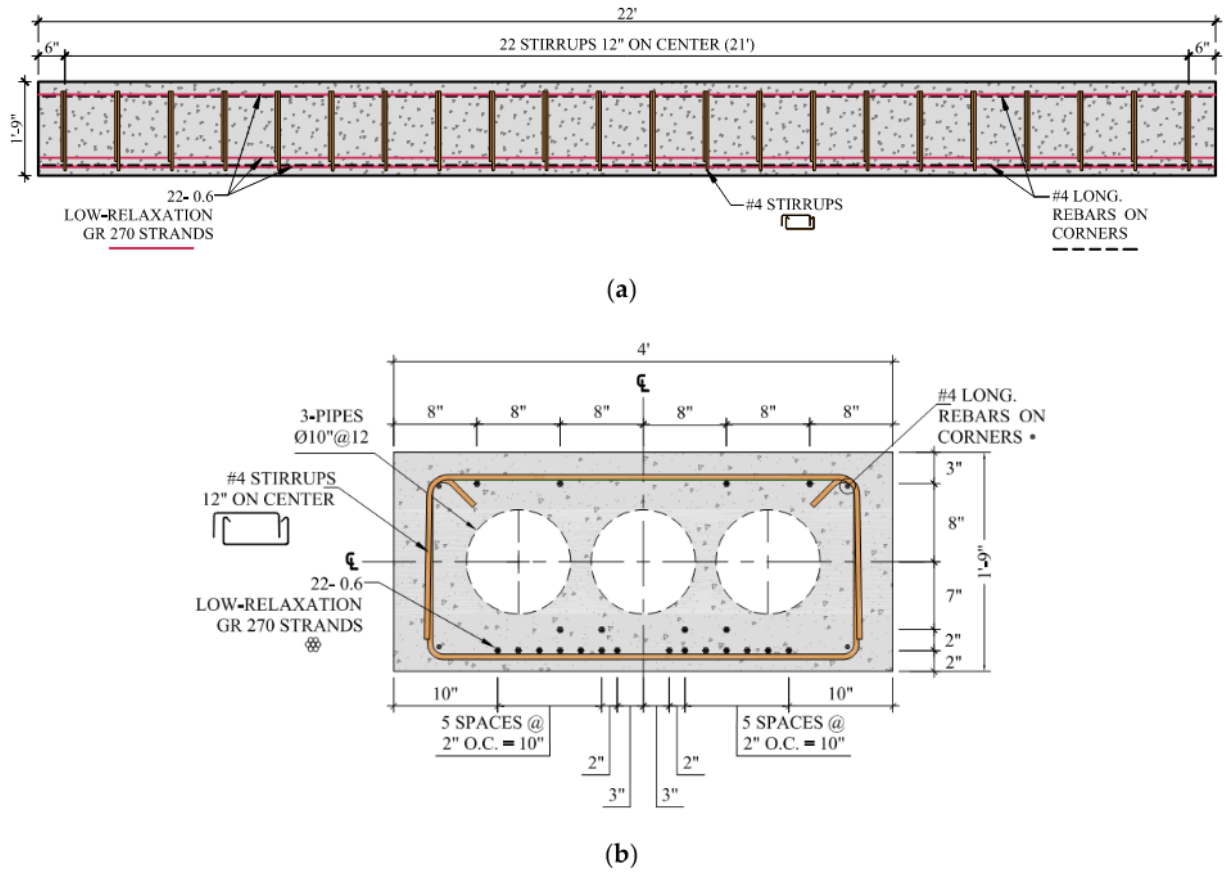

Figure 12: Girder design utilized by Markosian et al. (2021) - (a) Profile and (b) Section

The researchers in this study concluded that AASHTO approaches resulted in adequate predictions of creep and shrinkage, with a small degree of overestimation over time. Interestingly, the prestress losses measured for this single girder by Markosian et al. were significantly higher than those observed by Ramseyer and Floyd or Bowser at OU. One concern

with this research is the improper installation of the VWSG instrumentation; the paper published by Markosian et al. shows that the VWSG were tied directly to the prestressing strands with plastic cable ties. This approach is poor practice, and it is explicitly forbidden in manufacturer guidelines to impinge upon the end regions of the gage, because it could improperly influence strain measurement.

These researchers also concluded based upon the girder analysis that the AASHTO LRFD approach was conservative relative to the transfer and development lengths that were measured experimentally.

2.5 Research Needs

From the preceding discussions concerning leading research pertaining to BCSA cement concrete, as well as prestress losses and strand bond behavior in general, it has been observed that there are some critical research topics that should be addressed, in order for rapid-setting BCSA cement to be applied to pretensioned, prestressed concrete applications on a large scale.

2.5.1 SCC Mix Design and Fresh Properties

Use of self-consolidating concrete (SCC) for prestressed applications has proliferated in recent years, due to numerous advantages, including ease of placement, reduced labor costs, and high strength and durability (Khayat and Mitchell, 2009; Arezoumandi et al., 2020; Girgis and Tuan, 2004; Floyd et al., 2011 & 2015; Bymaster et al., 2015). However, in both the aforementioned studies where BCSA cement was used for prestressed beams, the concrete used had a high slump, but did not achieve the recommended flow properties to be considered SCC. Therefore, in order to increase the use of rapid-setting (RS) BCSA's in precast applications, a SCC mix design should be developed for this material and tested for prestressed specimens.

Additionally, temperature variations have been known to cause large variations in the dosage of retarding admixtures, such as citric acid, required to achieve a desired time to set. As a result, there is often some uncertainty concerning exactly how much placement time will be available for a given RS BCSA mixture. To remedy this issue, a study should be performed which records the setting time for many different RS BCSA mixes, at variable temperatures, citric acid dosages, and HRWRA dosages. In this way, mix design aids can be developed for precast manufacturers so that consistent workability and placement time can be maintained. In general, it is expected that increasing citric acid and HRWRA dosage will extend workability and/or set time, while increasing temperatures will decrease set time and workability.

2.5.2 Bond Performance Characterization

The two University of Oklahoma studies previously mentioned are the only known research directly addressing the bond performance of RS BCSA cements with prestressing strand. This work should be expanded to include more strand diameters, reinforcement and strand layouts, and concrete mix designs. The effect that these parameters have on transfer length, development length, and bond pullout strength should be analyzed, and direct comparisons should be made to PC behavior and current design codes. Of specific concern is an analysis of potential short-term or long-term detrimental effects that could result from releasing prestress on very early age concrete, even if it has reached sufficient compressive strength. Therefore, testing which targets the prestress release time or loading age of the BCSA cement concrete will be especially important.

2.5.3 Prestress Loss Prediction and Modeling

Previous research has shown that RS BCSA materials have drastically reduced time-dependent prestress losses, compared to what is expected of PCC and what is prescribed in current codes and recommendations for estimating prestress loss. The inadequacy of current models means that adaptations or entirely new models need to be constructed based on research data, so that design engineers can accurately estimate losses for BCSA based materials. This will ensure that camber, deflection, service stresses, and transfer length estimates will be more accurate.

2.5.4 Creep and Shrinkage Relationships

Since time-dependent prestress losses are primarily caused by creep and shrinkage of the concrete, accurate data concerning creep and shrinkage relationships for RS BCSA concrete will be required to develop improved prestress loss models. Although studies have addressed shrinkage of RS BCSA concrete, creep has not been studied extensively, especially for

commercially available BCSA cements in the U.S. Therefore, understanding the magnitude of creep that should be expected of these materials, for different mix designs and loading ages, is important.

3. Materials Testing

3.0 Introduction

Section 3.1 discusses the approach and testing for the mix design development. Section 3.2 discusses the setting time study and the comparison of the ASTM C403 penetrometer and the calorimetry approaches. Section 3.3 discusses the mixes which included MOR specimens to measure flexural strength. Section 3.4 discusses the MOE testing which was performed to understand the time-dependent changes in concrete stiffness to help estimate elastic shortening in later tests. Finally, Section 3.5 discusses the specimens for which creep and shrinkage were measured, specifically in order to help accurately model the prestress losses that were measured on the prestressed beams discussed in Chapters 4 and 5.

Table 7 presents a summary of the materials testing research batches, the identifiers used for each group of batches, the most pertinent tests for each group, and which shipment or lot of cement was used for that batch or group of batches.

Table 7: Batch Designation Overview with Key Tests (*Indicates Cement Lot #2 was Compromised)

Batch Purpose	Batch ID Number	Notes	Key Tests	Cement Lot
Mix Design Development	RS 1 - 24	No Fly Ash	ASTM C39 and ASTM C1611	Lot #1
	RS 25 - 35	With Fly Ash		
Temperature/Citric Acid Setting Time Study	T0 - T3	Low Temp Range	Semi-Adiabatic Calorimeter + ASTM C403	Lot #3
	T4 - T8	Med Temp Range		
	T9 - T13	High Temp Range		
Flexural Strength	RS 2A	Batches for MOR vs Time/Comp. Strength	ASTM C78	Lot #1
	RS LBPT			
Elastic Modulus	RS 2C	Round #1 (C/F=0.53)	ASTM C469	Lot #1
	RS HI AGG	Round #2 (C/F=0.82)		Lot #2*
Creep and Shrinkage	RS 2D	Single Batch for Creep, Shrinkage	ASTM C512	Lot #3

The chronology and usage of each cement lot is described in more detail immediately following in Section 3.1.1.

3.1 Mix Design Development

The first step in this research was to develop a self-consolidating concrete (SCC) mix design with rapid setting (RS) properties using commercially available BCSA cement. Hereafter, this concrete mix design or the resulting concrete material will be referred to as RS-SCC (rapid setting, self-consolidating concrete) made with BCSA cement. Since all testing in this research program involved the same BCSA cement, the concrete will often be referred to succinctly as RS-SCC. Table 8 shows the targeted parameters for this mix design.

Table 8: Targeted Performance Specifications for RS-SCC

Property	Quantity	Units
Slump Flow	**24-29**	**in.**
Final Set	**> ~ 60**	**min.**
f'_{ci} (2-3 hr.)	**3 - 4**	**ksi**
f'_c (28 days)	**10**	**ksi**
f_r	**~ 7.5√f'c**	**psi**

The targeted slump flow was chosen based upon the recommended range provided in NCHRP 628, on structural self-consolidating concrete for prestressed bridge components. The targeted final set time was selected to provide enough workable time to properly mix and place the concrete. The targeted early age compressive strength was selected based upon a preliminary analysis of the minimum required compressive strength for prestress release. The targeted flexural strength of 7.5√f'c was selected based upon the provision of ACI 318.

3.1.1 Constituent Materials

The cement used for this research was a rapid-setting BCSA cement supplied by CTS Corp. There were 3 lots or shipments of cement used for this research, as shown in Table 7. Lots #1 and #2 were from a group of 2000 lb super sacks of cement on hand at Fears Lab, leftover from other research projects. Lot #1 cement was either stored in sealed, unopened sacks or was transferred to lined and sealed drums for storage in between usage. Lot #2 cement was stored at first in a sealed super sack, but this sack was unsealed and not reclosed properly before batch RS HI AGG, thereby compromising the results as described in Section 3.4.2.2. Lot #2 cement was not used for any other materials testing apart from batch RS HI AGG. Lot #3 was a shipment of cement donated directly from CTS specifically for this research and arrived at Fears Lab during the summer of 2021. All Lot #3 cement was fastidiously stored in sealed drums once any sacks were opened and no known moisture contamination occurred. The bulk of the Lot #3 cement was

used for the structural testing (Chapter 4), but Lot #3 was also used for the creep and shrinkage specimens so that prestress loss predications developed from this data would be as accurate as possible. Finally, Lot #3 was also used for the setting time study, because this testing was conducted after the bulk of the Lot #1 cement had been exhausted and the Lot #2 cement had been contaminated.

Two different classes of fly ash from 3 different sources were used during mix design development. These included Class C fly ash from St. Mary (KS) and from Red Rock (OK) and a Class F fly ash from Ashgrove® (origin location unknown). Red Rock Class C fly ash was used throughout the remainder of materials testing after the mix design development, as well as all structural testing.

The retarder used in all research batches was food grade anhydrous, granular citric acid. This granular citric acid was added to the mixing concrete as an aqueous solution by dissolving it in the concrete mixing water. High range water reducing admixture (HRWRA) was required to achieve the targeted concrete slump flows, and Glenium® 7920 was used for all research batches.

All aggregates used throughout this research were provided locally by donations from Dolese Bros. The fine aggregate provided by Dolese was a standard ASTM C33 compliant Dover concrete sand. The coarse aggregate which was requested from Dolese was a crushed limestone that the company designated as 5/8 in. #3 cover coarse aggregate. This aggregate gradation was chosen because it was the closest gradation that Dolese carried to the ASTM C33 #7 coarse aggregate. The ASTM C33 #7 is the next size down from #67, which is a standard ¾ in. nominal coarse aggregate. In this research, a coarse aggregate slightly smaller than a normal ¾ in. aggregate was preferred to optimize slump flow and self-consolidation.

The properties and proportions of the fine and coarse aggregates used for this mix design are summarized in Table 9. Note that SSD denotes an aggregate in saturated surface dry condition. In order to optimize the mix design for flowability, a relatively low proportion of coarse aggregate was used. The coarse/fine (C/F) aggregate ratio was 0.53 volumetrically and was 0.54 by weight. More detailed explanation of the chosen C/F aggregate ratio is provided in Section 3.1.4.

Table 9: Aggregate Properties for RS-SCC

Property	Sand	Rock
Gradation	ASTM C33 Dover Sand (from Dolese)	ASTM C33 #7 (Dolese 5/8 in. #3 Cover)
Specific Gravity (SG)	2.63	2.68
Absorption Capacity (SSD)	0.70%	0.86%
Fineness Modulus	2.5	N/A

3.1.2 Mixing Procedure

The same mixing procedure was used for all batches of concrete mixed for this research, whether they were mixed in one of the two smaller capacity rotating drum mixers shown in Figure 13 or the larger capacity horizontal rotating shaft mixer at Fears Lab. The only slight variations in mixing procedure occurred for the large pour conducted with Schwarz Ready Mix (Section 4.1), in which a mixer truck was utilized, and for the slump flow loss batches conducted to investigate the importance of citric acid dosage sequencing (Section 4.2.3.2).



Figure 13: Small 1 ft^3 capacity rotating drum mixer (left) and medium 6 ft^3 capacity rotating drum mixer (right) – [listed capacities are maximum mix volumes not rated capacities]

The coarse aggregate was added to the mixer first, followed by the fine aggregate. While the aggregate tumbled in the mixer, all the granulated citric acid was added to the mixing water and stirred vigorously until all the crystal solids disappeared. Additionally, half of the required high range water reducing admixture (HRWRA) was added to the mixing water, which was again stirred. Next, half of this mixing water containing all the citric acid and half the HRWRA was added to the aggregates and allowed to mix for a few (up to 3) minutes to become relatively homogenous. After this initial mixing, all the BCSA cement and fly ash were added together to the mixer, the exact time of day was noted, and a stopwatch was started. The stopwatch was used to track the mixing time from the moment water touched cement, which was 3-6 minutes. Three

minutes was standard, but up to 6 minutes was used for especially large mixes to ensure adequate mixing of the constituents. The exact clock time that the cement was added to the wet aggregate was used as the reference time for the age of the concrete for all testing purposes. As soon as all the cementitious materials had been added to the mix, the other half of the mixing water (bearing the remainder of the citric acid and HRWRA) was added to the mixer, followed immediately by the half of the HRWRA that had not been added to the mixing water. The purpose of splitting the mixing water this way was to both ensure even distribution of the citric acid and HRWRA and to extend the working time of the mix as much as possible. Once the remaining half of the HRWRA was added, the final step was to allow the rest of the 3-6 minute mix time to elapse. During this final stage, extra HRWRA was added if visual inspection indicated it would be necessary to reach the desired initial slump flow. The mixing procedure is abbreviated as:

1.) Add all coarse aggregate to mixer;
2.) Add all fine aggregate to mixer;
3.) Add all citric acid and 50% of HRWRA to mixing water; stir vigorously;
4.) Add 50% of mixing water to aggregates in mixer; mix for 1-3 minutes;
5.) Add BCSA cement and fly ash to mixer at the same time; start 3-6 minute timer;
6.) Add remaining water to mixer;
7.) Add remaining HRWRA to mixer;
8.) Allow to mix briefly (1-2 minutes), and add extra HRWRA if necessary to increase flowability;
9.) Discharge mixer after 3 minutes for small batches, or up to 6 minutes for relatively large batches.

It should also be noted that, while not technically part of the mixing procedure per se, slump flow testing was conducted on every batch. To ensure consistency and ensure that slump flows could be compared between batches, this test was conducted immediately upon discharging the mixer for every batch.

3.1.3 Fresh Concrete Property Testing

A variety of tests were performed on the fresh concrete for each batch, depending on what parameters were of most interest and depending on available personnel. If available personnel were limited, cleanup had to be prioritized to ensure the rapid setting concrete was removed from the equipment before it could set, which could ruin the equipment. The following parameters were measured for every batch:

- Mix temperature;
- Slump flow (ASTM C1611);
- Visual stability index, VSI (ASTM C1611).

Mix temperature and slump flow are fundamental concrete fresh properties and do not bear significant description here. The VSI is a qualitative measure of the cohesiveness of a SCC mix described by ASTM C1611. The VSI scale runs from 0 (highly stable) to 3 (highly unstable) and a value of 0 or 1 is preferred, indicating that segregation of the SCC is unlikely.

The following parameters were not measured for every batch. Once the final mix design was chosen, unit weight and air content were measured intermittently to check concrete consistency a few times throughout the duration of the research. Setting time by penetrometer and by calorimetry were performed systematically on a series of batches as described in Section 3.2 to determine the effects of temperature and retarder dosage on set time.

- Unit weight (ASTM C138);
- Air content (ASTM C231);
- Setting time by penetrometer (ASTM C403);
- Setting time by calorimeter.

3.1.4 Test Batches and Results

An 8-sack mix design was chosen as the baseline for this research, based on a standard 94 lb cement sack terminology, for a total BCSA cement quantity of 752 lb/yd^3. This choice was made to ensure that very high early strength could be achieved, while still applying retarding admixtures in sufficient proportion to delay setting time for the sake of workability. This cement quantity also helped provide plenty of paste to achieve the desired slump flow range. A *w/cm* ratio of 0.42 was chosen as a starting point, since this value was slightly higher than the theoretical minimum hydration demand of BCSA cement which is around 0.40. At a given *w/cm* ratio, the HRWRA and retarding admixture dosages were varied, in order to achieve an acceptable slump flow, consistency (based on visual stability index, VSI), and compressive strength, at both very early age and at maturity (at least 28 days). The HRWRA used for this research was Master Builders Glenium® 7920, and the retarding admixture was granulated citric acid (added in aqueous solution). The ratio of coarse to fine (C/F) aggregate was originally set at 1:2 by volume, so that the concrete flowability would not be hampered by excessive coarse aggregate. This C/F aggregate ratio was selected initially based on the advisor's experience with self-consolidating concrete and was not intentionally changed throughout the parametric mix design development because other variables were prioritized. This ratio varied slightly between trials, due to variations in aggregate moisture content, *w/cm* ratio, and other minor changes like fly ash additions. These parameters changed the C/F aggregate ratio very slightly, because in every mix design the total coarse aggregate was held constant, and the sand was varied

volumetrically to sum to 1 yd^3 with 2% air voids. However, the coarse to fine aggregate ratio was generally around 0.53 by volume for most mixes and any variations were minor.

A matrix of test batches was performed to determine the optimal water-cementitious materials ratio (*w/cm*), superplasticizer dosage, and retarder dosage to provide adequate slump flow, workability, and compressive strength. This matrix is detailed in Table 10 for mixes utilizing only rapid setting BCSA cement (no fly ash).

Table 10: Test Batches for Mix Development (No Fly Ash)

Batch Number	***w/cm* ratio**	**HRWR Dosage (oz/cwt)**	**Citric Acid Dosage (lb/cwt)**
RS 1	0.42	16	0.00
RS 2	0.42	16	0.10
RS 3	0.42	16	0.20
RS 4	0.42	16	0.30
RS 5	0.42	20	0.00
RS 6	0.42	20	0.10
RS 7	0.42	20	0.20
RS 8	0.42	20	0.30
RS 9	0.42	18	0.00
RS 10	0.42	18	0.10
RS 11	0.42	18	0.20
RS 12	0.42	18	0.30
RS 13	0.38	18	0.10
RS 14	0.42	18	0.10
RS 15	0.40	18	0.10
RS 16	0.44	18	0.10
RS 17	0.46	18	0.10
RS 18	0.48	18	0.10
RS 19	0.38	18	0.20
RS 20	0.40	18	0.20
RS 21	0.42	18	0.20
RS 22	0.44	18	0.20
RS 23	0.46	18	0.20
RS 24	0.48	18	0.20
Constant Properties: 752 lb/yd^3 (8 sack mix) of RS cement, No Fly Ash (FA), C/F Agg. Ratio = 0.53			

Table 11 shows the slump flow, VSI, and compressive strength results for test batches RS 1 – 24, which include all test batches that used rapid setting BCSA cement only (no fly ash).

Table 11: Test Batch Results (No Fly Ash)

Batch Number	Slump Flow (in.)	Visual Stability Index (VSI)	3 hr. Comp. Strength, f'_{ci} (psi)	28 day Comp. Strength, f'_c (psi)
RS #1	23.00	0	5250	-
RS #2	25.50	1	6110	-
RS #3	26.50	-	5770	-
RS #4	24.00	1	5360	-
RS #5	29.00	3	5220	-
RS #6	28.50	1	6070	-
RS #7	28.50	2	6210	-
RS #8	29.50	3	5090	9460
RS #9	28.50	1	5600	8890
RS #10	27.50	2	6020	9680
RS #11	26.00	1	5950	10040
RS #12	26.75	2	5450	9700
RS #13	23.00	0	6320	10730
RS #14	30.00	3	5160	9580
RS #15	26.50	0	6540	11080
RS #16	28.50	3	5910	10350
RS #17	28.50	3	5190	9450
RS #18	29.00	3	5250	9400
RS #19	19.00	0	6680	10560
RS #20	25.00	0	5450	10240
RS #21	28.50	1	5200	10050
RS #22	30.00	2	4290	10530
RS #23	29.50	3	620	8900
RS #24	34.00	3	0	7330
Constant Properties: 8 sack mix, No Fly Ash (FA), C/F Agg. Ratio = 0.53				

Table 11 shows that batches RS 2, 3, 4, 6, 11, 15, 20, and 21 fully met the targeted mix design requirements, with the exception of 28 day compressive strength for mixes 2, 3, 4 and 6, which were unavailable due to logistical limitations related to the COVID-19 pandemic. These

mixes represent *w/cm* ratios between 0.40-0.42, citric acid dosages between 0.1-0.3 lb/cwt, and HRWRA (Glenium 7920) dosages between 16-20 oz/cwt.

After completing the first 24 trials, another sequence of test batches was initiated, with the purpose of determining whether the inclusion of fly ash was a viable means of achieving the desired fresh and mechanical properties at lower HRWRA dosages. For this batch sequence (RS 25-35), lower *w/cm* ratios were used because the inclusion of fly ash as a cement replacement reduced the BCSA cement content and using fly ash as an additive increased the total cementitious material (and therefore the total mix water). In either case, this led to decreased compressive strength because fly ash is not chemically reactive without calcium hydroxide which is not present in early age BCSA cement concrete. Table 12 shows the test batch sequence with the inclusion of fly ash.

Table 12: Test Batches for Mix Development (with Fly Ash)

Batch Number	***w/cm* ratio**	**HRWR Dosage (oz/cwt)**	**Fly Ash (%)**	**Fly Ash Location/Class**
RS 25	0.40	18	10*	St. Mary Class C
RS 26	0.40	18	15*	St. Mary Class C
RS 27	0.40	18	20*	St. Mary Class C
RS 28	0.40	16	10^{+}	St. Mary Class C
RS 29	0.40	12	15^{+}	St. Mary Class C
RS 30	0.40	6	20^{+}	St. Mary Class C
RS 31	0.37	14	10^{+}	St. Mary Class C
RS 32	0.35	10	15^{+}	St. Mary Class C
RS 33	0.34	10	20^{+}	St. Mary Class C
RS 34	0.34	11.7	20^{+}	Ashgrove Class F
RS 35	0.34	10.8	20^{+}	Red Rock Class C
Constant Properties: Nominal 8 sack RS mix (reduced in FA replacement mixes), Citric Acid = 0.10 lbs/cwt, C/F Agg. Ratio = 0.53				
**Fly ash percentage replacement of BCSA cement* *$^{+}$Fly ash percentage in addition to BCSA cement*				

As shown in Table 12, two Class C and one Class F fly ash from different sources, which were readily available at Fears Lab, were tested to determine whether any particular type or source provided the most desirable concrete properties.

Table 13: Test Batch Results (with Fly Ash)

Batch Number	Slump Flow (in.)	Visual Stability Index (VSI)	3 hr. Comp. Strength, f'_{ci} (psi)	28 day Comp. Strength, f'_c (psi)
RS #25	25.50	0	3840	10560
RS #26	27.50	2	3420	8580
RS #27	26.75	3	2280	7470
RS #28	29.50	1	4820	10820
RS #29	30.50	2	5020	9480
RS #30	25.50	0	4160	8090
RS #31	24.00	0	5990	10970
RS #32	22.00	0	6010	10220
RS #33	26.50	0	6010	10830
RS #34	26.50	0	6490	11690
RS #35	25.00	0	6460	10900

Constant Properties: 8 sack mix, Citric Acid = 0.10 lbs/cwt, C/F Agg. Ratio = 0.53

In batches RS 25-27, where a percentage of the cement was replaced with fly ash, there was an unacceptably significant drop in early age compressive strength. For batches 28-30, where fly ash was added as an additive instead of a replacement, the strength reduction was lessened. However, since the total mix water increased with the addition of fly ash at a 0.40 *w/cm* ratio, the compressive strengths were still somewhat low (although staying just above the minimum threshold), and the slump flows were larger and less stable than the target values for the mix design. For batches 31-35, as the percentage of additional fly ash was increased, the total *w/cm* ratio was decreased in order to keep the ratio of water to RS cement close to 0.40. Since the fly ash in these mixes was not principally used as a pozzolanic SCM since RS cement produces little calcium hydroxide only at later ages, this reduction in total *w/cm* kept the effective *w/cm* for the RS cement high enough to meet hydration requirements (around 0.40) without adding so much extra mix water that strength gain was hampered. This resulted in the

most optimal combination of adequate slump flows, stability (VSI=0), high 3 hr. compressive strength (>6 ksi), and high 28 day compressive strength (>10 ksi). More importantly, this addition of fly ash in mixes 31-35 met all the same targeted mix design parameters as the optimal non-fly ash mixes, but did so at HRWRA dosages of 10-14 oz/cwt instead of 16-20 oz/cwt.

Each trial batch utilized the minimum concrete volume possible to allow tests for slump flow and compressive strength at 3 hours, 7 days, and 28 days. This volume varied between 0.5 – 0.6 ft^3 for each test batch. Ideally strength would have been measured at other times, but the volumes were minimized to limit materials used, to fit the batches in a small rotating drum mixer, and to make the workflow feasible for one individual. Most test batches were performed between Summer 2020 and early Spring 2021 during strong COVID-19 restrictions at Fears Lab, when social distancing requirements and lack of manpower availability due to university undergraduates being in entirely online learning dictated that at most only one student was available to assist the author. Due to the rapid hardening nature of the BCSA cement-based concrete, this limited manpower meant that the batches had to be as small and efficient as practical for the desired properties to be measured and cleanup procedures completed before the concrete reached initial set.

3.1.5 Final Mix Proportions

The final mix design proportions chosen for material property and structural testing based upon the results of the trial mixes are summarized in Table 14. This mix design was utilized for all subsequent research, unless noted.

Table 14: Mix Design Proportions for RS-SCC

Material	Quantity	Volume (yd^3/yd^3)	Comment
Rapid Set Cement	752 lb/yd^3	0.15	8 sack mix
Fly Ash	150.4 lb/yd^3	0.03	20% of RS cement
Water	306.8 lb/yd^3	0.18	w/cm ratio = 0.34
Coarse Agg.	950 lb/yd^3	0.21	-
Fine Agg.	1763.2 lb/yd^3	0.40	-
2% Air Voids	-	0.02	Theoretical air content
Granulated Citric Acid	0.1-0.25 lb/cwt	-	Set time retarder/ workability extension
Glenium 7920	8-12 oz/cwt	-	High range water reducing admixture
Total	3923 lb/yd^3	1.00	-

Note that in Table 14, the typical citric acid dosage varied from 0.10 to 0.25 lb/cwt, but the optimal dosage can vary more depending on temperature.

3.2 Setting Time

One limitation of the data obtained from the mix design development was the variation in temperature between batches, which ranged from 45 to 90 degrees Fahrenheit ($^{\circ}$F), as the mixes were performed between Summer 2020 and Spring 2021. This phase of the research was intended to more formally characterize the relationship between admixture and retarder dosage and set time for the RS-SCC at varying temperatures. This is crucial so that precast concrete manufacturers, as well as researchers, can extend workability and maintain reasonably consistent setting times as seasonal variations in temperature occur.

3.2.1 Procedures

In order to simulate the effects of mixing in environments with varying temperatures, the aggregates and mix water were conditioned to low, moderate, or high temperatures prior to

mixing. Because the mix temperature could only be controlled with limited precision since an environmental chamber large enough to place the mixer in was not available, and because the environmental chambers available at Fears Lab had to be left at their normal temperatures for curing other specimens, relatively coarse temperature ranges were chosen. The low temperature range was set at 50 °F nominal (50 - 60 °F), the moderate temperature range was set at 70 °F nominal (70 - 80 °F), and the high temperature range was set at 80 °F nominal (80 - 90 °F).

The low temperature range was achieved by using aggregates chilled with a standard window unit air conditioner mounted to an insulated wooden box constructed for this purpose (Figure 14), chilled mix water with 50% ice by weight, and room temperature cementitious materials (ambient temperature from high bay storage). The actual mix temperatures ranged from 50-57 °F, with all mixes falling within the targeted low temperature range. The high temperature range was achieved by using aggregates which were heated to around 100 °F in the Grieve® oven at Fears Lab, warm mix water from the tap between about 85-95 °F, and room temperature cementitious materials. The actual mix temperatures ranged from 81-87 °F, with all mixes falling within the targeted high temperature range. The moderate temperature range was achieved by using room temperature aggregates, mix water, and cementitious materials. All these materials were brought to consistent temperatures by storing them in the lab high bay in advance of mixing. The actual mix temperatures ranged from 70-75 °F, with all mixes falling within the targeted moderate temperature range.



Figure 14: Insulated container used for conditioning aggregates for setting time mixes

Table 15 shows the citric acid dosages and mix identifiers that were used within each temperature range to help establish the relationship between temperature and setting time for the RS-SCC mix design. The citric acid dosages were chosen to bracket setting times on both the higher and lower ends of what was expected to be the preferred range. The HRWRA dosage was varied slightly so that the slump flow of the fresh concrete would not vary drastically at extreme temperatures or citric acid dosages.

Table 15: Testing Matrix with Citric Acid Dosages used to Characterize Setting Time/Temperature Relationships

Temp. Range	Batch ID Number	Citric Dosage (lb/cwt)	HRWRA Dosage (oz/cwt)	Slump Flow (in.)	Actual Batch Temp. (°F)
Low (50 - 60 °F)	T3	0.00	12.0	25.50	54
	T0	0.10	10.0	27.75	53
	T1	0.20	8.0	25.75	57
	T2	0.30	8.0	26.50	50
Medium (70 - 80 °F)	T4	0.00	12.0	25.75	70
	T5	0.10	10.0	25.00	72
	T6	0.20	10.0	25.25	71
	T7	0.30	8.0	23.50	73
	T8	0.40	10.0	25.00	75
High (80 - 90 °F)	T9	0.10	10.0	27.00	81
	T10	0.20	9.0	21.00	86
	T11	0.30	10.0	27.75	86
	T12	0.40	9.0	22.50	87
	T13	0.50	9.0	24.75	85

A challenge that had to be met to successfully analyze the setting time behavior was to implement a consistent curing environment for the concrete used in the setting time test for each temperature range. Ideas such as warm and cool water baths around the concrete container used for the ASTM C403 penetrometer setting time test were entertained. However, there were significant logistical challenges pertaining to maintaining consistent hot or cold temperatures for the ASTM C403 specimen environment.

The chosen solution for this issue was the use of a semi-adiabatic calorimeter to analyze the setting time behavior. The use of this Calmetrix® F-Cal 4000 calorimeter significantly reduced the labor associated with measuring setting time according to the ASTM C403 penetrometer, but more importantly, it provided a consistent curing regime for every specimen. The well-insulated calorimeter significantly reduced environmental effects so that the mix temperature would be more nearly maintained until the heat evolution from the concrete

chemical reaction began, compared to attempting to devise warming or cooling systems for the ASTM C403 specimen. However, since ASTM C403 is widely used to characterize concrete setting time, both the calorimeter approach and the ASTM C403 method were used to measure set time for the low temperature range. For the low temperature range, the C403 penetrometer specimens were cured inside the insulated box shown in Figure 14 to keep them insulated from their surroundings similarly to the semi-adiabatic calorimeter. Once the results from the low temperature range were analyzed and it was determined that both methods yielded very similar results, the calorimeter approach only was used for the moderate and high temperature ranges. Figure 15 shows the calorimeter used for the setting time experiments.



Figure 15: Calmetrix® Semi-Adiabatic Calorimeter

3.2.2 Results

Figure 16 shows the graphical results comparing the calorimeter data to the penetrometer data for the setting time of the low temperature mix T2, which was mixed with a concrete temperature of 50.5 ˚F and a citric acid dosage of 0.3 lb/cwt.

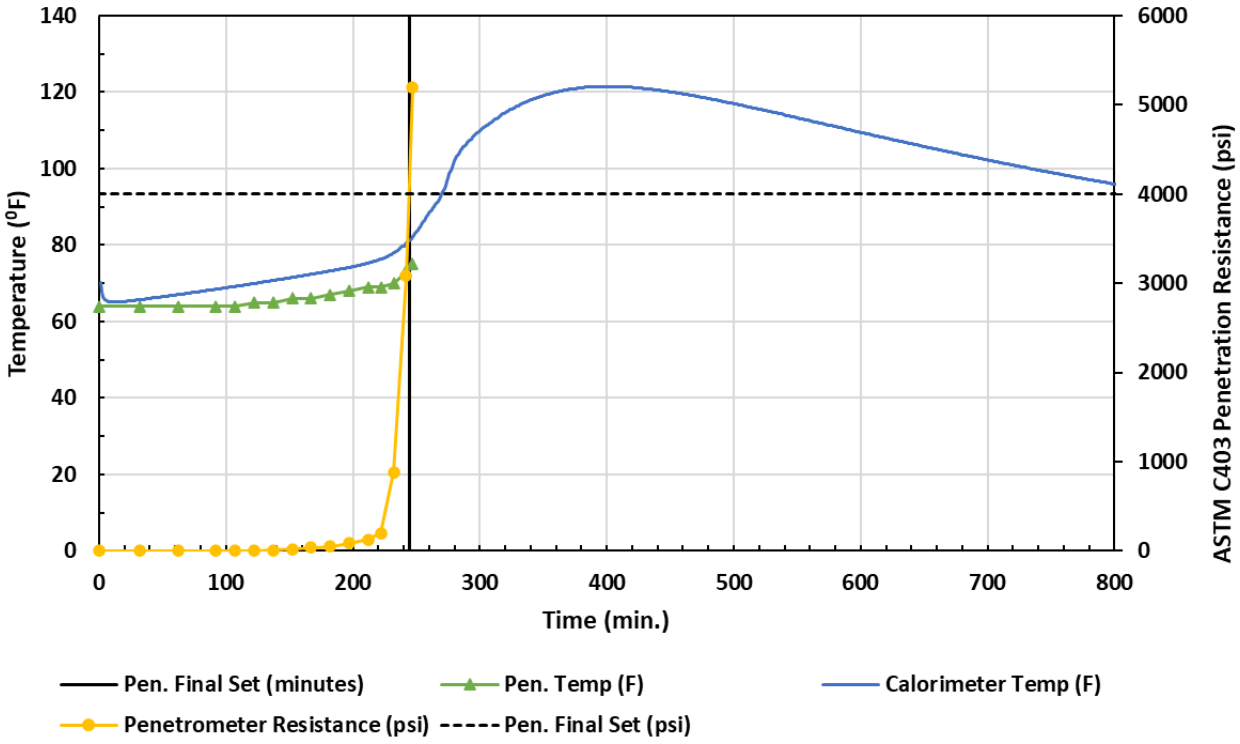

Figure 16: Correlation of calorimeter data with setting-time penetrometer

ASTM C403 stipulates that the point of final set (setting time) for the concrete is considered a penetration resistance of 4,000 psi, represented in Figure 16 by the horizontal dashed black line. Linear interpolation was used to identify the time at which the measured penetration resistance (yellow curve, round markers) crossed this threshold. Then, the vertical solid black line was drawn at that location representing the final setting time according to the penetrometer. This process was repeated for every mix performed in the low (50 ˚F) temperature range, and the trend shown in Figure 16 was observed consistently, in that the penetrometer

setting time closely correlated to the “knee”, or first change in slope, in the calorimeter temperature data (blue curve) within a few minutes more or less. Therefore, it was concluded that determining the final setting time as the slope change from the semi-adiabatic calorimeter heat evolution curve was sufficiently accurate for the purposes of performing a parametric study with a wide range of variables.

Figure 17 shows the heat evolution curves for each citric acid dosage in the 70 ˚F temperature range. Figure 17 for the 70 ˚F range is included here as an example, but curves for every temperature range are available in the Appendices.

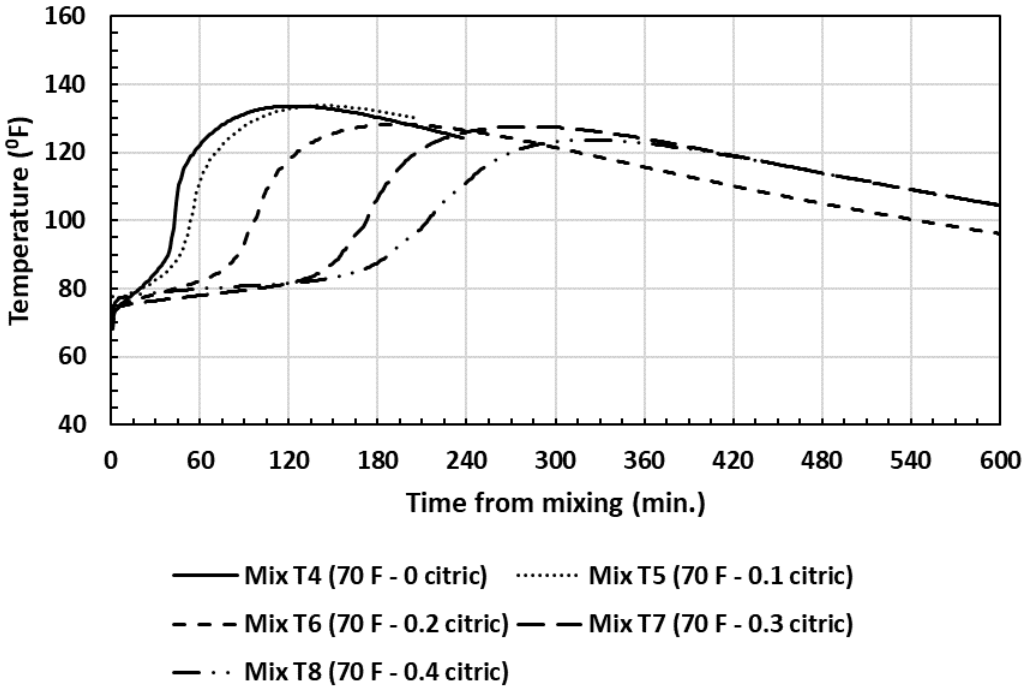

Figure 17: Calorimetry temperature curves for 70 ˚F mix series

Figure 17 shows that, as expected, the “knee” in the curve where the slope suddenly changes shifts to the right as the citric acid dosage increases. Therefore, the estimated final setting times increase from around 40 minutes with no citric acid, to greater than 2 hours for 0.3-

0.4 lb/cwt of citric acid. The process of plotting each temperature curve and identifying the estimated final set time based on the slope change in the curve was performed for every mix within each temperature range. Each temperature curve is available individually in Appendix A and the resulting setting times are plotted with temperature and citric acid dosage in Figure 18.

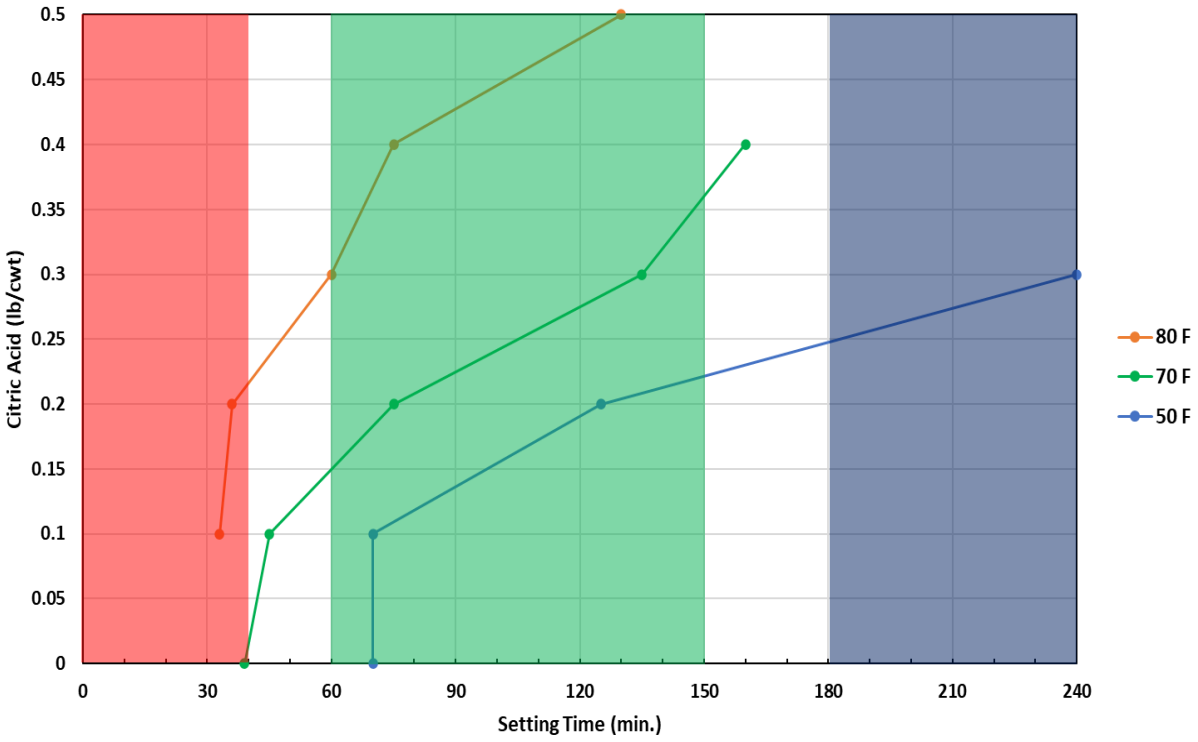

Figure 18: Setting-time data from calorimeter with operating ranges highlighted

In Figure 18, the colored panes are qualitative ranges that have been superimposed to help visualize setting times that are likely too rapid (red), likely acceptable (green), and likely too long (blue). Whether a given setting time is acceptable depends on the application. Therefore, the ranges in Figure 18 are based on a precast operation where high early compressive strength in 2-4 hours is required, and workability only needs to be retained long enough to mix the concrete, transfer directly to the formwork, and place the concrete. In the red range, if the concrete reaches final set in 40 minutes or less, the workability will diminish so quickly that

proper mixing and placement could be compromised. In the blue range, if the concrete takes close to 3 hours or more to reach final set, the early workability will be adequate but the concrete will not reach high early compressive strength at a 2-4 hour age. The ideal green range is selected as between one hour and up to 2.5 hours. With a final setting time in this range, slump flow and workability can be maintained for at least 30 minutes, and the concrete will have the potential to reach high compressive strength in 2-4 hours.

Figure 19 repeats the same calorimeter setting time estimates from Figure 18, but with the addition of the results of 7 ASTM C403 setting time penetrometer tests. These penetrometer tests are included to show the agreement between the two methods. The blue triangular markers were mixed at 50 $^{\circ}$F and were cast from the same mixes as the calorimeter specimens to serve as the calibration mixes described previously. The purple diamonds were mixed with the concrete temperature in the 40 $^{\circ}$F range and the green square was a research batch mixed with the concrete temperature in the 70 $^{\circ}$F range.

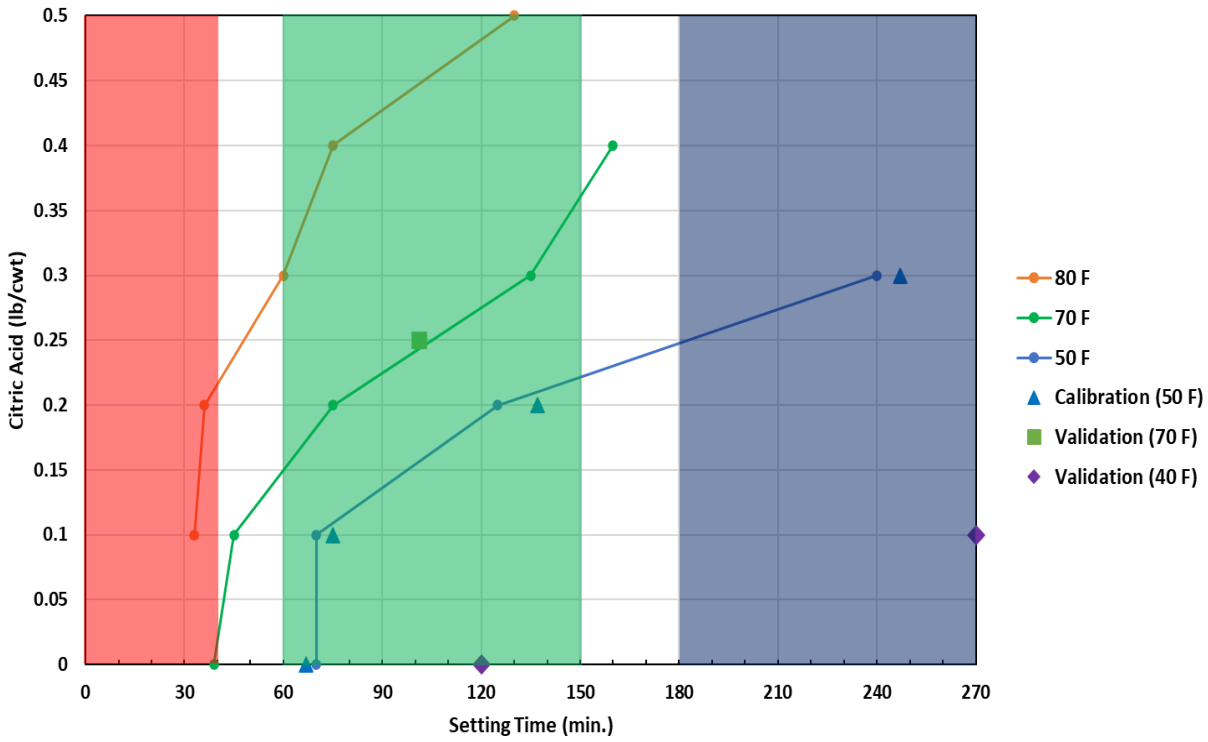

Figure 19: Calorimeter setting time data plotted with penetrometer setting time data for validation

Figure 19 shows that for penetrometer tests at a variety of temperatures and citric acid dosages, the calorimetry approach yielded a framework that agreed consistently with the penetrometer whether the tests were both conducted on the same batch of concrete or not.

Figure 20 shows the setting time data from the calorimetry testing plotted against workability time data supplied by CTS Cement, the manufacturer of the BCSA cement used in this project.

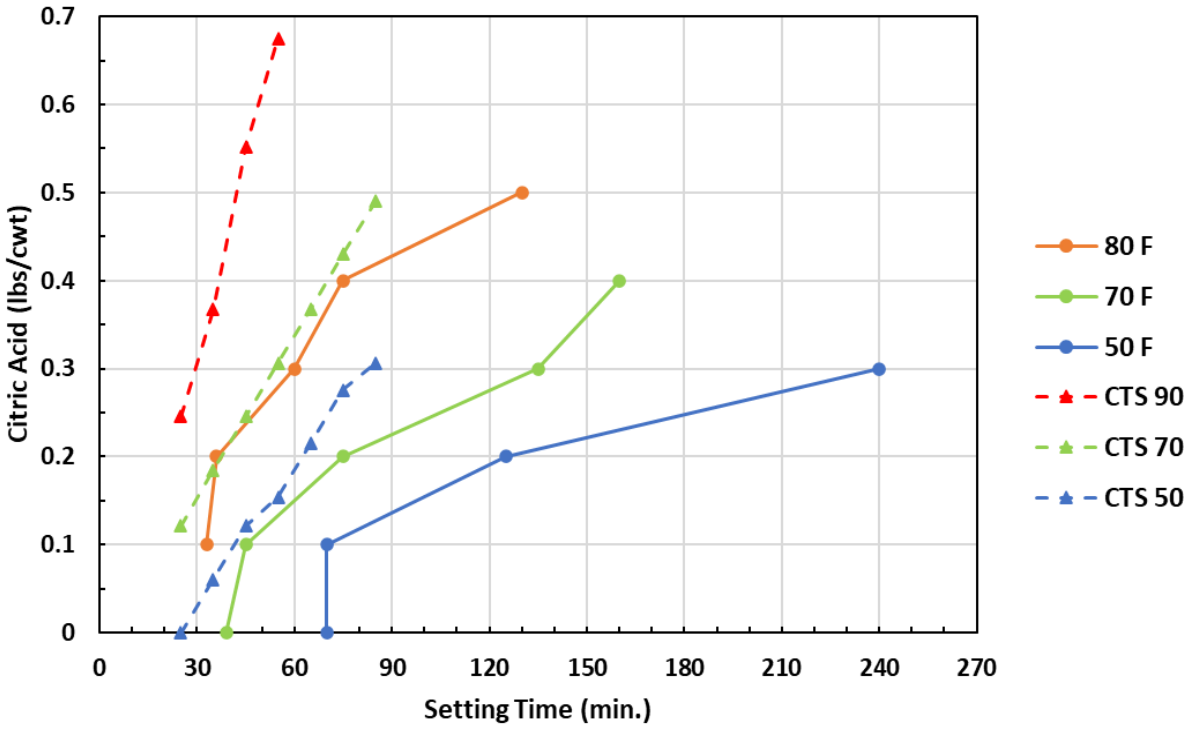

Figure 20: Calorimeter setting-time data plotted against CTS workability time data

The CTS data shown in Figure 20 were taken from a technical bulletin published by the company entitled "Retarder Dosage Guideline" (CTS Corp, 2021). In this document, CTS defined the working times presented as "the amount of time after discharging that concrete can rest in place and be workable with vibrators, shovels, or other tools." Obviously, this working time should be less than the final setting time of a comparable concrete mixture. Another difference between the CTS data and the calorimeter data from this research is that the CTS data used a 7-sack BCSA cement mix design instead of the 8-sack mix with fly ash which was used in this research. Finally, the CTS bulletin does not explicitly specify how the mix temperatures were controlled or how working time was measured per se. Even with these differences, the CTS data is presented here for comparison, because it is the only other data in the literature identified by the author which attempts to quantify how quickly workability diminishes or the concrete sets as temperature and

citric acid dosages are varied for BCSA cement concrete. In Figure 20, the CTS data curves which coincide with the same temperature ranges studied in these experiments (50 °F and 70 °F, blue and green respectively) lie to the left of the curves from the calorimeter data. In addition, the CTS curves stay closer to linear and do not roll over like the curves from the calorimeter data. Both of these observations are logical. First, the CTS curves should indicate shorter effective times because that data is referring to workable time, which will always be shorter than setting time for the same or similar mixes. Also, the CTS curves should indeed be steeper. This is because even if a relatively high citric dosage at a given temperature may extend the setting time, the concrete may still stiffen up and lose its workability at a steady rate. Finally, the highest temperature range tested by CTS (90 °F) also lies to the left of the 80 °F calorimeter temperature range. This is also reasonable, because the concrete should lose workability and set faster at higher temperatures. Finally, it is also interesting to note that the CTS researchers chose not to perform the lowest citric acid dosages at the higher mix temperatures. In a similar manner, a mix with 0 lb/cwt citric acid was not performed for the 80 °F range for this research. In both cases, the underlying reason is that at these elevated temperatures it is risky to mix with little to no citric acid due to the potential for damaging the testing equipment. Even if the data could be gathered without damaging equipment, it would provide little useful information and would never be recommended to actually batch BCSA cement concrete at these elevated temperatures with so little citric acid retarder.

3.3 Flexural Strength (Modulus of Rupture)

Flexural strength of the final selected mix design was measured using Modulus of Rupture (MOR) testing performed in general accordance with ASTM C78, in order to round out the material characterization of the final selected mix design.

3.3.1 Procedures

MOR testing was performed at early age (3-4 hours), 24 hours, and 28 days from two separate batches of the same mix design in order to examine how the flexural strength increased with maturity and/or compressive strength. Figure 21 shows the testing configuration and typical failure mode of the MOR specimens. Every MOR specimen was tested on the Forney compression machine shown in Figure 21 under manual load rate control at 25-35 lb/sec and every specimen failed in its middle third. Each MOR result presented is the average value resulting from testing two (unless otherwise noted) 6 in. x 6 in. x 22 in. beams with an 18 in. span under third point loading. In order to correlate the MOR to compressive strength, 4 in. x 8 in. cylinders were tested for compressive strength on a separate Forney® compression machine during each MOR test.



Figure 21: MOR Testing with Forney at Fears Lab

3.3.2 Results

Figure 22 shows the average MOR measured at each time increment for the specimens cast from Mix 2A. Figure 23 shows the average MOR for Mix 2A at each time increment, divided by the square root of the accompanying compressive strength in order to normalize the data. Figure 24 shows the compressive strength measured at each testing age where MOR was concurrently measured.

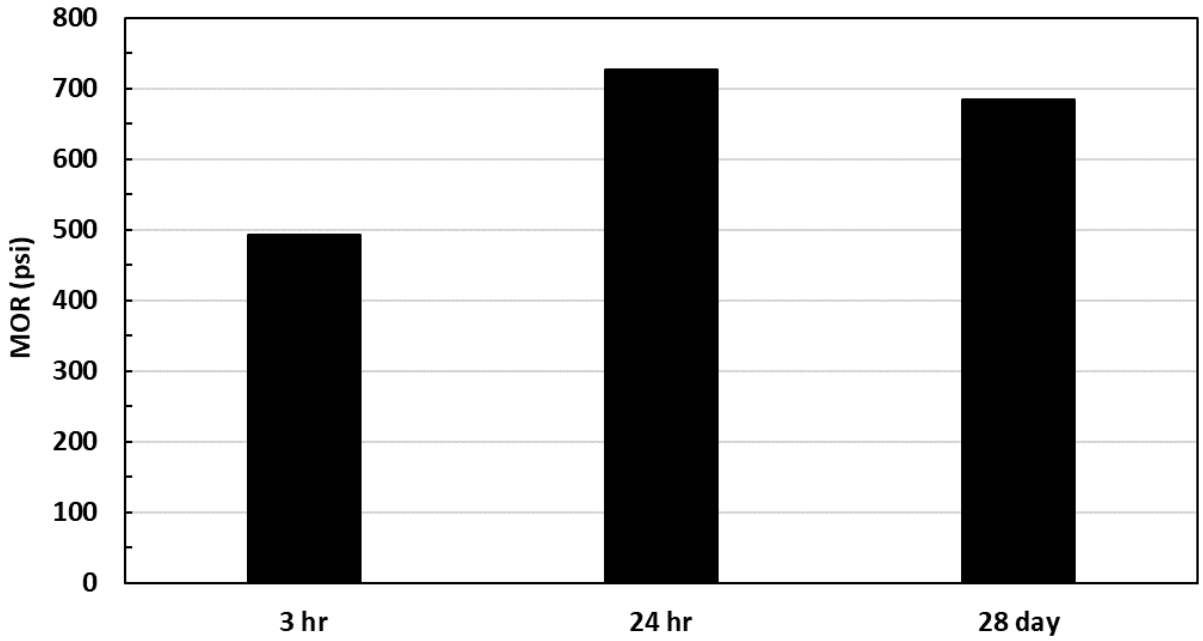

Figure 22: MOR data from RS Mix 2A

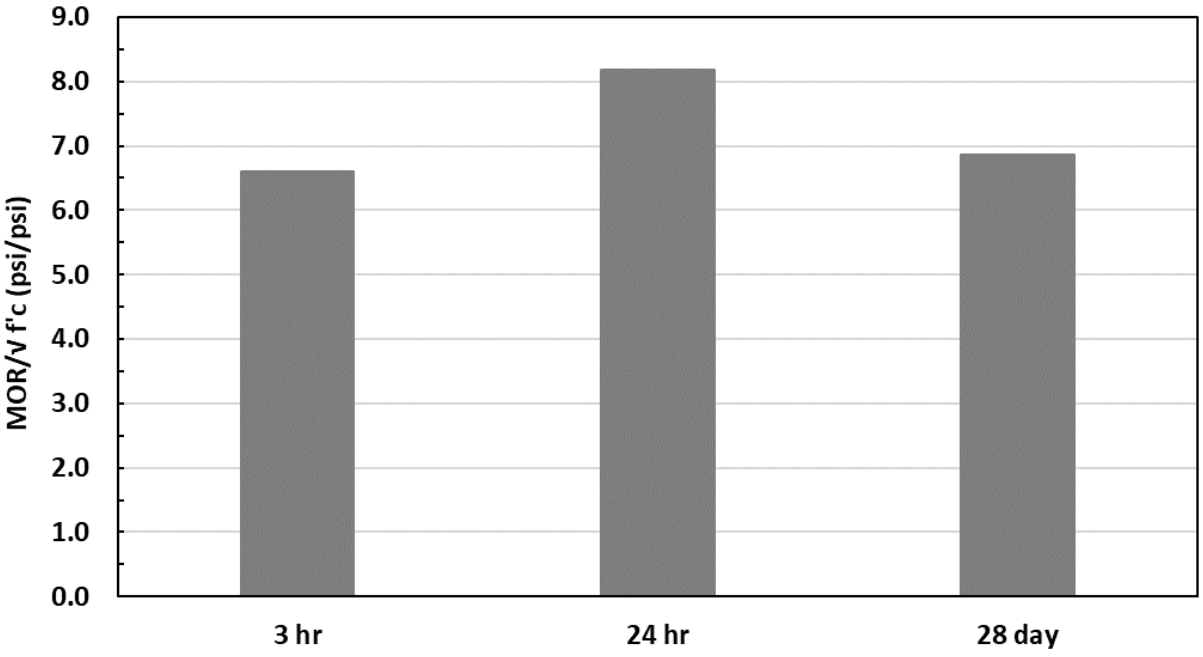

Figure 23: MOR data from RS Mix 2A normalized by square root of compressive strength

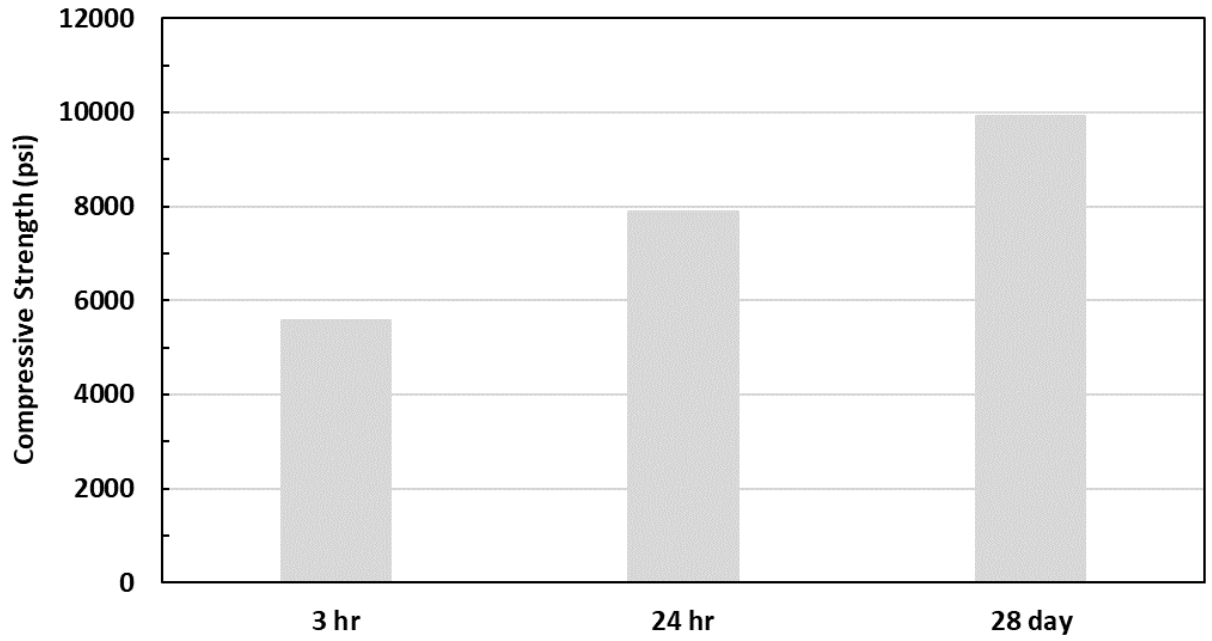

Figure 24: Compressive strength data from RS Mix 2A

Figure 25 shows the average MOR measured at each time increment for the specimens cast from the Large Block Pullout Test (LBPT) Mix (see Chapter 4, section 4.1). Note that in Figure 25, because over an hour elapsed between the first and second early age MOR tests (at ages of 3.4 and 4.5 hours respectively), these tests were treated as separate tests and therefore each presented result is a single data point, not the average of two beam failures. This elapsed time between the first and second early age MOR test was due to interference with the strand testing for the LBPT described in Chapter 4. The 24 hour and 28 day MOR results are the average of two beam failures, just like the tests from Mix 2A. Figure 26 shows the average MOR for the LBPT Mix at each time increment, divided by the square root of the accompanying compressive strength in order to normalize the data. Figure 27 shows the compressive strength measured at each testing age where MOR was concurrently measured.

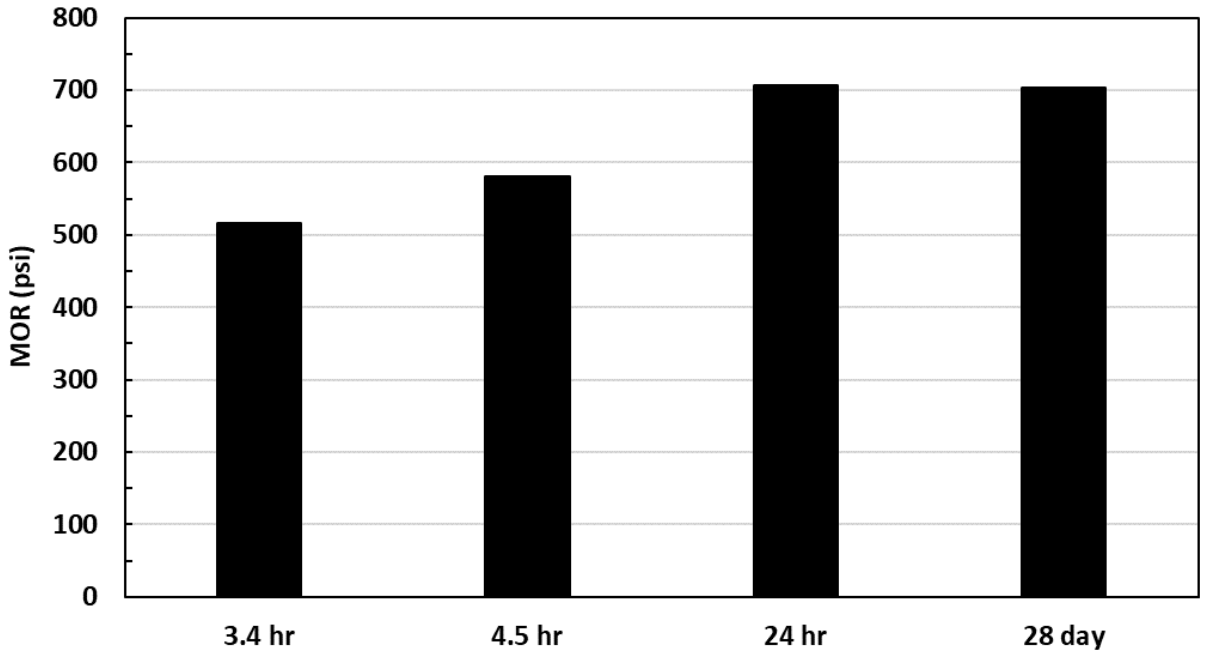

Figure 25: MOR data from LBPT RS Mix

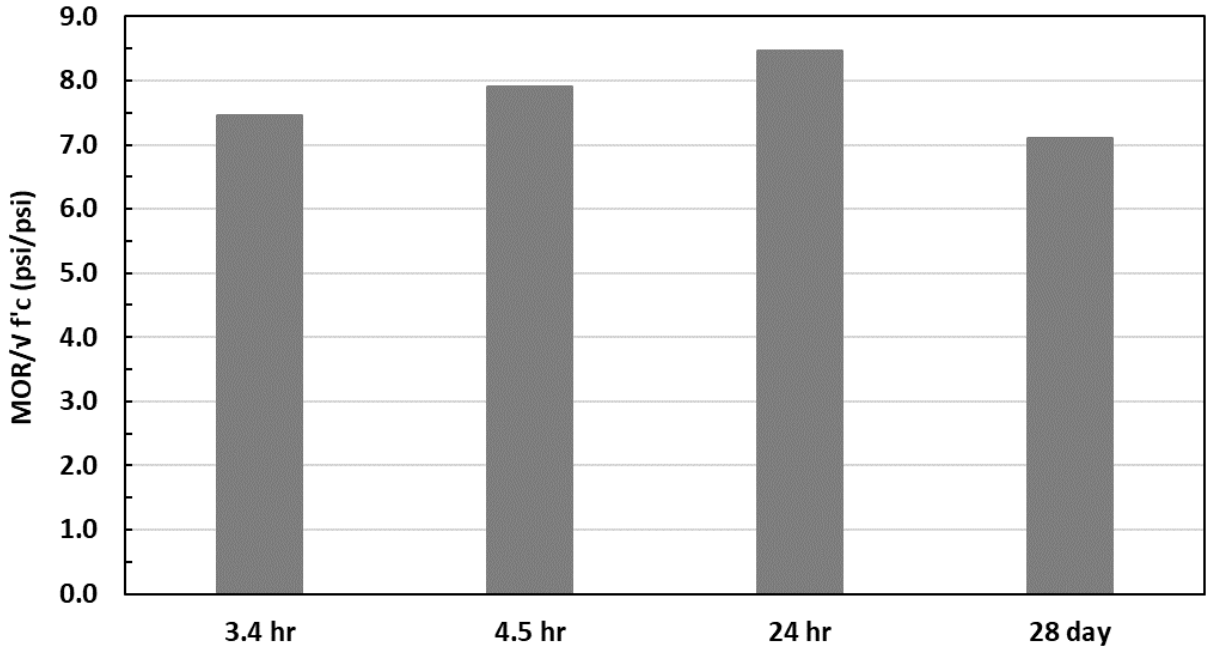

Figure 26: MOR data from LBPT RS Mix normalized by square root of compressive strength

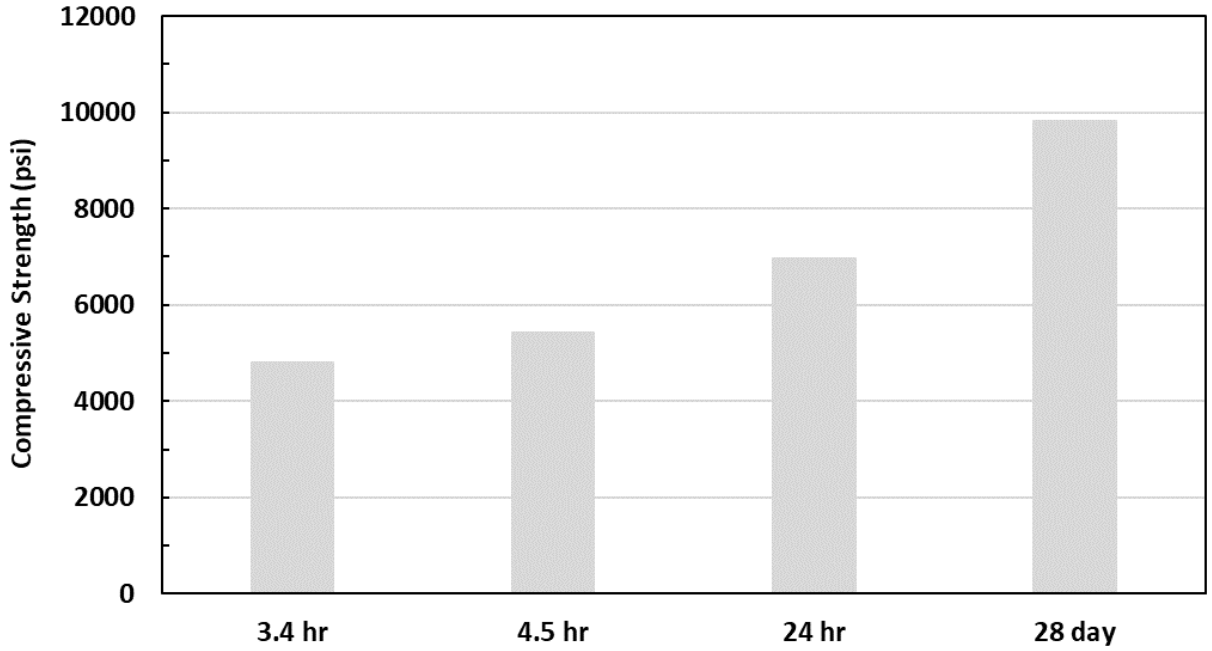

Figure 27: Compressive strength data from LBPT RS Mix

Several important observations can be drawn from this MOR data. First, the RS-SCC reached around 500 psi flexural strength at between 3 and 3.5 hours of age. The flexural strength increased to between 700 – 720 psi at 24 hours and between 680 – 700 psi at 28 days. Importantly, the flexural strength was not observed to increase substantially between 24 hours and 28 days for either batch. This indicates that this material may gain the majority of its flexural strength at very early ages, mainly within the first 3 – 4 hours. Even though the MOR essentially flatlined between 24 hours and 28 days, the compressive strength continued to increase incrementally over this time period for both batches. This resulted in the normalized MOR values ($f_r/\sqrt{f'_c}$, psi/psi) declining from over 8.0 at 24 hours to around 7.0 at 28 days. It is important to note that this pattern of compressive and flexural strength gain may depend on the curing regime used in this research, which entailed curing the concrete in dry, room temperature conditions (approximately 50% RH on average, with 60 – 70 ^{o}F average temperatures). Moist curing the concrete specimens could affect the observed strength gain patterns.

Finally, the goal of the MOR testing was in large part to evaluate the last remaining targeted mix design parameter, which was to reach an average mature flexural strength of around $7.5\sqrt{f'_c}$. Since the MOR mostly flatlined after 24 hours, it is reasonable to say that mature flexural strength was reached at 1 day. The average of the normalized 24 hour and 28 day flexural strengths for both batches is $7.65\sqrt{f'_c}$, with the values ranging from 6.87 to 8.46. Therefore, the MOR testing performed on the RS-SCC would indicate that this material has excellent flexural strength properties, and, on average, reached the target of $7.5\sqrt{f'_c}$. It is also worth noting that the low coarse aggregate content of the mix design proportions will have an impact on flexural strength and these strengths may be different for other mix proportions. Finally, since it appears that the compressive strength gain continues after 24 hours at a greater rate than the flexural strength gain, it is possible that better normalization techniques exist than the square root of the compressive strength at the time of testing. This question is an excellent topic for further research.

3.4 Modulus of Elasticity

Modulus of Elasticity (MOE) testing was performed in general accordance with ASTM C469, with the ultimate goal of determining and modelling how the stiffness of the RS-SCC changes with either time or compressive strength so that instantaneous elastic shortening (ES) prestress losses can be estimated accurately. As stipulated by ASTM C469, each cylinder was loaded up to 40% of its compressive strength at time of testing 3 times at between 28-42 psi/sec and the MOE was calculated based upon the results from the latter 2 loading cycles. This process was repeated for 3 specimens at each time increment, meaning that each MOE value represents the average of 6 loading cycles.

Two rounds of MOE testing were performed. Round #1 was performed using the mix design developed in Section 3.1 with a C/F aggregate ratio of 0.53. Round #2 was performed using a very similar mix design, but with the C/F aggregate ratio increased to 0.82, a proportional increase in the coarse aggregate of a little over 50%. The purpose of adding Round #2 to the MOE testing was to expand the mix design analysis and determine whether the lower coarse aggregate content in Round #1, chosen to optimize the slump flow of the original mix design, had any undesirable effect on the concrete stiffness.

3.4.1 Procedures

3.4.1.1 Round #1 - 0.53 C/F Aggregate Ratio

A sufficient number of 4 x 8 in. cylinders were cast to perform both MOE and companion compressive strength testing on the chosen mix design specified in Table 14 at 3 hr, 6 hr, 9 hr, 12 hr, 24 hr, 28 days, 56 days, and 90 days. All MOE specimens were loaded to 40% of the compressive strength measured at the time of testing as stipulated in ASTM C469, which presented a major logistical challenge due to the rapid strength gain of this material. This challenge was solved by utilizing both Forney compression testing machines at Fears Lab simultaneously as shown in Figure 28.



Figure 28: MOE test on Forney 1 (left) with compression test on Forney 2 (right)

To ensure that each MOE specimen was loaded to the appropriate stress level relative to its compressive strength at a given time interval, companion compressive strength cylinders were tested repeatedly on Forney 2 while the MOE tests were being performed on Forney 1. In this way, a log of the compressive strength gain was kept in "real-time", so that every MOE cylinder was loaded to 40% of the compressive strength at the time of testing. An additional benefit of this approach was that all MOE data could be normalized to compressive strengths from the same time intervals in order to discern maturity trends.

3.4.1.2 Round #2 - 0.82 C/F Aggregate Ratio

In order to broaden the scope of the work from a mix design perspective, and to determine how the coarse aggregate content may have affected the MOE, this testing was repeated with a slightly different mix design. The coarse/fine (C/F) aggregate ratio was increased from 0.53 to 0.82, an increase of a little over 50% in the coarse aggregate relative to the fine

aggregate content. Otherwise, all other mix parameters were left constant. Importantly, however, even though this testing was repeated using the same cement content as the first round of MOE testing, it was performed nearly a year later meaning that the cement had aged substantially by the second round of MOE testing. Additionally, it was determined that the cement sack was not sealed properly at some point between rounds of MOE testing, meaning that it was vulnerable to moisture intrusion for an extended time period after the first round of MOE testing but before the second round. These facts, which affected only the second round of MOE testing with the 0.82 C/F ratio, were noted when evaluating the resulting data. The 0.82 C/F MOE testing was performed at 3 hr, 6 hr, 9 hr, 12 hr, 24 hr, and 28 days.

3.4.2 Results

3.4.2.1 Round #1 - 0.53 C/F Aggregate Ratio

Figure 29 shows the average MOE measured at each time increment for the specimens cast from Mix 2C. As mentioned previously, the MOE value reported at each time increment is the average result of the latter 2 load increments on 3 separate specimens. Figure 29 shows that the average measured MOE gradually increases over time, starting at about 3500 ksi at 3 hours and reaching nearly 4500 ksi between 28 and 90 days.

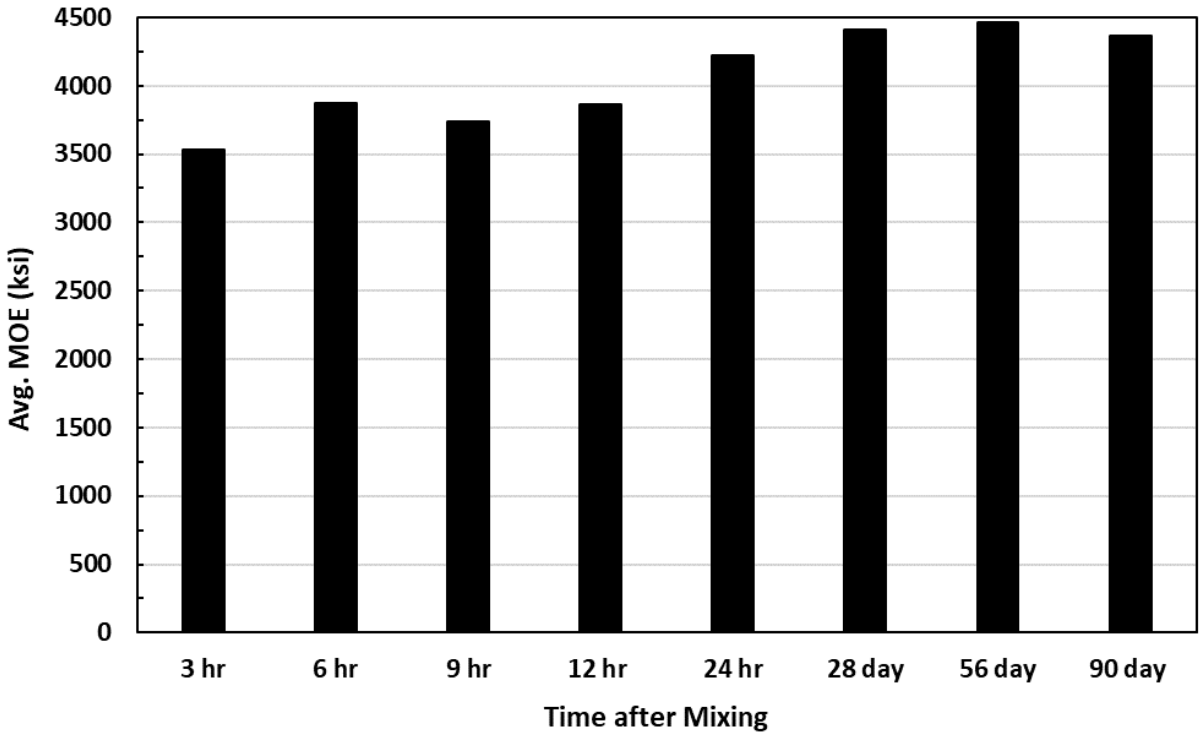

Figure 29: MOE data from RS Mix 2C

Figure 30 shows the compressive strength gain of Mix 2C with time. The compressive strength presented for 3 hours is the average of 7 individual test results, performed immediately before, during, and immediately after MOE testing at 3 hours. The 6 hr, 9 hr, and 12 hr compressive strengths are each the average of 6 individual tests performed during their respective MOE tests. From 24 hours onward, all compressive strengths are the average of 3 individual tests performed at the same time as the MOE tests.

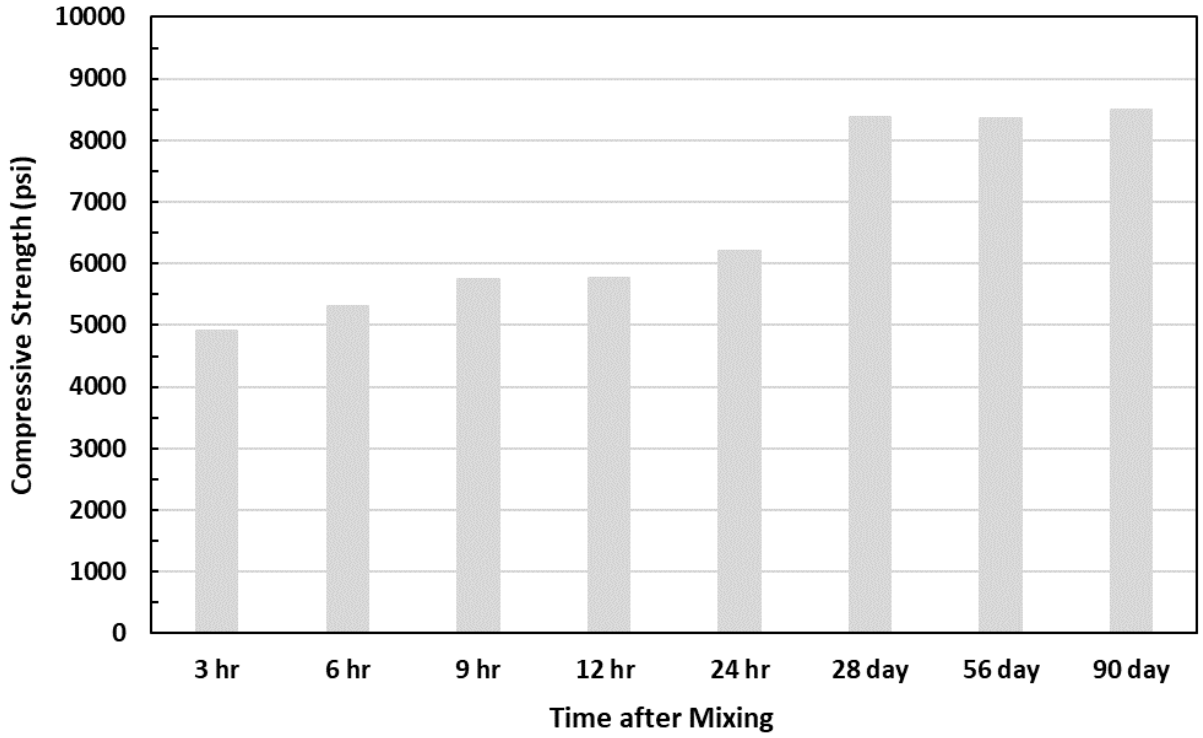

Figure 30: Compressive strength data from RS Mix 2C

Figure 30 shows that the compressive strength steadily increased from just under 5 ksi at 3 hours, to just over 6 ksi at 24 hours. The average mature compressive strength varied between 8.3 and 8.5 ksi from 28 days to 90 days.

Figure 31 shows the average MOE at each time increment from Figure 29 normalized by division with the square root of the compressive strengths from Figure 30.

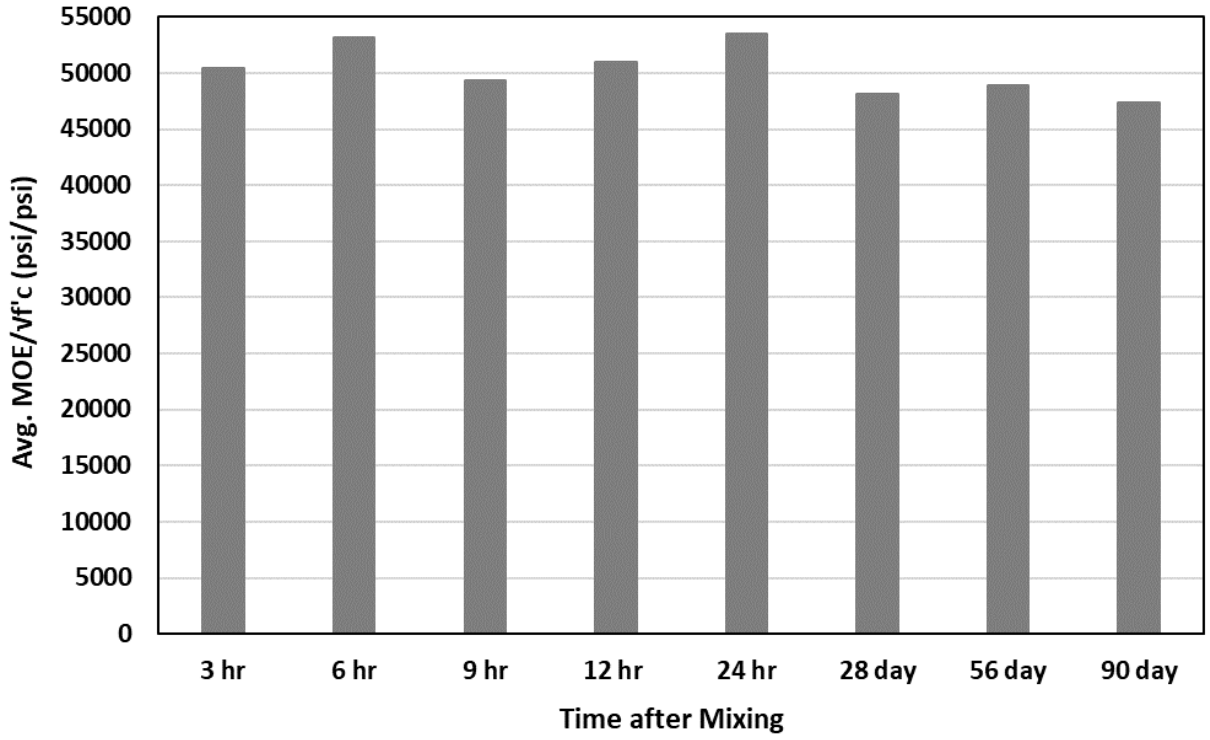

Figure 31: MOE data from RS Mix 2C normalized by square root of compressive strength

Figure 31 shows that, although there is some variation, the normalized MOE generally declined over time. While 4 of the first 5 normalized MOE values were above the average value of around 50,000, all of the last 3 values, from 28 – 90 days, failed to reach this threshold. This would indicate that in general, when compared on the basis of equivalent compressive strength, the MOE was not increasing with age or maturity.

Figure 32 shows the average MOE at each time increment from Figure 29 normalized by division with only the average compressive strengths from Figure 30 instead of the square root of the average compressive strength. The purpose of this analysis was to use a different normalization technique to further explore the interplay of concrete age or maturity with the compressive strength.

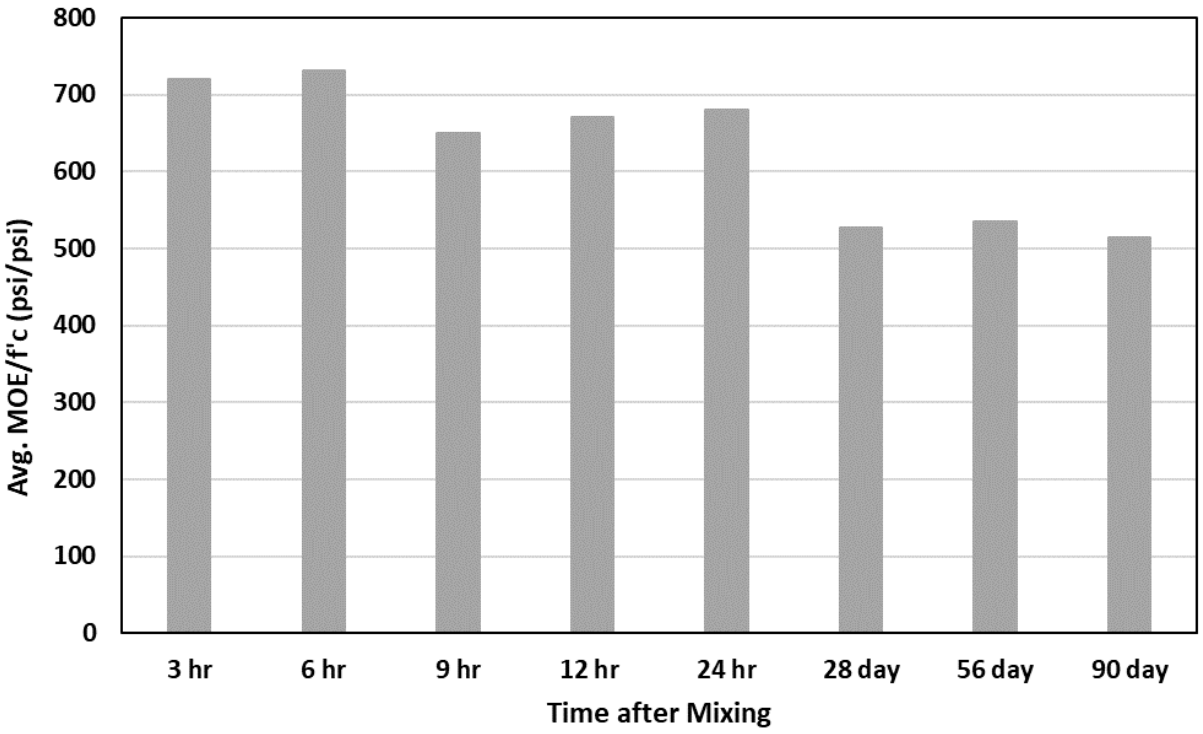

Figure 32: MOE data from RS Mix 2C normalized by compressive strength

Figure 32 shows the same trend as Figure 31 but with substantially less variation between time increments. The average MOE divided by the compressive strength drops steadily between most time increments, falling from over 700 at 3-6 hours, to between 650 and 680 in the 9-24 hour range, and ending slightly over 500 at full maturity (between 28 and 90 days). Similar to Figure 31, this trend indicates that increasing compressive strength may be more influential on the MOE than the maturity of the concrete alone. Another way of understanding this data analysis may be that the stiffness of the concrete is a sort of cross product of both the maturity and the compressive strength of the concrete, but that there is not a reduced or diminished relative maturity at very early ages as evidenced by the fact that the normalized MOE at 3 hours tended to be as high or higher than the average normalized MOE across the entire age range.

Figure 33 shows another visualization of the results of the MOE testing for Mix 2C, by tracing out the stress-strain curve that was recorded from testing each individual specimen.

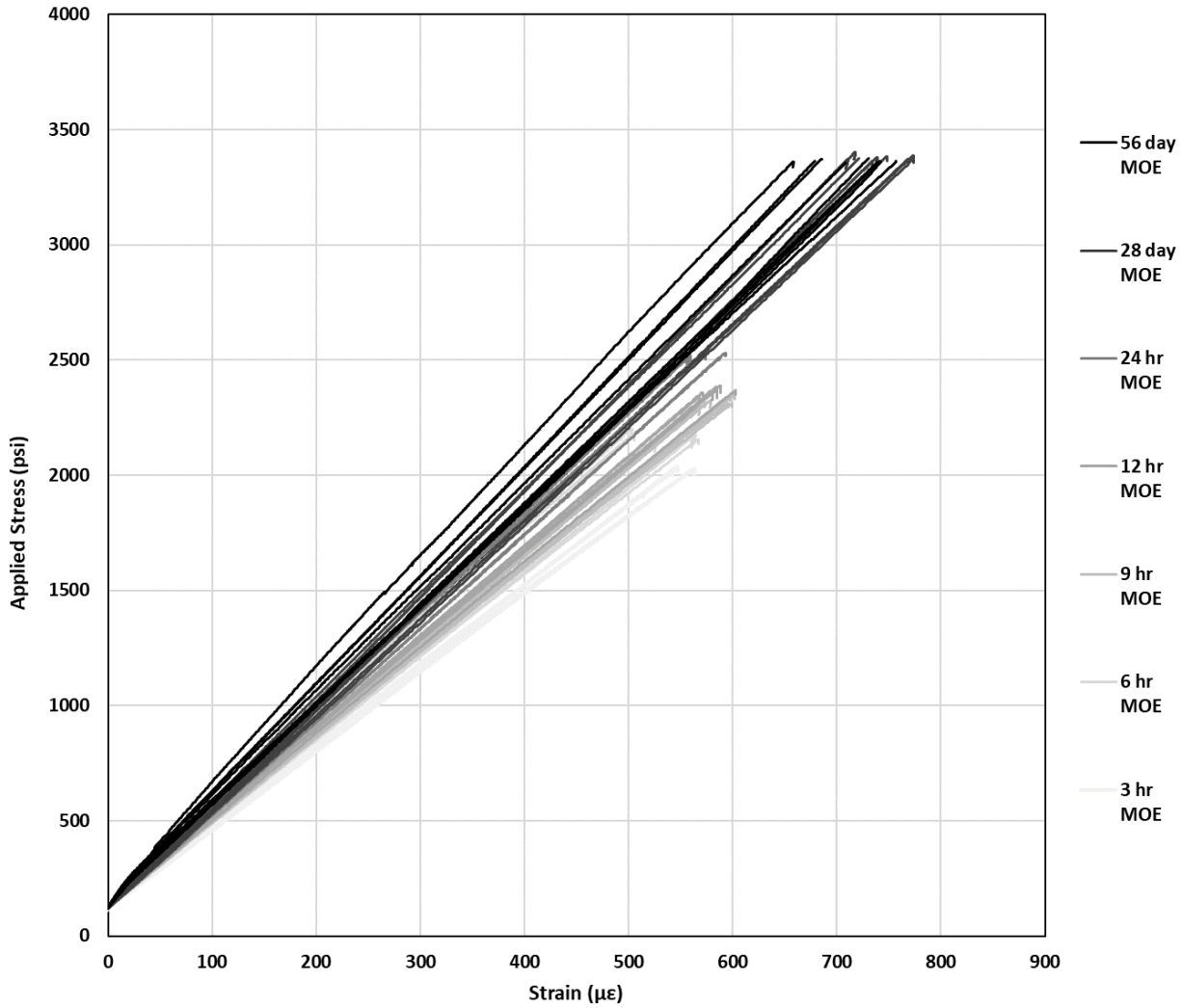

Figure 33: MOE stress-strain data variation with time from RS Mix 2C

In Figure 33 the curves are colored darker with increasing time increments and the slopes of the curves generally increase showing the gradual increase in MOE with time. Another interesting observation is that each curve is very linear, indicating that each specimen was most

likely loaded within its linear-elastic range (which is the intent of the $0.40f'_c$ limit from ASTM C469) and that the load and deflection measurement instruments were behaving consistently.

Figure 34 shows a plot of the best fit simple linear regression between the average MOE from each time increment plotted against the square root of the average companion compressive strength.

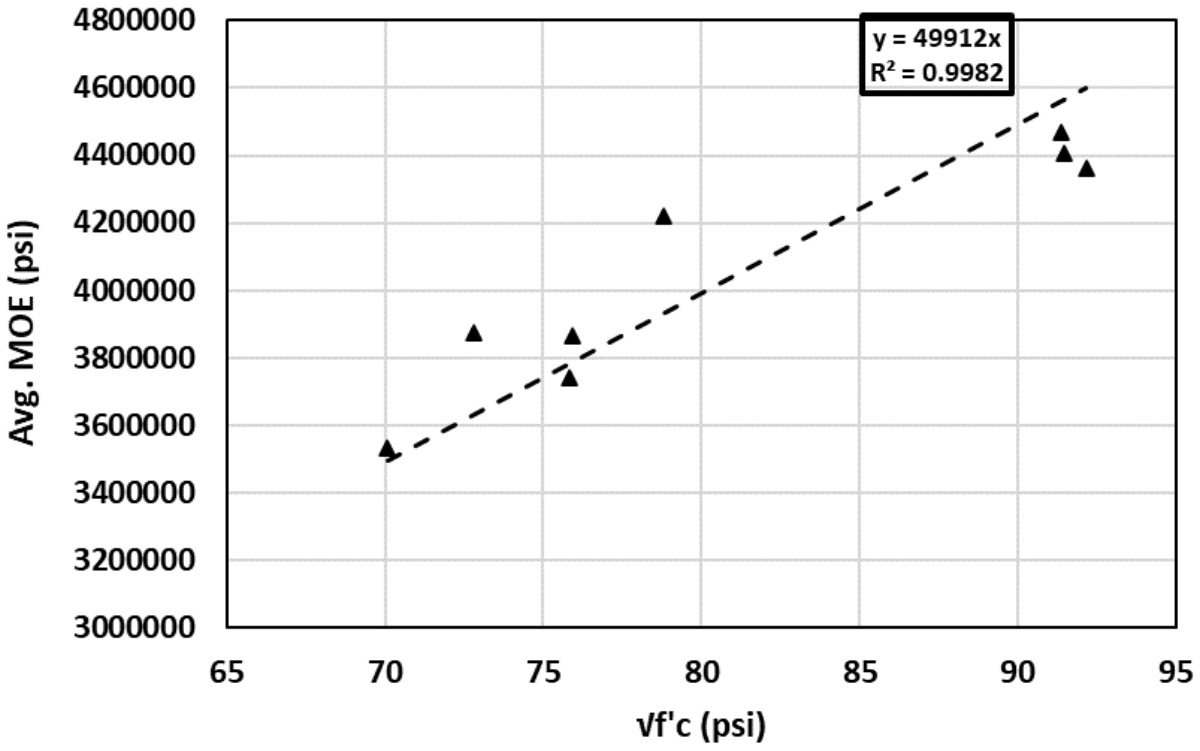

Figure 34: Best fit simple linear regression analysis to model/predict MOE using square root of compressive strength

The purpose of the model shown in Figure 34 was to provide an accurate and straightforward means of estimating the MOE for the RS-SCC for applications such as calculating the elastic shortening portion of prestress beam losses or the elastic strain component from loading the creep specimens. Figure 34 shows that the best fit linear trendline had a strong correlation coefficient (R^2) of 0.998 with the measured data at a slope of 49,912. This agrees

closely with an alternate approach of averaging the modulus values normalized by the square root of the compressive strength, which yields a result of 50,227.

Based upon the results of this data analysis, Equation 5 was chosen to model the MOE for the RS-SCC mix design employed in this research.

$$E_c = 50{,}000\sqrt{f'_c} \qquad (5)$$

with f'_c (concrete compressive strength at any specified age) and E_c in psi.

Although the data also had a strong linear correlation coefficient with the data normalized by only the compressive strength, the square root normalization was chosen because it is already a widely used approach in the concrete industry and because the correlation coefficient for the square root normalization was slightly higher.

3.4.2.2 Round #2 - 0.82 C/F Aggregate Ratio

Figure 35 shows the average MOE measured at each time increment for the specimens cast for the Round #2 MOE testing with an increased coarse aggregate proportion. Like in the previous section, the MOE value reported at each time increment is the average result of the latter 2 load increments on 3 separate specimens.

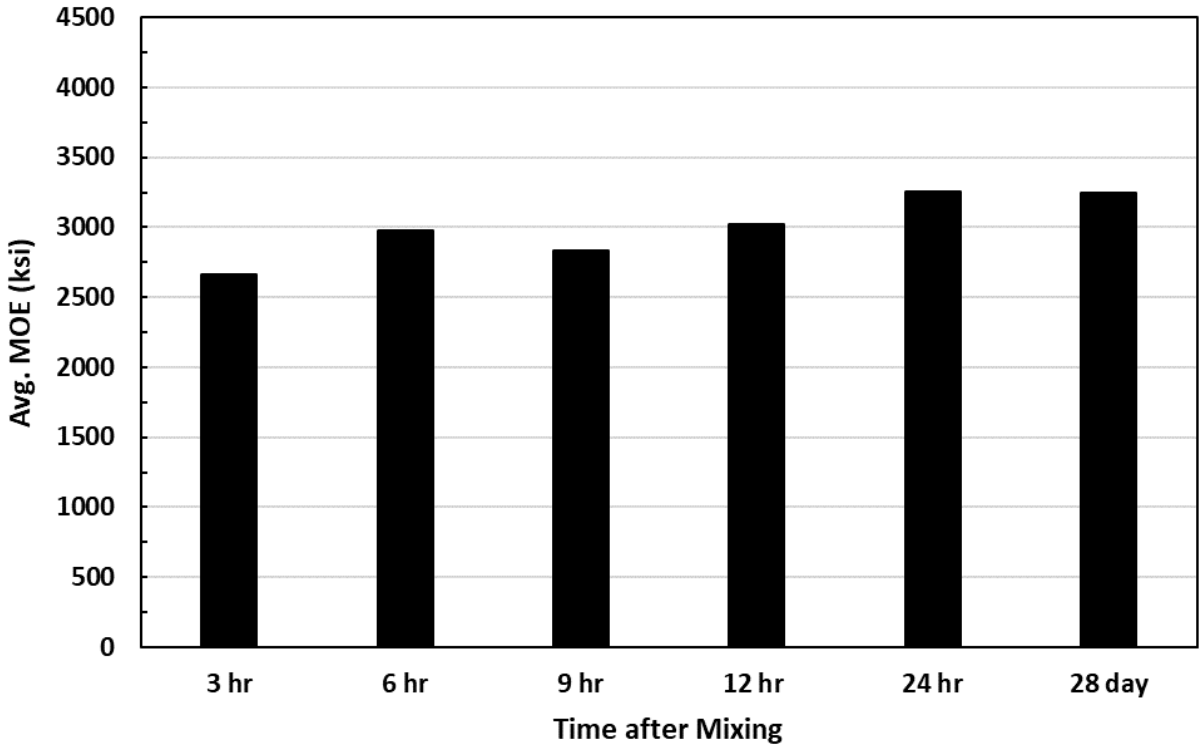

Figure 35: MOE data from RS HI AGG Mix (round #2 high coarse aggregate)

Figure 35 shows that the average MOE generally increased over time, starting at just over 2500 ksi at 3 hours and reaching approximately 3200 ksi between 24 hours and 28 days. The highest MOE achieved in this testing (3259 ksi at 24 hours) is lower than the lowest MOE from the first round of testing (3531 ksi at 3 hours), which implies degradation of the cement that was used for the second round of MOE testing for the reasons described in Section 3.1.1. Further evidence that this was a cement issue comes from the fact that a significant increase in the coarse aggregate proportion should increase the stiffness of the concrete, or at least not cause a noticeable change. Increasing the coarse aggregate should not cause a significant decrease in the MOE performance. This reinforces the importance of storing cement properly in well-sealed containers if it is to be stored for extended periods of time during the course of a research project.

Figure 36 shows the compressive strength of the companion compressive specimens for Round #2 MOE testing over time. The compressive strength at 3 hours is constituted by the average of 6 individual test results, performed immediately before, during, and immediately after the MOE testing at 3 hours. The 6 hour compressive strength is similarly the average of 5 individual tests and the 9 hour strength is the average of 4 tests. From 12 hours onward, all compressive strengths are the average of 3 individual tests performed at the same time as the MOE tests.

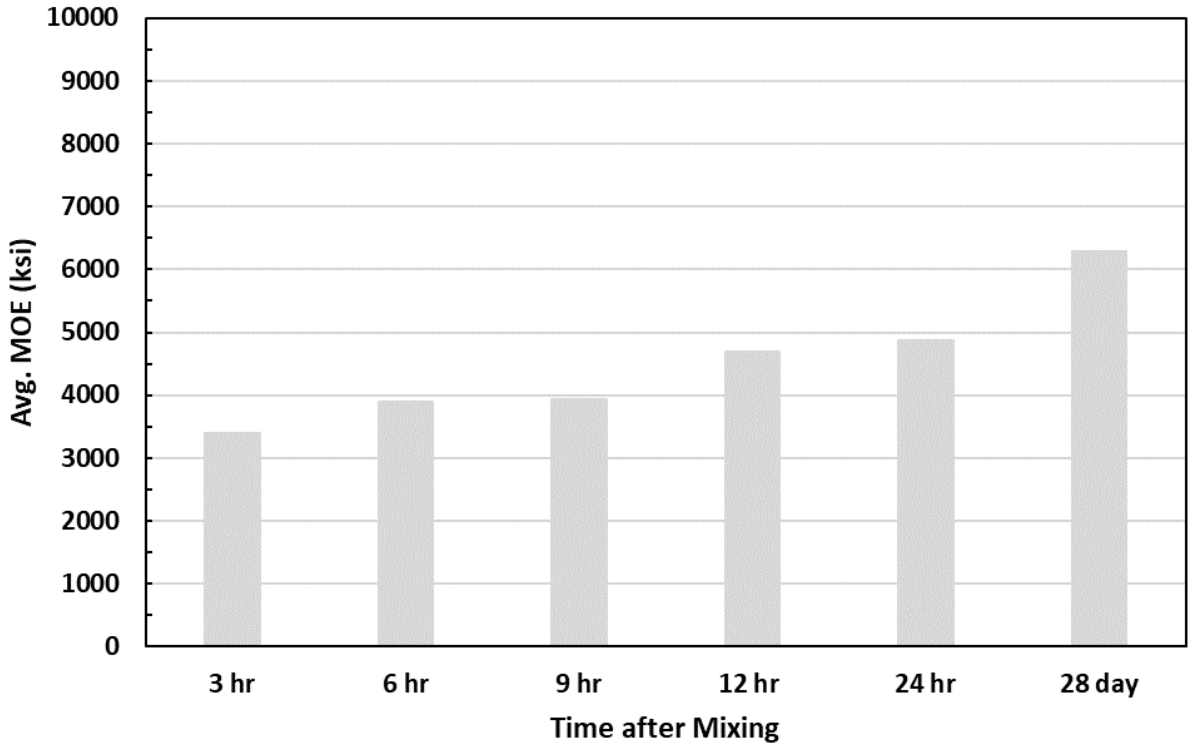

Figure 36: Round #2 MOE compressive strength data (high coarse aggregate)

Figure 36 shows that the MOE Round #2 compressive strength steadily increased from around 3.4 ksi at 3 hours, to just under 5 ksi at 24 hours. The 28 day compressive strength average was around 6.3 ksi, a nearly 25% reduction from the 8.3 ksi 28 day compressive strength from the Round #1 MOE testing on Mix 2C. The significantly reduced compressive strength at

every time increment compared to the Round #1 MOE testing further reinforces the cement viability issue which was caused by improper storage of cement Lot #2 in the lab. This mistake did not occur with any other lots of cement used in this research, however, and making targeted compressive strengths was not an issue that repeated.

Figure 37 shows a plot of the best fit simple linear regression between the average MOE from each time increment plotted against the square root of the average companion compressive strength for the Round #2 MOE testing with 0.82 C/F aggregate ratio.

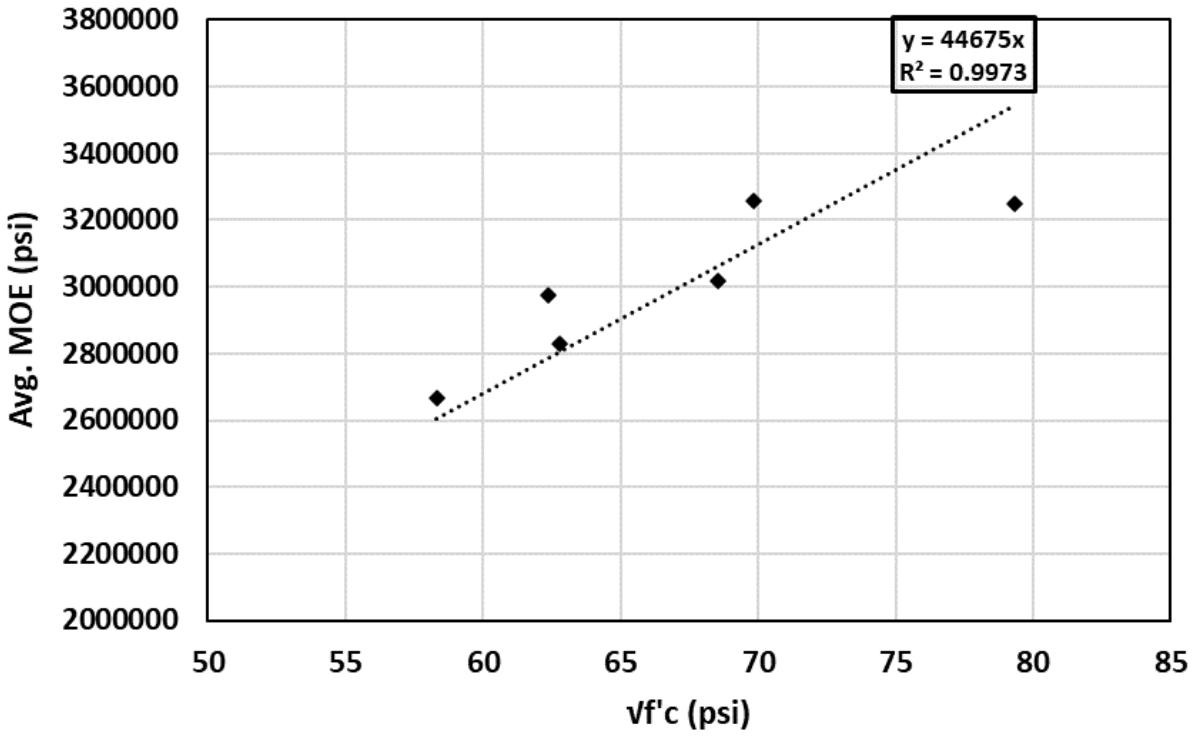

Figure 37: Best fit simple linear regression analysis to model/predict MOE using square root of compressive strength for Round #2 MOE with 0.82 C/F aggregate ratio

Figure 37 shows that although the Round #2 MOE data has a strong correlation coefficient for the linear trendline, it fits the data at a lower proportionality constant than the Round #1 data (44,675 for Round #2 vs. nearly 50,000 for Round #1, a reduction of over 10%).

Therefore, in addition to the reduction in both MOE and compressive strength, the cement storage issue used for the materials in Round #2 may have also resulted in a depressed proportional growth rate for the stiffness of the concrete. Another way of understanding this data may be that the cement moisture contamination hampered the stiffness gain more than the compressive strength gain, resulting in a reduced slope of the normalized trendline comparison. It is unclear whether or to what extent the increased coarse aggregate content may have defrayed this normalized reduction in modulus. The answer is dependent upon whether BCSA cement concrete derives its stiffness primarily from the paste or the aggregate, compared to portland cement concrete. More research with varying aggregate proportions would be required to make this determination.

3.5 Creep and Shrinkage

In order to develop accurate models for losses and time-dependent effects in RS-SCC for prestressed applications, creep and shrinkage data was collected for long-term analysis. Another motivation for the creep study was that, to the knowledge of the author, creep relationships have not been developed for rapid-setting BCSA cement concrete.

3.5.1 Creep Testing Procedures

Of specific interest in the compressive creep testing was the effect of the maturity of the concrete when it was placed under load, and to what extent that maturity might affect long-term creep response. This strategy was consistent with the approach utilized for the later structural testing, by directly comparing the observed material behavior resulting from both early age and later age load applications. The loading ages chosen for these tests were 3 hours and 24 hours, to bracket early and conventional prestress release times, and 28 days, to follow the conventional ASTM C512 procedure. Three individually instrumented, concentrically stacked 6 in. x 12 in. cylinder specimens were loaded in a single creep frame for each of the three loading ages. The

initial stress levels chosen were 70% of the 3 hour compressive strength for the 3 hour and 24 hour loading ages and 40% of the 28 day compressive strength for the 28 day loading age. The high initial stress level was chosen for the 3 hour and 24 hour creep tests because this testing was intended to be used for predictive modelling of prestress losses in later testing, where the expected stress level is up to $0.7f'_{ci}$ (f'_{ci} is defined as the concrete compressive strength at prestress release). Unfortunately, both the 3 hour and 24 hour tests had to be set at 70% of the compressive strength at 3 hours, because 70% of the compressive strength at 24 hours resulted in a required compressive force that was deemed too high for safe operation of the reaction frames. The 28-day creep tests were set at 40% of f'_c at 28 days, to provide a baseline for creep behavior that fully aligned with ASTM C512.

As stated previously, creep testing was performed in general accordance with ASTM C512, using an apparatus similar to that shown in Figure 38.

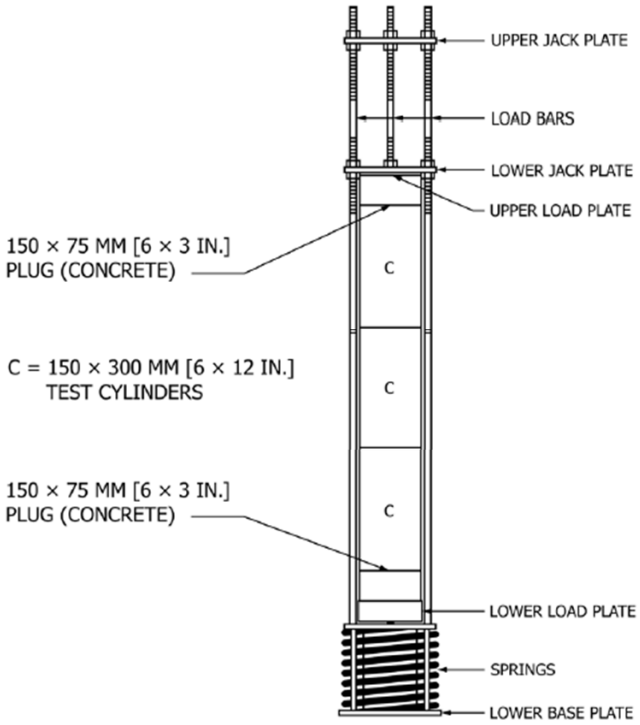

Figure 38: Creep measurement testing configuration (adapted from ASTM C512)

Due to the dimensions of the 6 in. x 12 in. compressive creep test specimens specified by ASTM C512, relative to the 6 in. length vibrating wire strain gages (VWSG) used to gather the creep data, a provision in ASTM C512 allowed the plug concrete pieces shown in Figure 38 to be omitted, such that the upper and lower load plates were seated directly on the upper and lower test cylinders in these experiments. The VWSG were chosen for the creep testing in part because they conformed to the dimensional requirements stipulated by ASTM C512.

To maintain consistency in analyzing the maturity effects of loading age on creep behavior, all test cylinders were made from the same concrete, and were cast at the same time. Figure 39 shows the preparation of the test cylinder molds and the VWSG instrumentation.



Figure 39: Creep specimen molds prepared for placement of the VWSG

Figure 40 shows a close-up view of the VWSG installation in the 6 in. x 12 in. cylinder molds, as well as the brass insert placement used to locate the DEMEC studs which were used for surface-strain measurements to complement the more accurate internal strain measurements. Before installation of the VWSG in the cylinders, the VWSG measurement ranges were shifted to near the top of their tension limits according to manufacturer recommendations, since the specimens and gages were going to be placed in compression throughout the duration of the creep tests. This provided ample measurement range throughout the testing and accommodated both the instantaneous and long-term shortening of the specimens.

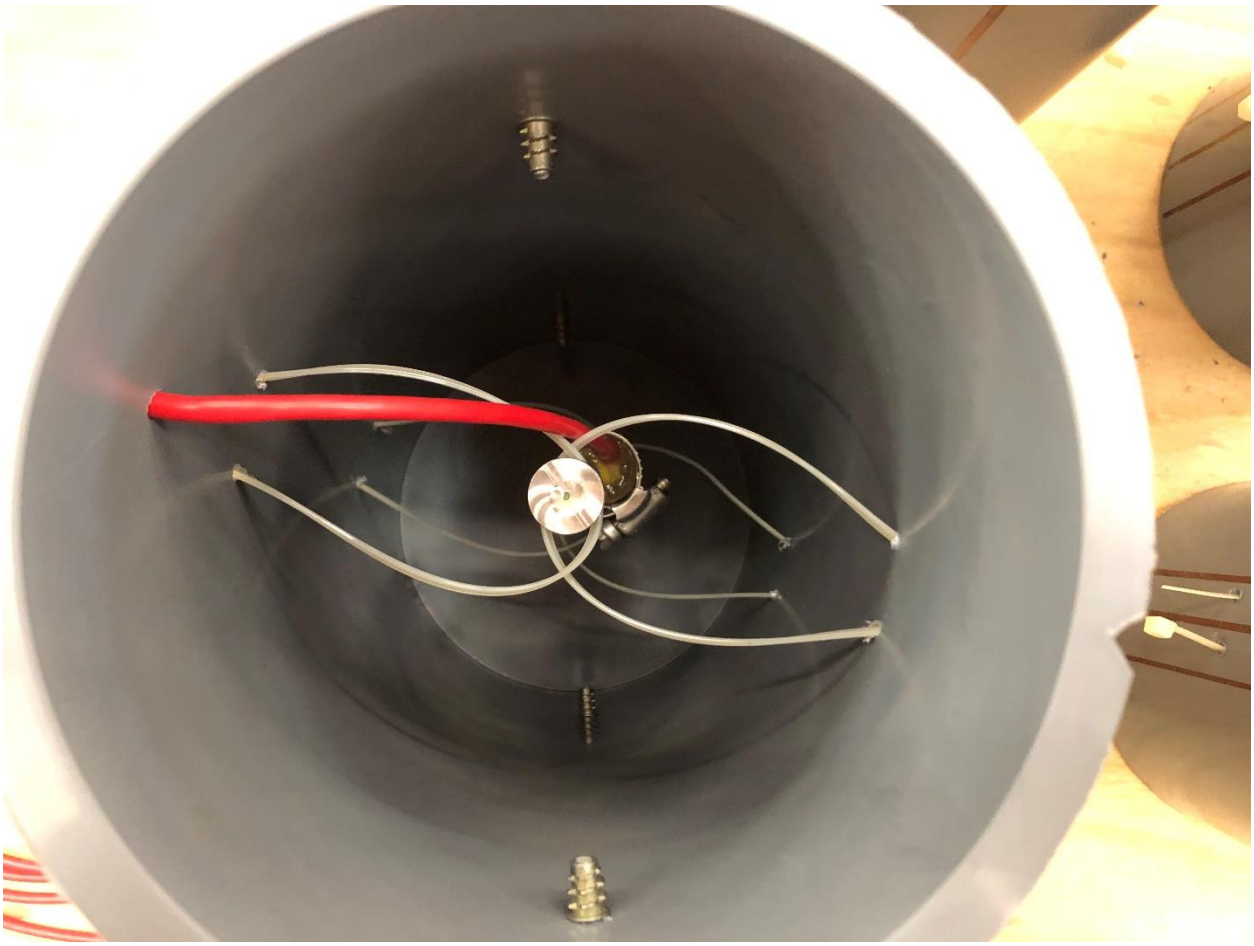

Figure 40: Creep specimen VWSG installation

The threaded studs shown on the sides of the molds shown in Figure 40 were carefully located based upon the 200 mm gage length of the DEMEC measurement gage and were fastened in place on the cylinder molds with set screws running through a hole in the side of the mold. Each pair was centered vertically on the cylinder mold and was placed on the diametrically opposite side from another pair, with 2 pairs on each specimen. The set screws were loosened when it was time to remove the molds from the cylinders (the plastic cable ties were cut from the outside to liberate the cylinder molds without trauma to the specimens or gages) and DEMEC measurement points were glued directly to the face of the threaded studs with a two-stage accelerated epoxy. The purpose of this approach was to avoid the widespread issue of DEMEC measurement points falling off of instrumented test specimens because of poor bond between the glue or epoxy and the "green" concrete surface. The goal was to provide a metal on metal interface where the epoxy would more securely hold the DEMEC points in place.

Figure 41 shows the surface of a typical metal stud at the surface of the creep specimen after the forms were stripped, along with an example of a DEMEC point in its final configuration glued to the stud surface.

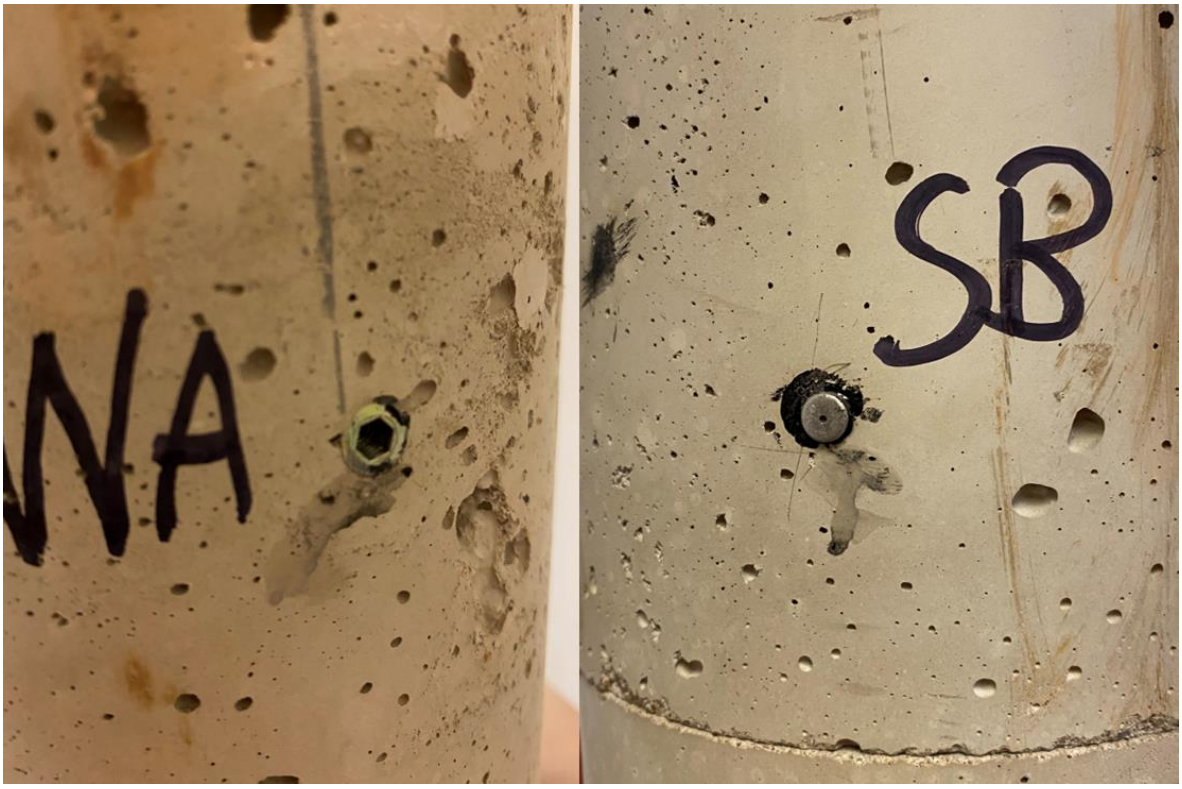

Figure 41: Typical metal stud after stripping forms (left) and DEMEC point glued to stud (right)

When the concrete was cast for the creep specimens, no specific actions were required for consolidation, since the mix was fully self-consolidating. The only special concern was to not pour concrete directly onto the VWSG in each specimen, to avoid damaging the gages. Along with the 6 in. x 12 in. creep and shrinkage specimens, a sufficient number of 4 in. x 8 in. cylinders were cast to determine companion compressive strength at each key age. All specimens were cast inside the environmental chamber (72 °F, around 50% average RH) where the creep and shrinkage testing would take place, and they were covered in plastic sheets to prevent early age desiccation. As soon as the concrete was fully set, the molds were removed from all the cylinders, and an end grinding machine was used to plane their ends for the creep tests. Although ASTM C512 refers to ASTM C617 for capping procedures to plane the cylinder ends, grinding is standard practice in Fears Lab and capping equipment was not available. In addition, end

grinding allowed rapid loading of the specimens without major delays, which was important for the early, time-critical loading windows. As each set of cylinders was end-ground, the DEMEC studs were glued on, and the baseline DEMEC measurements were taken. While the specimens were prepared for creep testing, a set of 4 in. x 8 in. cylinders were tested for compressive strength, so that the initial load for the creep test could be calculated and the specimens could be loaded as close to the 3 hour mark as possible. Figure 42 shows a set of the creep cylinders loaded into the reaction frame and the reaction plates being set for load application. The hydraulic jack used to apply load and the load cell used to measure applied load are also visible.

Figure 42 is labeled for clarity in outlining the loading process for the creep specimens. Bottom reaction plate “A” rests on 4 heavy railroad springs used to equilibrate the compressive force on the specimens as they crept and shrank over time. Upper reaction plate “B” rested on the top creep specimen and was locked in place with the nuts “1”. The loading plate “C” was only used as a temporary reaction plate for the hydraulic jack while load was being applied to the creep specimens. Loading plate “C” was temporarily secured during loading using the nuts “2”.

Before loading each specimen, the hydraulic jack and load cell were placed on reaction plate “B”. Loading plate “C” was lowered down the threaded rods and was gently placed in contact with the top of the load cell. Nuts “2” were threaded onto the rods and were firmly secured against the top of loading plate “C” at each corner.

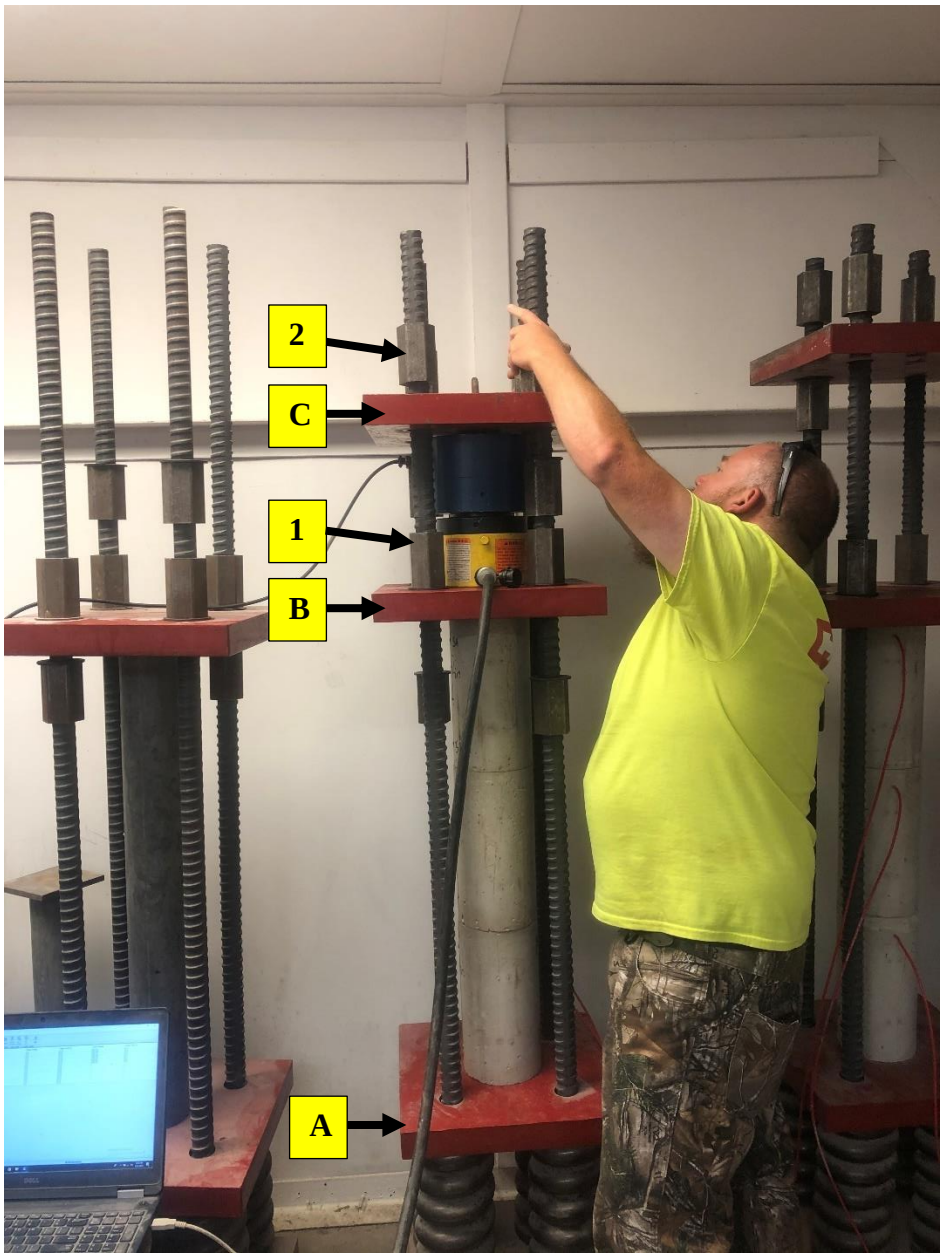

Figure 42: Setting reaction plates to load creep specimens

Figure 43 shows the load plates being leveled to ensure concentric loading. Nuts “2” were tightened alternately across the plate as needed to ensure that loading plate “C” was level before load was applied. Bottom reaction plate “A” was also leveled where necessary, using steel shims between the plate and the springs. The levelness of the entire loading arrangement was ensured by checking the clear distance from plates “A” to “B” at each corner.



Figure 43: Levelling reaction plates to load creep frames

Figure 44 shows the expanded steel safety cage in place on the creep frame prior to stressing the specimens.



Figure 44: Creep frame with safety cage for stressing creep specimen in place

Once the entire loading apparatus had been levelled and the safety cage was ready, a hydraulic hand pump was connected to the hydraulic jack and load was steadily applied to the creep specimens.

Once the target load on the specimens had been reached, nuts “1” were firmly tightened down against the reaction plate B, in order to lock in the compressive force on the test specimens. Then, the hydraulics were retracted, the upper nuts “2” were loosened, and the loading plate “C” was extracted. Figure 45 shows the completed creep testing apparatus, with the loading equipment removed and the top plate “B” locked off with nuts “1”.



Figure 45: Creep specimens in final configuration, after load application, with instrumentation set and loading apparatus removed

Figure 46 shows the DEMEC gage being used to take strain measurements for one of the creep specimens.



Figure 46: DEMEC gage being used to take creep strain measurements

DEMEC measurements were taken immediately before and immediately after loading the creep specimens. The DEMEC measurements were repeated daily thereafter for the next 2 weeks, weekly until 56 days, and then once every month or so until 1 year, at which point the specimens were unloaded, except for the 28 day ASTM C512 compliant set of specimens which were left for longer term monitoring. The VWSG measurements were recorded every 1 minute during loading and unloading, to achieve the most granularity possible with the data loggers which were being used. The VWSG measurement frequency was changed to 15 minutes after loading and again to 30 minutes after several months to limit data file sizes and save data logger battery life.

3.5.2 Shrinkage Testing Procedures

3.5.2.1 Shrinkage Companion Specimens for Creep Test

In addition to the three sets of specimens which underwent sustained creep loading, two otherwise identical 6 in. x 12 in. cylinders, also equipped with VWSG and DEMEC studs, were cured in the same room as the creep frames. These shrinkage companion specimens were treated in every way the same as the creep specimens, without being loaded. They were end-ground in the same manner (starting at the same time as the 3 hour creep specimens), had each end covered with a steel plate, so that their volume to surface area (V/SA) ratio would match the creep specimens, and measurements were taken at the same increments. Since the specimens under sustained load were creeping and shrinking simultaneously, the companion shrinkage data was deducted from the total shortening of the creep specimens to isolate only the compressive creep strain. Using VWSG equipped cylinders to measure concrete shrinkage was appropriate because the specimens needed to match the ASTM C512 compliant specimens as closely as possible and because previous research has shown this approach to be successful (Roswurm, J.S., 2018; Roswurm, S.J., 2018; Roswurm, S.M., 2013; Tanksley, S.D., 2018).

3.5.2.2 ASTM C157 Shrinkage

Another mechanism used to establish a baseline for the shrinkage of the RS-SCC was the ASTM C157 standard test for length change of concrete. Three of the 3 in. x 3 in. x 11.5 in. prisms specified by ASTM C157 were cast from the same batch of concrete as the creep and shrinkage cylinders. These C157 shrinkage specimens were stripped around the same time as the creep specimens (3-4 hours after casting) and the initial measurements were taken as soon as the molds were removed. The ASTM C157 specimens were stored in a different environmental chamber from the creep specimens set at 73 $^{\circ}$F and precisely 50% RH, and were measured on the same schedule as the creep specimens; daily for 14 days, weekly for 2 months, and monthly or bi-monthly thereafter.

3.5.2.3 Beam Companion Shrinkage Specimens

The last strategy used to approach shrinkage measurement in the RS-SCC was using miniature, reinforced but non-prestressed, beams equipped with either VWSG or DEMEC instrumentation. Similarly to the way that unloaded cylinders were used as companion specimens to deduct shrinkage effects from the total strain to determine creep strain, these miniature beams were used to help separate estimates for prestress losses due to shrinkage from the total prestress losses measured in the larger scale fully prestressed beams. See section 5.1.1 of Chapter 5 for further discussion of the shrinkage companion beam specimens.

3.5.3 Results

3.5.3.1 Creep Results

The concrete compressive strength at the time of loading was 5.9 ksi for the 3 hour loading age. The maximum load deemed safe to apply to the creep frame was 123 kips, causing an initial applied compressive stress of 4.4 ksi, approximately 74% of the compressive strength. Due to form stripping, end-grinding, and DAQ logistics, load was placed on these specimens at closer to 4 hours of age.

The concrete compressive strength at the time of loading was 9.1 ksi for the 24 hour loading age. The initial applied compressive stress of 4.4 ksi in this case was about 48% of the compressive strength. With more time to prepare the specimens compared to the 3 hour window, this group was loaded at very nearly 24 hours.

The concrete compressive strength at the time of loading was 10.2 ksi for the 28 day loading age. An initial applied compressive stress lower than the capacity of the creep frame was targeted to reach 40% of the 10.2 ksi compressive strength. The initial applied stress of 4.3 ksi was approximately 42% of the compressive strength.

Figure 47 presents a summary of the raw VWSG data collected from the creep tests, including all 3 loading ages (3 hour, 24 hour, and 28 days). Curves for the different loading ages are generally arranged top to bottom and compressive strain is shown as positive values.

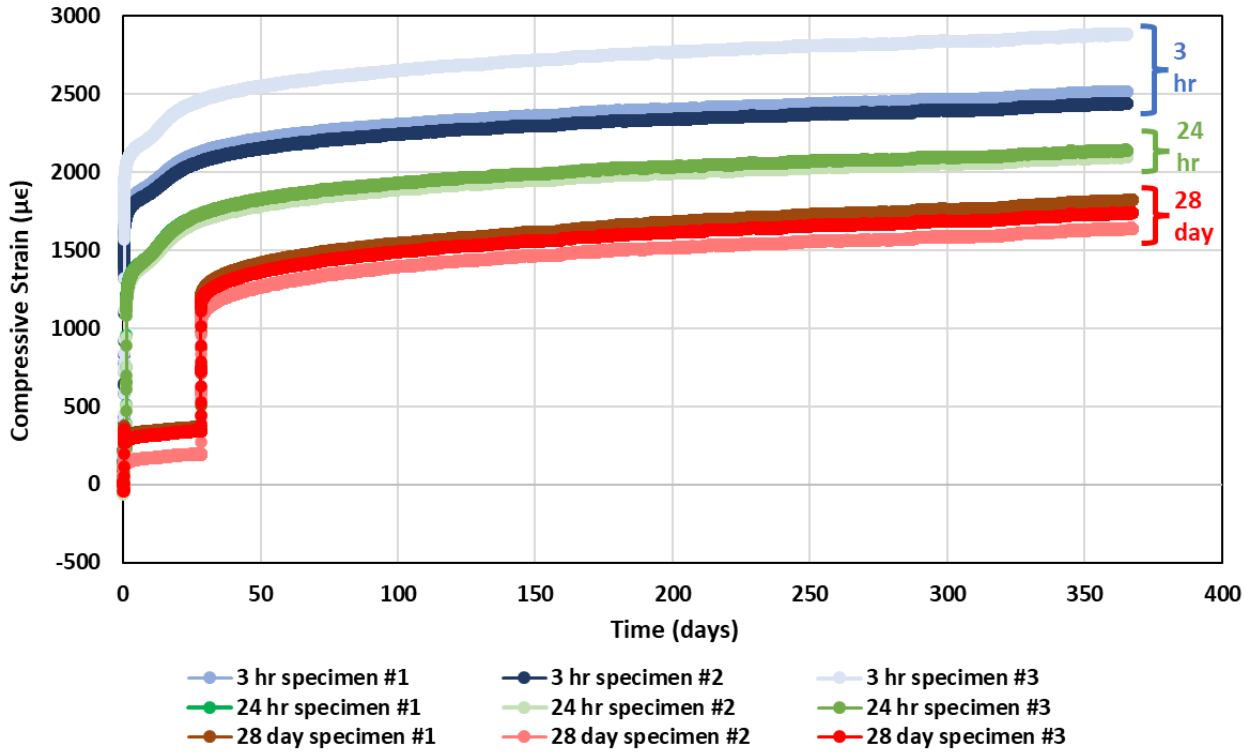

Figure 47: Raw VWSG data from creep testing (time measured from casting)

Figure 48 shows the raw creep testing data, with each specimen zeroed back to its respective loading age, instead of the common casting time that all specimens shared. As a result, the "shelf" that appeared in Figure 47 in the 28 day data before loading, where essentially only shrinkage and thermal effects occurred, disappears, and accordingly the 28 day data no longer reaches to the same final time in Figure 48 because it was loaded approximately 4 weeks after the other specimens.

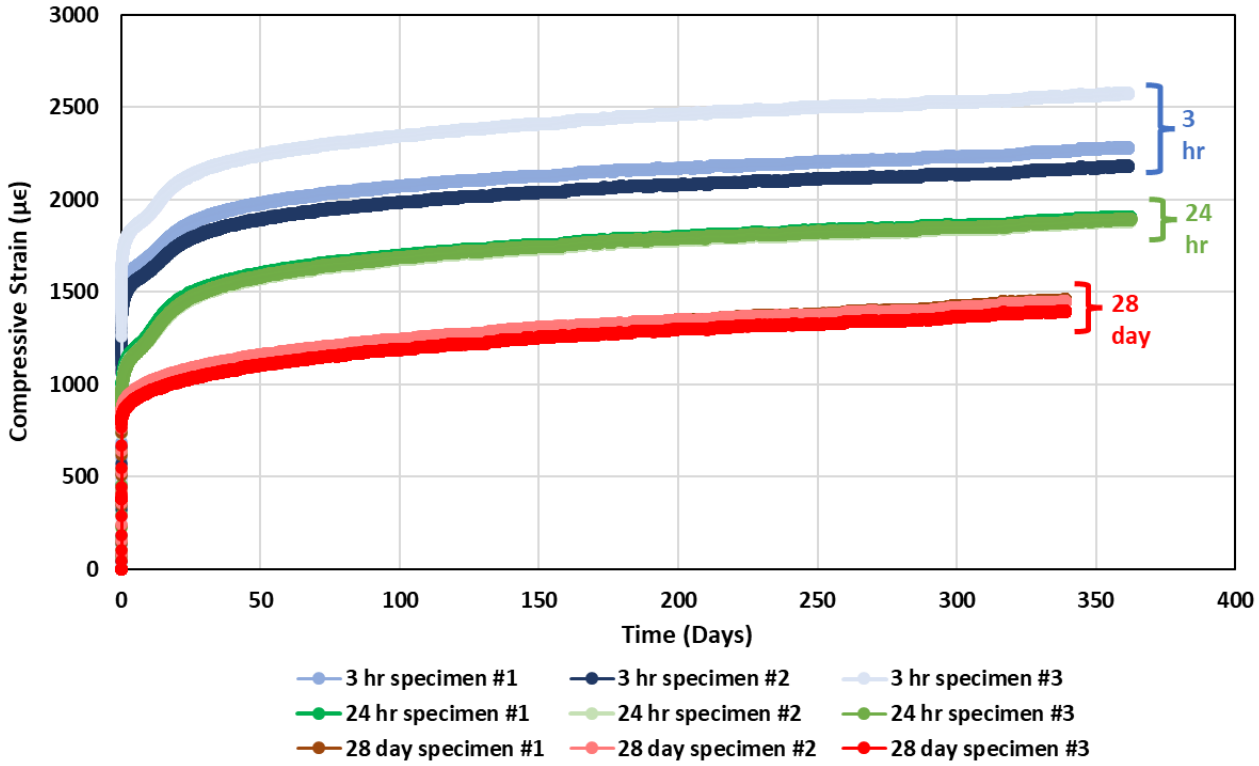

Figure 48: Raw VWSG data from creep testing (time measured from loading)

Figure 49 shows the reduced creep testing data, with each specimen zeroed back to its respective loading age and the instantaneous strain or elastic shortening (ES) from the initial loading of the specimens deducted. In addition, the shrinkage strains measured on the companion

cylinders have been deducted from the data shown in Figure 49. Therefore, the data shown in Figure 49 most nearly represent the strains caused solely by compressive creep over time.

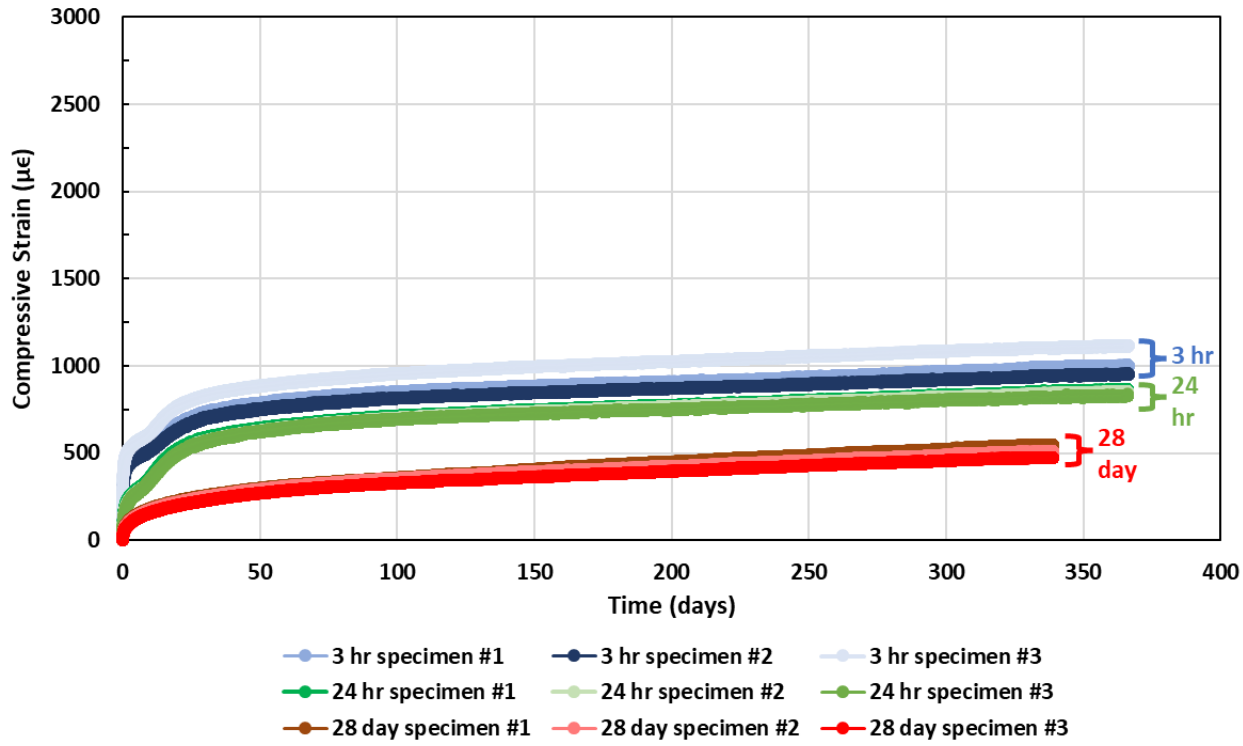

Figure 49: Compressive creep VWSG data with ES and shrinkage removed (from loading time)

Figure 50 shows a comparison of the total compressive strain (including ES, creep, and shrinkage) measured by the embedded VWSG compared to the measurements from the surface mounted DEMEC system. Because of large variability in DEMEC measurements and because some specimens lost a few or all of their DEMEC targets over time, the compressive strain curves shown for the DEMEC measurements represent the average over all 3 specimens in each loading age instead of individual measurements for each specimen within a loading age.

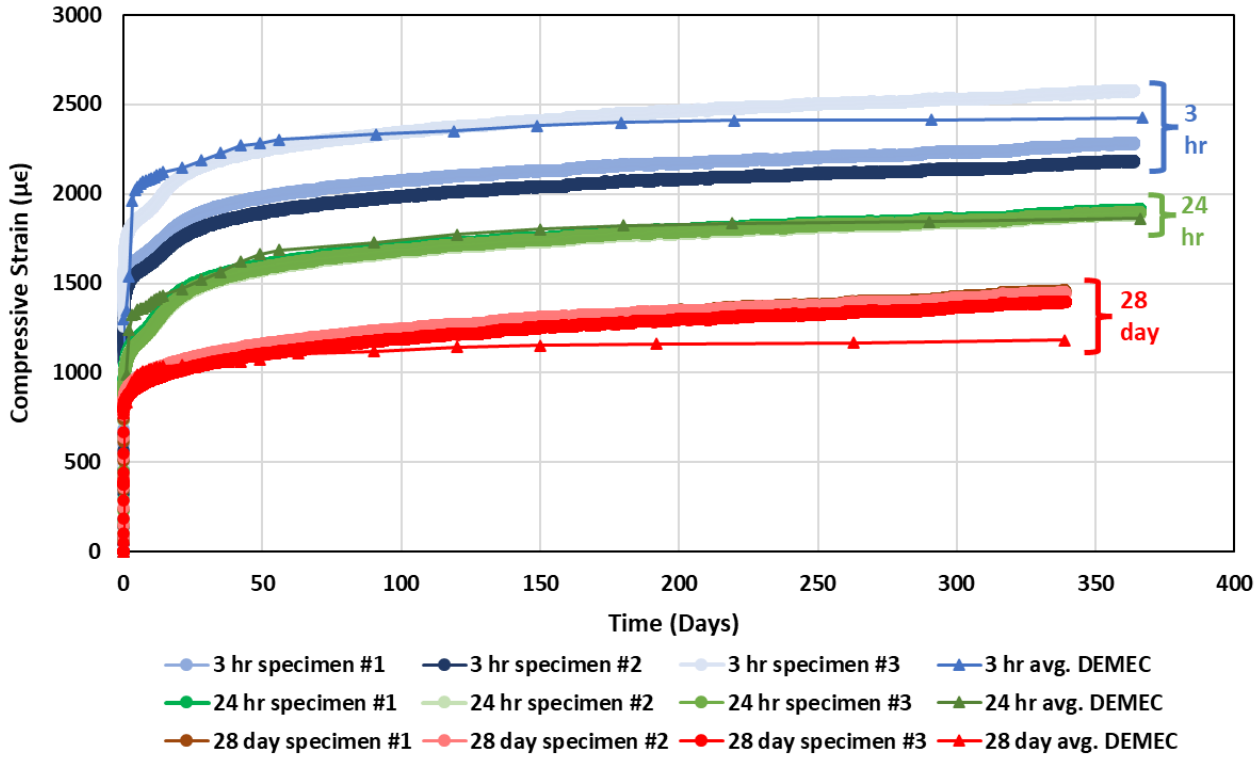

Figure 50: Comparison of total strain measurements from VWSG and DEMEC

Figure 50 shows that there is general agreement between the total compressive strains measured with the two approaches. The DEMEC data falls in the same order as the VWSG data, with the 3 hour loaded specimens exhibiting the highest strains, followed by the 24 hour, and 28 day loading ages. In addition, the overall magnitude of the DEMEC strains essentially falls within the spread measured with the three VWSG for each loading age. The primary exception would be the DEMEC strains being higher than the VWSG data at early ages for the 3 hour specimens and the DEMEC strains being lower than the VWSG data at later ages for the 28 day specimens. In general, however, considering the variability and difficulty in obtaining the DEMEC measurements in a repeatable way, the overall agreement with the VWSG is good. Some of the difficulties with obtaining reliable DEMEC readings for the creep study included the target point glue failing and the target points falling off, lack of temperature compensation if the

chamber temperature varied when the air conditioning occasionally malfunctioned, and the vertical orientation of the DEMEC gage required to take the readings. Manufacturer recommendations state that handheld DEMEC strain measurement equipment is intended to be used in a horizontal orientation to attain maximum accuracy. This is because it is very difficult to hold the gage in a vertical position firmly enough to keep it from falling without excessive hand pressure changing the observed gage reading.

Figure 51 shows a comparison of the long-term compressive strain (creep and shrinkage only, ES deducted) measured by the embedded VWSG and the surface mounted DEMEC system.

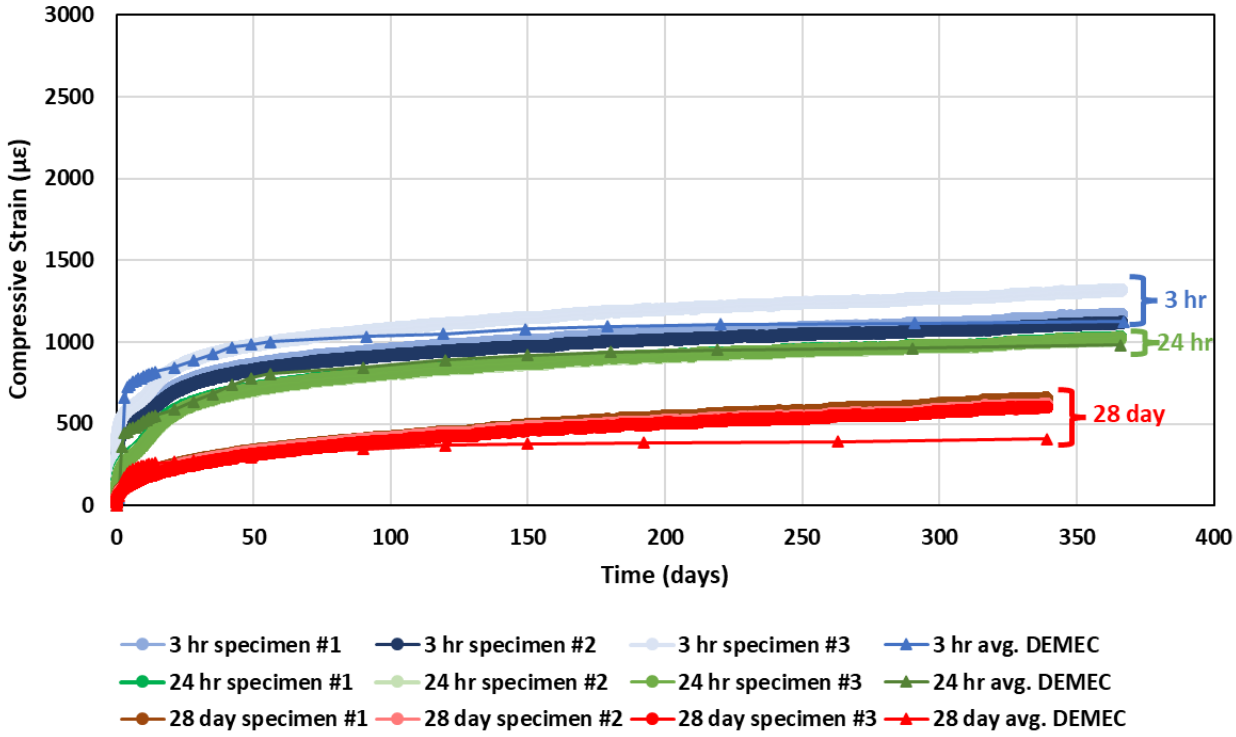

Figure 51: Comparison of creep and shrinkage strain measured with VWSG with DEMEC (ES removed from total)

Figure 51 shows similarly strong agreement between the VWSG and DEMEC measurements for the compressive strain in the creep specimens as did Figure 50. The ordering top to bottom (3 hour, 24 hour, 28 day) follows the same expected layering and the magnitudes of the DEMEC measurements remain reasonably close to those from the VWSG. This indicates that both the instantaneous elastic shortening measurements and the long-term measurements taken with the DEMEC gage were relatively accurate. When interpreting the DEMEC data, it is important to recall that instead of an individual curve for each of the three specimens for each loading age like for the VWSG, the DEMEC strains are represented with a single curve for each loading age. This is because there was high variability in the DEMEC measurements. Therefore, in order to obtain relatively stable results, the DEMEC measurements on diametrically opposed sides of each cylinder were taken in both the forward and reverse directions and then the strains were averaged across both sides of each cylinder. Then, the strains were averaged across all three cylinders to obtain the overall strain data results. One reason that this approach was necessary was because most of the DEMEC points flaked off over time as the epoxy adhesive failed, leaving some individual cylinders with few or no measurement points. Therefore, averaging across all specimens in each loading age to obtain an overall strain value for the DEMEC data was a reasonable approach to obtain some useful data.

Table 16 shows a summary of the elastic strain, creep strain, and 1 year creep coefficients measured using the VWSG in each creep specimen, along with the average values for each loading age.

Table 16: VWSG Summary of Instantaneous Strains, Creep Strains, and Creep Coefficients

Loading Age	Specimen	Elastic Strain (ES - με)	Creep Strain (CR - με)	Creep Coeff. (φ)
3 hr.	#1	1142	1003	0.878
	#2	1090	954	0.875
	#3	1291	1117	0.866
	Avg.	1174	1025	0.873
24 hr.	#1	905	864	0.955
	#2	892	854	0.957
	#3	895	832	0.930
	Avg.	897	850	0.947
28 day	#1	823	549	0.667
	#2	850	512	0.603
	#3	813	475	0.584
	Avg.	828	512	0.618

As the loading age increased and the initial applied stress level decreased (74%, 48%, and 42% of compressive strength at time of loading for 3 hour, 24 hour, and 28 day loading ages respectively), the elastic shortening decreased both on average and for every individual specimen. In addition, the same pattern held true for the overall creep strain, with the 3 hr specimens averaging nearly 1000 με and the 28 day specimens less than 500 με. Interestingly, however, because the elastic strain for the 3 hr specimens was so much higher than for the 24 hr specimens, the highest creep coefficient (creep strain divided by elastic strain) belonged to the 24 hr specimens instead of the 3 hr specimens. This effect is somewhat analogous to the relationship between lightweight concrete and normal weight concrete where creep is concerned. Because the lightweight concrete typically has a reduced MOE compared to the normal weight concrete, the lightweight concrete may show a reduced creep coefficient, even if it experiences more total creep overall. A similar effect may be occurring here, whereby the 3 hr specimens are experiencing high elastic strain partly due to the fact that their MOE is lower than for the other loading ages. Another reason for this behavior, however, may be the fact that although the 3 hr

and 24 hr specimens were loaded to the same initial stress, the 3 hr specimens were loaded to a much higher stress proportional to their compressive strength at the time of loading (74% of compressive strength at 3 hours vs 48% of compressive strength at 24 hours). The observed increased ES and decreased creep coefficient for the 3 hour loading age compared to the 24 hour loading age is likely a combination of both maturity effects and ratio of initial stress to compressive strength at the time of loading.

For the 28 day loading age compared to the 24 hour loading age, the ES at 28 day loading was less than 10% lower than the ES at the 24 hour loading age. In addition, the initial applied stress ratios were only about 6% different between the two groups. However, the long-term creep strain for the 28 day specimens was nearly 40% lower than the long-term creep strain for the 24 hour specimens. Finally, the difference in initial compressive strength at loading (10.2 ksi vs 9.1 ksi) was just over 12% different. The fact that the ES, initial applied stress ratios, and initial compressive strengths for the 28 day and 24 hour specimens were not significantly different, yet the resulting creep was nearly 40% different, indicates that perhaps the effect of maturity on the creep potential of this concrete can be substantial at later ages. As a result, an intriguing future research need would be to repeat creep tests with loading ages of 56 or even 90 days.

Table 17 presents a summary of the elastic strains resulting from the initial load placed on the creep specimens measured using both the embedded VWSG and the external DEMEC approach. In Table 17, these measured elastic strains are compared to the elastic shortening calculated with basic mechanics using Equation 5 to estimate MOE with the concrete compressive strengths that were measured at each loading age for the creep specimen concrete mix.

Table 17: Comparison of Calculated Elastic Strains and those Measured using VWSG and DEMEC Strain Gages

Loading Age	Modelled ES (με)	VWSG Meas. ES (με)	% Diff.	DEMEC Meas. ES (με)	% Diff.
3 hr	1132.2	1147.5	1.3	1299.4	12.9
24 hr	912.9	874.7	4.4	882.1	3.5
28 day	850.5	807.2	5.4	774.9	9.8
		Avg. % Diff.	**3.7**	**Avg. % Diff.**	**8.7**

Table 17 shows excellent agreement between the calculated elastic strains based on the MOE modelled using measured data in Section 3.4.2.1 and the elastic strains measured at the time of loading the creep specimens. There is especially close agreement with the VWSG measurements, as the measured strains vary from the theoretical strains by around 1-5% with an average departure under 4%. However, the DEMEC measurements also correlate well with the theoretical strains. Although the 3 hour loading age measurements vary by nearly 13%, the 24 hour and 28 day elastic strains both have errors less than 10%, and the average error of the DEMEC measurements is less than 9% (considering the "true" values to be those calculated according to the estimated concrete modulus).

3.5.3.2 Shrinkage Results

Figure 52 shows the shrinkage strains measured using the VWSG for the two 6 in. x 12 in. cylinders set aside as companions to the creep tests. Note that the graph has been inverted for clarity and consistency, but negative values are used to indicate net shrinkage.

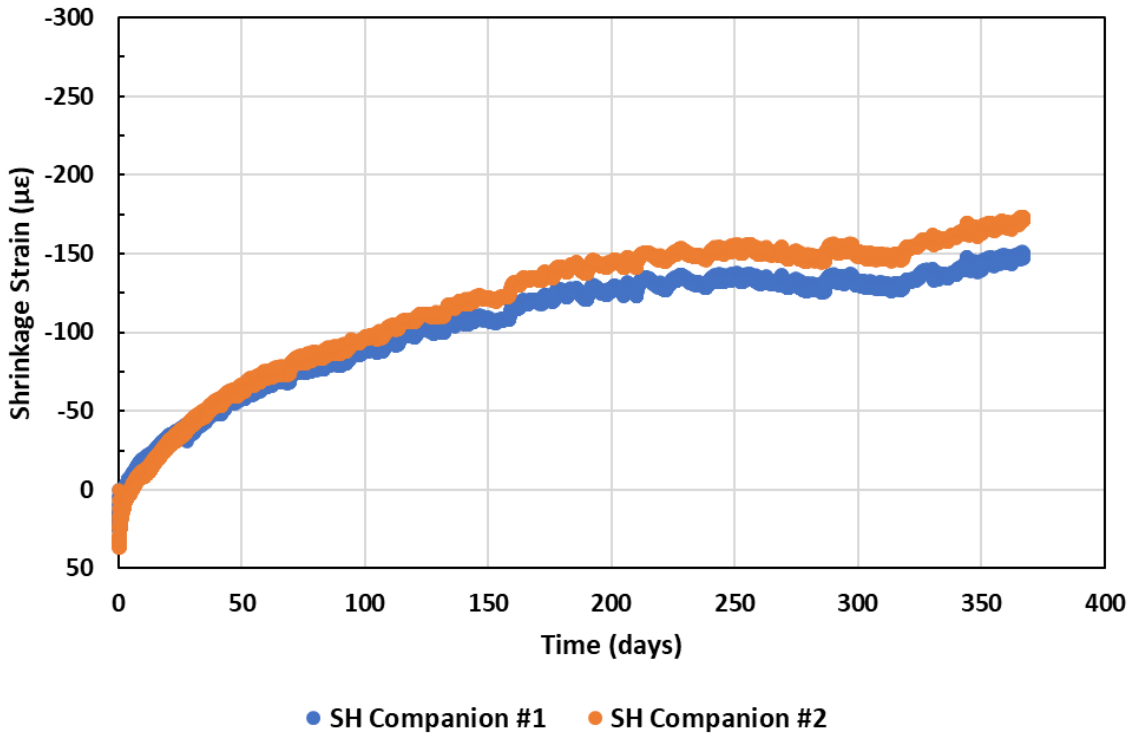

Figure 52: Strains measured for creep test shrinkage companion specimens over time

Figure 52 shows that the ultimate shrinkage strains measured for the two specimens were closely grouped, with an approximately 20 microstrain differential at 1 year. Both specimens also showed a 25-35 microstrain expansion within around the first 8 hours after casting, which is a typical result of the concrete expansion due to heating as the hydration reaction proceeds. Note that this expansion is not due to thermal error on the VWSG since this data was temperature compensated. Considering the early age expansion, the gross shrinkage observed for these specimens was between 175 and 210 microstrain.

Figure 53 shows the shrinkage strains with time, measured according to ASTM C157 using prisms cast at the same time and from the same concrete mix (RS Mix 2D) as the other creep and shrinkage specimens. The curve in Figure 53 represents the average of three individual C157 prisms at every time increment.

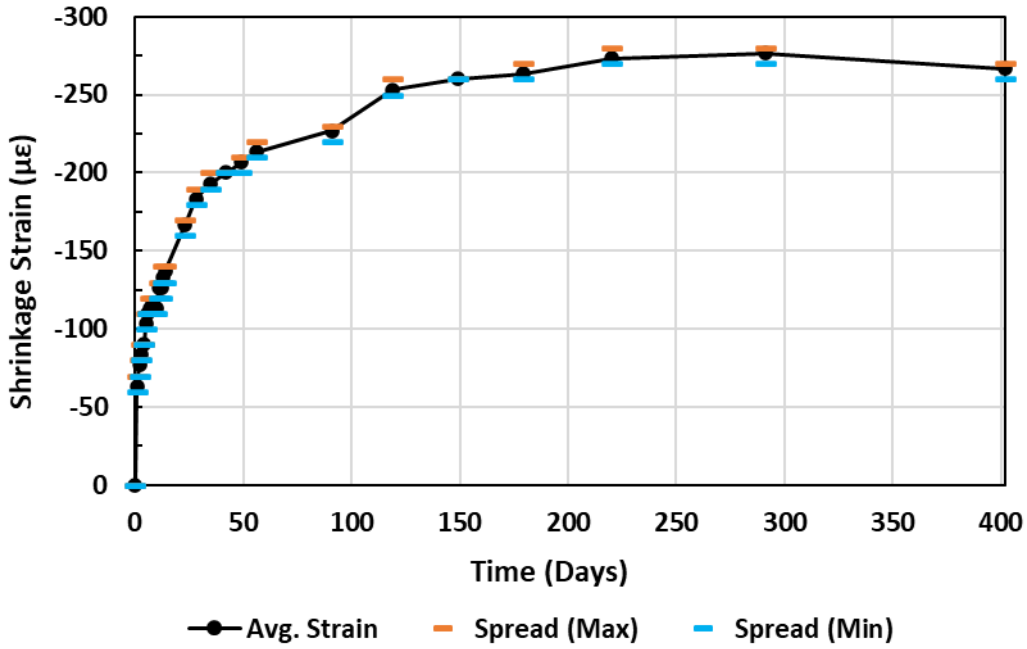

Figure 53: Unrestrained drying shrinkage of RS Mix 2D measured using ASTM C157

Figure 53 shows that the ultimate shrinkage strains measured using the ASTM C157 approach were higher than those measured using the VWSG embedded in the 6 in. x 12 in. cylinders (see Figure 52). One likely reason that this was the case is that the V/SA ratio for the C157 prisms of around 0.67 is significantly lower than the V/SA ratio for a 6 in. x 12 in. cylinder, which is around 1.2. In addition, since the ends of the 6 in. x 12 in. cylinders were covered to match the creep specimens, their true V/SA ratio was around 1.5, which is more than double that of the C157. Therefore, it is reasonable that the C157 test would exhibit a higher apparent drying shrinkage than the 6 in. x 12 in. cylinders with embedded VWSG. However, the measured range of ultimate drying shrinkage of 150 – 275 με between the two tests is still very low at 1 year compared to conventional portland cement concrete.

The proportionality of V/SA effects on shrinkage for the RS-SCC was compared to AASHTO provisions for conventional concrete by examining AASHTO LRFD Equation

5.4.2.3.2-2. This equation produces an adjustment factor for total concrete shrinkage based on the V/SA ratio for the concrete specimen. The ratio of adjustment factor values for a VWSG equipped cylinder compared to an ASTM C157 specimen would indicate a reduction in ultimate shrinkage of about around 8% according to AASHTO LRFD Equation 5.4.2.3.2-2. The actual reduction in ultimate shrinkage for the VWSG specimens compared to the ASTM C157 specimens was in the range of 24 – 45%. This could indicate that the RS-SCC shrinkage is more strongly impacted by changes in V/SA ratio than the AASHTO LRFD code estimates for conventional concrete. However, there are other factors that could be influencing this comparison, including the effects of ambient curing humidity for example. In addition, a greater number of data points would be required in order to make a more formal quantitative assertion concerning the V/SA ratio influences on the shrinkage of concrete made with BCSA cements, including mix designs like the RS-SCC used in this research.

4. Structural Testing

4.0 Introduction

Chapter 4 covers the application of the RS-SCC mix design presented in Chapter 3 to larger-scale structural testing, in order to observe the performance of this concrete with regard to prestressing strand bond and prestressed beam behavior. Section 4.1 discusses the untensioned pullout testing performed to measure basic strand bond strength according to the large block pullout test (LBPT). Section 4.2 discusses the design and fabrication of the prestressed beams used in this research, as well as the trial beams which were cast to refine construction and instrumentation workflows. Section 4.3 addresses the beams which were tested for development length, and Section 4.4 discusses the beams which were tested for transfer length. Additional mix design, fresh property, and pretensioning data are included in the appendices. Note that all structural testing utilized the same lot of 0.52 in. prestressing strand, donated from Coreslab Structures, Inc. Basic ASTM 1081 strand bond testing was not performed for this research, because researchers at OU had previously qualified this particular lot of strand according to the ASTM standard (Sadhasivam et al., 2017).

4.1 Direct Pullout Testing

Large block pullout tests (LBPT) performed in general accordance with the methods proposed by Logan and Moustafa (1997) and fundamentally derived from the original work by Moustafa (1974) were used to develop a baseline for the bond performance of RS-SCC and to examine how the combination of compressive strength and maturity of the RS-SCC affects prestressing strand bond/anchorage over time.

In order to have the six strands per test proposed by Logan (1997) for each age to be tested, two full size (2 ft x 2 ft x 6 ft - 8 in.) LBPT specimens, each with 18 strands, were required. The two LBPT specimens would provide 6 strands per test at each time period,

including tests at 3 hours, 6 hours, 12 hours, 24 hours, 28 days, and 1 year. A strand size of 0.52 in. was chosen to match the strand size to be used for the beam testing. The test procedures recommended by Logan (1997) were for qualifying 0.5 in. strand, and Logan suggested two threshold values for pullout strength, 16 kips for pullout load at first slip and 36 kips for peak pullout load. Since these experiments utilized 0.52 in. strand, those threshold values were scaled up based on the corresponding increase in cross-sectional area. Figure 54 shows the typical strand layout and block reinforcement configuration for the LBPT specimen.

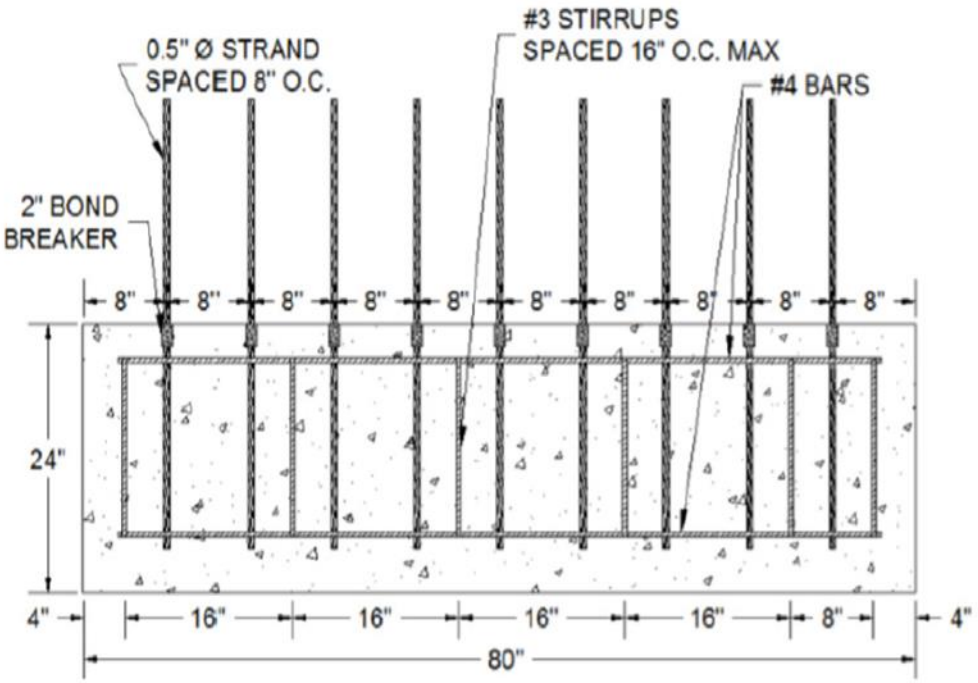

Figure 54: LBPT specimen configuration (Arezoumandi et al., 2020 - after Logan, 1997)

As stated previously, these experiments utilized 0.52 in. strands instead of the 0.5 in. strands shown in Figure 54. Note the 2 in. bond breaker on each strand, placed with the top of the bond breaker level with the top of the block. The purpose of the bond breakers is to prevent a stress concentration at the surface of the block, which could skew the test results or interfere with the strand pullout mechanism. Finally, the bottom cover for the ends of the strands is specified as

4 in. (Logan, 1997), which leaves 18 in. of bonded strand after accounting for the 2 in. bond breaker (24 in. total block depth).

The volume of each block was almost 1 yd^3, so the concrete required to cast both blocks from the same batch of concrete exceeded the capacity of the largest mixer at Fears Lab, a Praschak®/MIX Mixer Systems® horizontal shaft mixer rated for 21 ft^3 (model no. 21 DD RH) but that is practically limited to mixing around 20 ft^3. Instead of breaking the pour into multiple small mixes, this problem was used as an opportunity to demonstrate the scalability of the RS-SCC mix design. A local ready mix producer, Schwarz Ready Mix (SRM), was contacted about assisting the research project by mixing the RS-SCC in a ready mix truck on site at Fears Lab.

4.1.1 Half-Scale Trial LBPT

SRM almost immediately agreed in principle to assist with the project. However, it was decided that a single half-scale LBPT specimen would be cast using the horizontal shaft mixer at Fears Lab before performing a large mix to cast the full-size LBPT specimens. The half-scale specimen was cast for three reasons. First, the half-scale LBPT specimen would require a mix of around ½ yd^3, which would be the largest batch of the RS-SCC that had been mixed for this research to that point. The half-scale specimen provided an excellent opportunity to ensure that admixture dosages and other details would behave as expected for a larger batch of concrete. The second reason for the half-scale specimen pour was to provide an opportunity for SRM personnel to come to Fears Lab and observe BCSA cement concrete being mixed and placed, to allay any logistical concerns SRM had about the rapid-setting behavior of the concrete. Third, the half-scale specimen provided an opportunity to fine tune the testing apparatus for strand pullout and ensure all data acquisition (DAQ) for the full-scale specimens functioned as expected.

The half-scale LBPT specimen was constructed according to the methods for the LBPT recommended by Logan (1997), with a width and height of 2 ft, and strands placed at 8 in. on center (O.C.). The only modification was to make the block length 38 in. instead of 80 in. with 4 pairs of strands instead of 9 pairs of strands. Additionally, the edge cover for the strands on one end was changed from 8 in. to 6 in. Figure 55 shows the reinforcing bar cage tied for the half-scale LBPT specimen. It is worth noting that the test method described by Logan (1997) includes the No. 4 longitudinal bars enclosed by No. 3 ties (as shown in Figure 54), but not the diagonal No. 3 bars seen in Figure 55. These diagonals were found to be necessary to make the cage rigid enough for lifting, moving, and being used to position strands without excessive instability.



Figure 55: Reinforcement cage for half-scale trial LBPT specimen

Figures 56 and 57 show the reinforcing bar cage placed in the formwork, with the strands positioned and tied to the cage. The formwork was built for a full-size LBPT specimen, and a partition was inserted 38 in. from one end so that the formwork could be reused for the later full-scale LBPT pours. In addition, the interior of the forms was lined with plastic sheeting to protect the formwork from damage caused by bonding of the concrete to the wood so that it could be easily reused, and secondarily to prevent minor leaks or seepage. The plastic lining was chosen instead of conventional form release oil because there was concern about form release oil accidentally touching the strands and interfering with the bond interface.



Figure 56: Formwork for half-scale trial LBPT specimen



Figure 57: Strands tied in place for half-scale trial LBPT specimen

Figure 58 shows the horizontal shaft mixer at Fears Lab used to mix the RS-SCC required for the half-scale LBPT specimen placement.



Figure 58: Praschak®/MIX Mixer Systems® 21 ft^3 horizontal shaft concrete mixer at Fears Lab (model no. 21 DD RH)

Figure 59 shows the RS-SCC being placed into the large block formwork using a ½ yd^3 hopper connected to the overhead bridge crane in Fears Lab.



Figure 59: Placing RS-SCC with hopper and overhead crane

Figure 60 shows the RS-SCC flowing into the LBPT specimen formwork and filling around the reinforcement cage and lifting hooks. The 2 in. foam bond breakers are visible on each strand in Figure 60, which are called for in Logan's work to prevent stress concentrations from forming at the surface of the block when the strands are tested.



Figure 60: RS-SCC filling half-scale LBPT specimen formwork

While a portion of the concrete was being dispensed into the LBPT form as shown in Figure 60, the remainder of the concrete in the mixer was dispensed for fresh testing and casting compressive strength cylinders. The initial slump flow test after discharging the mixer occurred 10 minutes after cement was added to water in the mixer and resulted in a measurement of 24 in. After another 10 minutes (total of 20 minutes after adding cement to water), the slump flow test was repeated, resulting in a measurement of 20 in.

Figure 61 shows the completed half-scale LBPT specimen, along with the 21 companion 4 in. x 8 in. compressive strength cylinders, after casting but before testing commenced.



Figure 61: Half-scale LBPT specimen and compressive strength cylinders after casting

Figure 62 shows the testing and data acquisition apparatus used for the LBPT. The formwork was not stripped prior to running the first test due to the necessity of commencing testing as quickly as possible when the age of the concrete reached 3 hours. In order to be consistent for future tests to match the early age tests, the formwork was left in place. This came with the added advantage of easily moving the specimen around the lab with either the crane and lifting hooks or the forklift from underneath the specimen formwork. The targeted testing ages for the half-scale LBPT specimen were 2 strands each at 3 hours, 6 hours, 24 hours, and 28 days. Since these tests were mainly to streamline the testing procedures, the testing windows varied slightly due to logistics and the actual testing ages were 3.5 hours, 6.5 hours, 28 hours, and 29 days.

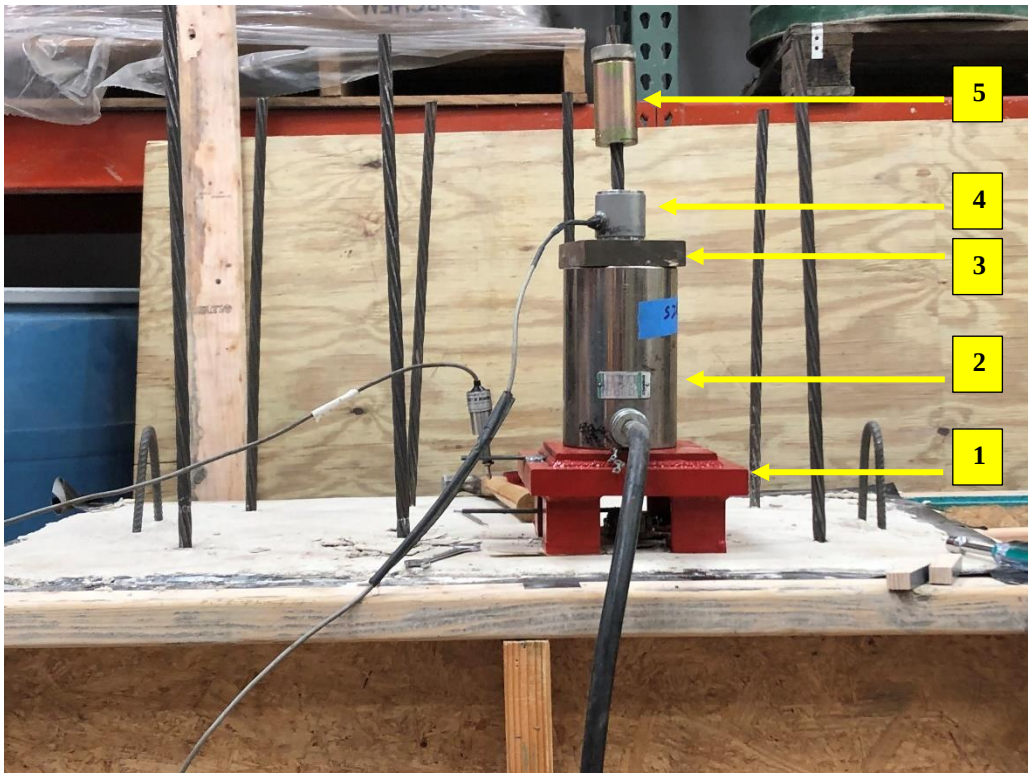

Figure 62: Testing setup for direct strand pullout with load and slip measurement used for the LBPT

The testing apparatus in Figure 62 consists of 5 major components. From bottom to top, the first component is the red steel platform (1) which was designed to react against the block's surface without crushing the concrete at the expected pullout loads. Next is the hydraulic ram (2), connected with the black hose to a hand pump not pictured in Figure 62. Both the platform and the ram were equipped with holes through the center to allow the strand to pass through. A steel bearing plate (3) was placed between the ram and a through hole load cell (4) used to measure the axial force required to pull the strand free. Finally, a standard prestressing chuck (5) was placed above the load cell so that the entire assembly could be used to pull each strand out of the block. To the left of the red platform in Figure 62 is a linear voltage differential transformer (LVDT) mounted to a clip on the platform. This LVDT was used to measure movement of a reference plate welded to a block clamp which was fixed to each strand. The

displacement and load data were recorded concurrently with a single data acquisition system so that the load-slip behavior could be monitored. Of specific interest was the load at 0.10 in. of strand movement, which is often taken as the load causing first slip.

4.1.2 Full-Scale LBPT

Two LBPT specimen forms and reinforcing bar cages were constructed matching the dimensional requirements set forth by Logan (1997) and described in Section 4.1. The only deviation from previous research was the aforementioned No. 3 reinforcing bar diagonals used to stiffen the cages so that they could be moved, and the strands could be located accurately. Figure 63 shows the sequential progression of the completed formwork, the completed cage, the strands tied in place, and the specimen ready for concrete to be cast. In order to reduce the risk of marring the strands and reducing their bond capacity, plastic was used to line the formwork interiors so that form release oil was not required.

4.1.2.1 Preparation and Casting



Figure 63: Full-scale LBPT specimen formwork, reinforcing bar cage, and tied strands (clockwise from top left)

For the sake of consistency, SRM obtained the same aggregates used in the mix design development for this research. For the fine aggregate, this was a standard ASTM C33 concrete sand stored in outdoor bins at the SRM yard as shown in Figure 64.



Figure 64: ASTM C33 fine aggregate (Dover sand) storage at Schwarz Ready Mix facility

The coarse aggregate utilized was donated to SRM by Dolese and was Dolese's 5/8 in. #3 cover crushed limestone aggregate. This aggregate gradation is comparable to an ASTM C33 #7 coarse aggregate. Figure 65 shows the outdoor storage of the coarse aggregate at the SRM yard.



Figure 65: Dolese 5/8" #3 cover coarse aggregate storage at Schwarz Ready Mix facility

The aggregates and mix water were brought to Fears Lab in an SRM concrete truck, where the admixtures and cement were charged into the truck. Figure 66 shows the 10 yd^3 concrete truck provided by SRM at their facility.



Figure 66: 10 yd^3 concrete truck at Schwarz Ready Mix facility

A large construction forklift rented by Dr. Chris Ramseyer was provided to the research crew in order to lift the cement hoppers high enough to charge the cement into the concrete truck. The hoppers were placed on the forks of the large lift using the smaller forklifts from Fears; the hoppers were then strapped securely to the mast of the large lift; the hoppers were raised up into position; and the cement was dispersed into the truck, being struck firmly with a mallet to ensure all the cement powder was discharged from the hoppers. Figure 67 shows the process of charging the mixer truck.



Figure 67: Charging concrete truck with BCSA cement at Fears lab using construction forklift and two separate hoppers

It is important to note that just like in all test mixes, the citric acid was added to the mix water in the truck, so that there was citric acid with the aggregates when the cement first went into the mix, and more citric acid went into the mix when the remainder of the mix water was added after the cement was charged. Similarly, half of the HRWRA was added to the initial mix water, and the other half was added directly to the mix after the remainder of the mix water. After a few minutes of mixing, a small portion of concrete was dispensed as shown in Figure 68 for slump flow measurement.



Figure 68: Dispensing small portion of LBPT mix to measure the slump flow

Figure 69 shows the stages of performing the slump flow test on the fresh concrete for the LBPT mix. As the figure shows, the targeted slump flow range was achieved with a flow slightly exceeding 24 in. This initial slump flow was performed 18 minutes after the cement was first added to water in the truck. The total mixing time was longer than typical (16 minutes) because of the time required to switch rigging and charge both hoppers of cement into the truck. For reference, the 16 minute mix time consisted of 10 minutes to add all the cement followed by 6 minutes to complete the mixing process.



Figure 69: Slump flow measurement for full-scale LBPT pour (clockwise from top left)

As soon as the slump flow was measured and determined to be adequate, the mixer truck chute was pivoted over to the LBPT specimen formwork, and both forms were filled with concrete. Since the concrete was self-consolidating, no rodding, agitation, or vibration was necessary for the blocks. Two more slump flow measurements were taken at 29 minutes and 40 minutes after adding cement to the mixer, resulting in values of 20 in. and 16 in. respectively. Figure 70 shows the progression of discharging the concrete, filling the formwork, finishing the surfaces, and a finished specimen.



Figure 70: Positioning the mixer truck chute, filling the formwork, finishing the LBPT specimen surface, and a finished specimen (clockwise from top left)

While the forms were being filled, the research crew cast smaller scale test specimens and performed other fresh tests. Thirty companion 4 in. x 8 in. compressive strength specimens were cast to be tested with each set of strands, in addition to six MOR specimens. These MOR specimens were tested in pairs at early age (3 - 4 hours), 24 hours, and 28 days as described in Chapter 3. And in addition to slump flow, air content, unit weight, and setting time were also measured. Figure 71 shows the completed LBPT specimens along with the companion specimens and the setting time test.



Figure 71: Completed LBPT specimen (left) with MOR beams, compressive cylinders, and setting time test in progress, covered with green lid (right)

Once casting was completed, several pounds of citric acid (a very large quantity compared to typical doses), and water were added to the SRM concrete truck to prevent the remaining concrete in the truck from setting up prior to washout. SRM reported that they were able to return the truck to their facility and wash it out cleanly without any difficulty. After the concrete reached final set, compressive strength testing was commenced so that strand testing could begin on the LBPT specimens as close to an age of 3 hours as possible.

4.1.2.2 Testing

The testing apparatus utilized is shown in Figure 72 and is the same as that shown in Section 4.1.1 except for the addition of a swivel bearing (labeled “A”) beneath the load cell, with the bearing plate moved to between the chuck and load cell. The swivel “A” was added to prevent the apparatus from producing torsional resistance as the strand tries to rotate when it pulls through the concrete.



Figure 72: Hydraulic ram, load cell, and LVDT for strand pullout measurements

Load was steadily applied to the strands by means of the hand operated hydraulic jack, as close as possible to the rate specified by Logan (1997) of around 20 kips per minute. When 0.10 in. of strand movement was registered, the loading was paused briefly for each strand so that the

LVDT and block clamp with the reference plate could be removed. Otherwise, the large movements later in the test would damage the LVDT and wedge the block clamp against the bottom of the red reaction platform. Once the LVDT and block clamp were removed, loading was immediately resumed, and the strand was loaded until either the strand ruptured, slipped repeatedly such that the peak load would no longer increase, or the hydraulic ram reached its maximum stroke (around 2.25 in.). This was the same loading procedure used when testing the half-scale trial LBPT, but the loading procedure is not described in Section 4.1.1 since that testing was primarily to verify the performance of the testing apparatus and confirm the viability of the workflow, rather than to gather experimental test data.

4.1.3 Results

As mentioned previously, the slump flow of the concrete immediately upon discharge from the truck (about 18 minutes after cement was added to the water and aggregates) was around 24 in. At 29 minutes after adding cement to the truck, the slump flow was 20 in, and at 40 minutes after adding cement to the truck, the slump flow was 16 in. The air content, measured shortly after the initial slump flow, was 3.6%. The final setting time was around 90 minutes, approximately 1.5 hours after the first cement was added to the mixer.

The data resulting from the MOR beam tests are summarized in Chapter 3 with the other flexural strength data. For reference, Figure 73 shows the concrete compressive strength with time for the LBPT mix.

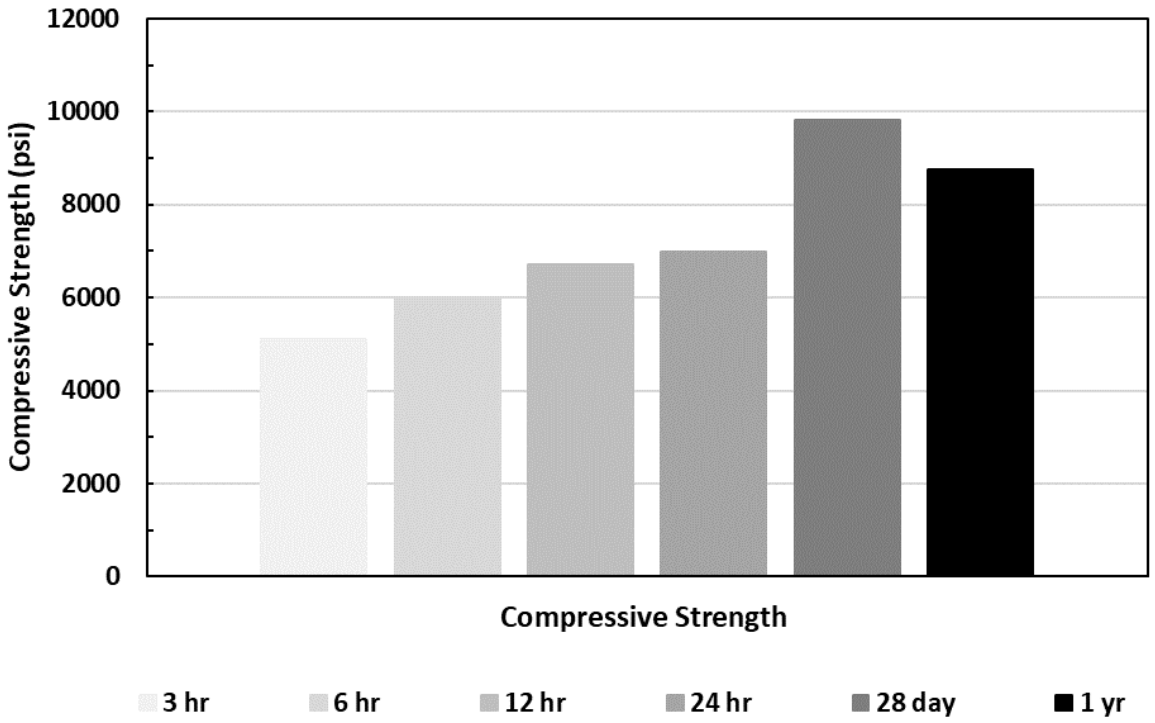

Figure 73: Compressive strength over time for the LBPT mix

Figure 74 shows a summary of the maximum strand pullout loads for first slip (0.1 in.) and overall peak at each age. The dotted red line represents the target pullout load (17.4 kips) for first slip and the dashed red line represents the target peak pullout load (39.2 kips). The solid red line shows the strand capacity (45 kips) based on a strand strength of 270 ksi. The values recommended by Logan were for 0.5 in. strand, so the values shown in Figure 74 were scaled up in proportion to the cross-sectional strand area for the 0.52 in. strand used in this research.

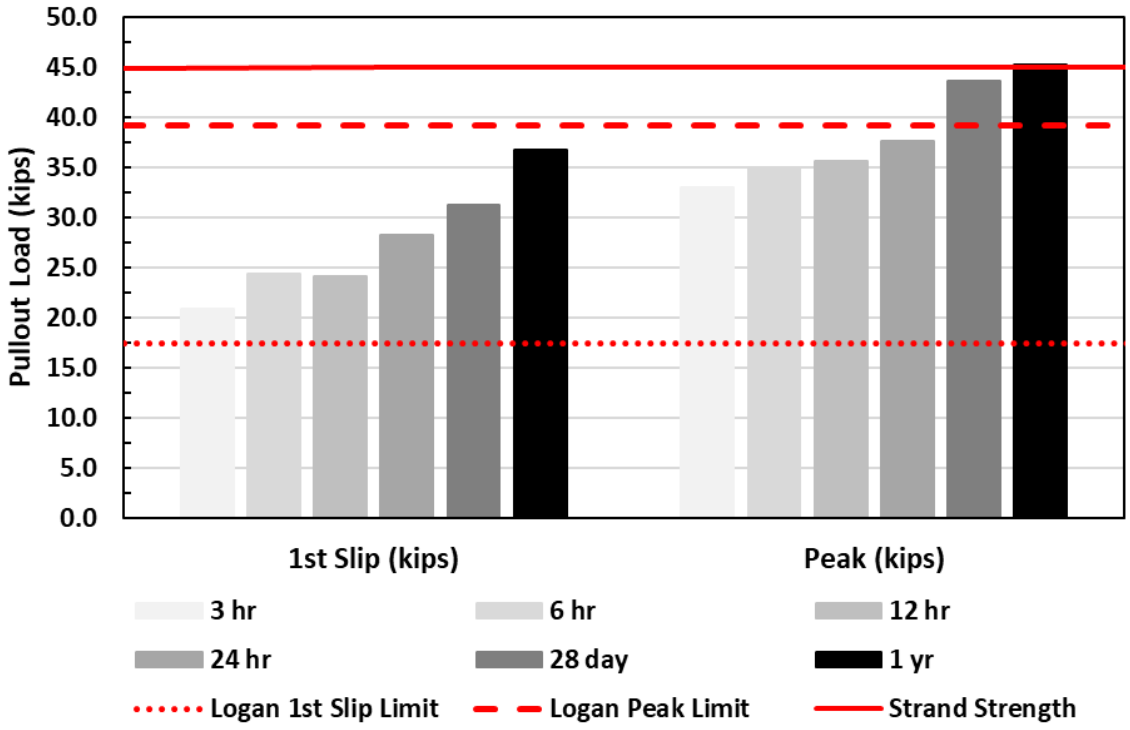

Figure 74: LBPT strand pullout load results

To interpret the results of Figure 74, it is important to understand the underpinnings of Logan's (1997) recommendations for the LBPT and the way that the LBPT was used in this research. There were two significant differences between this LBPT and that of Logan. First, Logan (1997) stipulated a compressive strength range of 3500-5900 psi at the time of testing which was taken to be 1 day after casting. Because of the very rapid strength gain of the BCSA cement concrete, only the 3 hour tests fell within this range, with an average compressive strength of around 5100 psi. The second difference is that Logan (1997) suggested the use of a very hard coarse aggregate such as a granite, and his mix design called for a high proportion of coarse aggregate (around 1.7 coarse/fine ratio). The reason for this stipulation was that soft or insufficient coarse aggregate could lead to reduced pullout values, because the coarse aggregate would be unable to "catch" the strand as it began to move through the concrete. In this research,

a crushed limestone coarse aggregate was used, which is softer than that recommended by Logan. In addition, the self-consolidating mix design utilized a high sand content, with a coarse to fine aggregate ratio of about 0.53. Finally, it is important to understand that a fundamental difference between this research and that of Logan is that Logan's work was primarily concerned with qualifying prestressing strands. This research was not concerned about qualifying strand, and instead utilized the same strand consistently throughout the testing to analyze changes in the mechanical bonding capacity of the concrete over time.

With these differences established, Figure 74 can be critically examined. First, as expected, the pullout values steadily increase with time as the concrete compressive strength increases. The pullout load reaches a maximum at 1 year, when the average maximum pullout value reached the full strand strength. At 1 year, 4 out of the 6 tested strands were confirmed to exhibit fracture of at least one wire or rupture of all 7 wires in the strand. The other 2 strands reached or exceeded a load corresponding to 270 ksi stress in the strand but testing was stopped for safety.

The early bond strength was also excellent. At 3 hours, when the compressive strength fell within Logan's recommended range for 1 day testing, the average pullout value of over 20 kips significantly exceeded the adjusted threshold value of 17.4 kips (scaled up from 16 kips as recommended by Logan (1997) based upon the comparative strand areas of 0.5 in. and 0.52 in. strands). The peak pullout capacity, however, did not reach the target of 39.2 kips at 3 hours, and did not exceed the peak threshold until the tests at 28 days. The reason for the 3 hour tests reaching Logan's threshold for first slip pullout but not the threshold for peak pullout is likely due to the failure modes. Adhesion, essentially the gluing effect between the paste and the strand, is lost when strand movement begins. Therefore, it is reasonable to say that adhesive forces

mostly dictate the 1st slip pullout strength, while aggregate interlock helps provide the peak pullout capacity by mechanically grabbing onto the strand. With very high early compressive strength, and excellent concrete consolidation, the paste had strong adhesion to the strand, allowing high early bond strength up until the strand began to slip significantly beyond 0.10 in. of movement. Once significant slip was occurring, however, there was not a high proportion of hard rock aggregate present to resist the strand moving through the concrete and provide high peak pullout loads. Eventually, the concrete paste gained sufficient compressive strength to overcome the reduced coarse aggregate issue and provide the required mechanical interlock, but it took more than 1 day before this occurred.

Figure 75 shows a summary of the maximum strand bond strengths for both first slip and overall peak at each age. The bond strengths were computed by dividing the pullout loads by the bonded length of the strands in the LBPT specimen times the gross strand circumference based on the strand diameter of 0.52 in.

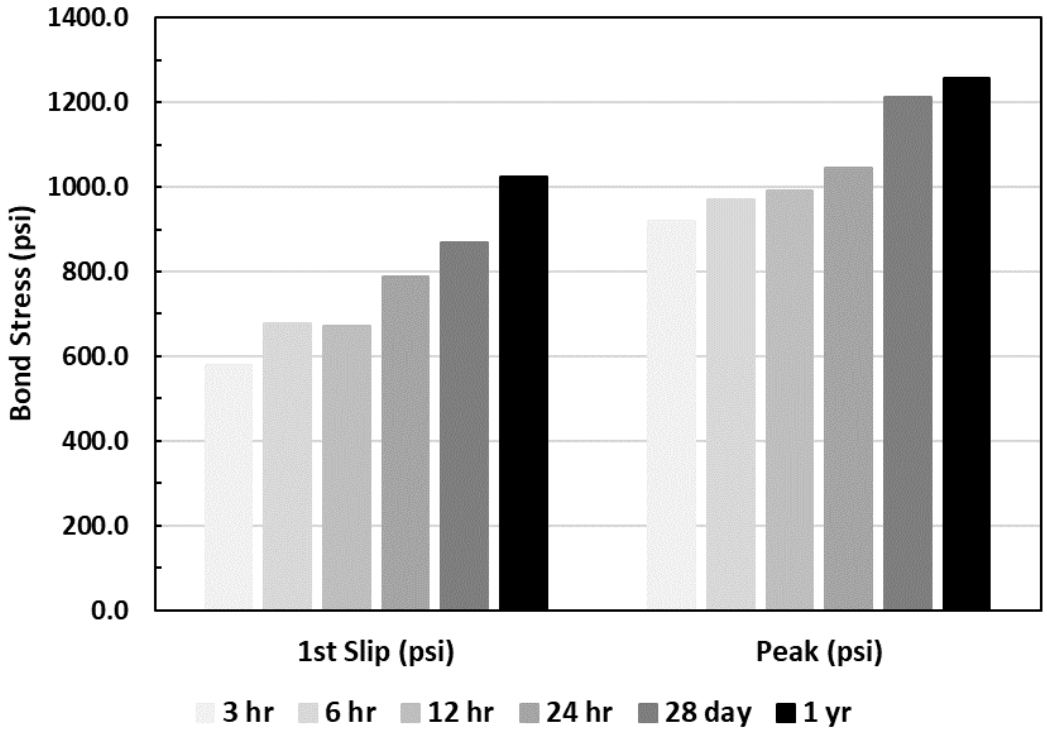

Figure 75: LBPT strand bond strength results

Figure 76 shows the bond strengths measured in the LBPT tests over time, normalized by the average concrete compressive strength at the time of testing. The purpose of this normalization is to visualize the relative contributions of maturity and compressive strength of the concrete to strand bond strength.

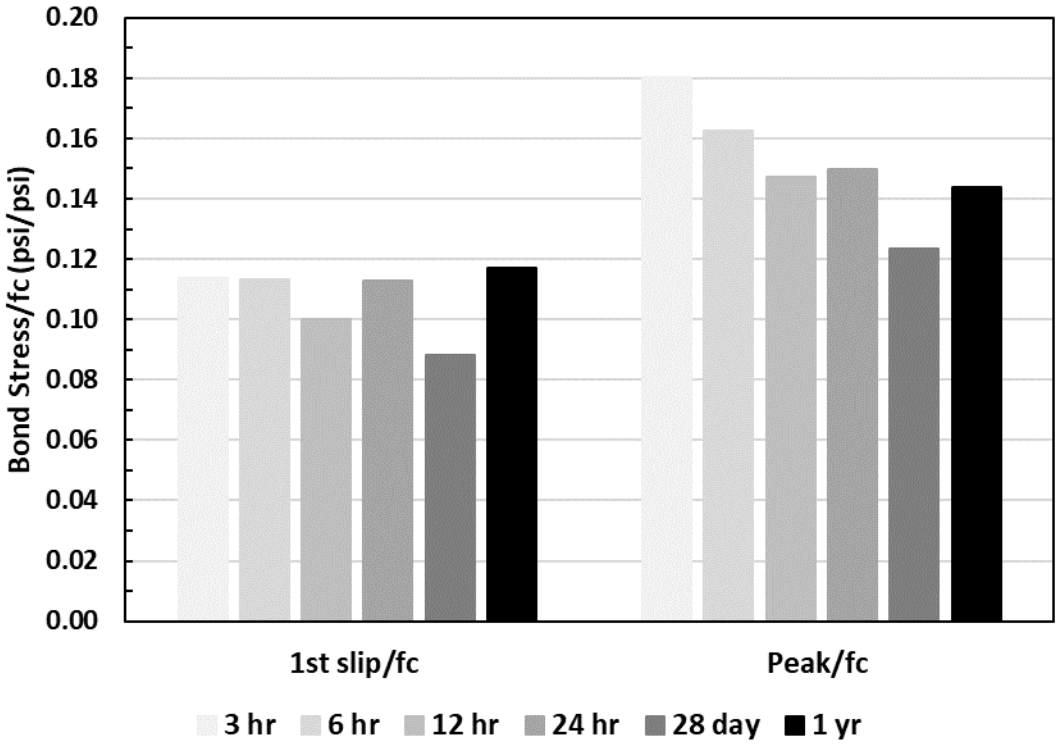

Figure 76: LBPT strand bond strengths normalized by concrete compressive strength at time of testing

Figure 76 shows that when the strand bond stress is compared on an equivalent concrete compressive strength basis, it does not increase with the age of the concrete. In fact, the normalized strand bond essentially flatlined with time for the first slip strength, and generally declined with time for the peak bond strength. Therefore, Figure 76 would indicate that for this normalization technique, there was not a reduced strand bond strength for the early age concrete, and that the development of strand bond strength was more strongly impacted by concrete compressive strength than concrete age or maturity.

Figure 77 shows the bond strengths measured in the LBPT tests normalized by the square root of the average concrete compressive strength at the time of testing. The purpose of this normalization was to compare to the previous method since normalization by the square root of

compressive strength is a fairly common technique in concrete design, especially for properties that may be affected by tension strength, such as bond/anchorage.

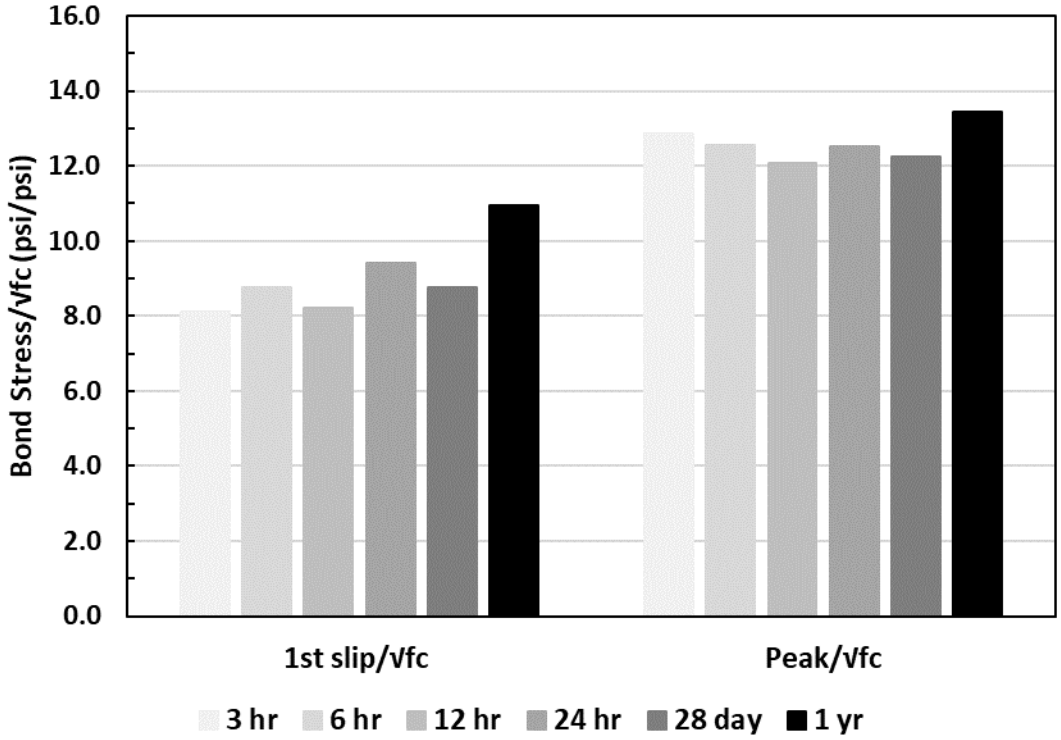

Figure 77: LBPT strand bond strengths normalized by square root of concrete compressive strength at time of testing

Figure 77 shows that although there is a slight increase in the normalized first slip bond strength as time progresses, the 1 year LBPT test is the only age which shows a markedly higher normalized bond strength, for either first slip or peak strength. In fact, if the 1 year test is excluded, the normalized peak bond strength shows a gently descending trend with age, similar to the first normalization technique. In summary, although the peak pullout loads all generally increased with time, normalization with concurrent compressive strength data shows that concrete compressive strength is strongly influencing the strand bond strength. This is rational, considering that strand bond tends to be impacted by compressive strength in conventional

concrete as well. By extension therefore, very early age strand bond for the RS-SCC does not appear to be adversely affected by a lack of maturity so long as compressive strength is sufficient.

4.2 Beam Specimen Design and Construction

Prior to beginning large-scale structural testing of the RS-SCC for transfer and development length and prestress losses, design calculations were performed using stipulations from ACI 318 (2014) to ensure that the beams would have the desired capacity. Additionally, trial beams were constructed before fully instrumented test specimens were cast. The purpose of the trial beams was twofold, first to practice the construction sequencing so that unforeseen issues would not waste valuable strain gages and second so that a control beam could be tested to experimentally verify the theoretical beam capacity and failure modes. These design calculations, the final design drawings, a description of the beam construction process, and a description of the trial beams are included in the following sections.

4.2.1 Beam Design

For this project, the transfer, development, and prestress loss beam testing utilized the same beam design. This was primarily to streamline beam construction, and to ensure that the data from the various tests would be comparable. Three primary criteria drove the design process for these beam specimens:

(1) Ensure that the predicted failure mode would be purely flexural, except for the possibility of bond failure at embedment lengths less than the development length.

(2) Ensure that shear cracking would not impact the failure mode, preferably using solely the concrete shear resistance. By avoiding the use of extensive shear reinforcement, the potential impact of confinement on the observed bond behavior in the transfer zone could be avoided.

(3) Ensure that the beams were proportioned such that the volume of concrete required for each beam could be handled by a single batch using the mixers available at Fears Lab. Mixing at another facility or utilizing a ready mix truck were feasible options, but mixing in-house would provide the greatest possibility for consistently repeating the same mix sequentially.

In this context, the embedment length refers to the bonded length of prestressed strand from the end of the beam to the section corresponding to the peak applied moment, in this case the location of the applied point load. This embedment length is critical because it is the maximum bonded area of strand which can effectively resist the stress induced by the imposed moment. Figure 78 shows both a section view and an elevation view for the beam design used in these experiments. The prestressing strands and top reinforcing bars were placed at 2 in. O.C.

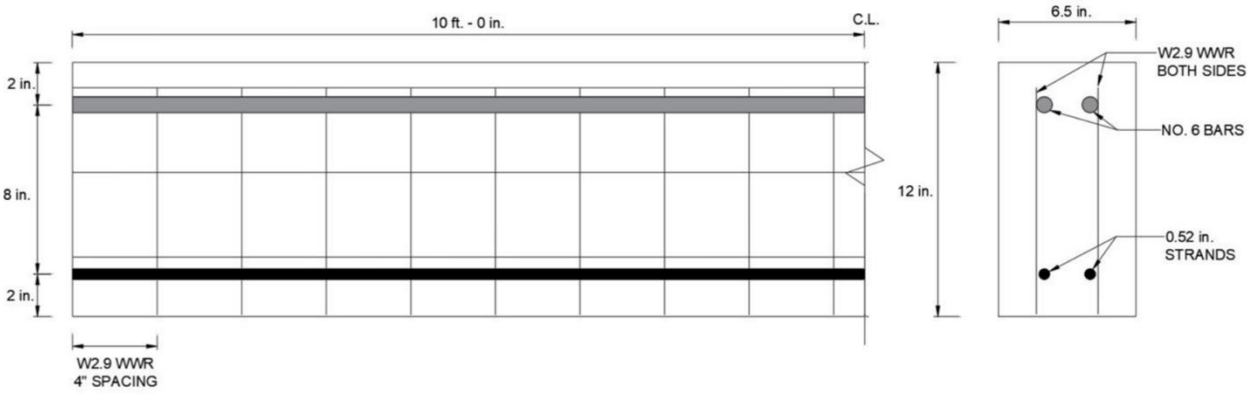

Figure 78: Section and elevation views for proposed beam design

In addition to the criteria listed above, the beam proportions were restricted to rectangular cross sections, primarily to streamline fabrication of the beams and to increase shear capacity contribution from the concrete to help avoid extensive shear reinforcement requirements. Utilizing this geometry also made the beams similar to those from previous research done for BCSA cement

concrete at OU for the sake of drawing comparisons to data from that research (Bowser et al., 2020). In addition, 12 in. wide formwork panels that were already tapped for DEMEC studs were readily available at Fears Lab, which saved labor and materials required to manufacture the required formwork.

Table 18 shows the design properties for the beam layout shown in Figure 78, based upon initial estimates for prestress losses and the projected concrete properties from Table 8 (Chapter 3).

Table 18: Summary of Beam Design Properties

Property	Quantity	Units
Gross Area	**78**	**in^2**
L_d*	**90**	**in.**
M_n**	**69**	**kip-ft**
V_{max}	**23.3**	**kips**
$V_{c\ min}$	**13**	**kips**

** Estimated from ACI 318-14 requirements*
*** By strain compatibility, estimated losses*

As discussed in Section 2.2.3.2 the development length testing at various embedment lengths would be conducted using a single point load on a simple span consisting of half the beam length (10 ft in this case). The estimated moment capacity (M_n) of 69 kip-ft, determined using a strain compatibility analysis, was converted to an equivalent point load at various embedment lengths on a simple span to determine the maximum probable resulting shear forces (V_{max}). The selected embedment lengths were estimated from a range based upon the ACI required development length (L_d). The maximum applied shear was estimated to be around 23.3 kips for a point load applied at a 3 ft embedment length on a 10 ft span with a total beam length of 20 ft. An embedment length of 3 ft, 40% of the ACI 318 (2014) development length, was

chosen as a likely minimum embedment length, partially based on results of previous research (Bowser et al., 2020 and Murray et al., 2019) and partially on prior laboratory experience with this material on the part of the research group. Finally, the ACI approach was used to estimate the contribution of the concrete to shear capacity of the beam, without any provision for shear reinforcement ($V_{c\ min}$). The maximum shear capacity from the concrete alone was determined to be 13 kips, based upon the projected concrete strength of 10 ksi. Even considering the ACI detailed shear capacity approach for a prestressed beam, there was some deficiency in shear capacity. Therefore, it was determined that transverse reinforcement was required. Welded wire reinforcement (WWR) was chosen as the shear reinforcement due to ease of placement and handling and reduced labor time compared to bending stirrups, and so that the shear reinforcement would not provide unwanted confinement to the prestressing strands in the transfer zone. In addition, the use of WWR for shear reinforcement matched Bowser et al. (2020). It was determined that W2.9 (6 gage) WWR with a 4 in. x 4 in. square opening layout provided on both sides of the section, as shown in Figure 78, would provide sufficient additional shear strength to exceed the theoretical moment capacity with a point load 3 ft from the beam end. No. 6 mild steel bars (Grade 60) were supplied in the top of the section to resist tensile stresses at release, which exceeded ACI 318 limits for the concrete alone due to the beam's aspect ratio and total prestress force. Finally, the overall beam length of 20 ft was chosen because it allowed a span configuration whereby each end of every beam could be tested for development length independently without influencing the opposite end. In this way, every designated embedment length could be tested twice on the same beam to obtain replicate tests that could be averaged and used to identify any potentially anomalous results.

4.2.2 Beam Fabrication Procedures

Other than the addition of DEMEC studs and VWSG instrumentation on the beams used to collect strain data for transfer length and prestress losses (see Section 4.4.1), the same process was repeated for the preparation and casting of every beam.

4.2.2.1 Bed, Formwork, and Reinforcement Preparation

Figure 79 shows the prestressing bed between the abutments used to pretension the strand. These abutments and beds were carefully levelled when they were initially placed, and laser levels and string lines were used between each beam casting to ensure that the beds remained aligned with the abutments. The abutments were configured far enough apart to cast one beam at a time. Although there was sufficient strong floor space and there were enough bed segments and form panels to cast two beams at a time, the volume of concrete required for two beams exceeded the capacity of the 21 ft^3 horizontal shaft concrete mixer at Fears Lab. It was determined that for the sake of consistency, every test sample should come from one batch, and it would have been logistically difficult to coordinate with SRM for every beam mix. Therefore, every beam was cast individually.



Figure 79: Prestressing bed and abutment configuration in Fears Lab

Figure 80 shows the prestressing bed being prepared for the addition of the form panels. The bed was covered with a plastic sheet, to prevent leakage and to debond the beam from the bed panels without the use of form release agent. Since the project objectives focused on bond of the strand with BCSA cement concrete, it was determined that form release agent would not be used because of the risk that it might contaminate the strands during beam preparation. The 2x4 dimensional lumber segments running longitudinally on the bed visible in Figure 80 were placed to set the proper beam width and to secure the form panels at their bases.



Figure 80: Prestressing bed prepared for form panel placement, looking toward live end abutment

Figure 81 shows the prestressing bed with the form panels in place. The form panels were also wrapped in plastic to avoid the use of form release agent. Upon repeated use, the plastic on the form panels would become wrinkled, which left creases in the surface of the beams after the forms were stripped. This issue was considered acceptable given the advantages offered by using the plastic in terms of ease of stripping forms, sealing against leaks, protecting the forms against damage, and eliminating the possibility of strand contamination with form release agent. After

every few beams were cast and the plastic became very wrinkled, the form panels would be recovered in plastic to limit creases in the beams.

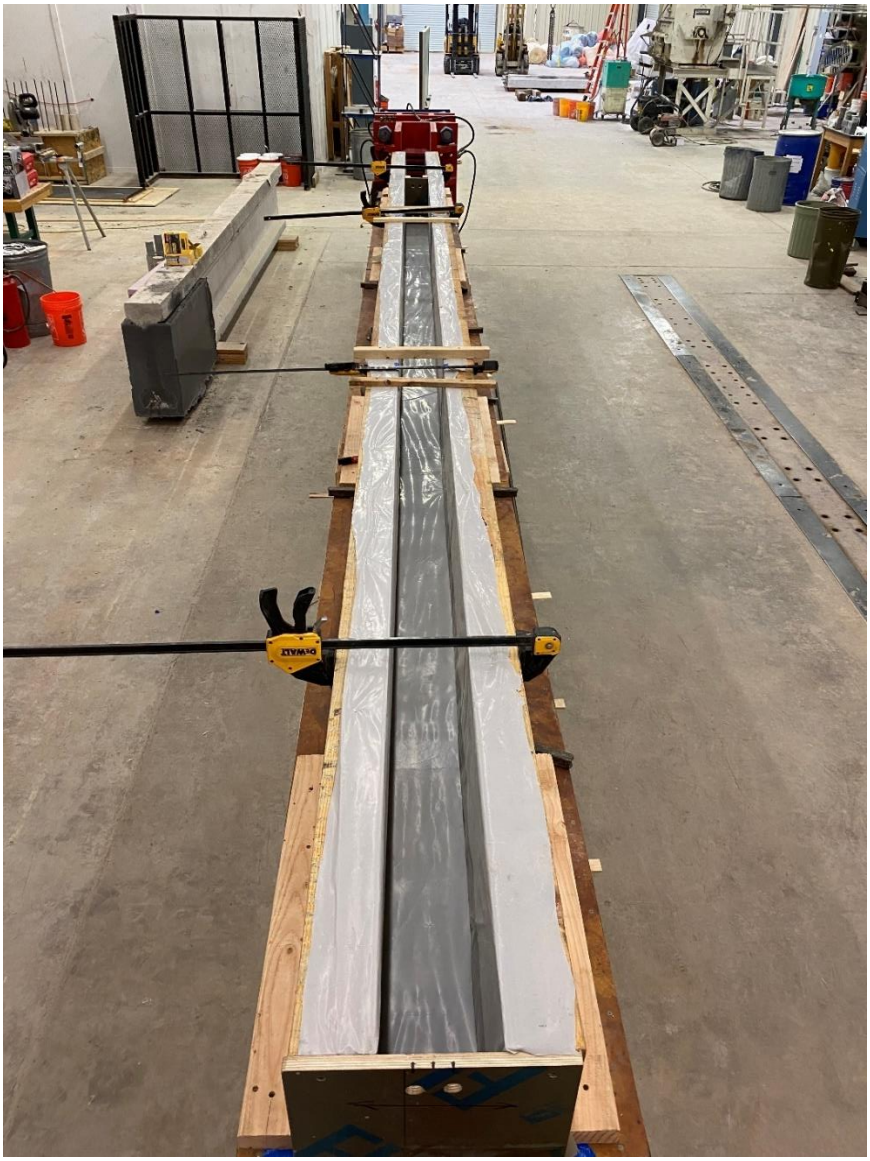

Figure 81: Prestressing bed with beam formwork in place, looking toward live end abutment

After the formwork was assembled, the reinforcing cage was put into place and the formwork top was clamped together to set the proper width. Figure 82 shows a close-up view of the reinforcement in the beam formwork.

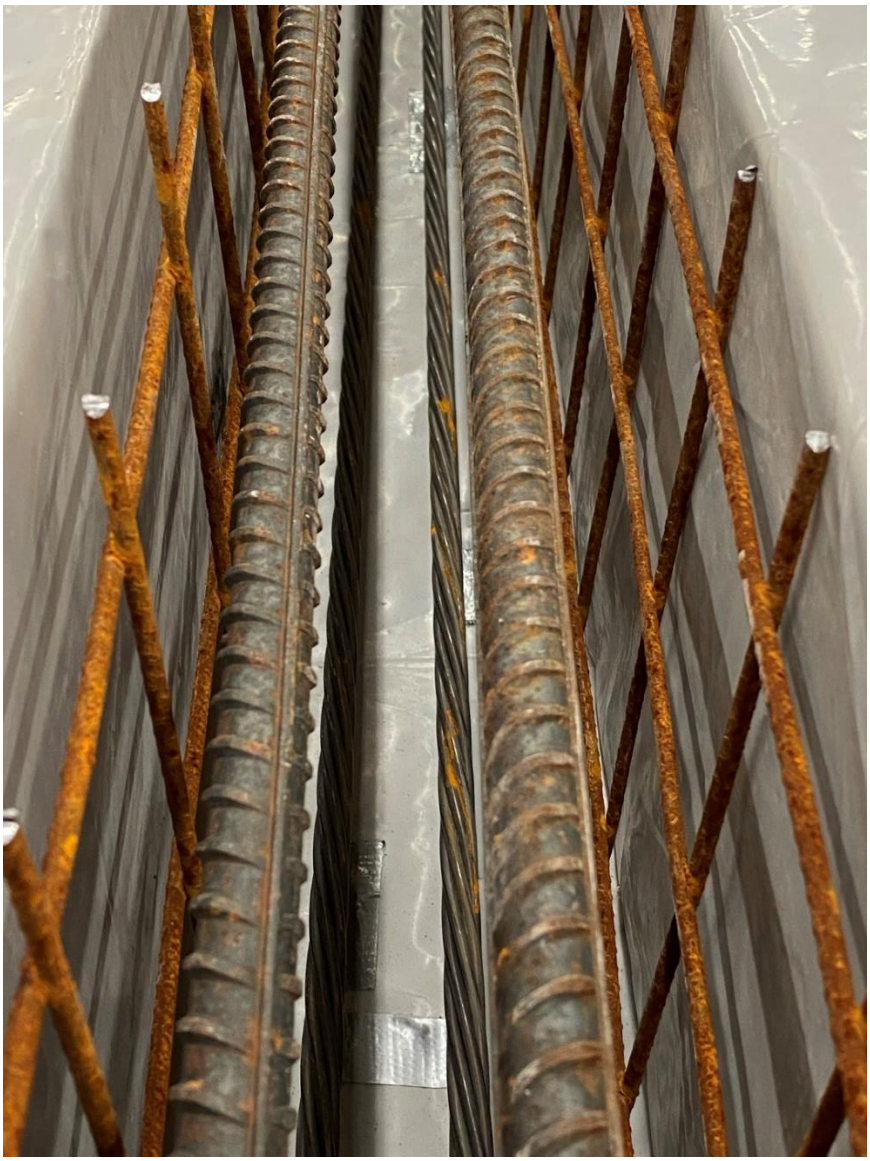

Figure 82: Close-up view of beam reinforcement placed for casting

Figure 83 shows the completed beam formwork with the reinforcement added and the clamps used at the formwork top in place, to keep the formwork from spreading apart due to the concrete pressure. In addition to resisting pressure on the formwork, the top clamps were used to suspend the No. 6 mild steel bars with ties to set their elevation at 2 in. O.C. from the top surface of the beam and ensure that the bars would not move when the concrete was cast.



Figure 83: Beam formwork with strand, mild steel top bars, and WWR in place for casting

For those beams which were to be tested for development length and were not instrumented with strain gages (DV series beams), the reinforcement was fully placed and tied and then the strands were tensioned. For the four beams instrumented with VWSG placed at the strand level (TR series beams – see Section 4.2.4 for beam testing breakdown), the WWR and top steel bars were not placed until after the strands were tensioned. This is because the elongation of the strands would cause the VWSG to shift when the strands were tensioned. The

final location of the VWSG was verified after tensioning the strands and then the WWR and top steel were placed before casting. Additional description of placement of the VWSG and other instrumentation is included in Section 4.4.1. Figure 84 shows the placement of the concrete into the completed formwork on the prestressing bed after the formwork, reinforcement, strand tensioning, and any relevant instrumentation were finalized.

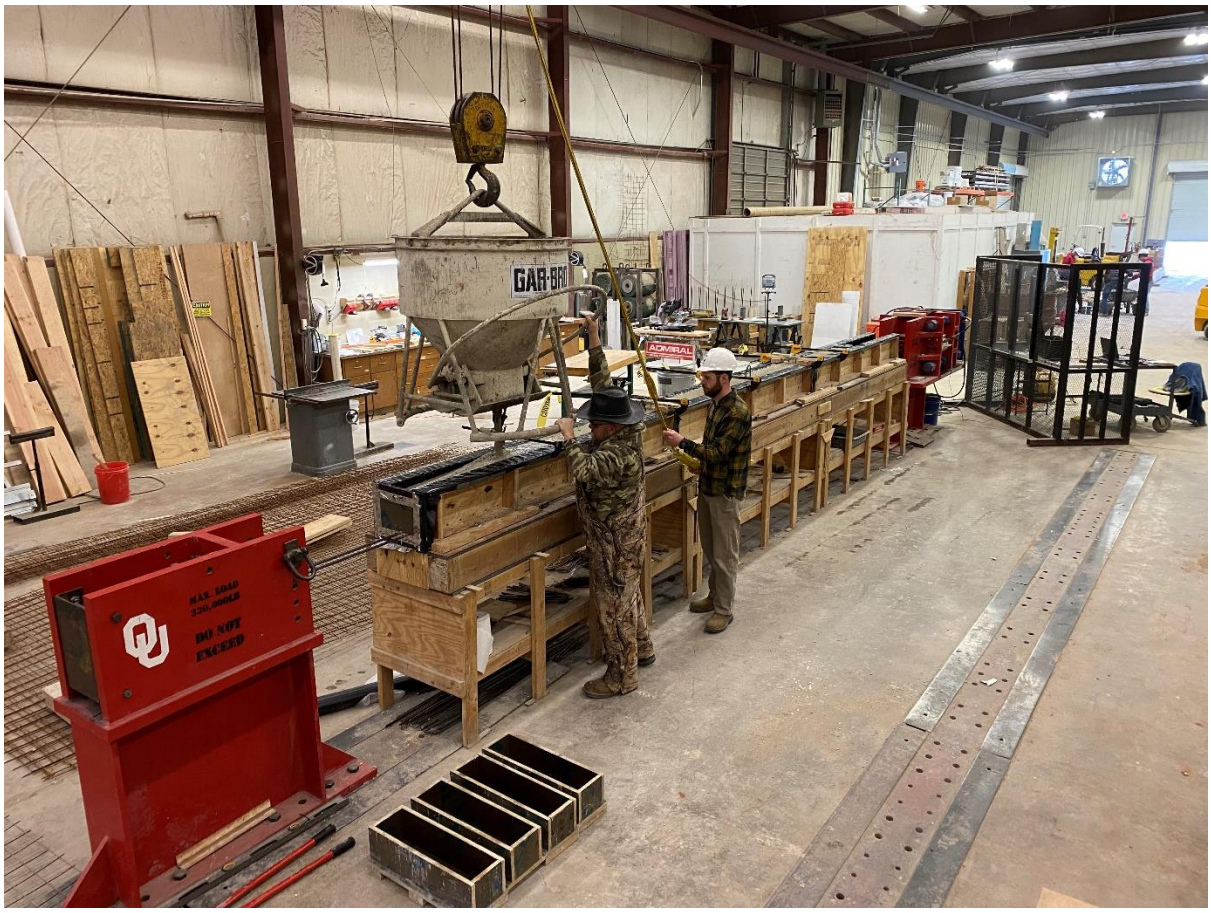

Figure 84: Filling beam formwork with concrete using a hopper and overhead crane

4.2.2.2 Strand Tensioning Procedures

The strand tensioning process followed a standardized procedure for the preparation of every beam. The two 0.52 in. strands were passed through a set of holes on the dead end abutment, laid along the prestressing beds, and passed through a set of holes on the live end abutment. These hole sets were positioned such that the spacing of the strands (2 in. O.C.) and

the bottom cover for the strands (2 in. to center of gravity of strands, cgs) were fixed in the appropriate locations. Sufficient strand was left overhanging both ends to allow for adding chucks to the strands.

The strands were chucked behind the static dead end abutment and in front of the movable bulkhead on the live end abutment, as shown in Figure 85.



Figure 85: Strands chucked behind static bearing plate on dead end abutment (top) and strands chucked behind tensioning bulkhead on live end abutment with load cell (bottom)

These chucks utilize a conical shaped steel wedge with hardened teeth that firmly anchor into the strand as the cone is pushed deeper into the reverse tapered chuck body. There is naturally some space between the wedge anchor and the chuck body which allows the strands to slip through the chucks slightly before the teeth fully engage and arrest the movement of the strand. This chuck slip contributes to the observed total strand elongation, which was measured with a scale and reference mark on the live end abutment. The strand elongation was monitored every time that strands were tensioned, so that the measured elongation could be compared to the theoretical strand elongation as a safety check against the strand stress estimated using a load cell placed on one strand to ensure that the strands would never be accidentally over tensioned. The chuck slip on each end of each strand was determined by placing a reference mark at a known stand-off distance from the chuck face and by measuring the change in this distance to the nearest 1/64 in. after tensioning the strands. These reference marks are the visible thin black lines on the strands in Figure 85.

Figure 86 shows the hydraulic ram and threaded rod system used to push the tensioning bulkhead on the live end abutment and then lock the tension in place so that the hydraulic pressure could be disengaged between strand tensioning and prestress release.

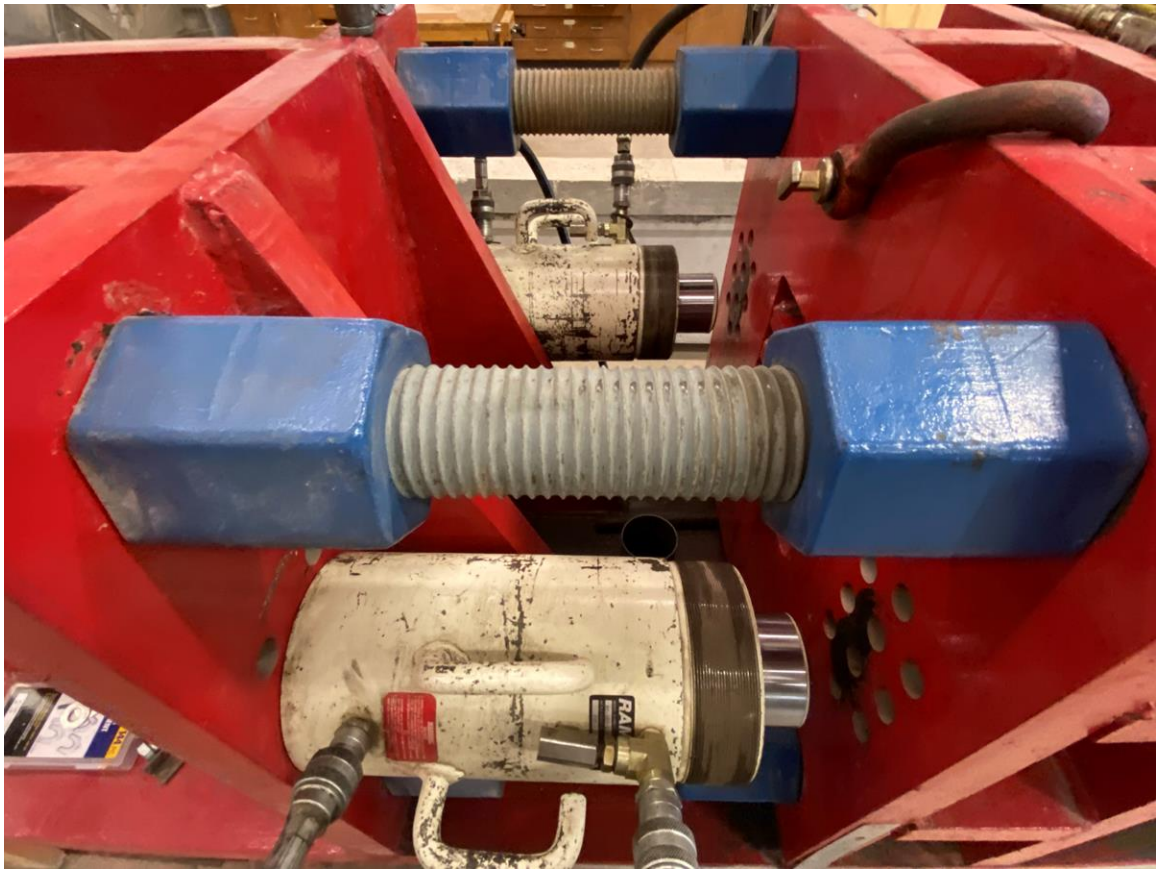

Figure 86: Live end prestressing abutment configuration with hydraulic rams behind tensioning bulkhead and threaded bar/nut assembly to lock bulkhead in place after tensioning

The hydraulic rams shown in Figure 86 were slaved to the same hydraulic pump so that they would exert equal forces and move the tensioning bulkhead uniformly when strand tension was applied. When the hydraulic rams had pushed the bulkhead far enough to reach the full jacking stress for the strands, as indicated by the live end load cell and confirmed by the observed strand elongation, the blue nuts directly behind the bulkhead in Figure 86 were advanced and tightened down hand tight against the back of the tensioning bulkhead. Then the hydraulics were reversed and the rams were retracted such that the threaded bars and nuts maintained the strand stress until time for prestress release. Because there was a known drop in strand stress when transferring the force from the hydraulic rams to the threaded bars, the strands

were over tensioned by approximately 2% so that the final strand stress after disengaging the hydraulics would be close to 202.5 ksi.

The strand jacking stresses (f_j) and initial prestress immediately prior to prestress release (f_{si}) were obtained by monitoring the load cell output between the live end tensioning bulkhead and the strand chuck. The load cell was connected to a National Instruments (NI)® data acquisition (DAQ) chassis, powered by a variable output power supply, and calibrated at an operating voltage of 10 V DC. The NI chassis transferred signals to an NI LabView® program on the laptop computer shown in Figure 87, where the prestress force and stress were displayed and saved to data files.

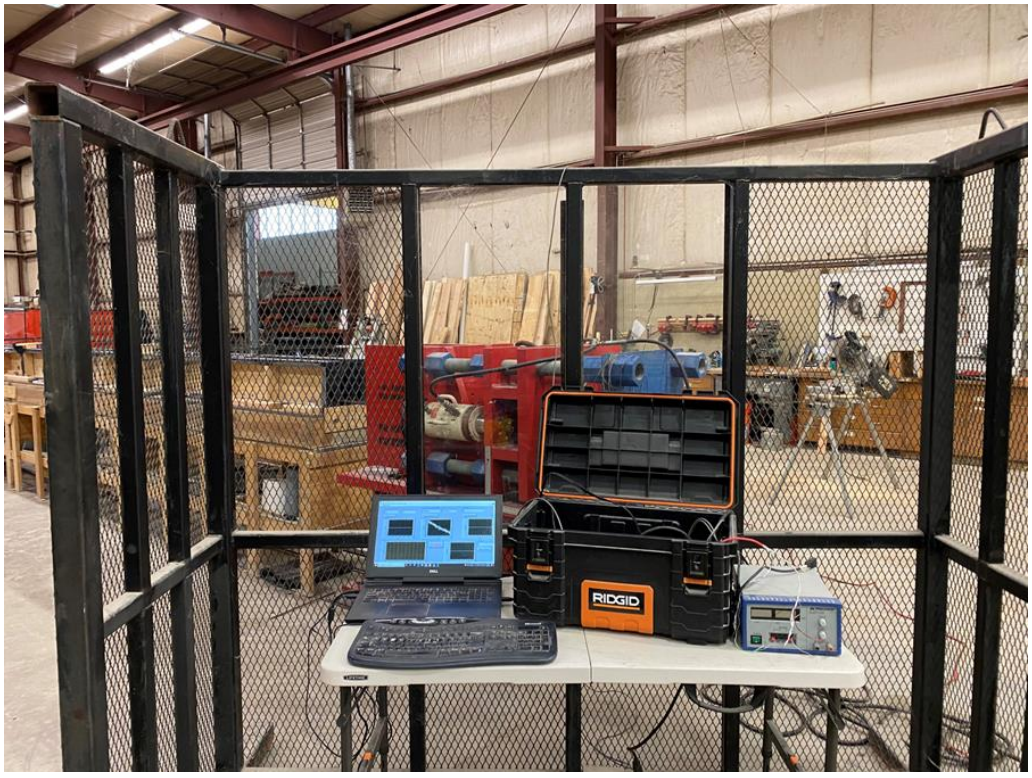

Figure 87: Data acquisition hardware connected to load cell on live end abutment to measure stresses for strand jacking and prestress release (DAQ area protected with safety cage)

Note that since the measurements being registered were loads, the jacking and release stresses were computed by dividing the force on each strand by the cross-sectional area of a 0.52 in. 7 wire prestressing strand which is 0.1667 in^2. This computation was preprocessed in the LabView® code, so that both the measured load and the calculated stresses were directly displayed and saved to the data files. On a typical basis the DAQ equipment was left set up and recording data between tensioning, casting, and prestress release for the early (3 hr) release beams. For the typical (24 hr) release beams, the DAQ equipment was usually turned off and disconnected after casting was completed and then turned back on and reconnected shortly before the prestress release time the next day. This is because at the sampling rate chosen to obtain high resolution data during strand tensioning, the recorded data file after running continuously for 24 hours would have been extremely large. However, for one 24 hr release beam, it was determined that a full profile of the strand stress between tensioning, casting, and prestress release would be helpful for data analysis. For this beam, the sampling rate was compressed by a factor of 10 only for the data stream sent to memory in the laptop computer, and the DAQ system was left running from tensioning until prestress release. This data was key in helping understand thermal effects on the initial prestress force (Section 4.3.1).

4.2.3 Trial Beams

It was intended that one trial beam be cast and tested to verify the constructability of the beam design and ensure that it would fail in the intended mode. Numerous issues were encountered during casting of the first trial beam (B1), and a second trial beam (B2) was cast after investigating the issues that influenced B1 and identifying potential solutions to those issues.

4.2.3.1 Trial Beam B1

The process described in 4.2.2 to prepare for casting was followed for B1, including the formwork setup, reinforcement layout, and strand tensioning. The horizontal shaft mixer in Fears Lab was charged with materials and mixing began shortly after tensioning the strands. The process of charging the mixer and the mixing procedure was intended to follow the standard procedure described in Chapter 3, which was followed for the large SRM mix and all of the smaller test mixes. The batch size for Beam B1 was 15 ft^3, which was only slightly less than the batch size for the SRM demo pour (16.6 ft^3) and was comparable to all the subsequent beam batch sizes, which were mostly around 15.5 ft^3. The concrete was dispensed into the transfer hopper after about 3 minutes of mixing from the time that the cement was added to the aggregate with half of the mixing water already added. Visual inspection indicated high flowability in the mixer and in the hopper as the concrete was dispensed from the mixer. By the time the hopper was transferred to the prestressing bed and casting began (a distance of less than 100 ft and a time of under 5 minutes), the concrete was noticeably stiff coming out of the hopper. The concrete was not flowing freely in the formwork as expected based on experience casting the LBPT specimens, so the concrete vibrator was immediately employed to aid in consolidation. After only a few additional minutes, however, the concrete was so stiff that the vibrator was required to push the concrete out of the hopper and into the forms. At this point, it was agreed

that the mix needed to be discarded immediately to protect the equipment. By the time the hopper could be moved outside of the lab for cleanout, the concrete (around 10 ft^3) had set in the hopper. This entire sequence occurred in under 20 minutes from the time cement was added to the mixer. In addition to a significant volume of concrete hardening in the hopper, only a small portion of the beam was filled and some concrete had also hardened on the surfaces inside the mixer before it was washed out.

Figures 88-90 show trial beam B1 in the formwork immediately after casting and after removal of the formwork. Strand pretension was carefully released due to the limited amount of concrete surrounding the strands and the beam was discarded. Several days were required to remove the hardened concrete from the hopper, the mixer, and various tools.



Figure 88: Trial beam B1 in the formwork after casting



Figure 89: View of trial beam B1 from the end after prestress release and cutting of the strands

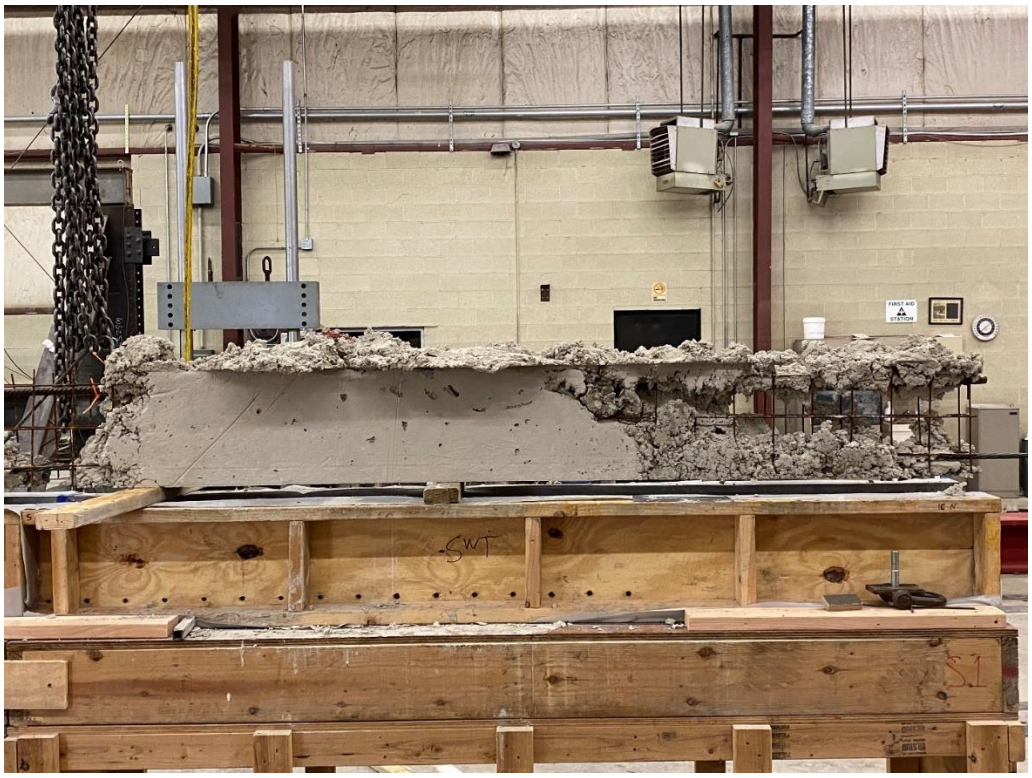

Figure 90: Profile view of trial beam B1 after formwork removal

The premature setting of the RS-SCC for trial beam B1 was unexpected based on experience with other mixes. It behaved like BCSA cement concrete when it is either mixed without citric acid or when the ambient temperature is extremely high. Neither condition existed for beam B1; the ambient temperature and concrete temperature were 70 °F and the citric acid dosage was 0.12 lb/cwt. These conditions were typical of the previous test batches and the large-scale LBPT batch, and test batches performed in much warmer temperatures had not exhibited this behavior. The construction of subsequent beams was suspended while the cause of the behavior exhibited during casting of beam B1 was investigated.

4.2.3.2 Citric Acid Sequencing and Slump Loss

Based on discussions with the students who assisted with the pour, it was determined that the standard order of operations (see Chapter 3) for addition of the materials to the mixer utilized for all previous test and specimen batches described in Sections 3.1 – 3.5 and 4.1 was not followed precisely during mixing and casting of beam B1. Instead of dissolving the citric acid in the mix water prior to adding 50% of the mix water to the aggregates, 50% of the mix water was added to the aggregates without any citric acid, and then all of the citric acid was dissolved in the portion of the mix water added after the cement was charged into the mixer. Importantly, this meant that citric acid was not present in the concrete when the cement could first begin hydrating with mix water. It was hypothesized that this was the cause of the issues experienced for beam B1 since no other deviations from typical procedures could be identified. The hypothesis was tested by experimenting with the order of citric acid addition and its effect on the rate of slump loss with a series of small-scale batches.

Figure 91 shows the results of a key pair of test batches (FR1 and FR2) performed to test the citric acid sequencing hypothesis after the mixing discrepancy from trial mix B1 was identified. Slump flow and concrete temperature were measured over time at 5-15 minutes increments (5 minutes increments were used for mixes FR 2 – FR 4; just over 15 minutes elapsed between measurements for FR 1 because this mix was performed by a single operator). Both mixes used a citric dosage of 0.12 lb/cwt and had temperatures very close to 70 °F to match trial beam mix B1. HRWRA was dosed at 10 oz/cwt for both mixes to match mix B1 and achieve initial slump flows that were as similar as possible so that the total slump flow losses would begin at comparable points for the two mixes. For mix FR1 all citric acid was added after addition of the cement while for mix FR2 citric acid was split with the mixing water using the standard procedures from material property and LBPT batches.

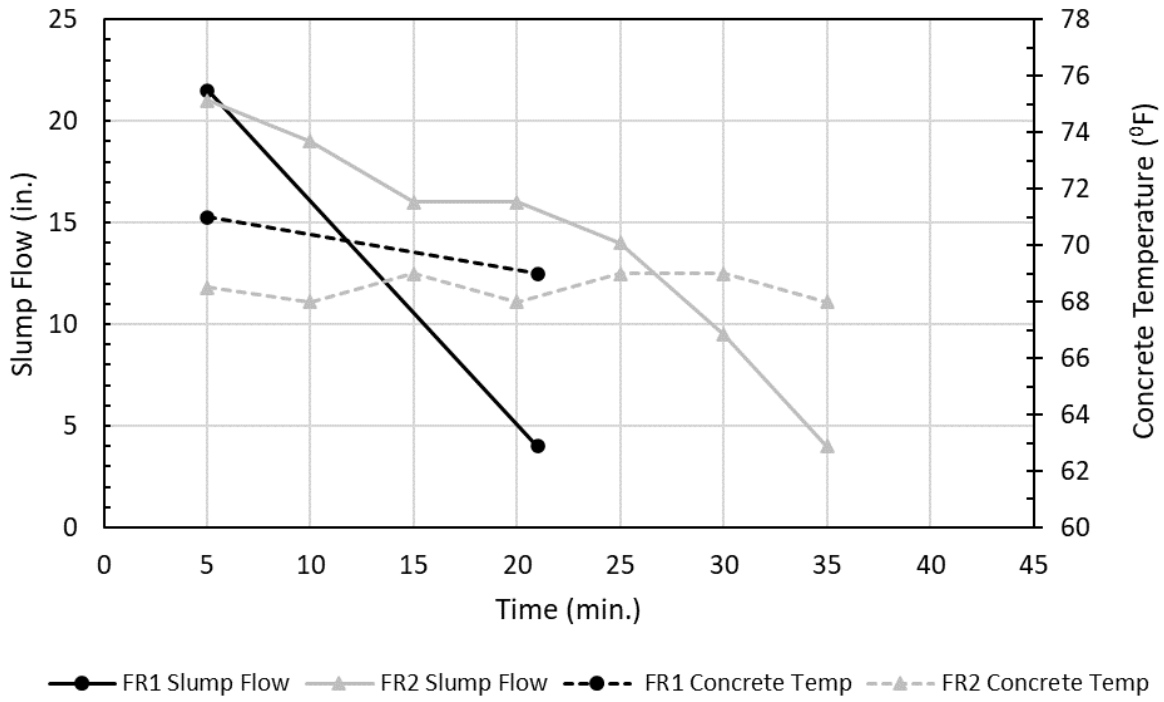

Figure 91: Rate of slump flow loss comparison for equivalent starting temperatures at 0.12 lb/cwt citric acid dosages with citric acid added after cement (FR1) and before and after cement (FR2)

Figure 91 shows that the concrete temperature ranges for the two mixes were very similar. Over the duration of each sequence of slump flow tests, the temperature of FR1 varied from about 69 to 71 °F and the temperature of FR2 varied between about 68 and 69 °F. In addition, the starting slump flows of 21.5 in. for FR1 and 21 in. for FR2 were nearly identical. It is also important to note that since the slump flow tests were performed with the slump cone in the inverted orientation as permitted by ASTM C1611, the apparent flow diameter cannot be smaller than the lesser slump cone end diameter of 4 in. Therefore, when the concrete was no longer flowable and a slump flow could no longer be effectively measured, the minimum possible slump flow of 4 in. was assigned for the purposes of plotting the data.

Most importantly, Figure 91 shows that when the citric acid was added according to typical protocol (mix FR2), that is, dissolved evenly throughout the mix water added in even

parts to the aggregates in the drum and after the addition of the cement, the slump flow was extended significantly compared to mix FR1, where the citric acid was added to the mix only with the water placed in the mixer after the cement, which mimicked trial beam B1. The time required to fall to zero flowability (4 in. slump flow) was more than 50% longer for mix FR2 compared to mix FR1. In addition, at approximately 20 minutes after casting, while mix FR1 had zero flowability (4 in. slump flow), mix FR2 had a slump flow of 16 in. Finally, the sudden drop from a high flowability to no flowability exhibited by mix FR1 in approximately 20 minutes mirrored the behavior of mix B1 almost perfectly. Figure 92 compares the slump behavior of FR1 and FR2 after 20 minutes had elapsed from water first touching the cement.



Figure 92: 20-minute slump comparisons for mixes FR1 (conventional slump, left – 0 in.) and FR2 (slump flow, right – 16 in.)

Note that for all slump flow tests, the cone was placed in its inverted orientation as permitted according to ASTM C1611. For those tests where the concrete was no longer flowable and a conventional slump test was performed in order to gauge the remaining workability (at which point the presumed slump flow was taken as the minimum of 4 in.), the slump cone was placed in its upright orientation according to ASTM C143.

The results from test mixes FR1 and FR2 strongly indicated that the sequencing of the citric acid addition was the likely cause of the premature setting of mix B1. However, another pair of test batches was performed to ensure that the issue was addressed. Mixes FR3 and FR4 utilized the same mixing procedures as FR1 and FR2 respectively, but instead of a citric acid dosage of 0.12 lb/cwt, a dosage of 0.24 lb/cwt was used. There were two main reasons for performing mixes FR3 and FR4. The first reason was to isolate whether the mixing procedure was an important consideration, even if there was more total citric acid in a given volume of concrete. The second reason was that a new shipment of BCSA cement had arrived from the manufacturer for casting the subsequent prestressed beams. Although there was nothing different about this cement other than being slightly newer than the cement used for the test batches, the extra tests FR3 and FR4 were used as a final check to make sure that the mixing procedure and citric acid dosage would have the intended effect on the slump flow over time of the RS-SCC made with the new shipment of cement.

Figure 93 shows the slump flow and temperature measurements of test mixes FR3 and FR4 over time (approximately every 5 minutes). These mixes used a HRWRA dosage of 10 oz/cwt like FR1 and FR2 and were performed with ambient temperatures in the low 70s °F like the previous mixes FR1 and FR2.

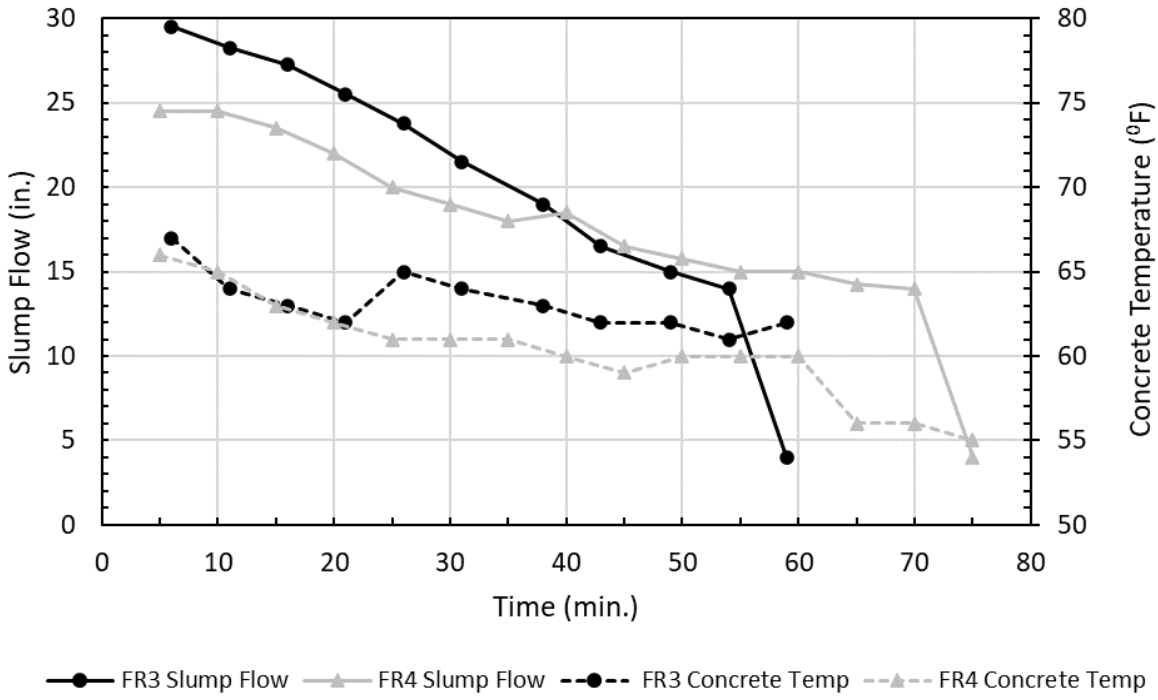

Figure 93: Rate of slump flow loss comparison for comparable starting temperatures at 0.24 lb/cwt citric acid dosages with citric acid added after cement (FR3) and before and after cement (FR4)

Figure 93 shows that the initial slump flow for mix FR3 was just over 29 in. and the initial slump flow for FR4 was just over 24 in. These values bracketed the targeted range of slump flows, and the slump flow of FR3 being initially higher than FR4 is likely due to typical variations in fresh properties between mixes due to aggregate moisture content, for example. Despite starting with a higher slump flow, however, the slump flow of FR3 declined at an average rate of about 0.3 in./min. By 55-60 minutes after casting, mix FR3 had no measurable slump flow (slump flow = 4 in., minimum inverted cone diameter) and did not have any workability as measured by a conventional slump test either. The slump flow loss over time for mix FR4 was half that of FR3 with an average rate of only 0.15 in./min. At 55-60 minutes after casting, FR4 still had a slump flow of 15 in. and its workability as measured by a conventional

slump test lasted beyond 75 minutes. Figure 94 shows comparisons of the remaining workability for each mix approximately 1 hour after water touched the cement in the mixer.

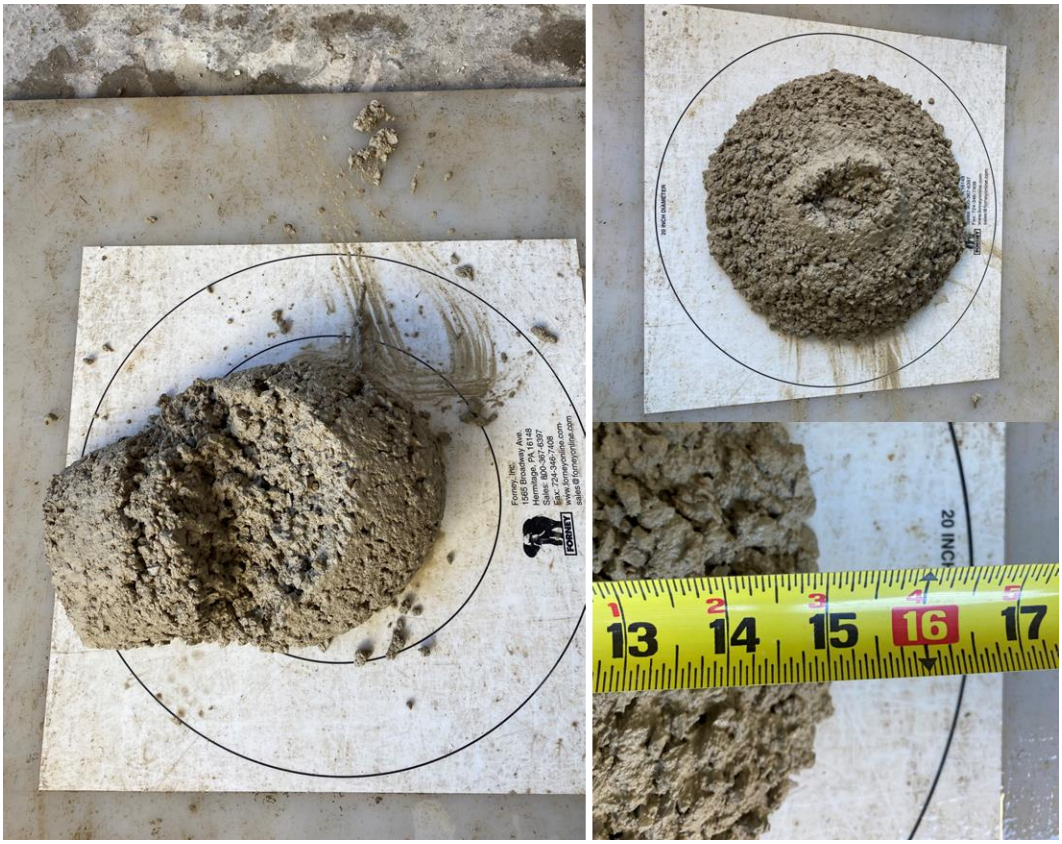

Figure 94: 60-minute slump comparison for mixes FR3 (conventional slump, left – 0") and FR4 (slump flow, right – 15")

Mix FR4 was discarded after the 75 minute mark since there was no longer any measurable slump flow, but before discarding it a conventional slump test was performed to gage the remaining workability. Figure 95 shows that even though there was no measurable slump flow, mix FR4 still had a conventional slump of more than 7 in.



Figure 95: Conventional slump test of FR4 at 75 minutes (7.5 in.)

This contrasts with the point when mix FR3 no longer had a measurable slump flow, because at that time the concrete from mix FR3 also had no measurable conventional slump – see Figure 94 where the slump cone crumbled. Although the slump concrete sliding sideways/crumbling in this manner technically marginalizes the test result, it was clear that the concrete was extremely stiff and unworkable at this stage. The findings from test mixes FR1/FR2 and FR3/FR4 were sufficient to make 3 key observations:

1.) Adding citric acid out of sequence relative to the protocol developed for this mix design was most likely to blame for the sudden slump loss and premature set of the RS-SCC for trial beam B1. This is further reinforced by the fact that no premature slump loss issues were encountered for the 15 subsequent beam mixes of similar concrete volumes, where the citric acid addition followed protocol.

2.) The chemical reaction begins as soon as the BCSA cement touches any water and proceeds quickly. It is very important that the first water that the BCSA cement contacts already contains at least part of the citric acid dosage for the retarder to be most effective.

3.) Although dissolving the citric acid in the mix water and adding the mix water in equal parts before and after the addition of cement (as in FR2 and FR4) was clearly more effective than only adding the citric acid in the portion of the mix water added to the mix after the cement (as in trial B1, FR1, and FR3), there may be other even more effective batching sequences and citric acid addition techniques that would further optimize the workability extension for this RS-SCC. Additionally, if a retarder other than citric acid were used, a revision to the mixing sequence might be appropriate.

4.2.3.3 Trial Beam B2

After critically analyzing the outcomes from trial beam B1 and the subsequent trial batches, a second trial beam (B2) was prepared. The purpose of beam B2 was to ensure that the workability issue had been resolved, and to accomplish the original goal of producing a test specimen that could be used to verify the design parameters when loaded to ultimate capacity. The casting and prestress operations for trial beam B2 followed the same procedures as for B1 with the adjustment to the citric acid addition and were successful. Appendix B contains summary sheets for the B2 mix proportion and fresh property data and Appendix C contains a tabular summary of the prestress data for beam B2. Figure 96 shows trial beam B2 in the formwork shortly after casting was completed.



Figure 96: Trial beam B2 immediately after casting

The initial slump flow of the concrete was just over 26 in. when the concrete was discharged from the mixer, and it took approximately 27 minutes from the time that the cement was placed in the mixer to complete casting the beam and at least 15 compressive strength cylinders. In that 27 minute span, the concrete remained visibly flowable and the workability was adequate for concrete placement. No mechanical vibration or consolidation of any kind was required to cast the beam and there was ample time after casting to thoroughly clean all tools and equipment before the concrete set. Figure 97 shows trial beam B2 suspended from the overhead crane, with the forms stripped and the prestress released only 3.5 hours after cement was added to the mixer.



Figure 97: Trial beam B2 being removed from the prestressing bed after forms are stripped and prestress released at 3.5 hours of age

Figure 98 shows a close-up view of trial beam B2 after the forms were stripped. Apart from a few minor creases from the plastic wrapped on the formwork panels, the self-consolidating concrete resulted in a very smooth finish free of honeycombing, pock marks, or bugholes of any kind. The results of the trial beam construction process, and the testing of trial beam B2 (Section 4.3.3.1), led to continuation of beam fabrication for further structural testing.



Figure 98: Close-up view of Trial beam B2 showing smooth beam surface free of bug holes

4.2.4 Beam Production Data

Table 19 presents a summary of the prestressed beam testing matrix, including the identifiers for each beam, their use in the testing program, and the key fresh and mechanical properties of the concrete. Note that the number B'xx' denotes the casting order of the beams, while the number 'yy'TR or 'yy'DV denotes the nominal prestress release age (3 or 24 hours). The DV series beams were tested destructively to measure development length while the TR series beams were monitored over time to measure transfer length (as well as prestress losses, see Chapter 5).

Table 19: Prestressed Beam Testing Matrix and Key Concrete Properties (f'_{ci}=concrete compressive strength at release, f'_c= concrete compressive strength at 28 days, except as noted * at 35 days, + at 21 days)

Beam Usage	Release Age	Beam ID	Slump Flow (in.)	f'_{ci} (psi)	f'_c (psi)
Trial Beams	Early (3 hr) Release	B1	N/A	N/A	N/A
		B2	26.5	4320	7850
TR Series	Early (3 hr) Release	B4-3TR	31	5600	11720*
		B11-3TR	30.5	6460	10830+
	Typical (24 hr) Release	B3-24TR	28.5	9090	10920
		B5-24TR	31	9130	11930*
DV Series	Early (3 hr) Release	B6-3DV	32.5	4900	11960
		B7-3DV	28	5940	11780
		B8-3DV	31.5	4730	11870
		B9-3DV	37	5150	12420
		B10-3DV	30	5740	11190
	Typical (24 hr) Release	B12-24DV	28	9130	10500
		B13-24DV	30	8880	11080
		B14-24DV	23	8340	10560
		B15-24DV	25	9260	10840
		B16-24DV	29.5	9870	11270

Tables 20 and 21 present summaries of pretensioning data related to the fabrication of all 15 prestressed beams that were used to study transfer length, development length, and prestress losses for the RS-SCC. These data include the jacking stresses and strand elongations; chuck slip measurements; and the age, effective prestress, and concrete compressive strength at prestress release. Tables 20 and 21 summarize the maximum, minimum, and average key parameters for the beams from each release age group and data sheets with the detailed data for each beam are included in Appendix C. Note that in Tables 20 and 21, f_{si} denotes the initial strand stress, immediately prior to prestress release, as measured by the load cell between the strand chuck and live end abutment bulkhead. Note also that the theoretical elongation is constituted solely by elastic deformation and does not attempt to account for chuck slip or strand curvature.

Table 20: Pretensioning Data for Early (3 hr) Release Beams

Prestress Record				
Dates:	10/27/21 - 3/4/22			
	Jacking Stress		Elongation	
	Load (lb.)	Stress (ksi)	Ruler (in.)*	Δ (in.)
Min:	34,265	205.5	16	3.69
Max:	34,484	206.9	16-3/16	3.94
Average:	34,394	206.3	N/A	3.82
	Theoretical Elongation (in.)		Chuck Slip (in.)	
Min:	2.93		0.176	
Max:	2.95		0.223	
Average:	2.94		0.193	
	Prestress Release			
	Time (hrs.)	Load (lb.)	f_{si} (ksi)	f'_{ci} (psi)
Min:	2.83	31,811	190.8	4320
Max:	3.67	32,197	193.1	6460
Avg.	3.27	31,969	191.8	5360

Table 20 shows that the average age at prestress release was 3 hours and 16 minutes for the early release beams. The slight variation above and below the target mark of 3 hours was due to the logistics of rapidly stripping forms and performing required strand slip and DEMEC measurements, rather than due to variations in compressive strength gain. Table 21 repeats the pretensioning data for the 24 hour release age beams.

Table 21: Pretensioning Data for Typical (24 hr) Release Beams

Prestress Record				
Dates:	11/18/21 - 3/24/22			
	Jacking Stress		Elongation	
	Load (lb.)	Stress (ksi)	Ruler (in.)*	Δ (in.)
Min:	34,374	206.2	16	3.75
Max:	34,717	208.3	16-3/8	4.00
Average:	34,458	206.7	N/A	3.87
	Theoretical Elongation (in.)		Chuck Slip (in.)	
Min:	2.94		0.176	
Max:	2.97		0.195	
Average:	2.95		0.187	
	Prestress Release			
	Time (hrs.)	Load (lb.)	f_{si} (ksi)	f'_{ci} (psi)
Min:	24	32,943	197.6	8340
Max:	25	33,523	201.1	9870
Average:	24.21	33,224	199.3	9100

Similarly to the early (3 hr) prestress release beams in Table 20, the variation in the target mark of 24 hours for prestress release in Table 21 was due to the time required to strip forms and perform required strand slip and DEMEC measurements, which was especially reliant on research crew availability. Several key observations can be made from Tables 20 and 21:

- The target initial prestress of 202.5 ksi or 75% of f_{pu}=270 ksi was intentionally exceeded by 1-2% to around 206.5 ksi for every beam. This was done to account for well-characterized anchorage/seating losses associated with the prestressing configuration specifically used in Fears Lab. After anchorage/seating losses, the prestress was typically around 202 ksi.
- The actual strand elongation upon jacking exceeded the theoretical value by around 7/8 in. on average. Around 3/8 in. of this difference was due to chuck slip, with an average chuck slip of around 3/16 in. measured on each chuck. The

remaining ½ in. of average difference is most likely from slack in the strands before tensioning.

- The strand stress at prestress release, as indicated by the load cell measurement on the live end abutment plate, averaged nearly 200 ksi for the 24 hour release age beams, which was expected given the jacking stress and aforementioned anchorage losses.
- The strand stress at prestress release, as indicated by the load cell measurement on the live end abutment plate, averaged around 192 ksi for the early release age beams. This represents an initial prestress about 4% lower than the 24 hour release age beams.

The reduced apparent initial prestress for the early age release beams was identified early in the casting sequence and was determined to be the result of thermal expansion of the concrete. In the 1-2 hours after final set, the exothermic hydration reaction of the concrete releases significant heat and the concrete compressive strength rapidly rises. As the temperature of the beam increases, its length increases in proportion to its coefficient of thermal expansion. The dead and live end abutments which anchor the strands are stationary, however, meaning that as the beam heats up and expands, the strand segments which overrun the ends of the beam slacken somewhat. Since the load cell was placed between the back of the live end abutment plate and the face of the strand chuck, the strand beyond the beam slackening results in the load cell showing a reduced apparent strand stress. After the hydration reaction peaks, the concrete gradually begins to cool, the beam contracts towards its original length, and the strand between the beam and the abutments gradually regains tension. By around 24 hours, most if not all of the

strand tension outside the beam has been regained and the load cell will show an apparent strand stress much closer to the expected initial prestress.

This hypothesis was tested by leaving the load cell and data acquisition (DAQ) system running for a full day after casting, continuously from strand tensioning to prestress release for one of the last 24 hour age release beams, instead of shutting the DAQ system down between casting and releasing prestress, which was usual practice. A full profile of the apparent strand stress with time, as indicated by the load cell, was recorded and is plotted in Figure 99.

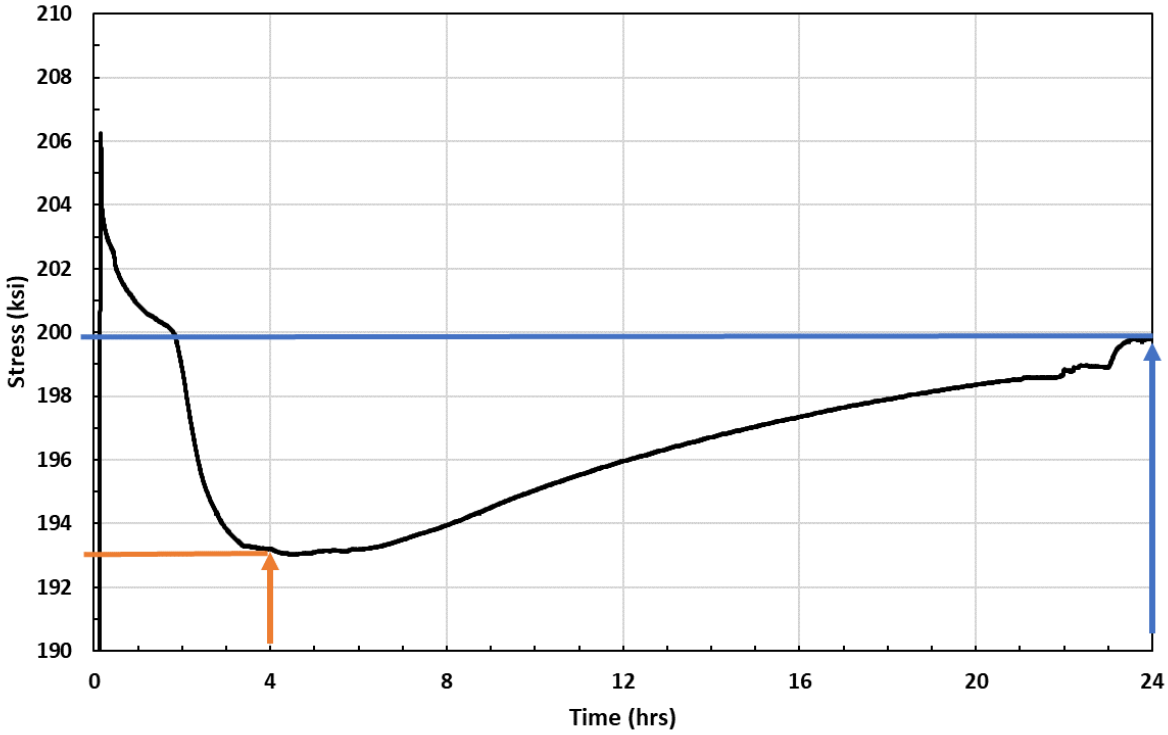

Figure 99: Time history of apparent change in strand stress between strand tensioning and prestress release as indicated by load cell located between chuck and live end abutment

Figure 99 clearly displays the initial jacking to a maximum of around 206.2 ksi, followed by an immediate drop in prestress when the force was released from the hydraulic jacks and transferred to the threaded rod and nut system used to hold the tensioning bulkhead in place. A

gradual decline in strand stress continues for 1-2 hours after jacking. During this time the beam reinforcement was finalized, the concrete was mixed, and the beam was poured. At around 2 hours after jacking, however, the beam has been poured, and the concrete heat evolution begins a rapid increase (correlating to the final set of the concrete), causing the observed strand stress to decline much more sharply until stabilizing at around 4-6 hours. The end of the apparent strand stress decline between 4-6 hours is shown with the orange line and arrow in Figure 99.

The beam undergoes an extended period of cooling from about 8 hours to around 22 hours after jacking. During the 8-22 hour window the beam cooling results in the apparent strand stress increasing back to around 199 ksi (note the blue line and arrow in Figure 99). It is also notable that the curve shows a sharp increase one more time, just after the 22-23 hour interval. At around 23 hours after jacking, stripping of the forms was initiated to prepare for prestress release; at this point the beam was still warmer than ambient. Once the insulation of the forms was gone, the beam could cool faster during the interval from 23-24 hours than it could while the forms remained, and the apparent strand stress jumped quickly from 199 ksi to 200 ksi. The prestress release is not shown in Figure 99, because prestress release was performed 24 hours from mixing not 24 hours from jacking.

The average drop in apparent strand stress between casting and early prestress release of 7-8 ksi or about 3-4% decrease in initial pretension, should theoretically be reconcilable against temperature data available from the beams instrumented internally with VWSG. This was executed with a series of simple computations. First, the average temperature increase between final set and prestress release was calculated for B4-3TR from the 9 internal VWSG, and was determined to be 34.4 ºF. Next, the gross thermal expansion of the strand within the beam was computed according to Equation 6:

$$\Delta L = \alpha L \Delta T \quad (6)$$

where L=20 ft or 240 in. (beam length), ΔT=34.4 ºF (avg. temperature increase), and α≈6.1 µin./in/°F (thermal expansion coefficient for high carbon, high strength steel). Using Equation 6 with these inputs gives a result of a gross thermal expansion of 0.0504 in. Since the abutment locations are fixed, this gross expansion allows the strand beyond the beam to shorten. With the prestressing configuration used for this project, approximately 16 ft of strand extended beyond the extents of the beam to anchor to the abutments. So, basic engineering mechanics could be used according to Equation 7 to convert the shortening induced in the overrunning strand to a decrease in stress:

$$\Delta\sigma = E\varepsilon = \frac{\Delta L}{L} E \quad (7)$$

where L=16 ft or 192 in. (surplus strand length), ΔL=0.0504 in. (From Eq. 6), and E=28,600 ksi (strand modulus of elasticity provided by the strand manufacturer). Using Equation 7 with these inputs gives a stress reduction equal to 7.51 ksi, which is almost exactly the same as the average reduction in initial prestress for the 3 hour release beams compared to the 24 hour release beams (an average stress reduction of 7.50 ksi).

Based upon this result, it can be said with a high degree of certainty that the apparent reduced initial prestress for the 3 hour release beams was a result of the thermal expansion of the beams causing the surplus strand to shorten and reduce the force applied to the load cell at the abutment. The 24 hour release beams regained this apparent stress due to cooling to near their starting temperatures before prestress release. However, over the continuum that exists from final set to early prestress release, as heat evolves and the beam expands, the concrete also rapidly gains strength. Therefore, by the time the strands are released from the abutments, it is unknown

what portion of that apparently reduced stress was already being supported by the concrete. If some portion of that stress was locked in because of the support from the concrete, the actual initial prestress at 3 hour release would be greater than the load cell measurement or the thermal expansion calculations would indicate.

4.3 Development Length Testing

Table 19 in Section 4.2.4 summarizes the nomenclature system for each DV series beam. Throughout Sections 4.3.2 and 4.3.3, the embedment length at which each beam was tested is described in the subsection heading. The beam nomenclature and associated tested embedment lengths are also summarized in Tables 22 and 23 of Section 4.3.4. Note that due to testing logistics, the casting order of the beams (as denoted by the number B'xx') did not match the testing order of the beams. This is because it was not certain what failure mode a test at a given embedment length would yield before that test. Therefore after a given test, it was common to double back and fill in other embedment lengths between tests which had already been conducted.

4.3.1 Beam Testing

Each of the 10 prestressed beams cast for development length determination (DV series) was tested at between 27 and 29 days from the time of casting, with most beams being tested at 28 days. Each beam test consisted of placing a point load at a specified distance from the beam end (embedment length) in order to induce a moment that, based upon the strand embedment between the beam end and the point load, would either cause a flexural bond failure resulting in general bond slip or would result in a flexural failure at the full moment capacity of the beam. As the embedment lengths grew shorter, there was also a chance that a shear failure could be induced, although reinforcement was designed to resist this failure mode (see Section 4.2.1).

The beams were designed to be long enough that one end would overhang from around midspan of the beam while the first end was being tested. Effectively, two independent data points could be gathered from each beam by testing both ends, one after the other. As soon as the first beam end was tested, the beam was removed from the load frame either the same day or the next, flipped around in the test setup, and loaded in an identical manner to the first end. In this way, a replicate data point was obtained for every strand embedment length, so that a more representative trend could be obtained. Figure 100 presents a schematic that demonstrates the span length, support locations, tested embedment lengths, and overall beam length.

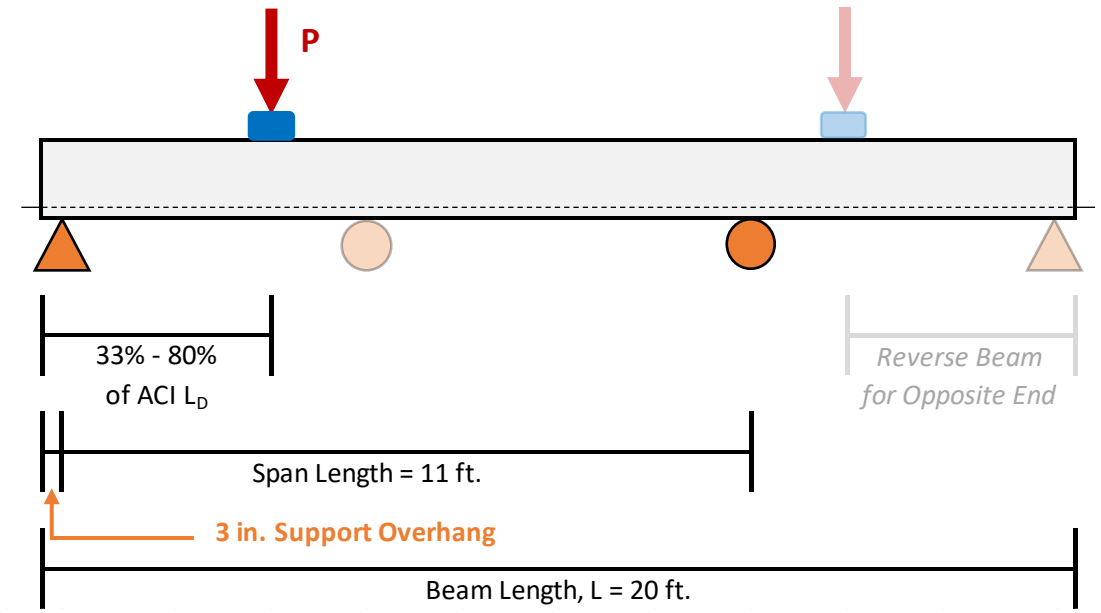

Figure 100: Span and support configuration for development length bending tests

An 11 ft span was used for all of the development length beam tests, except for one end of the trial beam B2 which was tested with a 10 ft span while the testing apparatus was being refined. The 3 in. support overhang on the end being tested was chosen so that the beam had enough clearance to safely rest on the support roller without slipping off as the beam rotated

during testing. A separate set of 3 compressive strength cylinders were typically tested for each beam end test, even if the two beam ends were tested on the same day. The overall average compressive strength results for both ends of each beam test are summarized in Table 19 of Section 4.2.4. The compressive strength results for each beam end test are presented individually with the corresponding test in Sections 4.3.2 and 4.3.3.

The same loading increments were used for testing both ends of every prestressed beam. Load was added in 5 kip increments until the beam cracked, as evidenced both by visual observations of the beam itself and by the shape of the load deflection curve which was plotted in real time on the front panel of the NI LabView® program used to gather the testing data. After the first crack(s) were observed, the beam was loaded in 2 kip increments until a failure state was reached, as evidenced by an inability to sustain additional load due to either concrete crushing, significant strand slip, shear cracking, or some combination of these failures.

Figure 101 shows the apparatus used to apply load to the beams and monitor the response of the beams.

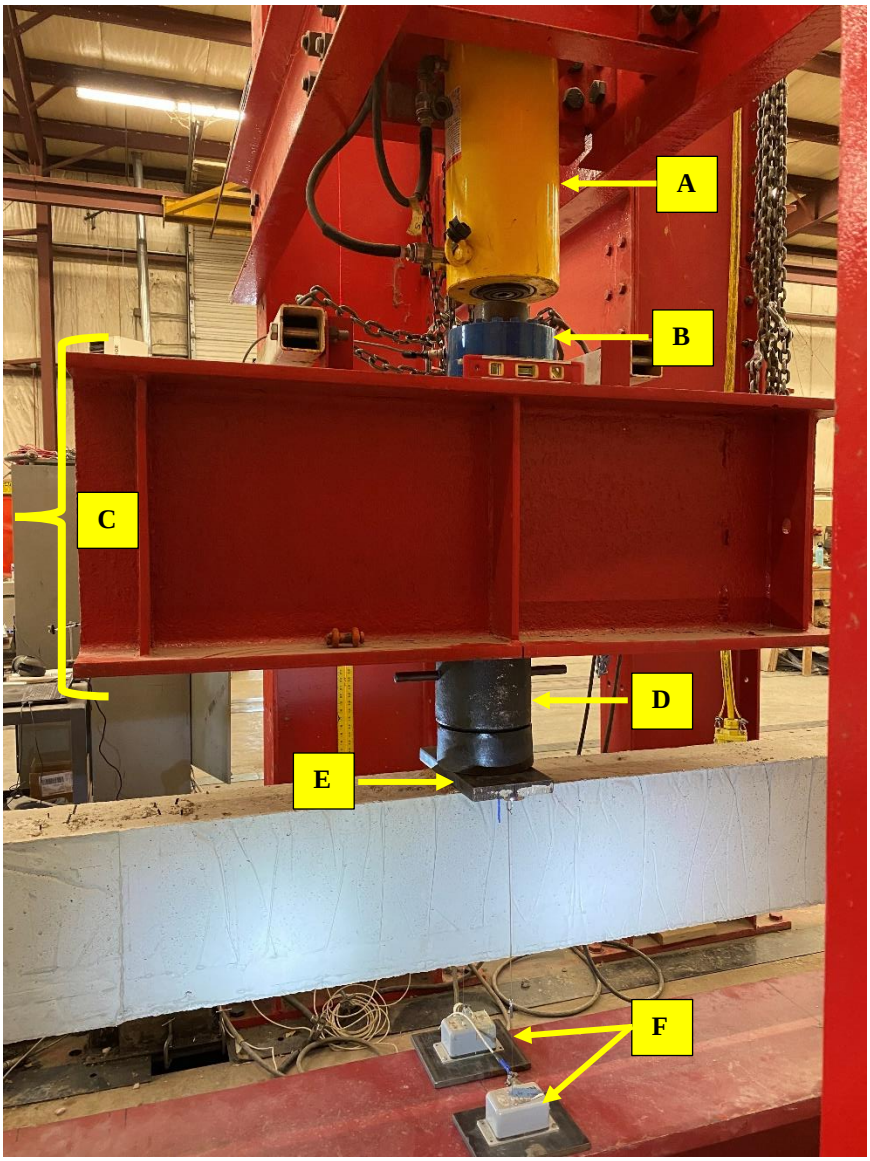

Figure 101: Development length beam testing apparatus with instruments

Hydraulic ram “A” in Figure 101 was plumbed to a hydraulic pump and applied load through the spacer block to the blue load cell “B” (200 kip capacity, Interface® compression only load cell). The load cell rested on top of the red spreader beam “C”, which was primarily used for safety to support the load cell if the beam failed catastrophically. The spreader beam was supported with control arms and an automotive hoist hanging from the reaction frame, so that it could not fall if the beam collapsed. Load was transmitted directly through spreader beam “C”

to the swivel “D” which was lubricated with grease and allowed the load to stay centered as the beam rotated throughout the test. Loading plate “E” (6 in. wide by 1 in. thick) was placed with its center at the desired embedment length away from the beam end, and was placed on a bed of sand to level any irregularities in the top beam surface. Finally, wire potentiometers “F” were positioned at the center of loading plate “E” and were securely affixed to the underside of the plate using magnets. Wire extensions were used to reach from the wire potentiometers to the magnet hooks. Additionally, the wire potentiometer deflection measurements were checked with external manual deflection measurements taken with a fixed scale and a laser level.

Figure 102 shows the LVDT’s which were mounted to the strand extensions beyond the face of the beam end on whichever end was being tested. The purpose of these LVDT’s was to monitor strand slip in synchronization with the applied load and deflection measurements so that inferences about the strand anchorage could be made in conjunction with the beam failure modes in order to accurately determine whether the strands were developed at a given tested embedment length.



Figure 102: LVDT's mounted to strands with block clamps to measure strand slip

LVDT's were not placed on the strand extensions opposite the end being tested, because with 20 ft of strand anchorage, there was no concern about slip on the opposite end of each test. Additionally, since the opposite end of each test overhung the far support by nearly 9 ft, there was almost no moment in the opposite end transfer zone and therefore no reasonable justification to monitor strand slip.

4.3.2 Results – Early (3 hr) Prestress Release

This section summarizes the results of the load testing for each beam constructed with an early prestress release, which varied between 2 hr and 50 min. and 3 hr and 30 min. (see Section 4.3.1). After the results from each load test are summarized, the resulting development length data is synthesized in Section 4.3.4.

4.3.2.1 B2 (Trial Beam)

Beam B2 was tested on November 15 and 16, 2021 at an age of 18-19 days. The average compressive strength at the time of testing was 7.8 ksi. The extreme expected strand embedment lengths for the testing program were tested; 3 ft - 4 in. on the dead end and 6 ft - 9 in. on the live end. The goal of testing this trial beam was to ensure that the beam design would perform as intended, and it was tested at an earlier age than the subsequent development length beams so that casting of the other beam specimens could proceed on schedule. Note that for the trial beam test, the dead end was tested with a 10 ft span, while the live end was tested with an 11 ft span. An 11 ft span was used for all of the subsequent development length beam tests.

Figure 103 shows the load-deflection response of Beam B2. The gray and black traces represent the individual tests on the live and dead ends respectively and consist of the load data plotted against the continuous deflection data obtained from a single wire potentiometer placed at the load point. A single wire potentiometer was used for the trial beam test due to data acquisition equipment constraints, but a pair of wire potentiometers on either side of the beam at the loading point were used for all the experimental development length tests. The gray and black diamond and triangle markers represent the manual deflection measurements taken with a laser level and scale with 1/16 in. graduations at each discrete load increment, with the purpose of verifying the wire potentiometer results. The gray and black dashed lines plotted on the

secondary horizontal axis represent the slip measurements on each strand for the dead end beam test. The live end beam test resulted in no measured strand slip, so that data is omitted for clarity.

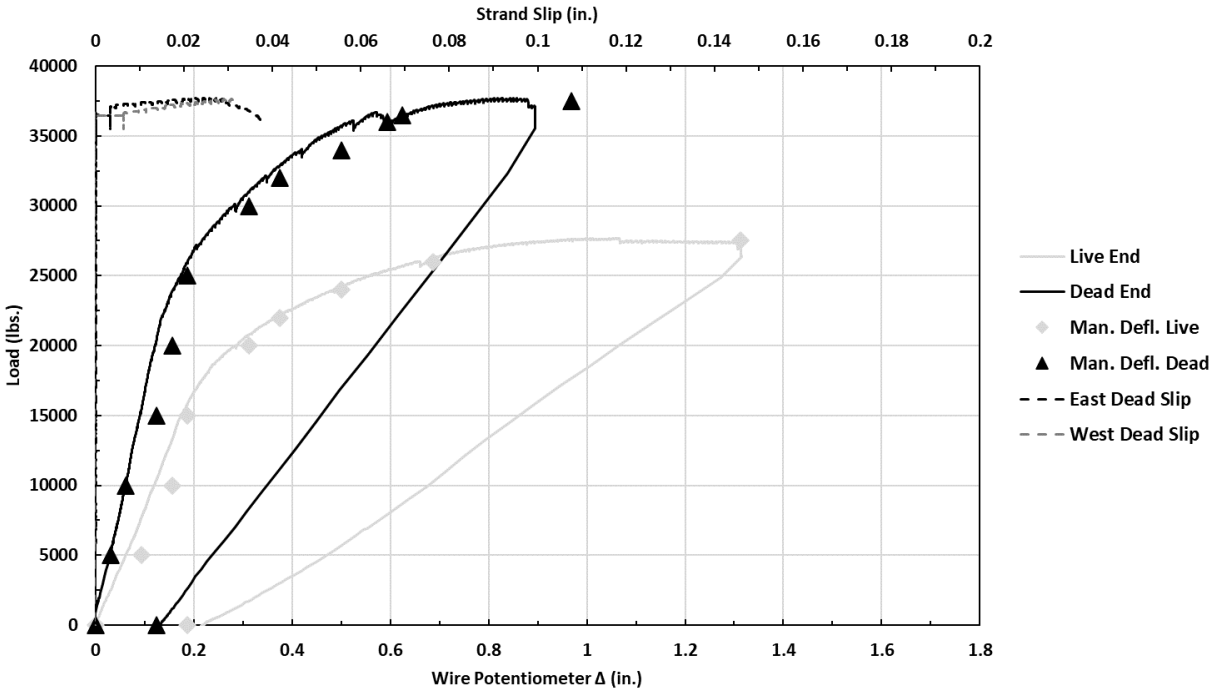

Figure 103: Trial beam B2 load-deflection and load-slip response (3 ft - 4 in. dead end embedment and 6 ft - 9 in. live end embedment)

Figure 103 shows that beam B2 demonstrated a flexural failure on both the live and dead ends. This conclusion is supported by the following observations:

- The live and dead end load tests reached peak loads of 27.7 and 37.7 kips respectively, equivalent to moments of 74.8 and 76.6 kip-ft. Both exceeded the theoretical moment capacity of 69 k-ft.
- The load-deflection curves experience an extended plateau at failure, a classical property of a flexural failure usually caused by yielding of tension steel. The dead end plateau is shorter because the test was stopped sooner than the live end test.

- Zero strand slip was measured for either strand on the live end. A few hundredths of an inch of slip occurred on each strand for the dead end test at near the maximum load, but after the theoretical moment capacity had been exceeded.

The beam failures were dominated by flexural cracking and crushing of the concrete in compression. Even though strand slip occurred on the dead end test, some compression block crushing was still achieved, as shown in Figure 104. Since the compression block damage occurred at a moment greater than the theoretical nominal moment capacity, it is unlikely that bond slip greatly influenced the failure mode.



Figure 104: Trial beam B2 dead end after failure showing flexural cracking and top crushing



Figure 105: Trial beam B2 live end after failure showing flexural cracking and top crushing

4.3.2.2 B9 – 6 ft Embedment

Beam B9-3DV was tested on March 17, 2022 at an age of 27 days with a strand embedment length of 6 ft, which was chosen as the longest strand embedment for testing corresponding to around 80% of the development length predicted by ACI 318-14 (see Equation 4, Chapter 2). The average concrete compressive strength at the time of testing was 12.4 ksi.

Figure 106 shows the load-deflection response of Beam B9-3DV. The gray and black traces represent the individual tests on the live and dead ends respectively and consist of the load data plotted against the continuous deflection data obtained by averaging the results of the two wire potentiometers placed at the load point. The gray and black diamond and triangle markers represent the manual deflection measurements taken with a laser level and scale with 1/16 in. graduations at each discrete load increment, with the purpose of verifying the wire potentiometer results. The gray and black dashed lines which are used to represent the slip measurements on

the secondary horizontal axis are omitted for clarity since no slip was measured on either beam end test for B9-3DV. It is also worth noting that the manual deflection measurements tracked closely with the load-deflection curves from the automated data collection, indicating that the data acquisition was reliable.

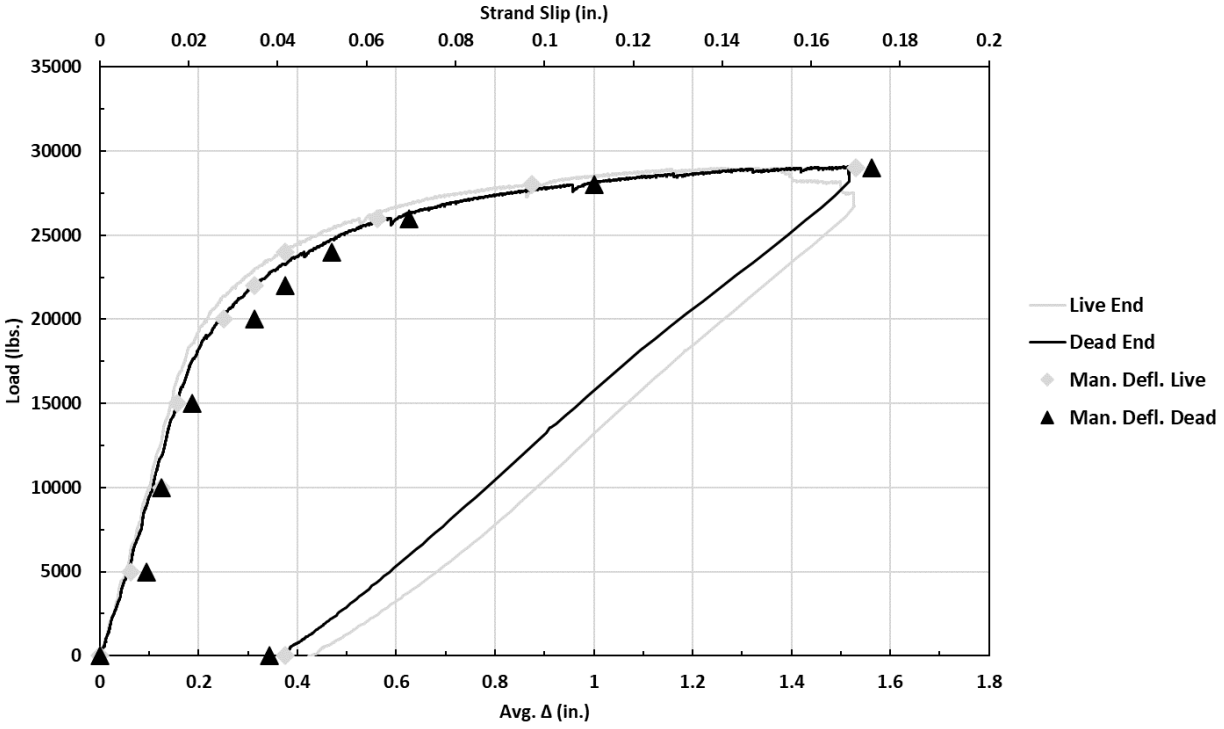

Figure 106: Beam B9-3DV load-deflection and load-slip response (6 ft embedment)

Figure 106 shows that at a 6 ft embedment, beam B9-3DV demonstrated a fully developed flexural failure. This conclusion is supported by the following observations:

- The load tests of the live and dead ends reached peak loads of 29.0 and 29.1 kips respectively, equivalent to moments of 79.6 and 79.8 kip-ft. Both exceeded the theoretical moment capacity of 69 kip-ft.
- The load-deflection curves experience an extended plateau at failure, a classical property of a flexural failure usually caused by yielding of tension steel.

- Zero strand slip was measured for both strands on both beam ends.

The beam failure was dominated by flexural cracking and compression block crushing as observed during testing and documented with photographs, some of which are shown in Figures 107 and 108. The first flexural cracks were visually observed at the 20 kip load increment, which is also apparent from Figure 106, where the shape of the load-deflection curve bends significantly and the behavior of the beam shifted from linear-elastic to a strongly non-linear response with permanent deformation. Additional flexural cracks developed and spread over the course of the test, corresponding with the continued non-linearity of the load-deflection curve. Figure 107 shows the mapped crack pattern at failure with the load increments marked on the cracks as they appeared on the dead end of beam B9-3DV, which was representative of both tests on this beam. In Figure 107 and subsequently, the crack pattern is only shown for one beam end when the failure modes were visually indistinguishable.

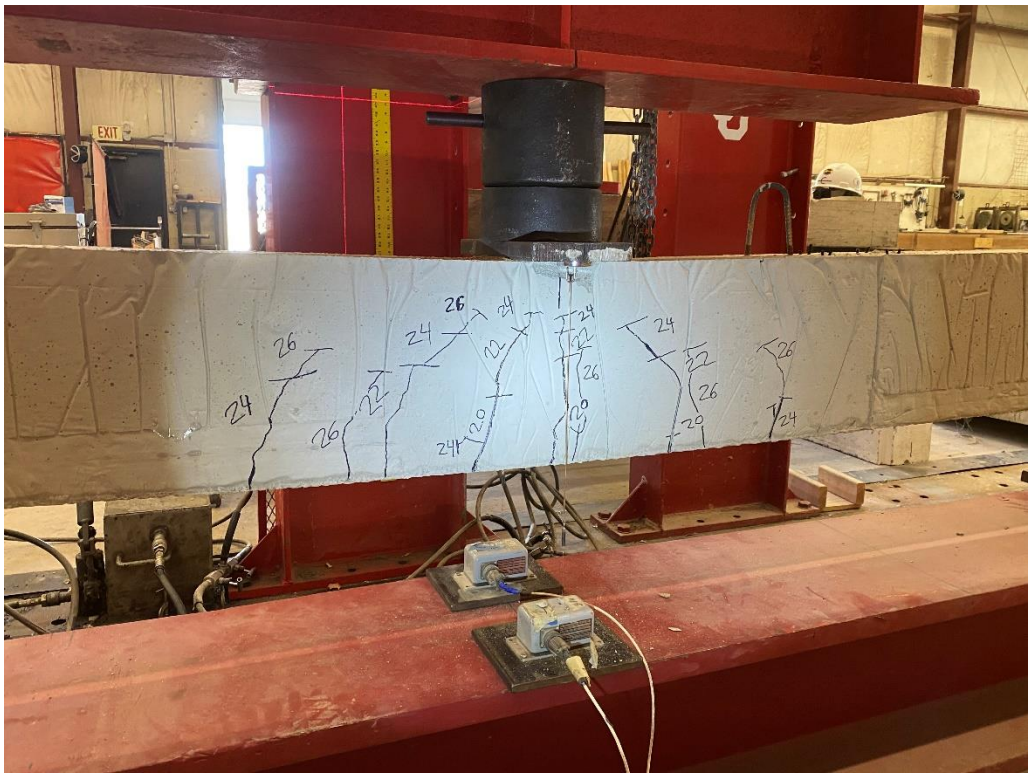

Figure 107: Cracking pattern at failure for B9-3DV with 6 ft embedment (dead end)

Figure 107 shows that the crack patterns were dominated by flexural cracking, running vertically from the bottom of the beam upwards towards the load point. In addition, crushing in the compression block is visible underneath the load plate. Figure 108 shows a view from the other side of the beam after the beam was removed from the load frame which better illustrates the compression block crushing.



Figure 108: Compression block crushing and flexural cracking in beam B9-3DV

It can be concluded from the physical observations of the failure mode for both ends of beam B9-3DV in Figures 107 and 108, along with the load-deflection data and absence of strand slip, that the strand was fully developed at an embedment of 6 ft or 80% of ACI 318 development length.

4.3.2.3 B6 – 4 ft Embedment

Beam B6-3DV was tested on March 7 and 8, 2022 at an age of 28-29 days with a strand embedment length of 4 ft, or around 53% of the ACI 318 development length. The live end was tested on March 7 (28 days) and the dead end was tested on March 8 (29 days). The average concrete compressive strength on March 7 was 11.8 ksi and on March 8 was 12.1 ksi; since the tests were performed within 20 hours of each other, it would be appropriate to take these tests as a group for an overall average concrete compressive strength of 12 ksi.

Figure 109 shows the load-deflection response of Beam B6-3DV. The gray and black traces represent the individual tests on the live and dead ends respectively, and consist of data from the automated data acquisition, while the gray and black diamond and triangle markers represent the manual deflection measurements. The gray and black dashed lines which are used to represent the slip measurements on the secondary horizontal axis are omitted for clarity since no slip was measured on either beam end test for B6-3DV. Again, the manual deflection measurements tracked closely with the load-deflection curves from the automated data collection, indicating that the data acquisition was reliable.

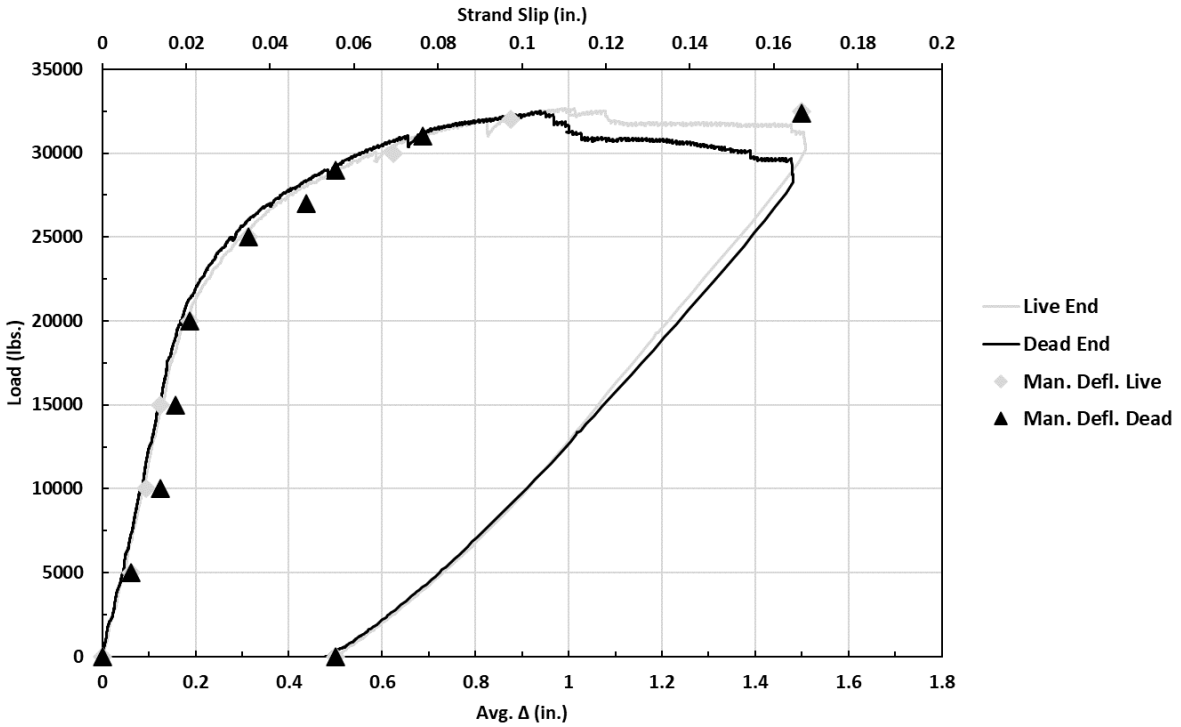

Figure 109: Beam B6-3DV load-deflection and load-slip response (4 ft embedment)

Figure 109 shows that at a 4 ft embedment, beam B6-3DV demonstrated a fully developed flexural failure. This conclusion is supported by the following observations:

- The live and dead ends reached peak loads of 32.7 and 32.5 kips respectively, equivalent to moments of 80.7 and 80.4 kip-ft. Both exceeded the theoretical moment capacity of 69 kip-ft.
- The load-deflection curves experience an extended plateau at failure.
- Zero strand slip was measured for both strands on both beam ends. The east strand on the dead end started with a 0.0003 in. offset, which did not propagate throughout the test.

The beam failure was dominated by flexural cracking and compression block crushing as observed during testing and documented with photographs, some of which are shown in Figure 110 and 111. The first flexural cracks were visually observed at around 23 kips for the dead end test and around 27 kips for the live end. This range encompasses the portion of the load-deflection curve in Figure 109 which bends where the linear-elastic portion of the behavior ends. Additional flexural cracks developed and spread over the course of the test, corresponding with the continued non-linearity of the load-deflection curve. Figure 110 shows the mapped crack pattern at failure with the load increments marked on the cracks as they appeared on the live end of beam B6-3DV, which was representative of both tests on this beam.

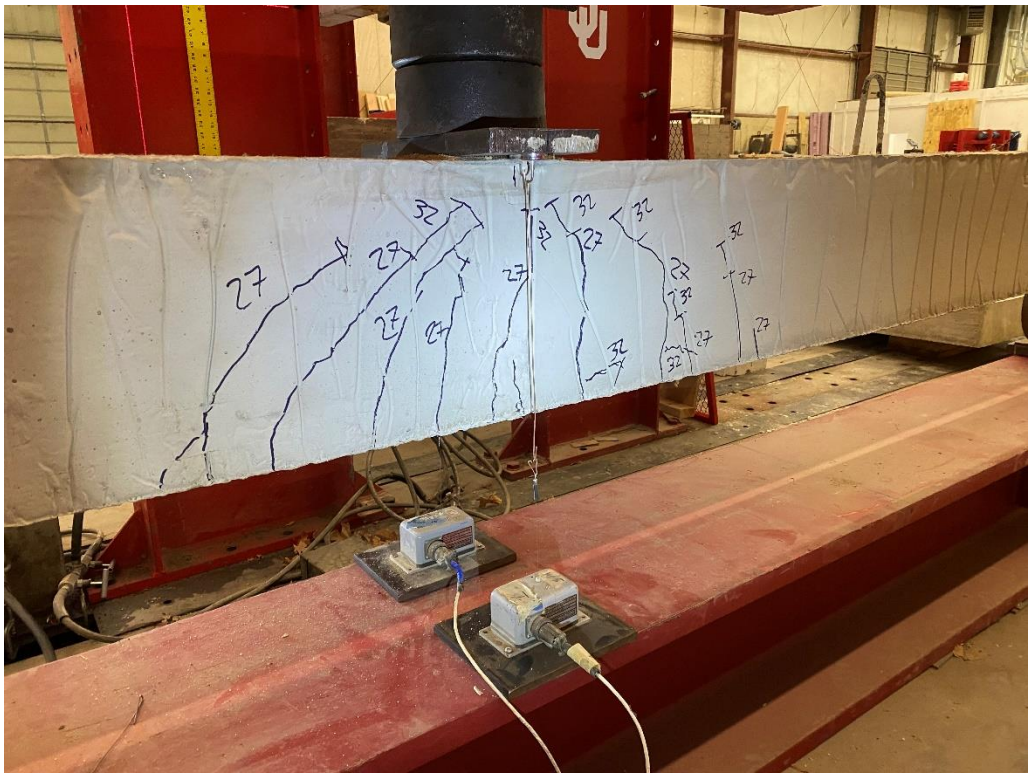

Figure 110: Cracking pattern at failure for B6-3DV with 4 ft embedment (live end)

Figure 110 shows that the crack patterns were dominated by flexural cracking, similarly to beam B9-3DV at the 6 ft embedment. Although crushing is not readily visible in Figure 110, beam B6-3DV did exhibit compression block crushing at both ends, as shown in Figure 111 (dead end is pictured).



Figure 111: Compression block crushing and flexural cracking in beam B6-3DV (dead end)

It can be concluded from the physical observations of the failure mode of beam B6-3DV in Figures 110 and 111 along with the load-deflection data and absence of strand slip that the strand was fully developed at an embedment of 4 ft, or 53% of the ACI 318 development length.

4.3.2.4 B10 – 3.5 ft Embedment

Beam B10-3DV was tested on March 21 and 22, 2022 at an age of 27-28 days with a strand embedment length of 3.5 ft, or around 47% of the ACI 318 development length. The live end was tested on March 21 (27 days) and the dead end was tested on March 22 (28 days). The average concrete compressive strength on March 21 was 11.5 ksi and on March 22 was 10.9 ksi. Since the tests were performed within 20 hours of each other, it would be appropriate to take these tests as a group for an overall average compressive strength of 11.2 ksi.

Figure 112 shows the load-deflection response of beam B10-3DV. As before, this plot displays the load-deflection curves and the manually measured deflection checks for the tests performed on each end of beam B10-3DV. As before, the manual deflection measurements tracked closely with the load-deflection curves from the automated data collection. The strand slip data has been omitted for clarity because there was no meaningful strand slip for either beam end test.

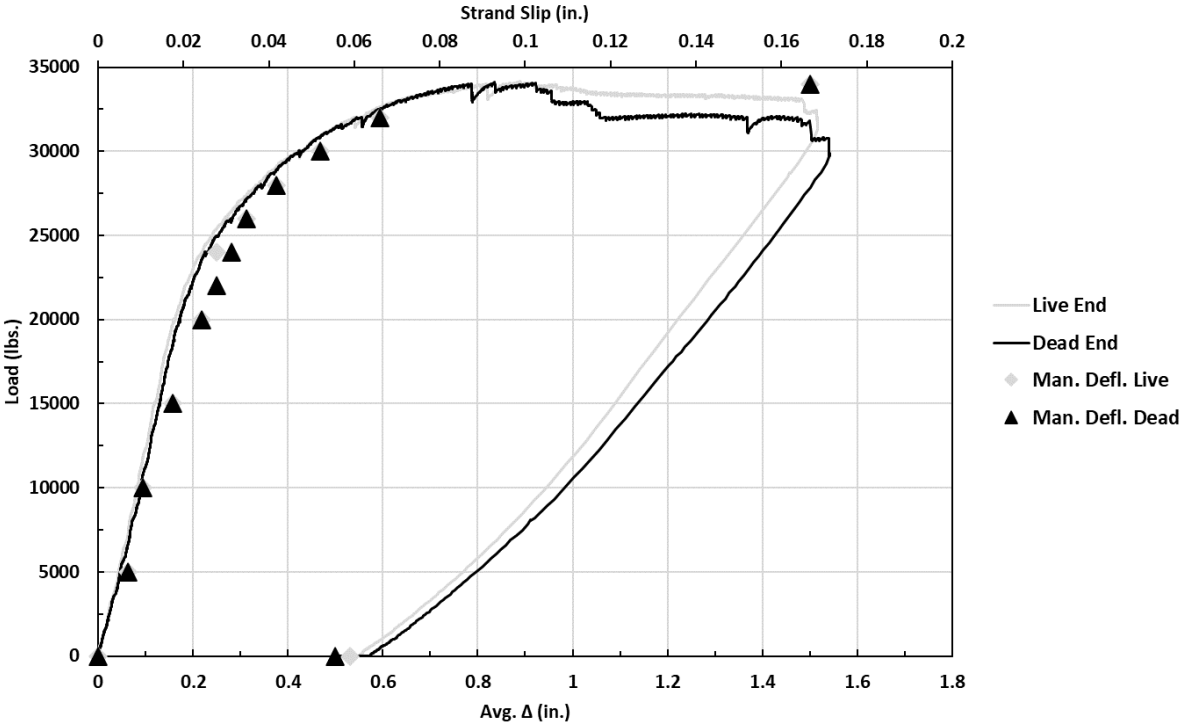

Figure 112: Beam B10-3DV load-deflection and load-slip response (3.5 ft embedment)

Figure 112 shows that at a 3.5 ft embedment, beam B10-3DV demonstrated a fully developed flexural failure. This conclusion is supported by the following observations:

- The tests of both the live and dead ends reached peak loads of 34.1 kips, equivalent to a moment of around 78.1 kip-ft, significantly exceeding the theoretical moment capacity of 69 kip-ft.
- The load-deflection curves exhibit an extended plateau at failure.
- Zero strand slip was measured for both strands on both beam ends. The east strand on the dead end showed a slight perturbation of 0.0002-0.0003 in. at the end of the test, but this was long after peak load was reached and therefore did not influence the failure mode.

The beam failure was dominated by flexural cracking and compression block crushing as observed during the tests and documented with photographs, some of which are shown in Figures 113 and 114. The first flexural cracks were visually observed at around 20 kips for the dead end test and around 24 kips for the live end. This range encompasses the portion of Figure 112, where the load-deflection curve begins to bend and linear-elastic behavior ends. Additional flexural cracks developed and spread over the course of the test, corresponding with the continued non-linearity of the load-deflection curve. Figure 113 shows the mapped crack pattern at failure with the load increments marked on the cracks as they appeared on the dead end of beam B10-3DV, which was representative of both tests on this beam.

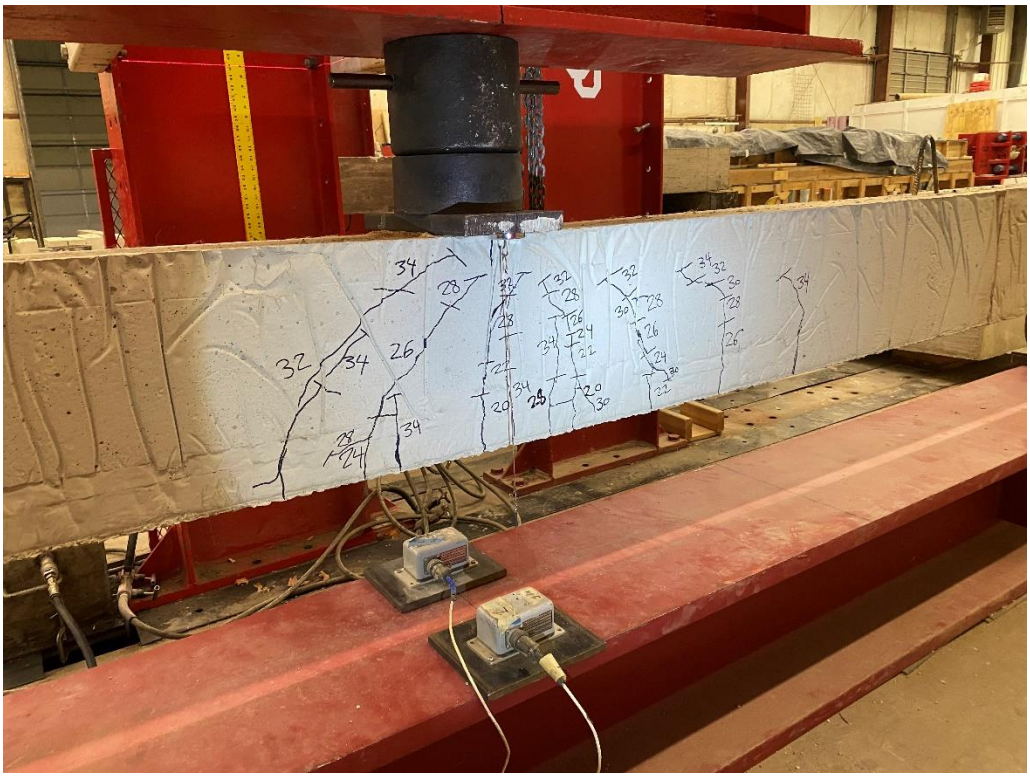

Figure 113: Cracking pattern at failure for B10-3DV with 3.5 ft embedment (dead end)

Figure 113 shows that the crack patterns were dominated by flexural cracking, similarly to beams B9-3DV and B6-3DV at 6 ft and 4 ft embedment lengths respectively. Although crushing is not readily visible in Figure 113, beam B10-3DV did exhibit compression block crushing for the tests at both ends, as shown in Figure 114 (live end is pictured).

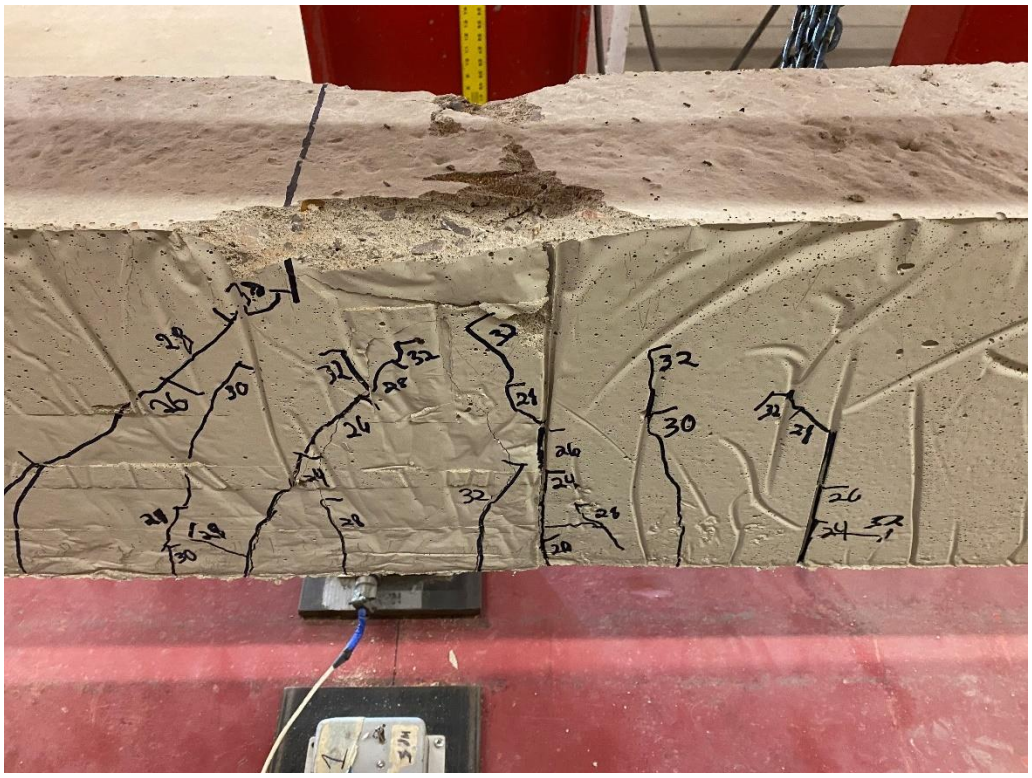

Figure 114: Compression block crushing and flexural cracking in B10-3DV (live end)

It can be concluded from the physical observations of the failure mode of beam B10-3DV in Figures 113 and 114 along with the load-deflection data and absence of strand slip that the strand was fully developed at an embedment of 3.5 ft, or 47% of ACI 318 development length.

4.3.2.5 B7 – 3 ft Embedment

Beam B7-3DV was tested on March 10, 2022 at an age of 27 days with a strand embedment length of 3 ft, around 40% of the ACI 318 development length. The average concrete compressive strength at the time of testing was 11.8 ksi.

Figure 115 shows the load-deflection response of beam B7-3DV. As before, this plot displays the load-deflection curves, the manually measured deflection checks, and the strand slip data for the tests performed on both ends of beam B7-3DV. As before, the manual deflection measurements tracked closely with the load-deflection curves from the automated data

collection. They diverge noticeably at the end of the test, likely because of the violent jolt that occurred when the beam failed.

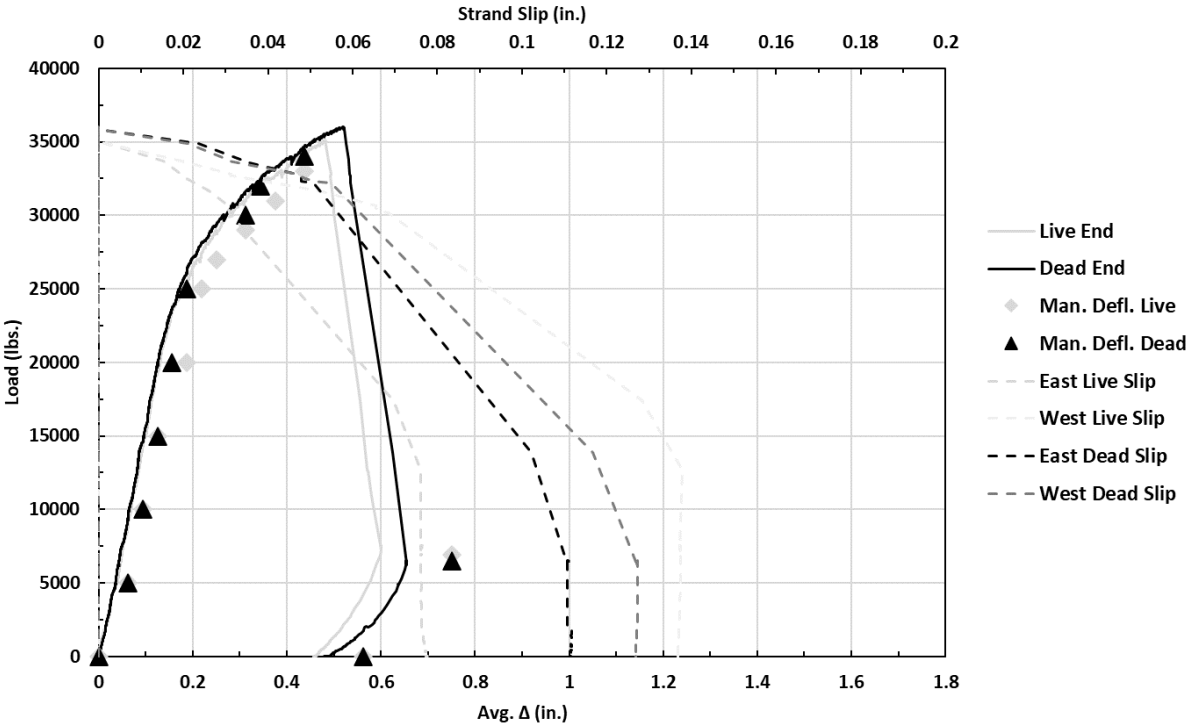

Figure 115: Beam B7-3DV load-deflection and load-slip response (3 ft embedment)

Figure 115 shows that at a 3 ft embedment, beam B7-3DV retained full strand development before experiencing a sudden failure. Direct observation of the cracking at failure made it clear that this sudden failure was due to shear. This conclusion is supported by the following observations:

- The live and dead ends load tests reached peak loads of 35.1 and 36.0 kips respectively, equivalent to moments of 72.4 and 74.3 kip-ft. Both exceeded the theoretical moment capacity of 69 kip-ft.

- The load-deflection curves exhibit a sudden and precipitous drop at failure, a classical property of a brittle shear failure. A small amount of residual load capacity was retained because the top reinforcing bars, strands, and some WWR held the failed beam together.
- Significant strand slip occurred on both strands for both beam end tests, but this strand slip occurred after shear cracking and did not represent a general bond-slip or flexural bond failure. As Figure 115 shows, the strands remained anchored and did not slip prior to the sudden failure. Instead, both strands slipped significantly when the large shear cracks that occurred at both ends disrupted the transfer zone and caused the strands to lose anchorage.

The beam ends experienced flexural cracking but failure was clearly controlled by a sudden and significant shear failure as shown in Figures 116 and 117. The first flexural cracks were visually observed at around 25 kips of load for the live end test and around 28 kips for the dead end. This range encompasses the portion of Figure 115 where the load-deflection curve begins to bend and the linear-elastic behavior ends. More flexural cracks gradually appeared as the test proceeded, correlating with the continued non-linearity of the load-deflection curve. When the large shear cracks suddenly occurred, however, the flexural cracks ceased propagating. Figure 116 shows the mapped crack pattern for beam B7-3DV with the load increments marked on the cracks as they appeared. The load increment at cracking was not marked on the shear rupture in Figure 116 for safety since the load was still in place; it was later marked once load had been fully removed.



Figure 116: Cracking pattern at failure for B7-3DV with 3 ft embedment (dead end)

Figure 117 shows a comparison of the crack pattern for the dead end and the live end of beam B7-3DV after it was removed from the load frame with the load increments marked on the cracks as they appeared.



Figure 117: Comparison of cracking pattern at failure for B7-3DV with 3 ft embedment - live end (top) and dead end (bottom)

Both ends of the beam ends seemed to reach the full compound shear strength. Instead of simply cracking the concrete by exceeding its shear strength, the shear failures also exceeded the tension strength of the WWR bridging the crack openings. On both beam ends, the crack openings were large enough that two failure modes of the WWR could be observed: tensile rupture of the gross cross section of the wire and a shearing type failure of the welded junction of a cell. Figure 118 shows a comparison of these two WWR shear failure modes.



Figure 118: WWR failure modes from beam shear - welded junction failure (left) and rupture of gross section (right)

It can be concluded from the physical observations of the failure mode of beam B7-3DV in Figures 116, 117, and 118 along with the load-deflection data that this specimen exhibited a brittle shear failure with some flexural cracking early in the test. However, the failure moment still exceeded the theoretical flexural strength of the member and the strands remained anchored until the shear crack penetrated the transfer zone. So, although the shear failure makes it more difficult to speculate about the degree to which the strands were developed at the embedment length of 3 ft, the failure was clearly not precipitated by general loss of flexural bond. At the very least, it can be said that the strands were fully developed (as evidenced by developing the full nominal moment capacity of the prestressed beam) in 3 ft of embedment length prior to experiencing disruption due to shear failure of the beam.

4.3.2.6 B8 – 2.5 ft Embedment

Beam B8-3DV was tested on March 15, 2022 at an age of 28 days with a strand embedment length of 2.5 ft, which was chosen as the shortest strand embedment for consideration at around 33% of the ACI 318 development length. At an embedment length of 2.5 ft, the a/d ratio for beam B8-3DV was equal to 3, meaning that beam B8-3DV was more likely than previous specimens to fail in shear. A review of the literature by Naji showed that an a/d ratio of 3.0 is the critical value below which bond shear failures become widespread (Naji et al., 2017). The average concrete compressive strength at the time of testing was 11.9 ksi.

Figure 119 shows the load-deflection response for both tests of beam B8-3DV. As before, this plot displays the load-deflection curves, the manually measured deflection checks, and the strand slip data for the tests performed on both ends of beam B8-3DV. The manual deflection measurements did not track as closely with the load-deflection curves from the automated data collection compared to the previous beam tests. They diverge noticeably throughout the test, likely for two reasons. First, the observed sudden shear failures are inherently more sudden and unpredictable, hence the failure loads and load-deflection curves being more variable than for other beams. Second, with the load placed so close to the beam end, the structural response was very stiff, meaning the deflections for each load increment were much smaller than for tests of other beams. The manual deflection measurements were read off of a 1/16 in. scale which made it difficult to accurately measure the small deflections experienced in this testing configuration.

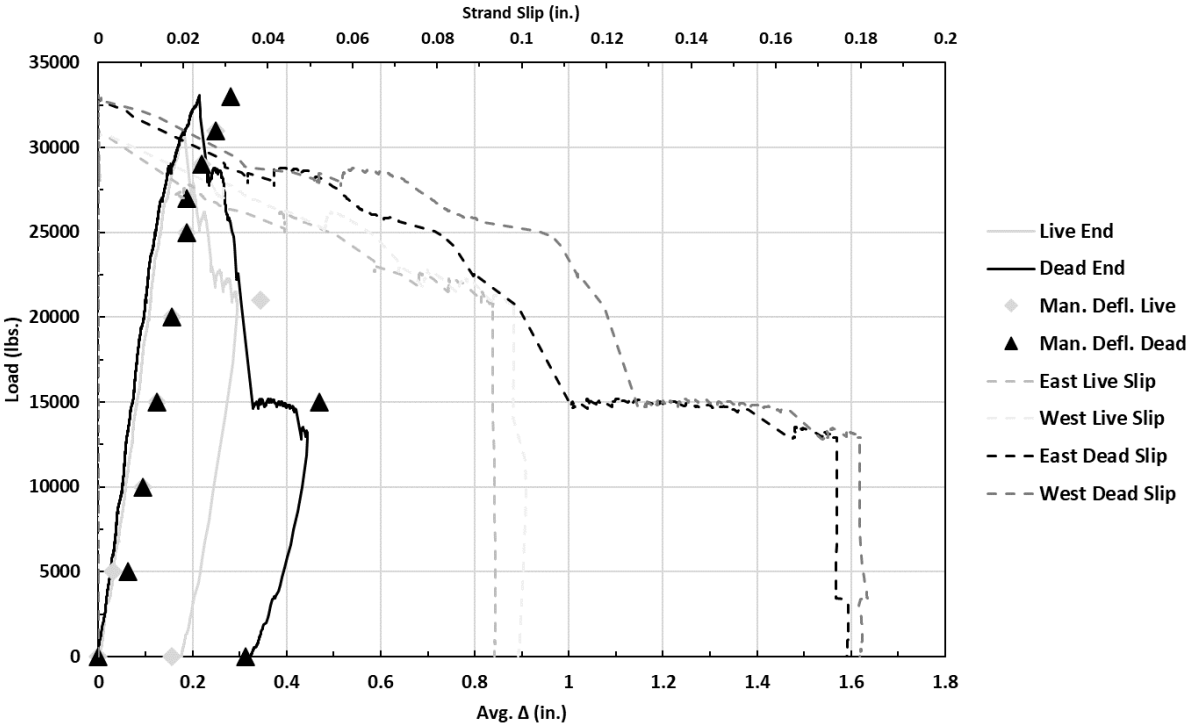

Figure 119: Beam B8-3DV load-deflection and load-slip response (2.5 ft embedment)

The data in Figure 119 shows that at a 2.5 ft embedment, beam B8-3DV experienced a more gradual failure than beam B7-3DV, but it was still abrupt and occurred at a capacity lower than the full flexural strength of the member. Direct observation of the beam during testing showed that this failure was clearly due to shear. The degree of strand development is unclear in this case because the strands still did not slip until the shear failure had initiated. This conclusion is supported by the following observations:

- The live and dead end load tests reached peak loads of 31.0 and 33.1 kips respectively, equivalent to moments of 55.5 and 59.2 kip-ft. Neither reached the theoretical moment capacity of 69 kip-ft.
- The load-deflection curves experience a sudden drop at failure, a classical property of a shear failure. More residual load was retained compared to beam

B7-3DV, however, because the failure was more gradual. Instead of a violent, sudden rupture, the shear cracks propagated more gradually with steadily increasing deflections.

- Significant strand slip occurred on both strands for both beam end tests, but this strand slip did not represent a general bond-slip or flexural bond failure. As Figure 119 shows, the strands remained anchored and did not slip prior to failure. Instead, both strands began to slip when shear cracks entered the transfer zone, and strand slip propagated as the cracks grew and the beam deflected.

The beam ends experienced some flexural cracking, but failure was overwhelmingly controlled by shear cracking as shown in Figures 120 and 121. The first flexural cracks were visually observed at around 29 kips of load for the live end test, which was only one load increment prior to the appearance of significant shear cracks at around 31 kips. For the dead end test, a small flexural crack was observed under the load point at between 23 and 24 kips, but significant shear cracks appeared at around 33 kips. The flexural cracks occurred at loads close enough to the point of shear failure that there is not a significant non-linear portion in the load-deflection curves shown in Figure 119. Instead, the shear failures appear to have occurred during or immediately after the end of the linear elastic range. Figure 120 shows the mapped crack pattern at failure for the live end of beam B8-3DV with the load increments marked on the cracks as they appeared. The dead end failure mode was consistent with the live end.



Figure 120: Cracking pattern at failure for B8-3DV with 2.5 ft embedment (live end)

The cracking pattern of beam B8-3DV at failure in Figure 120 exhibits several important differences from beam B7-3DV. First, the flexural cracking for beam B8-3DV was clearly far less extensive than for beam B7-3DV, or any of the other beam failures. Second, instead of one single significant shear crack like that observed for beam B7-3DV, both ends of the beam B8-3DV load test exhibited at least two or more relatively smaller shear cracks. This is likely because in the load test of beam B7-3DV, the beam was elastic enough to experience more deflection before shear failure occurred, thus storing up significant potential energy that was released suddenly when the shear capacity was reached. This sudden energy release resulted in a brittle, explosive failure mode. For beam B8-3DV, however, shear stress accumulated more quickly since the point load was so near to the beam end. Relatively speaking, the shear capacity was reached sooner, before as much energy had been stored up, and the resulting failure was

more gradual. Although it is conceivable that some of the WWR in beam B8-3DV may have failed in similar ways to those observed in beam B7-3DV, it is uncertain. This is because shear cracks in beam B8-3DV did not open wide enough to expose the reinforcement. It is also unlikely, because it was probably only because the WWR was broken in beam B7-3DV that the cracks opened wide enough for the reinforcement to be directly observed. Conversely, it could also be rationalized that wider cracks in beam B7-3DV led to enough strain accumulation to break the WWR.

A final observation concerning the failure mode of beam B8-3DV is the vertical and diagonal cracking shown in Figure 121 near the location of the roller support. The damage pattern shown in Figure 121 may indicate that the shear failure of beam B8-3DV was also compounded with a bearing failure caused by the large, concentrated force close to the beam end and support location.

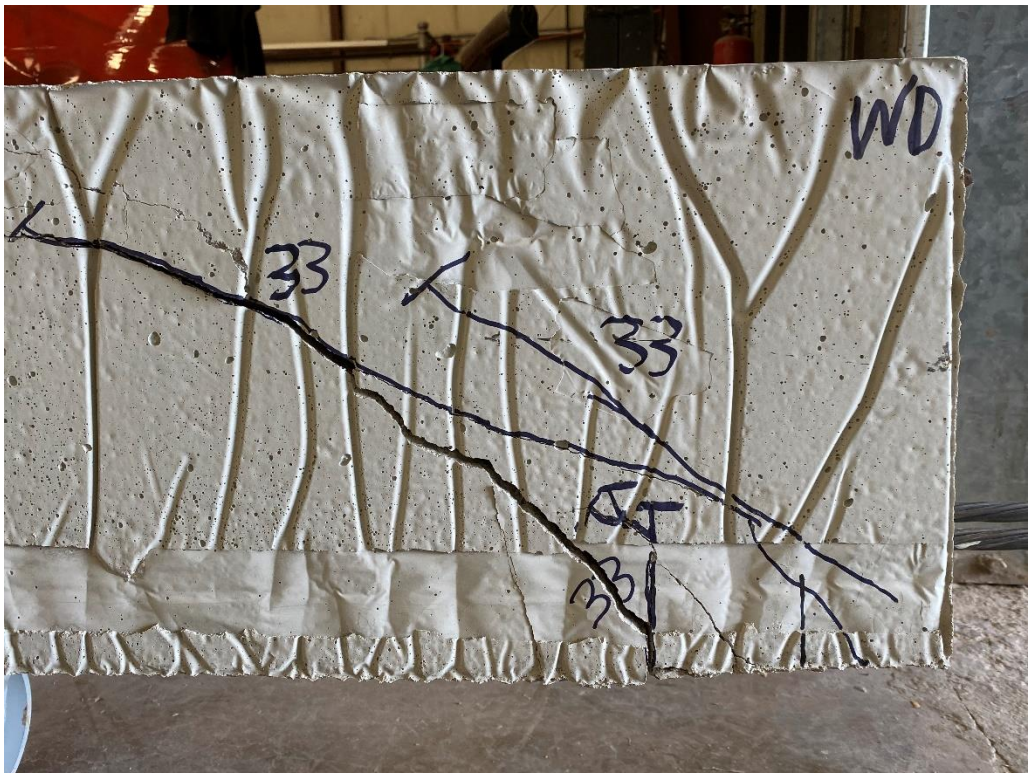

Figure 121: Vertical and diagonal cracking near support location in beam B8-3DV (dead end)

4.3.3 Results – Standard (24 hr) Prestress Release

This section summarizes the results of the load testing for each beam constructed with a typical age prestress release, which varied between about 24 hr and 24.5 hr (see Section 4.2.4). After the results from each load test are summarized, the resulting development length data is synthesized in Section 4.3.4.

4.3.3.1 B16 – 6 ft Embedment

Beam B16-24DV was tested on April 21, 2022 at an age of 28 days with a strand embedment length of 6 ft, or 80% of the development length predicted by ACI 318-14, to match the early release beam testing. The average concrete compressive strength at the time of testing was 11.3 ksi.

Figure 122 shows the load-deflection response of beam B16-24DV. As before, this plot displays the load-deflection curves and the manually measured deflection checks for the tests

performed on both ends of beam B16-24DV. The gray and black dashed lines which are used to represent the slip measurements on the secondary horizontal axis are omitted for clarity since no slip was measured on either beam end test for B16-24DV. As was typical for the other beams that experienced flexural failures, the manual deflection measurements tracked closely with the load-deflection curves from the automated data collection.

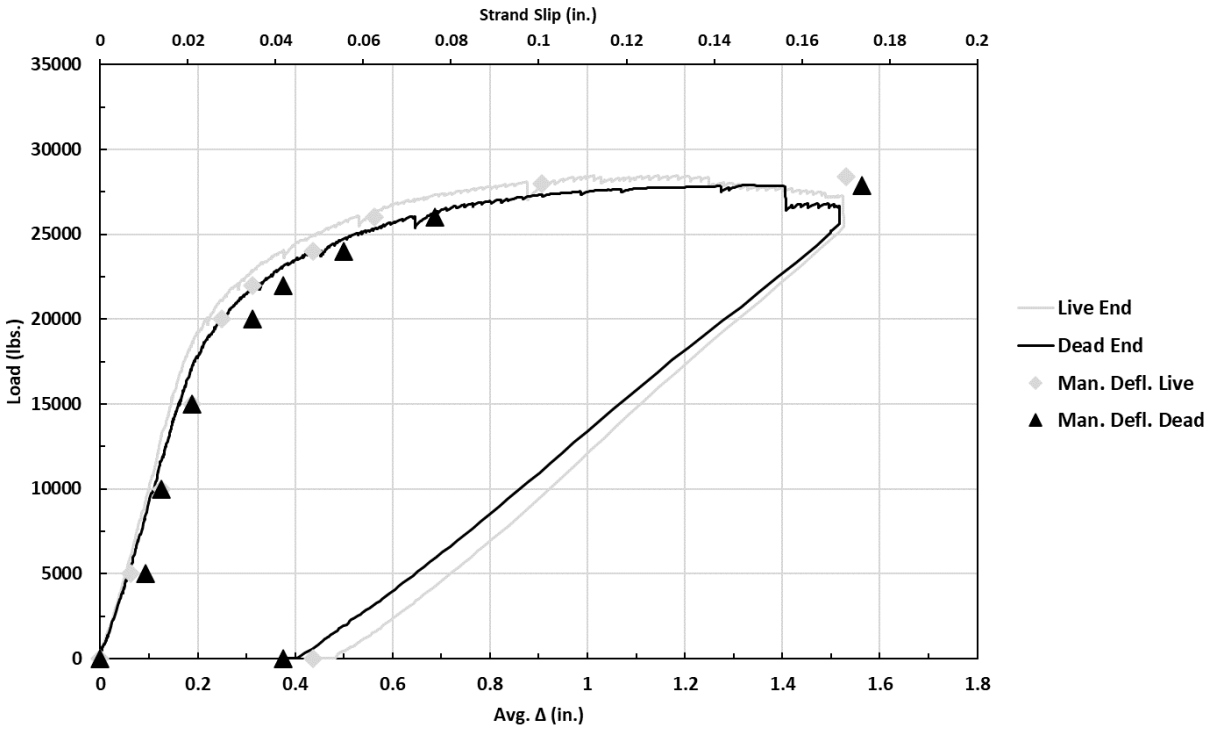

Figure 122: Beam B16-24DV load-deflection and load-slip response (6 ft embedment)

Figure 122 shows that at a 6 ft embedment, beam B16-24DV demonstrated a fully developed flexural failure. This conclusion is supported by the following observations:

- The live and dead end load tests reached peak loads of 28.5 and 27.9 kips respectively, equivalent to moments of 78.1 and 76.6 kip-ft. Both exceeded the theoretical moment capacity of 69 kip-ft.

- The load-deflection curves experience an extended plateau at failure, a classical property of a flexural failure usually caused by yielding of tension steel.
- Zero strand slip was measured for both strands on both beam ends.

The beam failure was dominated by flexural cracking and compression block crushing as observed during testing and documented with photographs, some of which are shown in Figures 123 and 124. The first flexural cracks were visually observed at the 20 kip load increment for both the live end and dead end tests. The 20 kip load increment was also when flexural cracking was first observed on both ends of B9-3DV, which was the early (3 hr) release beam tested at a 6 ft embedment. Figure 122 corroborates first cracking at around 20 kips for beam B16-24DV, as the shape of the load-deflection curve bent significantly after 20 kips and the behavior of the beam shifted from linear-elastic to a non-linear response with permanent deformation. Additional flexural cracks developed and spread over the course of the test, corresponding with the continued non-linearity of the load-deflection curve. Figure 123 shows the progression of the mapped crack pattern with the load increments marked on the cracks as they appeared throughout the test on the dead end of beam B16-24DV, which was representative of both tests on this beam.

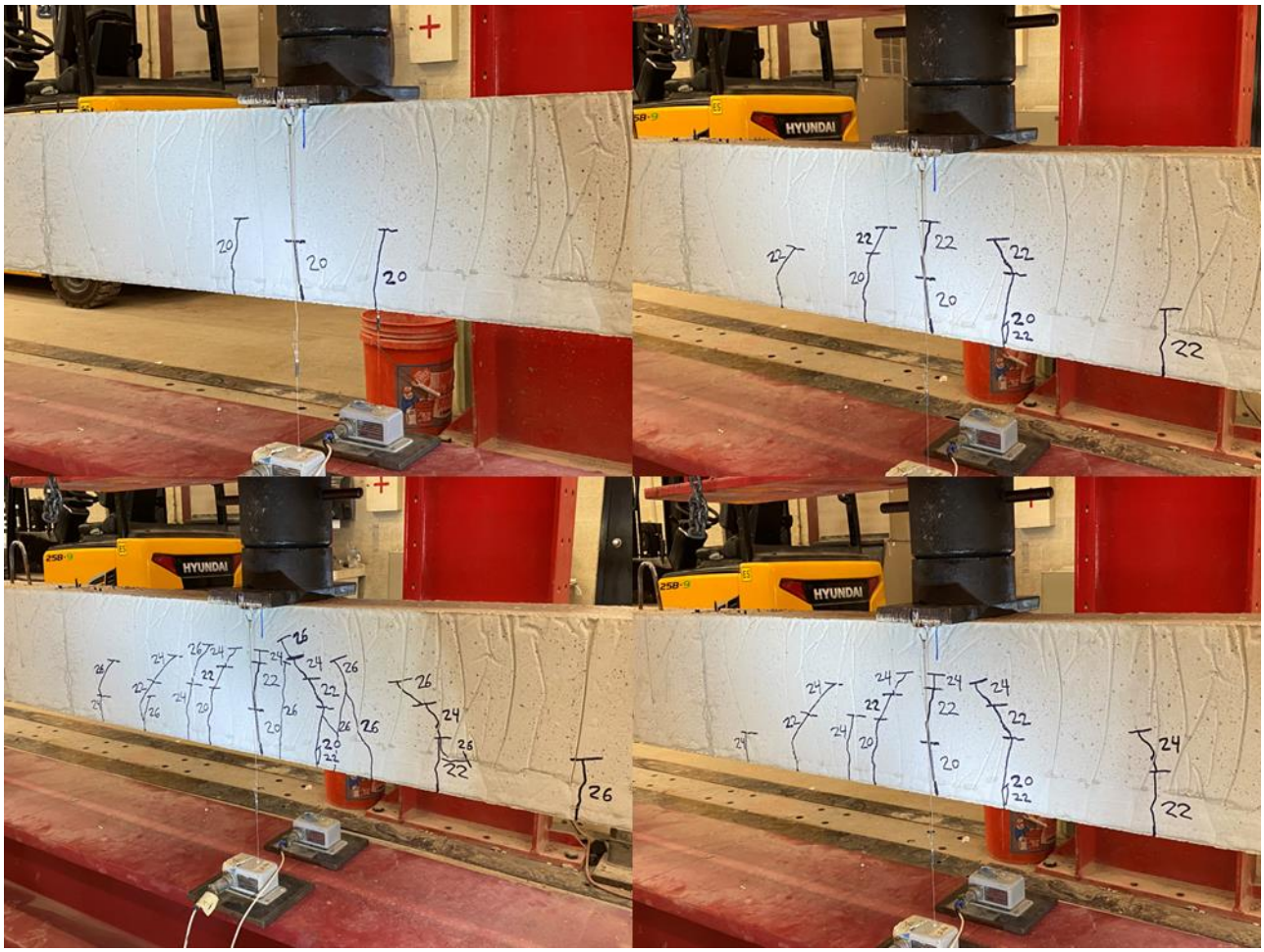

Figure 123: Cracking pattern at failure for B16-24DV with 6' embedment (with crack progression through the test, clockwise from top left – dead end)

Figure 123 shows that the dead end crack patterns were dominated by flexural cracking, running vertically from the bottom of the beam upwards towards the load point. Figure 124 shows a view of the compression block crushing observed at failure on the dead end from the other side of the beam once the loading apparatus was removed from the load frame. The live end of B16-24DV experienced very similar flexural cracking patterns and compression block crushing damage.

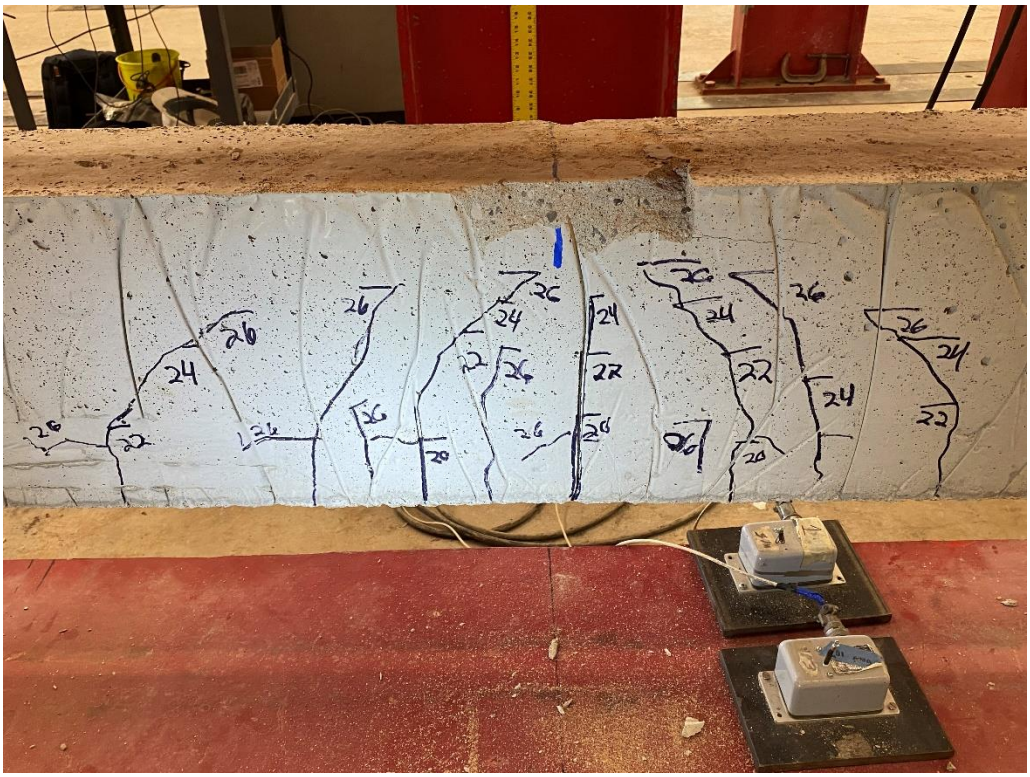

Figure 124: Compression block crushing and flexural cracking in B16-24DV (dead end)

It can be concluded from the physical observations of the failure mode of Beam B16-24DV in Figures 123 and 124 along with the load-deflection data and absence of strand slip that the strand was fully developed at an embedment of 6 ft or 80% of the ACI 318 development length.

4.3.3.2 B15 – 4 ft Embedment

Beam B15-24DV was tested on April 19, 2022 at an age of 28 days with a strand embedment length of 4 ft, or 53% of the development length predicted by ACI 318-14, to match the early (3 hr) release beam testing. The average concrete compressive strength at the time of testing was 10.8 ksi.

Figure 125 shows the load-deflection response of Beam B15-24DV. As before, this plot displays the load-deflection curves, the manually measured deflection checks, and the strand slip

data for the tests performed on both ends of beam B15-24DV. As was typical for the beams that experienced flexural failures, the manual deflection measurements tracked closely with the load-deflection curves from the automated data collection.

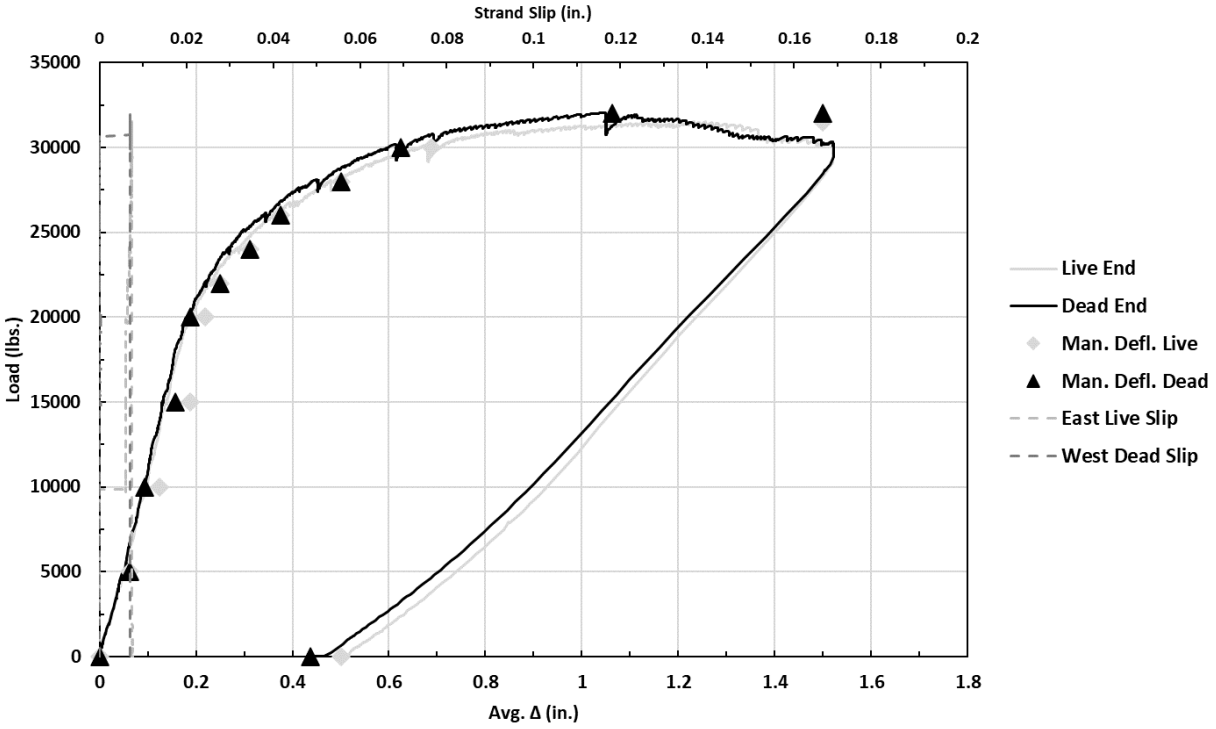

Figure 125: Beam B15-24DV load-deflection and load-slip response (4 ft embedment)

Figure 125 shows that at a 4 ft embedment, beam B15-24DV demonstrated a fully developed flexural failure. This conclusion is supported by the following observations:

- The live and dead end tests reached peak loads of 31.5 and 32.0 kips respectively, equivalent to moments of 77.9 and 79.2 kip-ft. Both exceeded the theoretical moment capacity of 69 kip-ft.
- The load-deflection curves experience an extended plateau at failure.

- Strand slip was measured for the east strand on the live end test at a load of around 10 kips and for the west strand on the dead end test at around 31 kips, and both occurrences were accompanied by audible popping sounds. Both strands slipped to around 0.007 in. but their movement was arrested before peak load or the yield plateau was reached.

The beam failure was dominated by flexural cracking and compression block crushing as observed during testing and documented with photographs, some of which are shown in Figures 126 and 127. The first flexural cracks were visually observed at the 20 kip load increment for both the live end and dead end tests. This was a lower cracking load than that which was observed for the early (3 hr) release 4 ft embedment test (B6-3DV) which had a cracking load between 23 and 27 kips. The decreased cracking load may be related to the early strand movement observed for beam B15-24DV which did not occur for beam B6-3DV. Both the early slip and the reduced cracking load for beam B15-24DV may trace back to a lower compressive strength compared to beam B6-3DV (10.8 ksi versus 12 ksi). The visually observed 20 kip cracking load for beam B15-24DV matches the change in slope of the load-deflection curves in Figure 125. Additional flexural cracks developed and spread over the course of the test, corresponding with the continued non-linearity of the load-deflection curve. Figure 126 shows the mapped crack pattern resulting from this behavior with the load increments marked on the cracks as they appeared.



Figure 126: Cracking pattern at failure for B15-24DV with 4 ft embedment (live end)

Figure 126 shows that the crack patterns for B15-24DV were dominated by flexural cracking, similarly to beam B6-3DV, tested at a 4 ft embedment. Compression block crushing damage is visible in Figure 126 along the top corner of the beam, directly above the location of the wire potentiometers at the load point location. Figure 127 shows a close-up view of the compression block crushing damage on the dead end of the beam, from the opposite side of the beam relative to Figure 126.

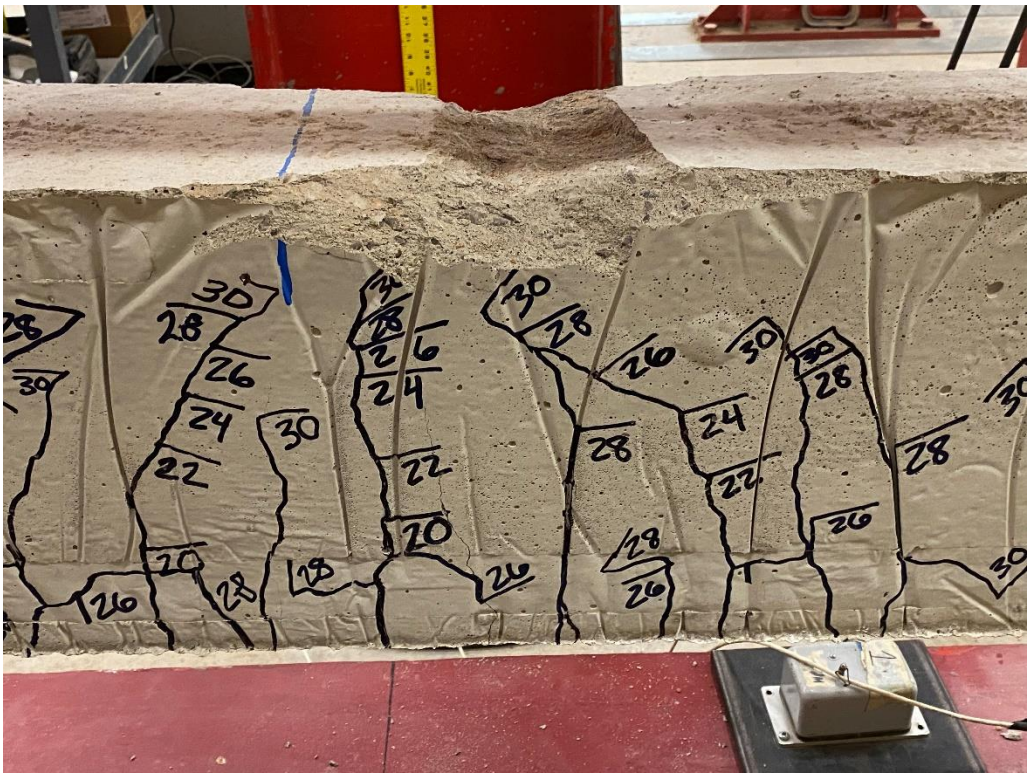

Figure 127: Compression block crushing and flexural cracking in B15-24DV (dead end)

It can be concluded from the physical observations of the failure mode of Beam B15-24DV in Figures 126 and 127 along with the load-deflection data and the nature of the strand slip measurements that the strand was fully developed at an embedment of 4 ft or 53% of the ACI 318 development length.

4.3.3.3 B12 – 3.5 ft Embedment

Beam B12-24DV was tested on April 5, 2022 at an age of 27 days with a strand embedment length of 3.5 ft, or 47% of the development length predicted by ACI 318-14, to match the early (3 hr) release beam testing. The average concrete compressive strength at the time of testing was 10.5 ksi.

Figure 128 shows the load-deflection response of Beam B12-24DV. As before, this plot displays the load-deflection curves, the manually measured deflection checks, and the strand slip

data for the load tests performed on both ends of beam B12-24DV. As was typical for the beams that experienced flexural failures, the manual deflection measurements generally tracked closely with the load-deflection curves from the automated data collection, although they diverged slightly for the live end test and at the maximum beam deflection for beam B12-24DV.

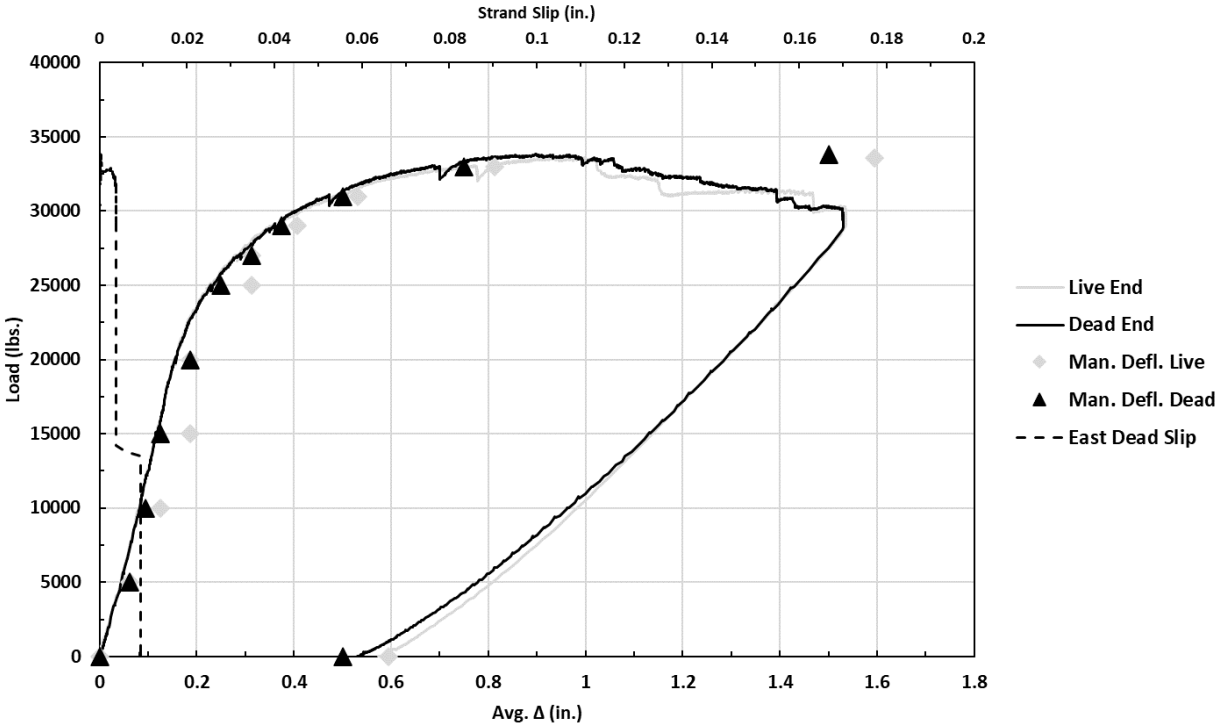

Figure 128: Beam B12-24DV load-deflection and load-slip response (3.5 ft embedment)

Figure 128 shows that at a 3.5 ft embedment, beam B12-24DV demonstrated a fully developed flexural failure. This conclusion is supported by the following observations:

- The live and dead end tests reached peak loads of 33.6 and 33.8 kips respectively, equivalent to moments of 77.0 and 77.5 kip-ft. Both exceeded the theoretical moment capacity of 69 kip-ft.
- The load-deflection curves experience an extended plateau at failure.

- Strand slip was only measured for the east strand on the dead end test at a load of around 32.7 kips. The west strand on the dead end experienced a perturbation at around the same load, possibly because the LVDT was jostled by the east strand popping. No slip propagated for the dead end west strand. The dead end east strand slipped to almost 0.004 in., but the slip ceased propagation towards the end of the yield plateau. This magnitude of slip is less than that usually considered to constitute general bond slip.

The beam failure was dominated by flexural cracking and compression block crushing as observed during testing and documented with photographs, some of which are shown in Figures 129 and 130. The first flexural cracks were visually observed at the 20 kip load increment for both the live end and dead end tests. These first cracks were very narrow and short, extending only 1 – 2 in. vertically from the bottom of the beam. The flexural cracking propagated more significantly between the 20 and 25 kip load increments for the tests of both ends. These observed cracking loads were around the same range of cracking loads observed for the early (3 hr) release 3.5 ft embedment tests (B10-3DV) which had cracking loads between 20 and 24 kips. The 20-25 kip cracking load for beam B12-24DV matches the change in slope of the load-deflection curves in Figure 128. Additional flexural cracks developed and spread over the course of the test, corresponding with the continued non-linearity of the load-deflection curve. Figure 129 shows the mapped crack pattern at failure with the load increments marked on the cracks as they appeared on the dead end of beam B12-24DV, which was representative of both tests on this beam.



Figure 129: Cracking pattern at failure for B12-24DV with 3.5 ft embedment (dead end)

Figure 129 shows that the dead end crack patterns were dominated by flexural cracking, similarly to beam B10-3DV tested at a 3.5 ft embedment (early 3 hr prestress release). The crack patterns were similar for the live end of beam B12-24DV. Compression block crushing damage is visible in Figure 129 at the load point location along the top corner of the beam, directly above the location of the wire potentiometers. Figure 130 shows a close-up view of the compression block crushing damage on the live end test of beam B12-24DV (opposite end as Figure 129).

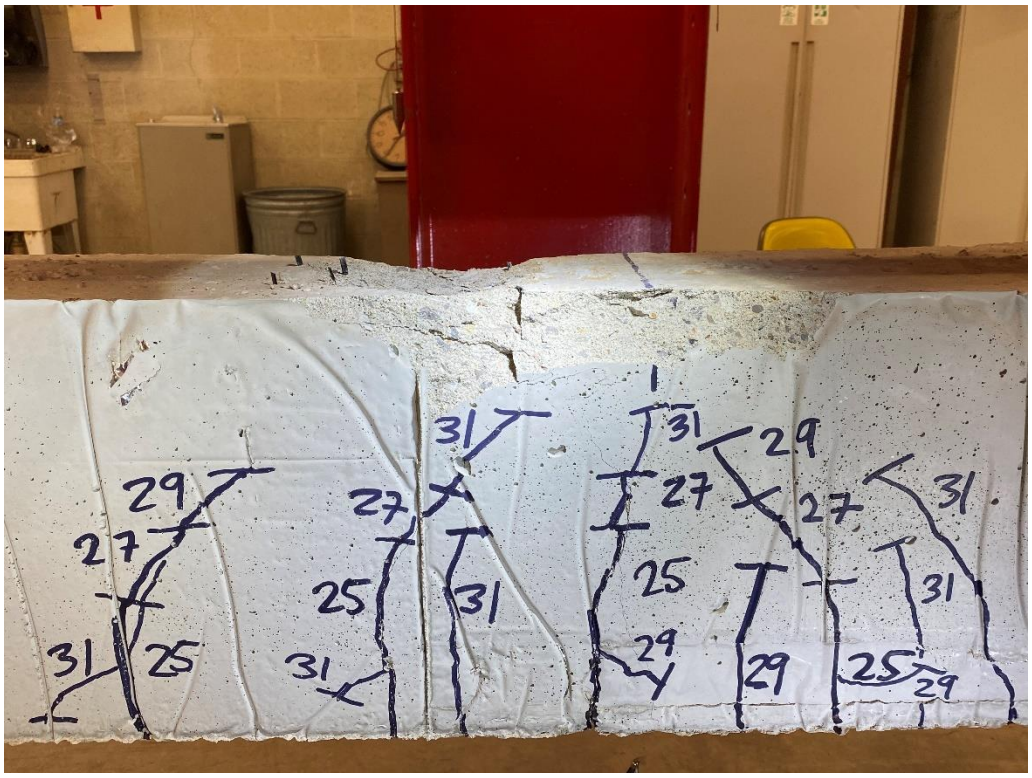

Figure 130: Compression block crushing and flexural cracking in B12-24DV (live end)

It can be concluded from the physical observations of the failure mode of Beam B12-24DV in Figures 129 and 130 along with the load-deflection data and the nature of the strand slip measurements that the strand was fully developed at an embedment of 3.5 ft or 47% of the ACI 318 development length.

4.3.3.4 B13 – 3 ft Embedment

Beam B13-24DV was tested on April 7, 2022 at an age of 27 days with a strand embedment length of 3 ft, or 40% of the development length predicted by ACI 318-14, to match the early (3 hr) release beam testing. The average concrete compressive strength at the time of testing was 11.1 ksi.

Figure 131 shows the load-deflection response of Beam B13-24DV. As before, this plot displays the load-deflection curves, the manually measured deflection checks, and the strand slip

data for the tests performed on both ends of beam B13-24DV. Except for the last data points at the maximum failure deflections, all manually measured deflection data points match the load-deflection curves closely.

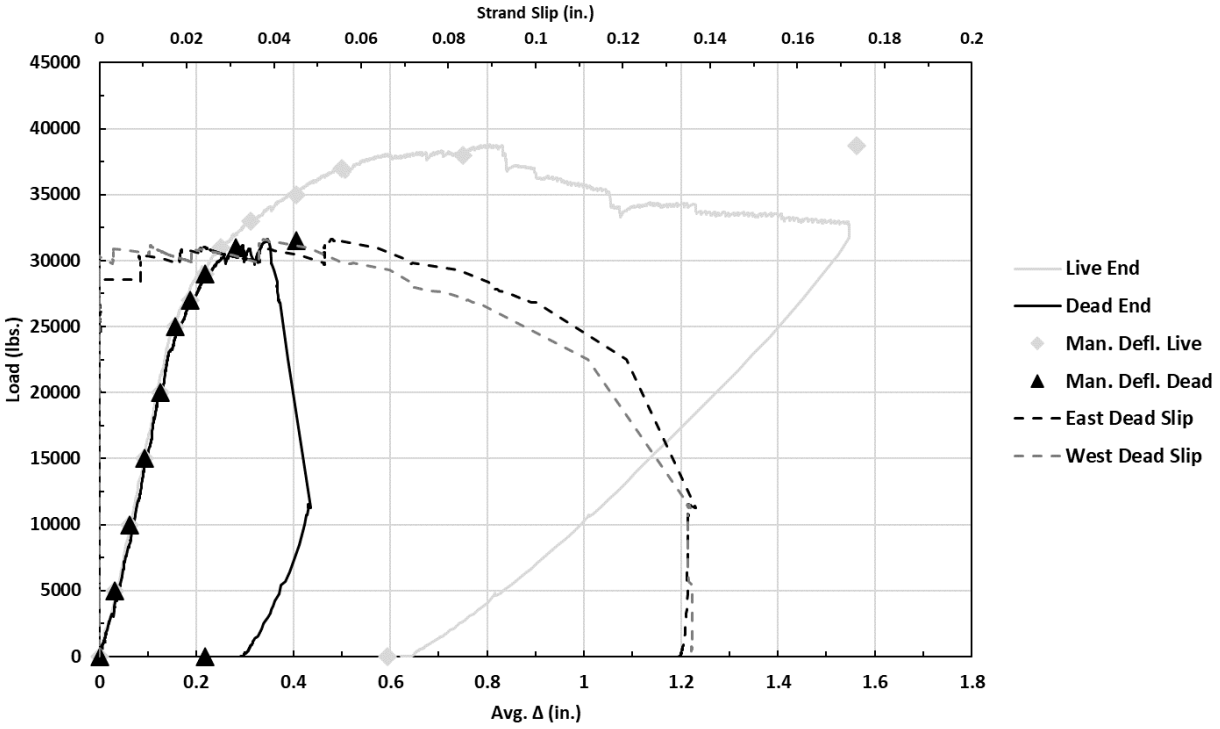

Figure 131: Beam B13-24DV load-deflection and load-slip response (3 ft embedment)

Figure 131 shows that beam B13-24DV was the first specimen to exhibit different failure mechanisms at either end of the same beam. While the live end demonstrated a fully developed flexural failure with no slip on either strand, the dead end exhibited a more abrupt failure with significant slip in both strands. Direct observation of the cracking pattern during the dead end test clearly showed that this sudden failure was caused by shear. It is important to note, however, that unlike the shear failures experienced by beams B7-3DV and B8-3DV, for the dead end of beam B13-24DV, slip initiated for both strands prior to the shear failure. This would indicate that for beam B13-24DV, general strand slip may have contributed to loss of capacity in the beam

end region, leading to the shear failure, instead of the shear failure disrupting the transfer zone and causing slip, which was the mode of the other shear failures of beams B7-3DV and B8-3DV.

Since the failure modes were totally disparate, the beam end tests for beam B13-24DV are discussed separately. The live end of B13-24DV displayed a fully developed flexural failure at a 3 ft embedment, as supported by the following observations:

- The live end reached a peak load of 38.8 kips, equivalent to a moment of 80.0 kip-ft. This exceeded the theoretical moment capacity of 69 kip-ft, and matched the maximum capacity observed from the other flexural failures.
- The load-deflection curve exhibited an extended plateau at failure.
- Zero strand slip was measured for both strands for the live end test.

The live end beam failure was dominated by flexural cracking and compression block crushing, as observed during testing and documented with photographs, one of which is shown in Figure 132. For the live end test, the initial flexural cracks were observed at the 25 kip load increment, which is slightly before the load-deflection curve of Figure 131 becomes non-linear. Additional flexural cracks developed and spread over the course of the test, corresponding with the continued non-linearity of the load-deflection curve. Figure 132 shows the mapped crack pattern for the live end of beam B13-24DV at failure with the load increments marked on the cracks as they appeared.

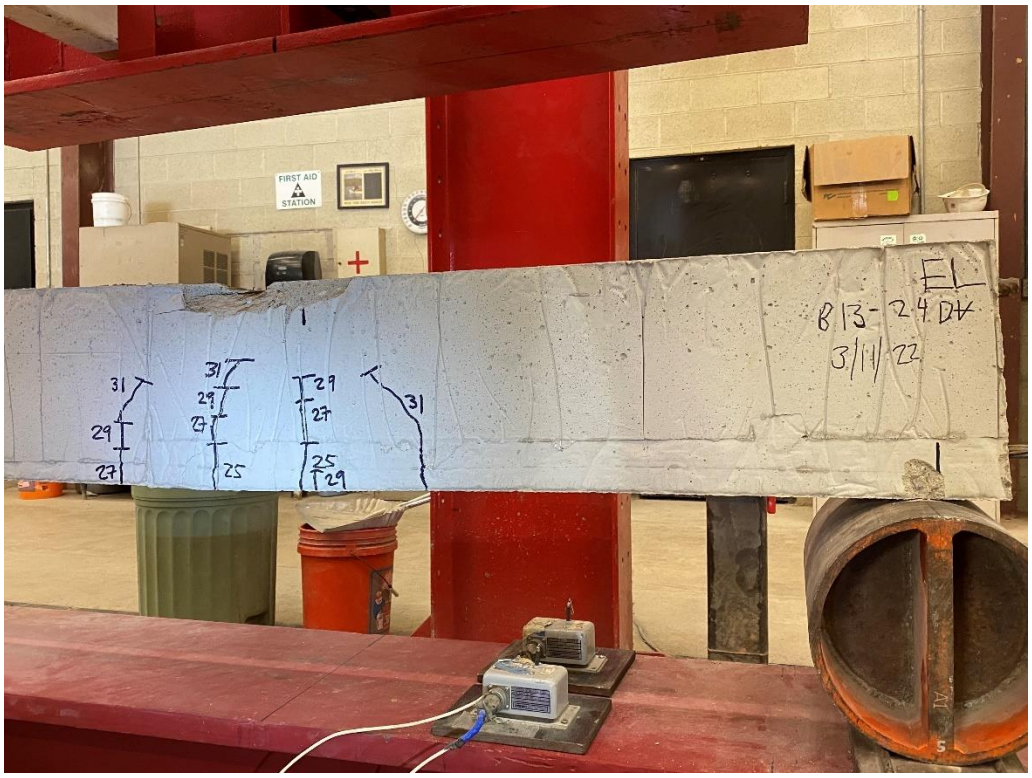

Figure 132: Cracking pattern at failure for B13-24DV with 3 ft embedment (live end)

Figure 132 shows that the crack pattern was dominated by flexural cracking, although load increments were not marked after 31 kips due to safety concerns about the imminent risk of a sudden shear failure. Figure 132 also shows that, in addition to the flexural cracking, the live end of B13-24DV clearly shows signs of crushing in the compression block at the load point location. It can be concluded from the physical observations of the failure mode of the live end of beam B13-24DV along with the load-deflection data and the lack of measured strand slip that the strand was fully developed for this particular test.

The same cannot be said for the replicate test performed on the dead end of beam B13-24DV, which displayed a bond-shear type failure at a 3 ft embedment as evidenced by the following observations:

- The dead end reached a peak load of 31.6 kips, equivalent to a moment of 65.2 kip-ft. This test failed to reach the theoretical moment capacity of 69 kip-ft.
- The load-deflection curve exhibits an abrupt drop from the peak load, typical of a brittle shear failure.
- Both strands on the dead end test slipped significantly, and began to do so prior to the shear failure. The east strand slipped first, at a load of around 28 kips as evidenced by an audible popping sound and by visual observation (Figure 131). The west strand slipped shortly after at a load of around 30 kips. After this point, both strands slipped steadily until the beam experienced a major shear failure at around 31.5 kips, at which point both strands slipped extensively because of a loss of anchorage in the transfer zone. Just before the shear failure, the strands had each slipped around 0.04-0.05 in., and after the shear failure both strands slipped beyond 0.10 in.

The dead end beam failure included some flexural cracking but no compression block crushing. The most significant damage was the large shear crack visible in Figure 133.



Figure 133: Cracking pattern at failure for B13-24DV with 3 ft embedment (dead end)

This shear failure was sudden and explosive, more similar to that observed for beam B7-3DV rather than beam B8-3DV. Although the shear crack for the dead end of B13-24DV did not open quite as wide as for the live or dead ends of beam B7-3DV, a large enough chunk of concrete was liberated near the bottom of the beam that the reinforcement was clearly visible. Figure 134 shows a close up of this location where it appears that the WWR has failed similarly to that in beam B7-3DV. Figure 134 shows that the horizontal wire appears to be disconnected from the vertical wire near the location of the outside face of the weld.



Figure 134: WWR damage from shear failure on test B13-24DV

It is difficult to make definite conclusions about the degree of strand development at the 3 ft embedment for the test specimen with a 24 hour release, because the failure modes for the replicate tests at either end of beam B13-24DV were so different. At the live end, the strands achieved maximum stress without any measured slip. But at the dead end, not only did a shear failure occur prematurely to full flexural capacity of the beam, the strands experienced general bond slip before the shear failure. Although it is possible that the strand slip at the dead end contributed to the shear failure, it is possible that this observation is due to the extremely high variability of concrete shear strength in general. Theoretically, the beams were designed to resist a shear failure with only the WWR and the minimum concrete shear strength without provision for extra capacity from the prestress force in the transfer zone, and 3 out of 4 beam ends tested at a 3 ft embedment (including the early 3 hour release beam) reached moments higher than the

theoretical moment capacity. So, it is possible that the dead end of beam B13-24DV only represented an abnormally low shear strength, and that the strand slip would have been arrested during the test, allowing the beam to reach full flexural strength if the shear strength had been higher. This is only speculative, however, and since the slip on both dead end strands preceded failure at a lower than designed moment, and due to the relatively large magnitude of this slip, it is likely that the strands were not fully developed.

4.3.3.5 B14 – 2.5 ft Embedment

Beam B14-24DV was tested on April 14 and 15, 2022 at an age of 27-28 days with a strand embedment length of 2.5 ft, or 33% of the development length predicted by ACI 318-14, to match the early release (3 hr) beam testing. At an embedment length of 2.5 ft, the a/d ratio for beam B14-24DV was equal to 3, meaning that beam B14-24DV was more likely to fail in shear than those beams which were tested at the longer embedment lengths (Naji et al., 2017). The dead end was tested on April 14 (27 days) and the live end was tested on April 15 (28 days). The average concrete compressive strength on April 14 was 10.7 ksi and on April 15 was 10.4 ksi; since the tests were performed within 20 hours of each other, it is appropriate to take these tests as a group for an overall average compressive strength of 10.6 ksi.

Figure 135 shows the load-deflection response of beam B14. As before, this plot displays the load-deflection curves, the manually measured deflection checks, and the strand slip data for the tests performed on both ends of beam B14. Except for the last data points after the peak failure loads, all manually measured deflection data points match the load-deflection curves closely. This observed difference is likely due to the jolting and rapid deflection caused by the sudden shear failures.

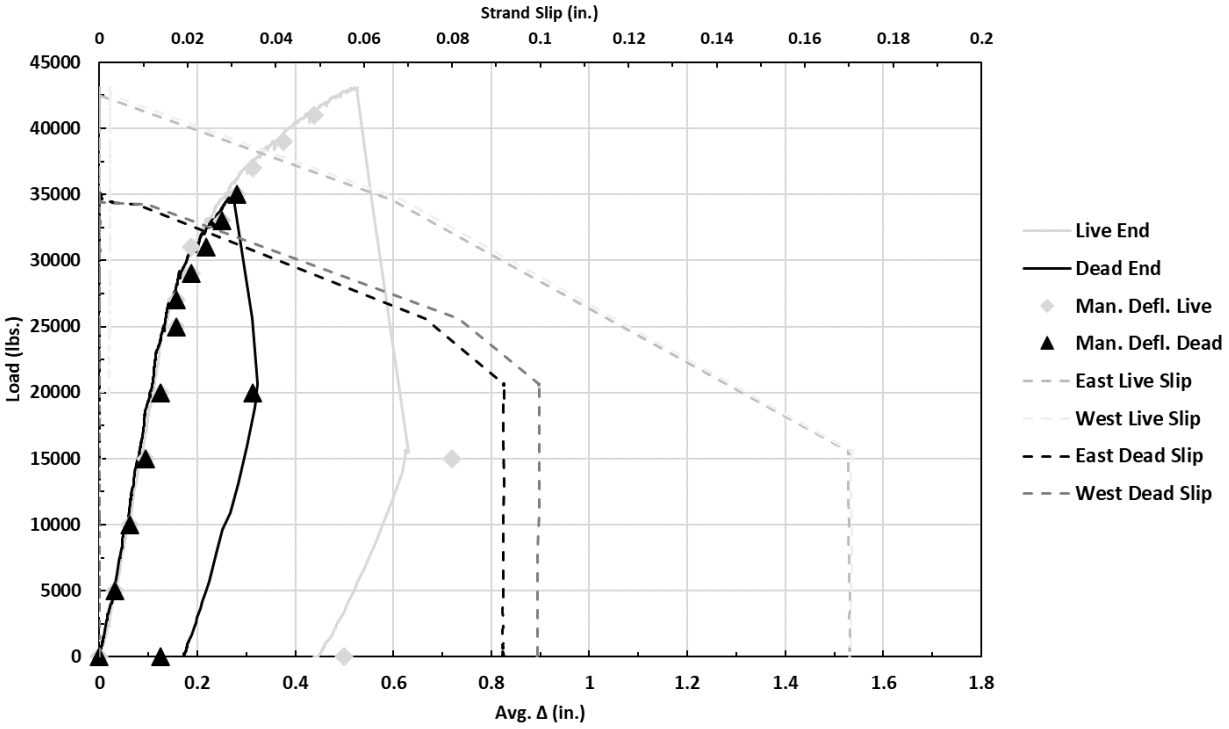

Figure 135: Beam B14-24DV load-deflection and load-slip response (2.5 ft embedment)

Figure 135 shows that at a 2.5 ft embedment, beam B14-24DV exhibited a sudden failure at both ends, although the live end test reached a significantly higher load. For both beam end tests, direct observation of the cracking patterns made it clear that the abrupt failures were due to shear. For both the live and dead ends, the strands still did not slip until after the shear failure initiated. Due to the observed failure modes and the disparity between capacities at either end, the degree of strand development for the 2.5 ft embedment length is unclear. This conclusion is supported by the following observations:

- The live and dead ends reached peak loads of 43.1 and 35.3 kips respectively, equivalent to moments of 77.2 and 63.1 kip-ft. The live end exceeded the theoretical moment capacity of 69 kip-ft, but the dead end did not reach the theoretical moment capacity.

- The load-deflection curves exhibit a sudden drop at failure, a classical property of a shear failure. Although the shear cracks occurred suddenly and were significant, both ends retained more residual load than the shear failures at the 3 ft embedment.
- Significant strand slip occurred on both strands for both beam end tests, but this strand slip did not represent a general bond-slip or flexural bond failure. As Figure 135 shows, the strands remained anchored and did not slip prior to failure (indicated by the sudden drop in load). Instead, both strands exhibited a single, significant occurrence of slip when shear cracks entered the transfer zone and disrupted the strand bond.

The beam ends exhibited some flexural cracking but failure was controlled by shear cracking as shown in Figure 136. The first flexural cracks were visually observed at 25 kips of load for both the live end and dead end tests. This correlates well to where the non-linear behavior begins in the load-deflection curves shown in Figure 135. New flexural cracks continued to form and propagate, correlating to the non-linear load-deflection curve, until the shear cracks occurred. Figure 136 shows the mapped crack pattern resulting from this behavior with the load increments marked on the cracks as they appeared on the live end of beam B14-24DV.

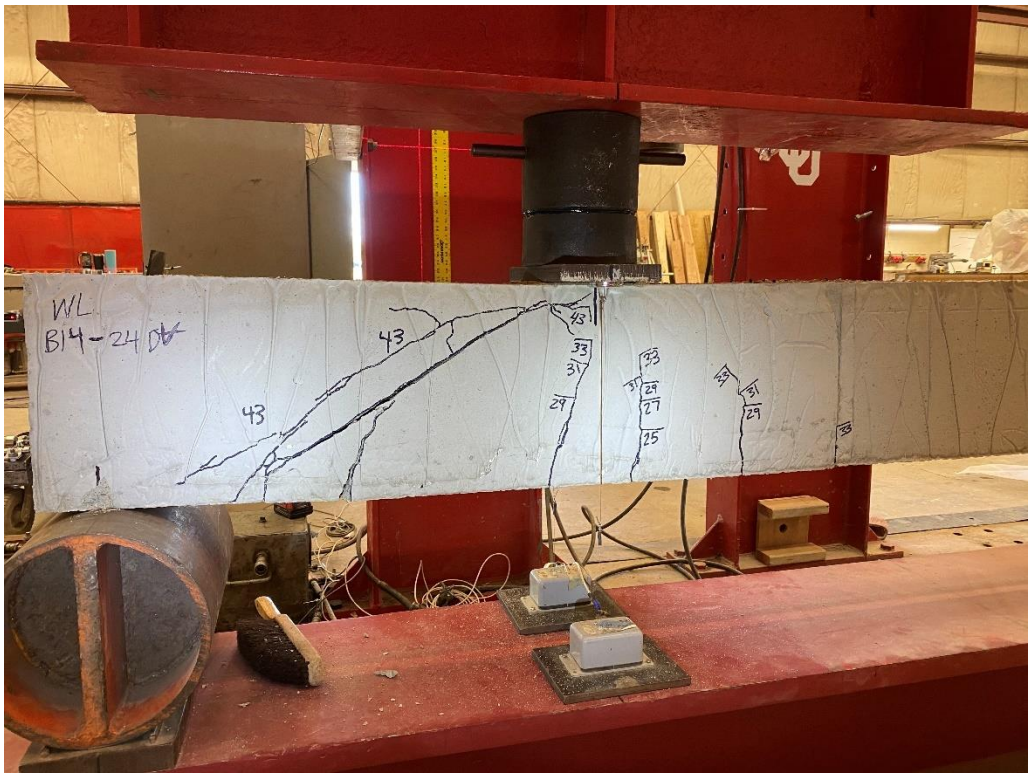

Figure 136: Cracking pattern at failure for B14-24DV with 2.5 ft embedment (live end)

When concrete surrounding the shear crack in beam B14-24DV was removed after testing, a third WWR failure mode was observed. Figure 137 shows a wire crossing the shear crack that exhibited obvious necking which indicates yielding of the wire. Figure 138 shows an enlarged view of the yielding failure.



Figure 137: WWR failure mode from shear failure in beam B14-24DV – tensile yielding of gross section



Figure 138: Magnified view of tensile yielding in WWR after beam B14-24DV shear failure

It is possible that the observed yielding failure mode of the WWR may help explain the residual capacity compared to the other specimens which experienced more sudden shear failures. If the horizontal welded wires were anchored firmly enough to develop significant strain and visibly yield, this mechanism would help hold the shear cracks closed and prevent the sudden loss of load carrying capacity observed when the large shear cracks occurred like in the cases of B7-3DV and B13-24DV.

4.3.4 Results – Development Length Summary

Tables 22 and 23 summarize the development length testing data for the early (3 hr) and typical (24 hr) prestress release beams, respectively. These tables represent an abbreviated form of the full descriptions of each test from Sections 4.3.2 and 4.3.3.

Table 22: Development Length Test Summary for Early (3 hr) Prestress Release Beams

Beam ID	Embedment Length (ft)	ACI Ratio (unitless)	Beam End	M_{max} (k-ft)	V_{max} (k)	M_{slip} (k-ft)	Max slip (in.)	Failure Mode
B9-3DV	6.0	0.80	Live	79.6	13.2	N/A	0.000	Flexure
			Dead	79.8	13.2	N/A	0.000	Flexure
B6-3DV	4.0	0.53	Live	80.7	20.8	N/A	0.000	Flexure
			Dead	80.4	20.7	N/A	0.000	Flexure
B10-3DV	3.5	0.47	Live	78.1	23.3	N/A	0.000	Flexure
			Dead	78.1	23.3	N/A	0.000	Flexure
B7-3DV	3.0	0.40	Live	72.4	25.5	72.4	0.137	Shear
			Dead	74.3	26.2	74.3	0.127	Shear
B8-3DV	2.5	0.33	Live	55.5	24.0	55.5	0.098	Shear
			Dead	59.2	25.6	59.2	0.180	Shear

Table 23: Development Length Test Summary for Typical (24 hr) Prestress Release Beams

Beam ID	Embedment Length (ft)	ACI Ratio (unitless)	Beam End	M_{max} (k-ft)	V_{max} (k)	M_{slip} (k-ft)	Max slip (in.)	Failure Mode
B16-24DV	6.0	0.80	Live	78.1	12.9	N/A	0.000	Flexure
			Dead	76.6	12.7	N/A	0.000	Flexure
B15-24DV	4.0	0.53	Live	77.9	20.1	24.4	0.007	Flexure
			Dead	79.2	20.4	76.0	0.007	Flexure
B12-24DV	3.5	0.47	Live	77.0	22.9	N/A	0.000	Flexure
			Dead	77.5	23.1	74.8	0.004	Flexure
B13-24DV	3.0	0.40	Live	80.0	28.2	N/A	0.000	Flexure
			Dead	65.2	23.0	58.9	0.135	Shear
B14-24DV	2.5	0.33	Live	77.2	33.3	76.1	0.170	Shear
			Dead	63.1	27.3	61.3	0.100	Shear

In order to identify development length from the beam testing data, the failure moment for each test was plotted against the corresponding strand embedment length. Figure 139 shows

this data visualization for the early release (3 hr) prestressed beams. The black triangles denote the average failure moment for each test with the black line linearly interpolating between data points and forced through the origin, the red bars denote the difference between the live and dead end results for each test, the dotted gray line represents the theoretical flexural capacity, the dashed gray line denotes the actual flexural capacity (as determined by averaging the results of those tests which experienced purely flexural failures), and the vertical dash-dot red line denotes the development length estimated according to ACI 318.

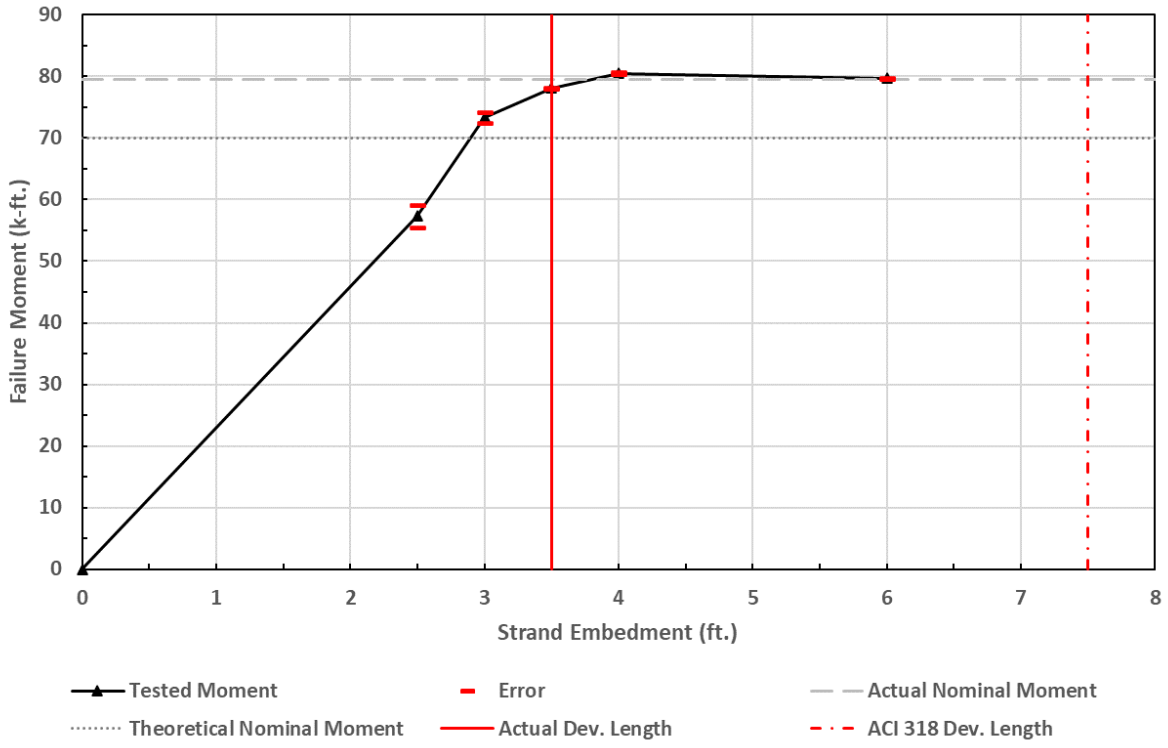

Figure 139: Failure moment versus strand embedment to identify development length for early (3 hr) prestress release

Figure 139 shows that for the early (3 hr) prestress release beams, the development length can be identified as a maximum of 3.5 ft from this particular test data. At strand embedment of 3.5 ft and larger, the failure modes were purely flexural, and Figure 139 shows that the failure

moments flatlined at nearly 80 kip-ft because the maximum flexural capacity of the section had been reached. It is possible that the strand development length is shorter than 3.5 ft for the conditions tested, but because shear initiated failure for the beams at 2.5 ft and 3 ft embedment lengths at maximum moments lower than the observed flexural capacity, the minimum strand development length cannot be determined with certainty from this data.

Figure 140 shows the failure moment plotted against embedment length for the typical (24 hr) release prestressed beams. The gray diamonds denote the average failure moment for each test with the gray line linearly interpolating between data points and forced through the origin, the black bars denote the difference between the live and dead end results for each test, the dotted gray line represents the theoretical flexural capacity, the dashed gray line denotes the actual flexural capacity (as determined by averaging the results of those tests which experienced purely flexural failures), and the vertical dash-dot red line denotes the development length estimated according to ACI 318.

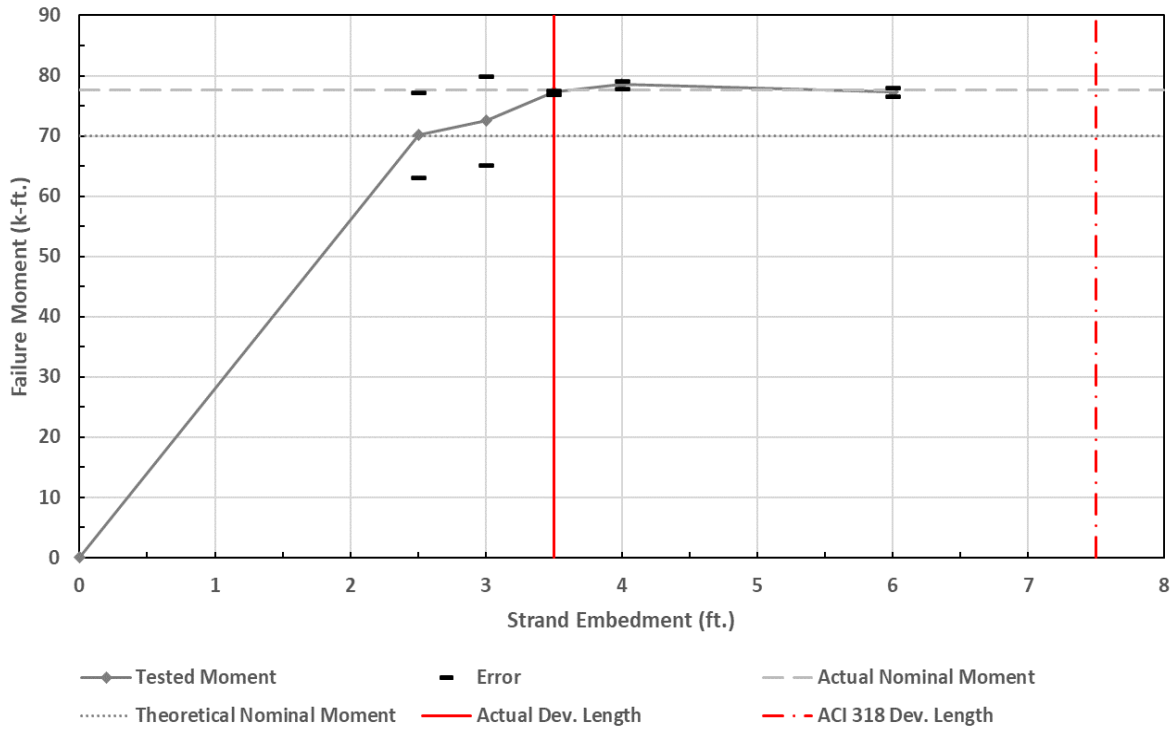

Figure 140: Failure moment versus strand embedment to identify development length for typical (24 hr) prestress release

Figure 140 shows that for the typical (24 hr) prestress release beams, the development length can be identified as a maximum of 3.5 ft for the conditions tested. At strand embedment of 3.5 ft and larger, the failure modes were purely flexural, and Figure 140 shows that the failure moments flatlined at nearly 78 kip-ft because the maximum flexural capacity of the section had been reached. Again, it is possible that the strand development length could be shorter than 3.5 ft. Interestingly, the disparity in failure modes between live and dead ends at the 2.5 ft and 3 ft embedment lengths resulted in two tests that reached or exceeded the maximum flexural capacity, one of which failed in flexure and one which failed at a very high shear strength, exceeding the calculated shear capacity by around 28%. But because either shear or bond-slip initiated failure for 3 of 4 beam ends at the lowest embedment lengths, the minimum strand development length cannot be determined with certainty from this data.

4.4 Transfer Length Testing

A total of four beams were instrumented specifically to measure long-term strain distributions for the purpose of determining both transfer length and prestress losses. Two beams underwent early prestress release (around 3 hr) and two beams underwent a more typical prestress release (around 24 hr). The data collection techniques and the results relative to transfer length are described in Section 4.4, while Chapter 5 presents the measured prestress loss results and the modelled prestress losses.

4.4.1 Instrumentation

All four beams used for transfer length and strain measurements (designated TR series in the testing, with a prefix of 3 or 24 to indicate early or typical prestress release age) utilized the same demountable mechanical (DEMEC) strain gage stud layout and block clamps for strand draw-in measurements. Two of the four beams (one for each release time) included only one vibrating wire strain gage (VWSG) at midspan to measure prestress losses. The other beam for each release time included one VWSG at midspan to measure prestress losses as well as four VWSG spaced evenly throughout the approximate transfer zone of each beam end to measure end region strain profiles. Companion shrinkage specimens with one VWSG each were also cast along with 2 of these beams.

4.4.1.1 Internal Vibrating Wire Strain Gages (VWSG's)

All VWSG were placed so that they would measure the strain in the concrete at the level of the prestressing strands at specific points along the beam length. The VWSG were placed in the middle of the transverse space between the strands, so that if there were any disparity in the prestress between the two strands or any lag in the prestress across the cross-section, the gages would most nearly represent the average strain state generated by the prestress force. Figure 141 shows the installation technique used for the VWSG – pictured in the figure is a model 4200

gage produced by Geokon®. The model 4200 was used for all but 2 gages, which were substituted with model 4202 gages because of equipment shortages. The model 4202 gage has a shorter gage length but higher measurement accuracy. When installing either gage type, great care was taken to ensure that the ends of the barbells were not impinged, which will skew the VWSG measurements. Both models of VWSG utilized for this testing are equipped with internal thermistors to measure the internal concrete temperature over time as well as the strain. This temperature data is useful for making observations about the setting and curing of the concrete and is necessary to correct the strain data for thermal effects due to the difference in coefficient of thermal expansion between the sensor filament and the concrete test specimens.

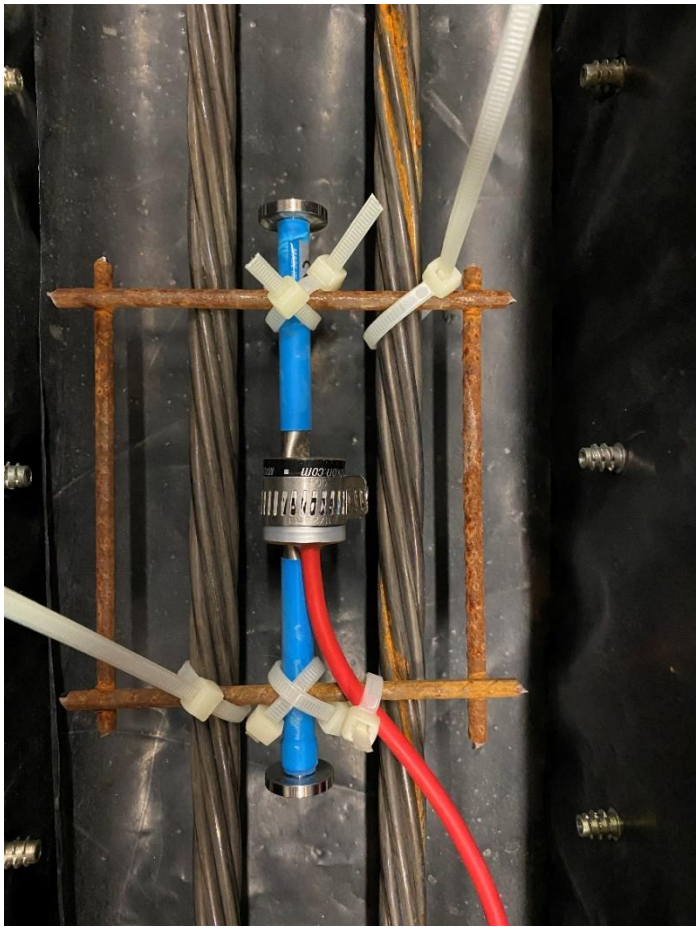

Figure 141: Mounting technique for VWSG instrumentation

The installation technique shown in Figure 141 was recommended by the manufacturer and was considered best practice by the doctoral advisor and members of the dissertation committee with extensive prior experience concerning VWSG instrumentation. Each gage was pre-tied to small diameter steel cross-pieces with plastic cable ties in the x-pattern shown in Figure 141. The steel cross-pieces used to mount the gages were simply individual square cells cut from leftover WWR used for the beam shear reinforcement. The cable tie x-pattern was used so that with moderate tension on the ties, the gage would not slide when concrete was placed in the formwork. The steel cross frame was then placed on the strands with the VWSG facing down so that its center hung at very nearly the same elevation as the center of gravity of the strand (cgs). The steel cross frame was then tied to the strands in an alternating corner x-pattern. Only 2 corners were tied before tensioning the strands. After the gages shifted slightly when the strands were tensioned, the steel cross frames were adjusted to their final position and all 4 corners were fastened tightly to the strands.

Table 24 shows the instrument layout for the VWSG in the 2 beams that utilized the embedded strain gages for transfer length measurement (B3-24TR and B4-3TR). The first gage at each end was placed with its center 11 in. from the beam end, and every gage thereafter was placed 12 in. on center for total of 4 gages in the end region on both beam ends. In addition, a single gage was placed at the midspan of each beam, 10 ft (120 in.) from either end.

Table 24: VWSG Instrumentation Layout for Long-Term Strain Monitoring (TR Series Beams)

Gage Spacing:	11 in. from end / 12 in. O.C.		
Dead End		**Live End**	
Gage #	Distance to Gage O.C. (in.)	Gage #	Distance to Gage O.C. (in.)
1D	11.0	1L	11.0
2D	23.0	2L	23.0
3D	35.0	3L	35.0
4D	47.0	4L	47.0
5M	120.0	-	-

Figure 142 shows a schematic which depicts the VWSG instrument locations which are described in Table 24. Note that the instrumentation layout is symmetric about the centerline of the beam.

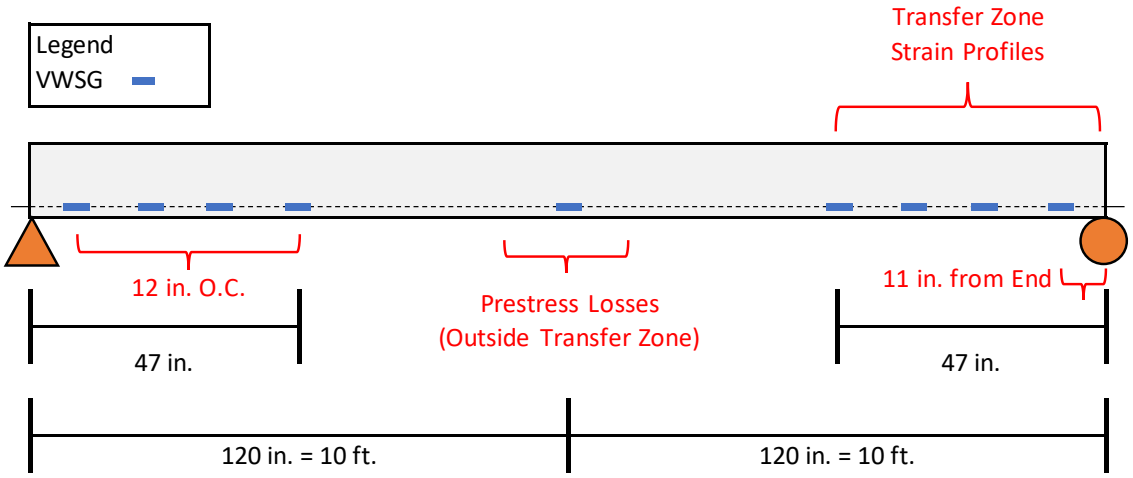

Figure 142: VWSG instrumentation schematic for long-term strain monitoring (TR series beams)

Figure 143 shows the longitudinal distribution of the VWSG in the transfer zone during the instrumentation setup for beam B3-24TR.

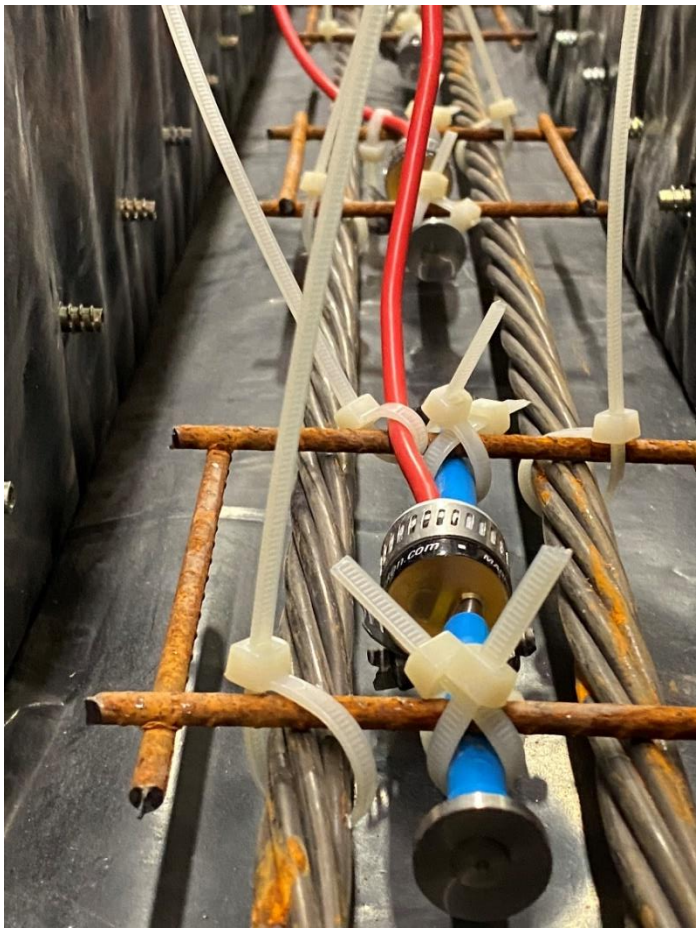

Figure 143: Longitudinal distribution of VWSG (interior DEMEC studs also visible on each formwork side)

The VWSG data was recorded as rapidly as the data loggers would allow during the casting and prestress release period for the beams with VWSG throughout the span, which was a rate of 1 sample every minute. This sampling rate was decreased to 1 sample per 15 minutes and later (after several months) to 1 sample per 30 minutes, in order to reduce data file sizes and save data logger battery power. For the two TR series beams with a single VWSG at midspan, the gages were read intermittently with a single channel discrete Geokon reader. The beams with single VWSG were not used for transfer length testing, however, so this measurement schedule is discussed in more detail with the prestress loss measurements in Chapter 5.

4.4.1.2 External DEMEC Strain Gages

A demountable mechanical (DEMEC) strain gage system was used for surface strain measurement on all 4 beams set aside for long-term testing. Table 25 shows the DEMEC target locations, which were placed at the level of the prestressing strand, 2 in. O.C. from the bottom of the beam. Note that in Table 25, the stud locations denote each place where a stud was affixed to the beam and therefore either end of the DEMEC gage was placed to take each measurement. Since the DEMEC measurement essentially represents an average strain over that gage length, the strain locations shown in Table 25 represent the midpoint between each consecutive pair of stud locations, and these strain locations were utilized when plotting the end region strain profiles for transfer length analysis.

Table 25: DEMEC Instrumentation Layout for Long-Term Strain Monitoring (TR Series Beams)

Stud Spacing	100 mm = 3 15/16 in. =	3.94	in.
Dead End		**Strain Location**	
Stud #	Stud Location (in.)	Span	Location (in.)
1	1.00	1_2	2.97
2	4.94	2_3	6.91
3	8.88	3_4	10.84
4	12.81	4_5	14.78
5	16.75	5_6	18.72
6	20.69	6_7	22.66
7	24.63	7_8	26.59
8	28.56	8_9	30.53
9	32.50	9_10	34.47
10	36.44	10_11	38.41
11	40.38	11_12	42.34
12	44.31	12_13	46.28
13	48.25	13_14	50.22
14	52.19	14_15	54.16
15	56.13	15_16	58.09
16	60.06		
Live End		**Strain Location**	
Stud #	Stud Location (in.)	Span	Location (in.)
1	3.94	1_2	5.91
2	7.88	2_3	9.84
3	11.81	3_4	13.78
4	15.75	4_5	17.72
5	19.69	5_6	21.66
6	23.63	6_7	25.59
7	27.56	7_8	29.53
8	31.50	8_9	33.47
9	35.44	9_10	37.41
10	39.38	10_11	41.34
11	43.31	11_12	45.28
12	47.25		

As Table 25 shows, the spacing for all the DEMEC targets was equal to the gage length of the DEMEC gage used which was 100 mm or equivalently about 3-15/16 in. However, due to limitations of the formwork used for the beams, which had been originally fabricated for a past

research project, the DEMEC target layout was not perfectly symmetric between ends. On the dead end, the first target was placed 1 in. from the beam end, while on the live end the first target was placed one full DEMEC gage length from the end. Additionally, the targets reached further into the beam span on the dead end compared to the live end. This was not an issue, however, because the DEMEC targets on both ends reached well beyond both the expected and measured transfer lengths and because measurements very near the beam end were not critical. Figure 144 shows a perspective view of the DEMEC measurement targets installed into the surface of the completed beam B3-24TR.



Figure 144: Longitudinal distribution of DEMEC instrumentation for surface strain profile measurement

The installation of these DEMEC targets utilized the same threaded stud mechanism as the DEMEC targets used for the creep measurement in Chapter 3. The primary difference in this case was that, instead of gluing flat target points to the face of the studs after removing the set

screws and stripping the forms, screws which had been tapped in their heads to serve as the DEMEC target points were threaded securely into the studs in the side of the beam. In this manner, there was no possibility for the target points to "flake away" when the glue failed, as was so pervasive with the creep specimens. A few threaded studs were stripped or fractured when pulling the formwork, but the strategy of using the tapped screws as thread-mounted DEMEC studs was far more successful than using adhesive anchorage. For detailed explanation of each step involved with using these thread-mounted DEMEC points please refer to past literature which outlines the process (Bowser, 2016) which was patterned after an earlier, similar approach (Bodapati et al., 2016).

Figure 145 shows the DEMEC strain gage being used to record a typical measurement, in this case on beam B5-24TR. Due to logistical constraints, the 200 mm DEMEC gage used for the creep testing (see Chapter 3) was not available, so the 100 mm gage pictured below was used instead. Due to the shorter gage length, the precision of this 100 mm DEMEC gage is less than the 200 mm instrument. However, the reduced precision was deemed acceptable due to the naturally high variability of DEMEC measurements and the fact that these DEMEC measurements were primarily intended as backup measurements to complement the VWSG data.

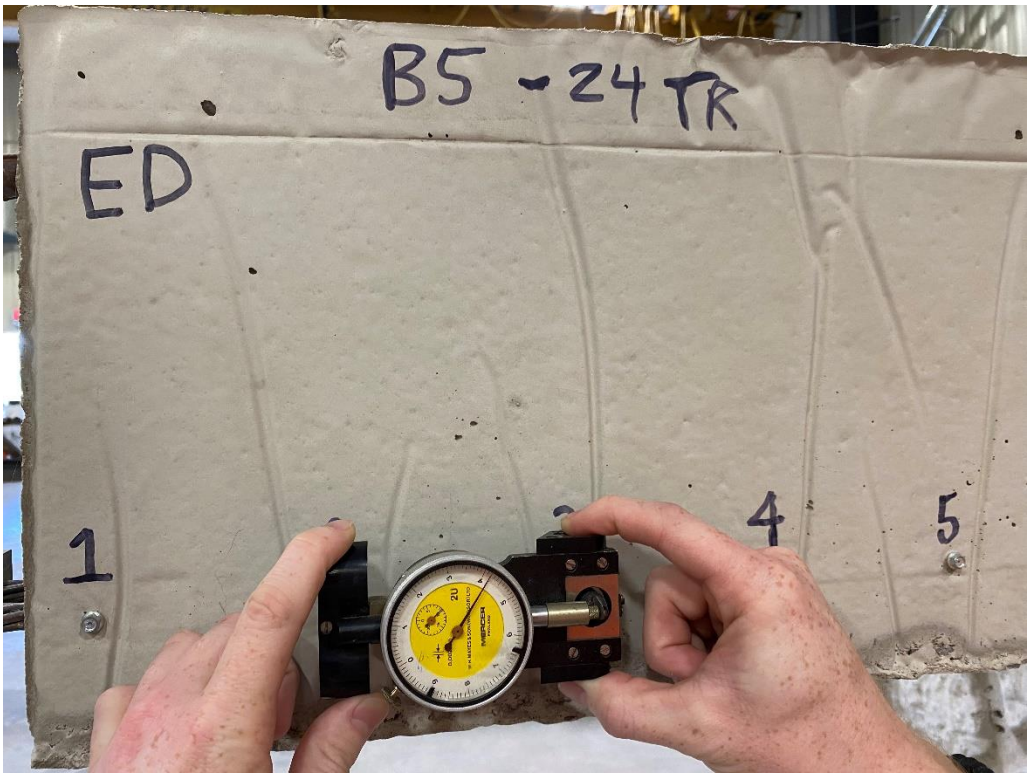

Figure 145: Typical DEMEC strain gage measurement for TR series beam

A complete set of DEMEC measurements was taken between every pair of targets on each TR series beam (on both sides of both ends), immediately before prestress release as quickly as the forms could be stripped and the target screws placed; as quickly after prestress release as practical; weekly for the first month; and monthly or every few months thereafter. Due to logistical conflicts, not every beam had a set of readings taken at 28 days, so 56 days was chosen as a common time of comparison for the TR series DEMEC transfer length measurements instead (see Section 4.4.2).

4.4.1.3 End-Slip/Strand Draw-In

In addition to the strain measurements obtained using the VWSG and DEMEC measurements, transfer length was estimated using strand draw-in measurements. Strand draw-in was measured by placing block clamps at known standoff distances from the beam ends immediately prior to prestress release. This initial standoff distance was measured with an analog

depth micrometer, accurate to the nearest 0.001 in. For the 4 instrumented beams cast specifically for transfer length measurement (TR series), strand draw-in measurements were taken each time that DEMEC measurements were taken for the duration that the beams were monitored. For the other 10 beams cast for development length testing, strand draw-in was measured from prestress release out to a maximum of 28 days. Strand draw-in measurement beyond 28 days was not possible for this group of beams because they were all destructively tested at between 27 and 29 days (see section 4.3).

A simple equation developed through integration of strain along the length of the strand which uses a bond stress distribution coefficient to relate the strand draw-in measurements to the transfer length (FIP, 1982; Dang et al., 2014 & 2016) was then used to estimate the transfer length, as shown in Equation 8:

$$L_t = \alpha \Delta \frac{E_{ps}}{f_{ps}} \quad (8)$$

where L_t is the transfer length estimate, α is the bond stress distribution coefficient, Δ is the measured strand draw in (minus the free strand elongation), E_{ps} is the strand modulus, and f_{ps} is the strand stress at prestress release.

The theoretical extreme values for the bond stress distribution coefficient (α) are bounded by 2.0 and 3.0 depending on whether a constant or a linear bond stress distribution is assumed. Research has shown that the true value usually lies somewhere in this range, and researchers have recommended values of 2.44 (Marti-Vargas et al., 2007), 2.61 (Dang et al., 2016), and others. A bond stress distribution coefficient of 2.61 was used for the strand draw-in data in these experiments based on discussion with the doctoral advisor, because this factor falls within the

theoretical range of 2-3, matches previous research, and is rationally founded on a thorough experimental and analytical approach (Dang et al., 2016).

Figure 146 shows the depth micrometer being used to take strand draw-in measurements. Because of the plastic sheathing used to protect the form end panels, the beam ends were generally extremely smooth (as seen in Figure 146) and there was no need for gluing a flat plate to the face of the beam for a strand draw-in reference point.



Figure 146: Typical strand draw-in measurement using a depth micrometer for TR series beam

4.4.2 Results

The following sections summarize the strain profiles obtained for the TR series prestressed beams from both the VWSG and DEMEC measurement approaches, as well as the strand draw-in measurements. Then the transfer lengths are summarized and compared to existing code provisions.

4.4.2.1 Internal VWSG Strain Profile

Figure 147 shows the strain profiles at release and at 56 days for beams B3-24TR and B4-3TR, which were the early release (3 hr) and the typical release (24 hr) beams that were fully instrumented with VWSG.

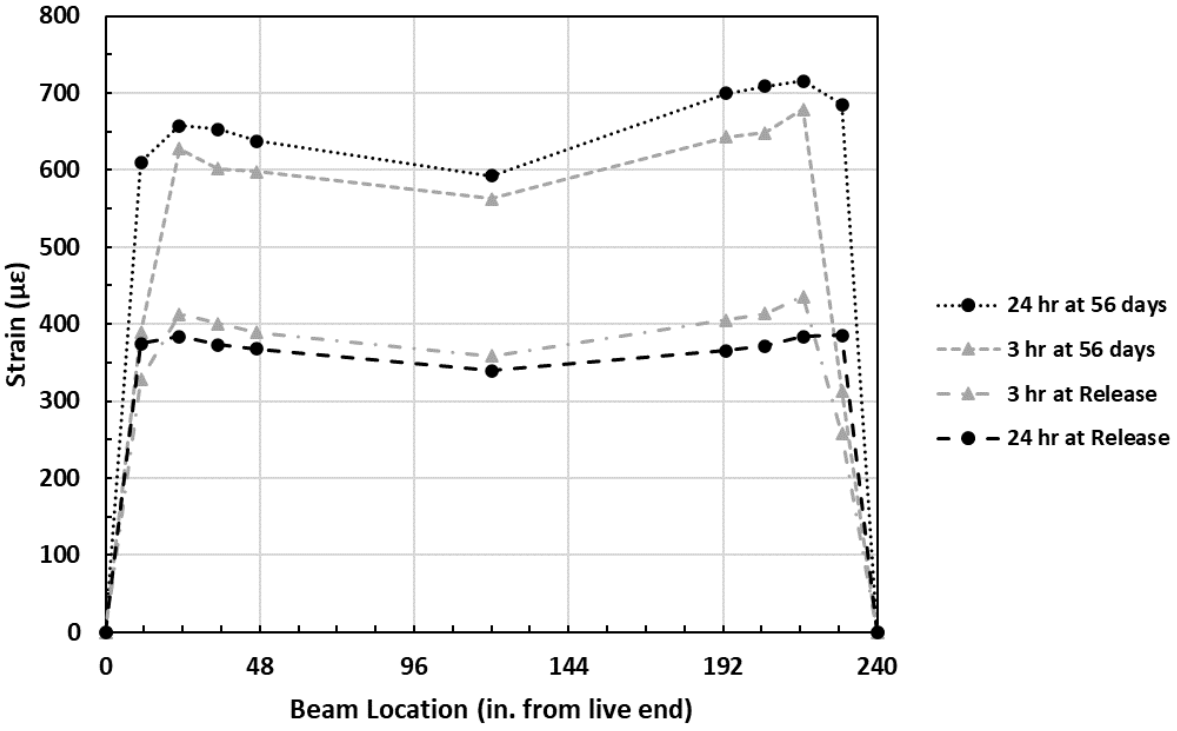

Figure 147: Internal strain profiles from VWSG data at prestress release and 56 days

Figure 147 shows that, as expected, the elastic strain at release is higher for beam B4-3TR than for beam B3-24TR. This was anticipated, because the compressive strength and therefore the elastic modulus at prestress release of the 24 hr beam is higher than that of the 3 hr

beam. For reference, the concrete compressive strength at release for B3-24TR was around 9.1 ksi, while the concrete compressive strength at release for B4-3TR was around 5.6 ksi. Despite the significant difference in compressive strength at prestress release, the elastic strains for beam B4-3TR are only slightly higher. More detailed analyses of these relationships are explored in Chapter 5 when the theoretical elastic shortening losses are computed. By 56 days the strain profiles flip and the 24 hour beam (B3-24TR) shows a higher average maximum strain than the 3 hour beam (B4-3TR). Additionally, at release, the transfer length for beam B4-3TR is clearly longer than that of beam B3-24TR. While the strain plateau included values from 3 of the gage locations for B4-3TR, for the 24 hour prestress release, results from all 4 gages fell along the plateau, indicating that the transfer length for beam B3-24TR was within 11 in. of the beam end.

Figure 148 shows the strain profiles at 56 days and at 120 days for beams B3-24TR and B4-3TR.

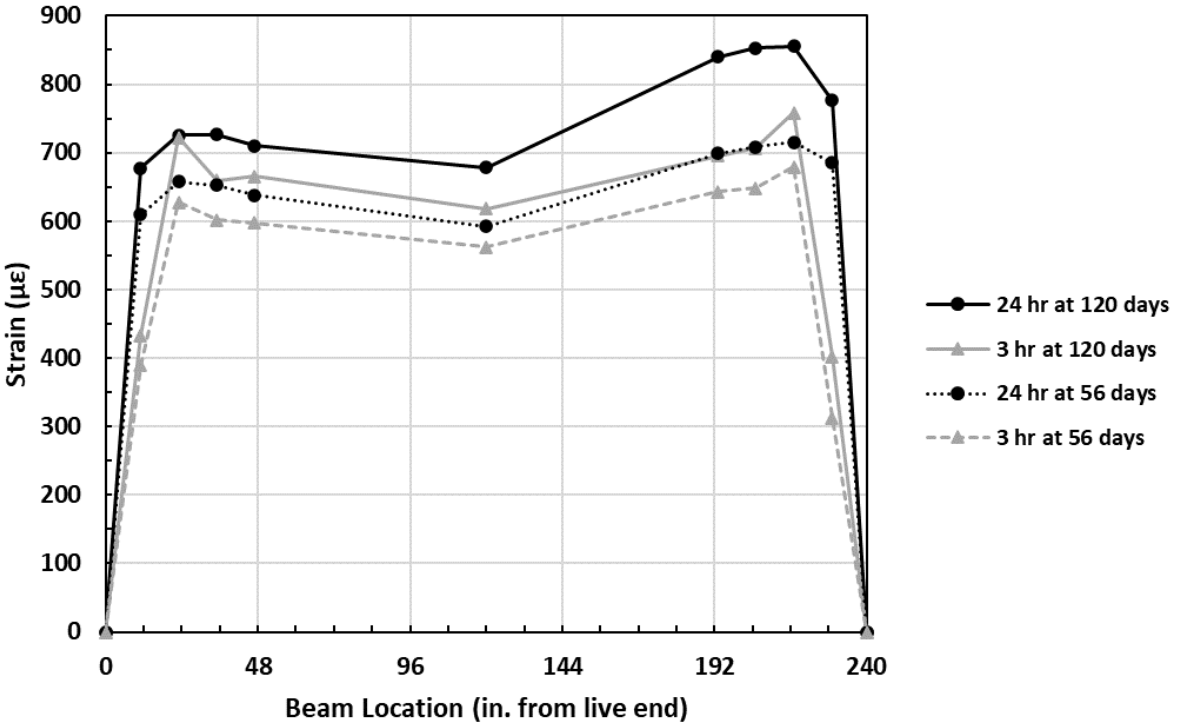

Figure 148: Internal strain profiles from VWSG data at 56 days and 120 days

Figure 148 shows that due to ongoing time-dependent prestress losses, the magnitudes of the strain profiles for both beams continued to increase between 56 and 120 days. By 120 days, the strain profile for beam B3-24TR had developed an asymmetric shape, with a higher strain plateau on the dead end region compared to the live end. Close examination of Figure 148 shows that the dead end of the beam B4-3TR is exhibiting a similar behavior, with higher strain values than the live end at 120 days. The difference between ends at 120 days is larger, however, for beam B3-24TR.

4.4.2.2 External DEMEC Strain Profile

The raw DEMEC data was reduced by first adjusting it by the gage factor associated with the 100 mm DEMEC gage, and then by plotting the raw strain profile data for each side of each end of each beam. The strains measured at every time step were zeroed relative to the pre-release measurements. Next, at every time step, the strain measurements taken on either side of each

beam end were averaged at each stud location to obtain an average strain profile for that beam end. Finally, to eliminate some of the extremes due to measurement noise, the strain profiles of each beam end were smoothed by applying a 3 point moving average along the beam end, from stud location to stud location.

Figure 149 shows a summary of the smoothed surface strain profiles at prestress release determined from the average of the DEMEC measurements for all 4 TR series prestressed beams. Additionally, for the 2 TR series beams that were also fully instrumented with VWSG (beams B3-24TR and B4-3TR) the internal strain profiles are included for comparison.

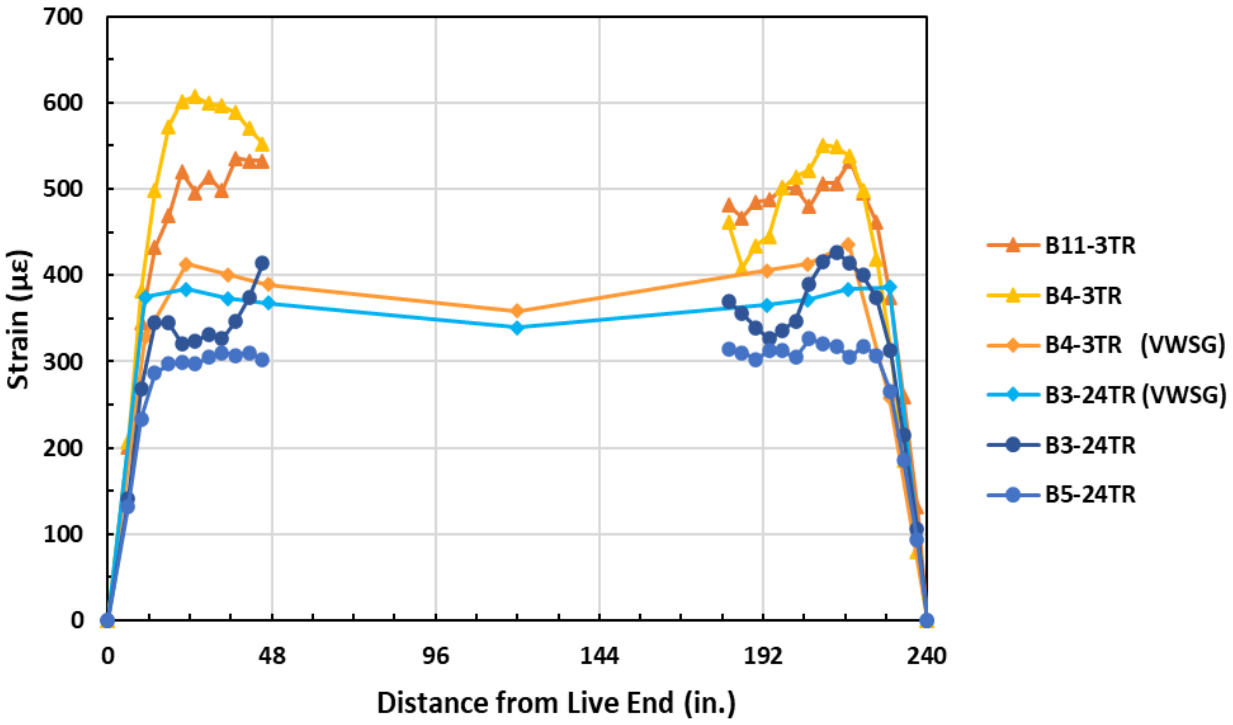

Figure 149: External strain profiles determined from DEMEC data at prestress release (VWSG strain profiles shown for comparison)

Figure 149 shows that the DEMEC data resulted in the strain plateau or average maximum strain (AMS) at release for the 3 hour release prestressed beams being significantly

higher than the average maximum strain for the 24 hour release beams. Although the VWSG strain profiles also showed higher initial strain for the early release, the difference in strain between release times is less. Even so, the strain profile measured with the VWSG is relatively close in average magnitude to the DEMEC strain profile for the 24 hour release beams. For the 3 hour release beams, however, the DEMEC strain profile had significantly higher average maximum strains than the VWSG profiles on both ends of both beams, with the DEMEC average maximum strain values exceeding the VWSG strain values by up to 40%. Temperature effects are likely responsible for this discrepancy. For the 24 hour release beams, the concrete had cooled to ambient temperatures by the time the initial pre-release DEMEC measurements were taken, and as a result, the pre and post-release measurements were taken with the beam at a stable temperature. For the 3 hour release beams, however, the pre-release measurements were taken as soon as the forms were stripped and the studs were installed. At this point, the beam had an internal temperature of up to 130-140 °F and was hot to the touch. The DEMEC and end slip readings were taken, and then prestress was released. Due to the time required to release prestress, cut the dead end strands, and usually take a short break before taking the post-release DEMEC measurements, the time between beginning the pre-release measurements and finishing the post-release measurements varied from half an hour to a few hours. At this stage of curing, with the forms removed, the beams were cooling rapidly and in that time frame the internal temperature could fall by 20-40 °F according to the thermistors in the VWSG. Therefore, part of the higher compressive strain at release shown in the 3 hr DEMEC data is due to contraction from cooling instead of purely elastic shortening. Unfortunately, due to the fact that the temperature gradient during cooling would vary across both the cross section and the length of the beam and because of the limited number of available sensors, it was not possible to develop a

thermal profile accurate and sufficient enough to effectively correct these DEMEC measurements for thermal differences.

Figure 150 shows how the 95% AMS method (Burns and Russell, 1997) was applied to a typical strain profile from one side of a prestressed beam end to determine transfer length, in this case the as-cast west side of the live end of B5-24TR.

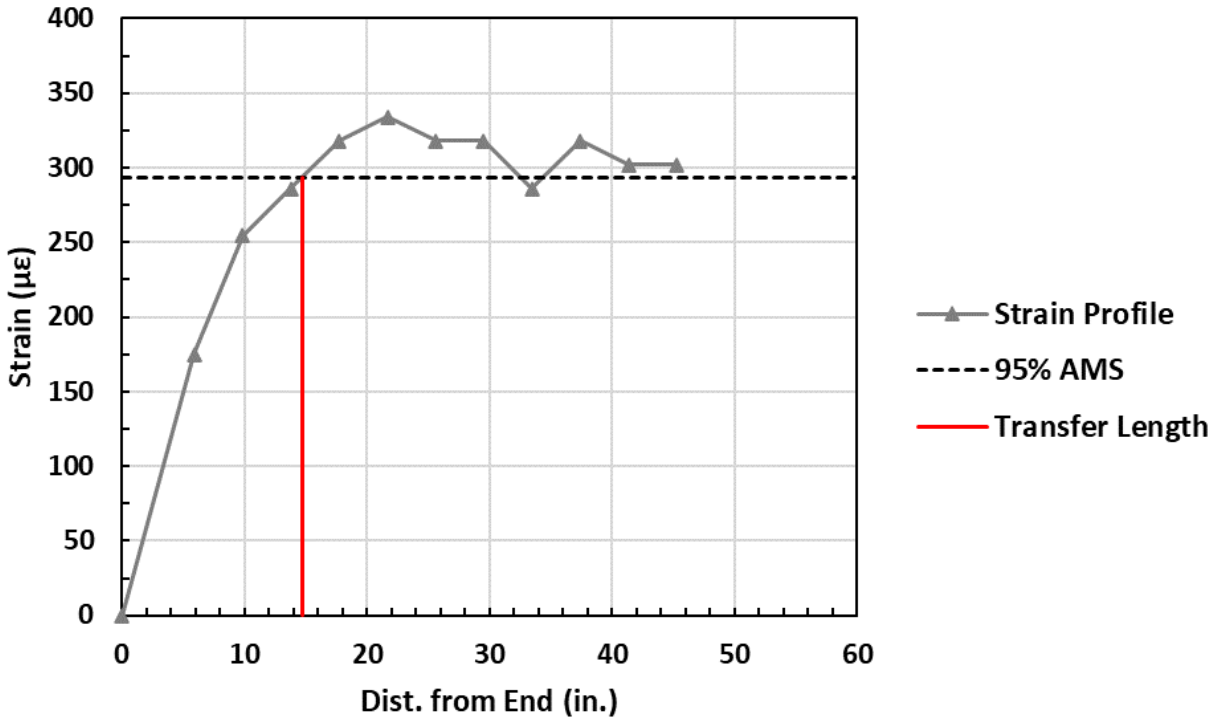

Figure 150: 95% AMS method applied to a typical beam end strain profile (B5-24TR, live end, west side)

For each side of each beam end where strain profiles were measured, the 95% AMS method was applied as shown in Figure 150 to obtain a measurement of the prestress transfer length. The strain plateau was averaged to obtain the average maximum strain (AMS), and 95% of that value was plotted against the strain profile. The points on the strain profile that fell on either side of the 95% AMS line were used to perform linear interpolation and identify the

corresponding location on the beam where 95% AMS intersected the strain profile. The resulting transfer lengths were averaged between either side of each beam end to obtain an average live end and dead end transfer length measurement for every TR series prestressed beam. Section 4.4.2.4 summarizes these average transfer length measurements at both prestress release and 56 days. Although DEMEC readings were taken at many more ages, transfer lengths were not determined from every set of measurements considering the relatively minor changes in transfer length observed between release and 56 days.

4.4.2.3 End-Slip/Strand Draw In

Table 26 summarizes the strand draw-in values measured for all 14 prestressed beams at release, including both the DV series and the TR series specimens.

Table 26: Strand Draw-In at Release for all Prestressed Beams

	Beam #	Strand End Slip (in.)		
		Live End	Dead End	Average
3 hr. release	B4	0.074	0.093	0.084
	B6	0.056	0.072	0.064
	B7	0.056	0.053	0.055
	B8	0.056	0.058	0.057
	B9	0.075	0.070	0.072
	B10	0.062	0.075	0.069
	B11	0.070	0.063	0.066
	Avg.	0.064	0.069	0.067
24 hr. release	B3	0.056	0.051	0.054
	B5	0.058	0.056	0.057
	B12	0.053	0.055	0.054
	B13	0.059	0.062	0.060
	B14	0.060	0.064	0.062
	B15	0.058	0.073	0.066
	B16	0.062	0.062	0.062
	Avg.	0.058	0.060	0.059

Although the difference in average strand draw-in values between live and dead ends are minimal, the average strand draw-in in Table 26 for the dead ends was slightly higher than for the live ends. In addition, out of 14 beams, 8 showed higher individual dead end strand draw-in

measurements, 1 showed the same, and only 5 showed higher individual live end strand draw-in measurements. This is notable, because with a sudden prestress release using a torch cut for example, the live end may experience a shock load that can lead to more observed strand drawn-in, if the strands on each end are not cut simultaneously. In this research, however, the live ends experienced a very gradual prestress release with the hydraulic system, while the dead ends still had to be cut with an angle grinder or torch. Due to anchorage from the beam and friction with the prestressing bed, the dead ends retained residual tension after release of the prestress at the live end, evidenced by the beams lurching and rocking on the prestressing beds when the dead ends were cut free. The strand draw-in measurements may indicate that the prestress and release procedures used in Fears Lab for this project may actually have "shocked" the dead ends slightly more than the live ends.

4.4.2.4 Summary and Comparison of Techniques

Table 27 summarizes the transfer lengths at prestress release computed from all 3 measurement methods for the TR series prestressed beams. For reference, Table 19 in Section 4.2.4 shows the compressive strength at release for each beam. The TR series early (3 hr) release beams averaged 6 ksi compressive strength at release and the TR series typical (24 hr) release beams averaged 9.1 ksi compressive strength at release.

Table 27: Comparison of Transfer Length Measurement Techniques at Release

Method	End	B4-3TR	B11-3TR	B3-24TR	B5-24TR	3 hr. Avg.	24 hr. Avg.
VWSG	Live	18.5	N/A	10.4	N/A	18.5	10.4
	Dead	20.4	N/A	10.2	N/A	20.4	10.2
	Avg.	19.5	N/A	10.3	N/A	19.5	10.3
DEMEC	Live	17.5	15.5	10.8	13.4	16.5	12.1
	Dead	17.7	16.0	12.0	12.6	16.8	12.3
	Avg.	17.6	15.7	11.4	13.0	16.7	12.2
End-Slip	Live	20.1	18.4	13.5	14.2	19.3	13.8
	Dead	27.1	16.0	11.7	13.5	21.6	12.6
	Avg.	23.6	17.2	12.6	13.8	20.4	13.2
Overall Avg.		20.2	16.5	11.4	13.4	18.9	11.9

Table 27 shows that overall, every measurement method resulted in transfer lengths that were on average smaller for the beams that had prestress released at 24 hours compared to those with prestress released at 3 hours. However, the transfer lengths measured for the 3 hour prestress release were still low in an absolute sense. For example, the ACI provision for the transfer length as it relates to shear capacity is 50 d_b, resulting in a value of 26 in. for these beams. Both the VWSG and DEMEC methods resulted in average transfer lengths of less than 20 in. for the 3 hour release beams, and even the end-slip method which can be prone to over-estimating transfer length resulted in an average value less than 21 in.

Table 28 summarizes the transfer lengths for the TR series beams computed from all 3 measurement methods at 56 days after casting. The TR series early (3 hr) release beams averaged 11.9 ksi compressive strength at 56 days. Cylinders were not tested for the TR series typical (24 hr) release beams at 56 days. However, the compressive strength for B5-24TR at 35 days was also 11.9 ksi, and the RS-SCC experiences most its compressive strength gain within the first month or so of age.

Table 28: Comparison of Transfer Length Measurement Techniques at 56 Days

Method	End	B4-3TR	B11-3TR	B3-24TR	B5-24TR	3 hr. Avg.	24 hr. Avg.
VWSG	Live	20.5	N/A	12.8	N/A	20.5	12.8
	Dead	21.2	N/A	10.8	N/A	21.2	10.8
	Avg.	20.9	N/A	11.8	N/A	20.9	11.8
DEMEC	Live	16.6	14.5	12.9	11.7	15.5	12.3
	Dead	16.3	14.2	13.2	14.0	15.2	13.6
	Avg.	16.4	14.4	13.1	12.8	15.4	13.0
End-Slip	Live	23.2	17.9	15.9	13.1	20.6	14.5
	Dead	26.9	16.2	18.2	18.8	21.6	18.5
	Avg.	25.1	17.1	17.0	16.0	21.1	16.5
Overall Avg.		20.8	15.7	14.0	14.4	19.1	13.7

The prestress transfer lengths were determined at a later age, to evaluate the change in behavior over time. It is not uncommon for transfer lengths to increase over time. This is because time-dependent effects, like creep and shrinkage, cause the compressive strain to continue to increase over time, so if the bond stress distribution shape does not vary drastically, it may take incrementally more bonded strand length to attain the higher maximum strains at later ages. An age of 56 days was chosen for the later time increment, because a complete set of DEMEC and end-slip measurements was not available at 28 days.

Table 28 shows that compared to Table 27 the transfer lengths measured using each method did increase somewhat between release and 56 days for both prestress release ages, with an increase of just over 7% on average. The only exception, importantly, is the DEMEC method for the early (3 hr) prestress release beams. The DEMEC determined transfer lengths for both early (3 hr) release beams were the only method that showed a marked decrease in transfer length between release and 56 days. This is a critical observation, considering the temperature effects observed between the pre-release and post-release DEMEC measurements for the early (3 hr) prestress release beams (see Section 4.4.2.2). It is reasonable to conclude that because the

apparent elastic strains were overestimated because of the thermal contraction of the beams, the DEMEC measurements at release for the early (3 hr) prestress release beams exaggerated the initial transfer length somewhat. Therefore, the subsequent DEMEC measurements may not have accurately represented the ongoing increases in strain due to time-dependent effects which likely disrupted the increasing transfer length trend observed for the other beams. In the broader sense, however, the changes in transfer length for all the beams were slight between release and 56 days. The early (3 hr) DEMEC transfer lengths only decreased by just over 1 in. (~8%). For the other measurement approaches, the average increase in transfer length varied from less than 1 to 2 in., corresponding to a range from around 3% to around 15% with the exception of some end-slip measurements which showed a greater change (up to 25% on average). Since the transfer lengths did not vary drastically between release and 56 days, a comparison between all techniques was not performed at intermediate ages.

Figure 151 shows the average transfer lengths determined from every measurement method for the TR series beams for the 3 hour and 24 hour release ages at prestress release and at 56 days. The ACI and AASHTO shear design transfer length estimates are shown with dashed lines for reference (ACI 318, 2014; AASHTO LRFD, 2017).

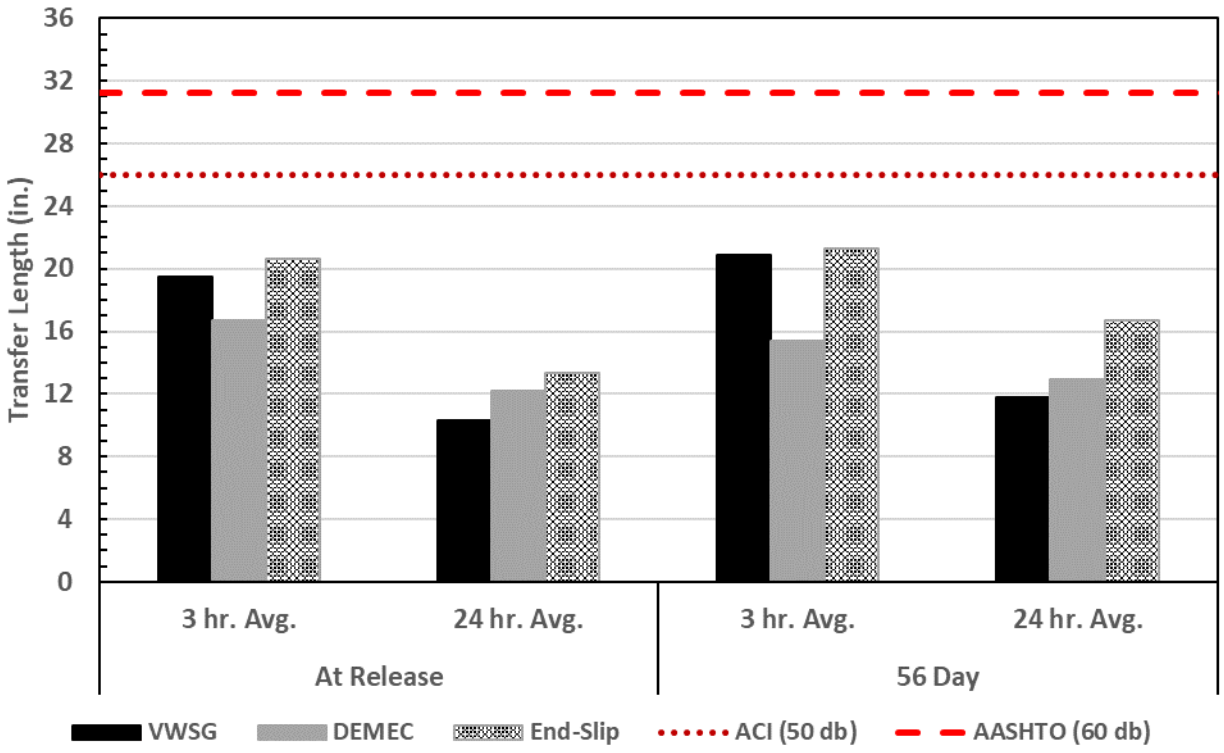

Figure 151: Average transfer length results at prestress release and at 56 days for 3 hour and 24 hour prestress release

In Figure 151, the value of 50 d_b is 26 in. and the value of 60 d_b is 31.2 in. The maximum measured average transfer length, arising from the end-slip method with a bond stress distribution factor of 2.61, was just over 21 in. at 56 days for the 3 hour prestress release. This value is almost 20% less than the ACI value of 50 d_b and is more than 30% less than the AASHTO value of 60 d_b. For the 24 hour release beams, the VWSG measurements gave the shortest transfer length, followed by the DEMEC measurements, with the end-slip method giving the highest transfer length at both prestress release and 56 days. The highest transfer length estimated using the end-slip approach for the 24 hour beams at release was 13.2 in. and at 56 days was 16.5 in. This means that at 56 days, the maximum transfer length estimate for the 24

hour beams was more than 35% less than the ACI value of 50 d_b and was more than 46% less than the AASHTO value of 60 d_b.

For the 3 hour release beams, the end-slip method still gave the highest transfer length estimate, but only by a small margin compared to the VWSG measurements. For the 3 hour beams, the DEMEC approach gave the smallest transfer length estimates. It is not entirely clear why this is the case, but the VWSG are considered to provide a more accurate strain profile for multiple reasons. The VWSG are properly temperature compensated, located concentrically at the center of gravity of the prestress (cgs), and are not prone to differential shrinkage or other surface effects like the DEMEC system. The VWSG are also not prone to the user error or bias that can greatly impact the accuracy and repeatability of the DEMEC measurements. Because of the numerous factors that can influence prestressed strand bond, it is difficult to say which method is "correct" in an absolute sense. At least for this testing, however, the VWSG approach seemed to have the fewest known deleterious influences.

Since the ACI/AASHTO transfer length estimates for shear design of 50 d_b = 26 in. and 60 d_b = 31.2 in. respectively do not fit the experimental data particularly well, it is reasonable to examine alternate approaches. Two common approaches used to better estimate the prestress transfer length are to consider either the initial or effective prestress force, the concrete compressive strength (typically at prestress release) or some combination of both.

The first alternate approach for estimating the measured transfer length was to use the ACI/AASHTO equation (Equation 3) which includes the consideration of the effective prestress force:

$$L_t = \frac{1}{3000} f_{se} d_b \quad (3)$$

where the variables have been previously described in Chapter 2. Equation 3 is the ACI formulation, and the AASHTO formulation is the same, except with units converted from psi to ksi. To use Equation 3 requires an accurate estimate of the total prestress losses resulting in the effective prestress force of interest. The prestress loss data is not presented until Chapter 5, but the measured prestress losses for these experiments (including elastic shortening and time-dependent losses) resulted in effective prestress in the range of 168 – 177 ksi. Using this data with Equation 3 would result in a transfer length estimate of between 56 and 59 strand diameters or about 29.1 to 30.7 inches. This estimate range falls between the 50 d_b and 60 d_b estimates and is therefore no more helpful in accurately estimating the measured RS-SCC transfer lengths.

Floyd, Howland, and Hale (2011) conducted a review of many formulations for transfer and development length that various researchers have proposed (Floyd et al., 2011). Many of these proposed equations utilize the initial prestress (f_{si}) instead of the effective prestress (f_{se}), and therefore the resulting transfer length estimates are much longer than the experimental transfer lengths measured in this research. Ramirez and Russell, however, proposed a formulation specifically for high strength concrete which utilizes the compressive strength at release as the key parameter as shown in Equation 9 (Ramirez and Russell, 2008):

$$L_t = \frac{120}{\sqrt{\frac{f'_{ci}}{1000}}} d_b \geq 40 d_b \qquad (9)$$

where f'_{ci} is the concrete compressive strength at release (psi) and d_b is the strand diameter (in.). For the early (3 hour) release TR series beams, f'_{ci} was 6000 psi and for the typical (24 hour) release TR series beams, f'_{ci} was 9100 psi (see Table 19, Section 4.2.4). Using Equation 9 would then predict transfer lengths of $49d_b$ (25.5 in.) for the early (3 hour) release beams, and $40d_b$ (20.8 in.) for the typical (24 hour) release beams. At prestress release, the

average measured transfer length across all methods for the early (3 hour) release beams was 18.9 in. and for the typical (24 hour) release beams was 11.9 in. The next closest transfer length estimation of 50 d_b (26 in.) has an average error of almost 38% for the early (3 hour) release beams and an average error of over 100% for the typical (24 hour) release beams. By using Equation 9 and comprehending the compressive strength at release, the average error of the estimate only decreases by 3% for the early (3 hour) release beams, but the average error of the estimate decreases by more than 43% for the typical (24 hour) release beams. Although Equation 9 from Ramirez and Russell still predicts longer transfer lengths than those measured in these experiments, it appears to provide a slightly more reasonable starting point for RS-SCC. Creating unique prediction equations for RS-SCC based on the data of this research alone is inadvisable due to the limited quantity of data overall. However, the data of this dissertation provides a starting point for subsequent research to build on, and it is advised that future prediction models for transfer length in RS-SCC include provisions for concrete compressive strength at least, and perhaps other parameters as well.

One final but very important observation to make about this data is that while the measured transfer lengths were consistent and very short in an absolute sense, the prestress release method can have a significant effect on the transfer length (Hanson and Kaar, 1959). When prestress is released with torch cutting, saw cutting, or bolt-cutters the prestress force can jolt and shock load the beam significantly especially on its live end (or whichever end is cut first if both ends are not cut at precisely the same time). Because prestress was released gradually in this study, it is important to understand the context of the data and know that the short measured transfer lengths are due in some part to the prestress release method and not entirely to the intrinsic bond properties of the BCSA cement concrete.

5. Prestress Losses: Measurement and Analysis

5.0 Introduction

The final phase of this research included three primary objectives. The first objective was to experimentally measure prestress losses for RS-SCC beams, with particular emphasis on determining any differences in immediate or long-term losses between early (3 hr) and typical (24 hr) prestress release. The second objective was to use the measured material property data including elastic modulus, creep, and shrinkage to develop a model to predict prestress losses for the RS-SCC. The third objective was to use the prestress loss data gathered from the instrumented beams constructed in the second phase of the project to critically evaluate the performance of the new model compared to existing frameworks. A secondary approach used to fulfill the third objective was to use data from the literature where prestress losses for BCSA cement concrete prestressed beams were measured in order to see how the model performed for other beam configurations or mix designs.

5.1 Prestress Loss Measurement

Prestress losses for the beams fabricated in this project were primarily analyzed using the data gathered from the VWSG embedded in the concrete at the level of the prestressing strands in 4 of the beam specimens with 2 early release (3 hr) specimens and 2 typical release (24 hr) specimens. The installation techniques and photos of the gages are described in detail in Chapter 4. Although in principle the prestress losses could be examined for every gage that was placed outside the observed transfer zone, the analysis was primarily restricted to the gages placed at midspan for two reasons. First, because beams B5-24TR and B11-3TR only had gages placed at midspan due to a limited number of instruments while beams B3-24TR and B4-3TR had gages throughout their length, prestress losses at midspan could be directly compared between all four beams that were monitored over time. Second, by analyzing the prestress losses at midspan, the

prestress will be fully developed and any end-region effects that might present problems in data analysis are eliminated. Analyzing the prestress losses for the VWSG at midspan introduced the necessity to consider the effects of beam self-weight, but this effect was determinate and simple to account for. Figure 152 shows the four beams that were monitored for long-term prestress losses in storage in the Fears Lab high bay.



Figure 152: Beams in storage for long-term prestress loss measurement in Fears Lab high bay

The concrete reaction blocks pictured in Figure 152 were used to set the beams high enough to facilitate the performance of long-term DEMEC measurements. Each time a beam was removed from the prestressing bed (usually a few days after casting for the TR series beams), the beam was moved with the overhead bridge crane and placed on 4 in. thick by 6 in. wide

neoprene bearing pads on the concrete reaction blocks. The beams then remained there for the duration of this project. The beams had to be staggered longitudinally to fit the bearing pads on the reaction blocks, so as a result, both beams with VWSG throughout their length (B3-24TR and B4-3TR) were placed with a center to center span of 13.5 ft and both beams with VWSG at midspan only (B5-24TR and B11-3TR) were placed with a center to center span of just over 11 ft. The difference in strain due to the change in self-weight moment was minor and did not appear to cause a noticeable difference between the two groups of beams.

5.1.1 Typical (24 hour) Prestress Release

Beam B3-24 TR was the designation for the typical (24 hour) age prestress release beam with VWSG both in the end regions and at midspan. The VWSG in B3-24TR were connected to a data logger that collected strain measurements at specified intervals. The measurement interval was set to 1 minute (the shortest increment possible for this particular logger) during casting, set, and prestress release. After prestress release, the measurement interval was increased to 15 minutes and after a few months it was increased to 30 minutes. This saved memory and battery power for the logger, and because the beam was no longer undergoing rapid changes in strain states, the small measurement intervals were no longer necessary. Figure 153 shows the strain data (compression positive) at midspan for beam B3-24 TR for the first 7 days, so that key features related to early age effects can be highlighted.

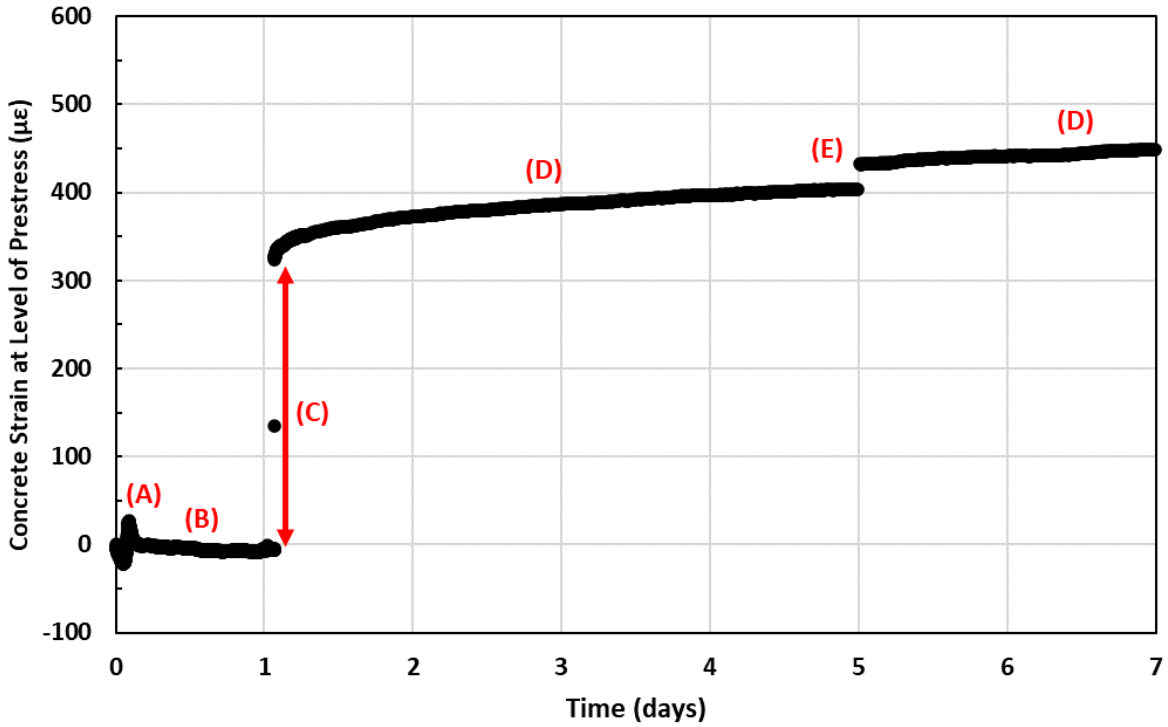

Figure 153: Early-age changes in midspan strain for Beam B3-24TR: (A) casting and setting, (B) shrinkage and thermal strains, (C) elastic shortening at prestress release, (D) time-dependent deformation (primarily creep and shrinkage), and (E) moving beam from prestressing bed to long-term supports

Figure 153 shows multiple key features worth exploring. Features (A) and (B) are fairly self-explanatory, as minor changes in strain occur when the concrete is cast and begins to harden enough that temperature and shrinkage cause measurable changes (VWSG zero point taken from time of casting). Elastic shortening, (C), is explored in detail in Section 5.2. Time-dependent deformation, (D), is discussed in detail when time-dependent prestress losses are analyzed in Section 5.3 and then modelled in Section 5.4. Feature (E) represents a discontinuity that was observed at the time when the beam was moved from the prestressing bed to its long-term supports as shown in Figure 152. While the beam was in place on the bed after prestress release, it was cambered such that its span was nearly the full 20 ft length of the specimen. As soon as the beam was moved to long-term storage, however, the span was approximately 13 ft from face

to face of the support pads. The resulting change in dead weight moment combined with transformed section properties would cause a theoretical decrease in tension (i.e. increased compression) at the strand level of about 0.105 ksi which equals 22.1 με assuming a concrete modulus of elasticity of just over 4700 ksi (9000 psi concrete). The actual instantaneous change in strain immediately after moving the beam measured by the VWSG and shown in Figure 153 was 28.8 με, which varies from the theoretical value by around 30%. Although this is not a small relative error, the agreement between the measured and theoretical values is outstanding on an absolute scale; the difference between the two is less than 7 με (millionths). Considering that the VWSG utilized in this research has a measurement resolution of 1 με, as much of the relative error between the measured and theoretical values could be due to uncertainty in the concrete modulus and cross-sectional properties as the gage accuracy. This speaks to the precision of the VWSG system and reinforces that the elastic modulus estimate developed from Chapter 3, combined with standard transformed section properties, satisfactorily predicts the behavior of the RS-SCC beam.

Figure 154 shows the shows the strain data at midspan for beam B3-24 TR, focusing on the long-term, time-dependent behavior with measurements out to around 330 days.

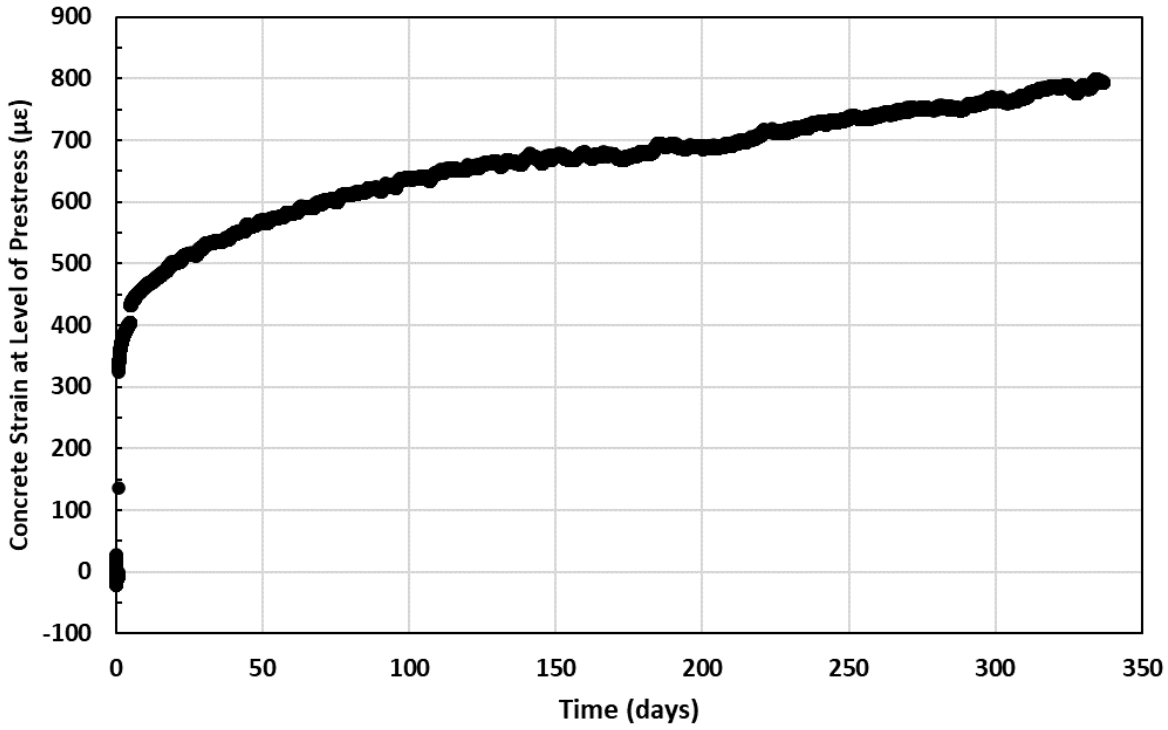

Figure 154: Time-dependent changes in midspan strain for Beam B3-24TR

The concrete strain in Figure 154 due to elastic effects, creep, and shrinkage (which shorten the strands and lead to the loss in effective prestress) steadily increases after prestress release and continues after the beam was set on its long-term supports at about 5 days of age. The rate of change gradually decreases between about 50 and 150 days and between 150 and 180 days there was very little additional strain. From approximately 180 days to 330 days, however, the compressive strain again increases almost linearly. This is most likely due to temperature effects; B3-24TR was cast on Nov. 18, 2021 so the 180 day (6 month) mark was May 18, 2022. This marked the beginning of significantly hotter weather, and corresponding higher ambient temperature in the Fears Lab high bay which is not climate controlled. If the beam were perfectly free to expand, thermal expansion would cause a net decrease in compressive strain. In this case, however, it is hypothesized that the bearing pads, which were stiff relative to the size and length

of the prestressed beams, were able to restrain the beams against expansion to some degree. Therefore, as seasonal warming occurred throughout summer 2022, the thermal expansion of the beams resulted in a net increase in compressive strain at the level of the prestress force. Monitoring will be continued into the subsequent winter months to see if the seasonal cooling produces the expected opposite effect, but this eventuality is beyond the scope of this discussion.

Figure 155 shows the shows the long-term strain data at midspan for B3-24TR and B5-24TR. B5-24TR had only 1 gage at midspan, and was read intermittently with a discrete, single-channel reader instead of being connected to a continuous data logger. These intermittent readings were taken weekly the first month (except 28 days which was missed), monthly until around 4 months, and once every few months thereafter.

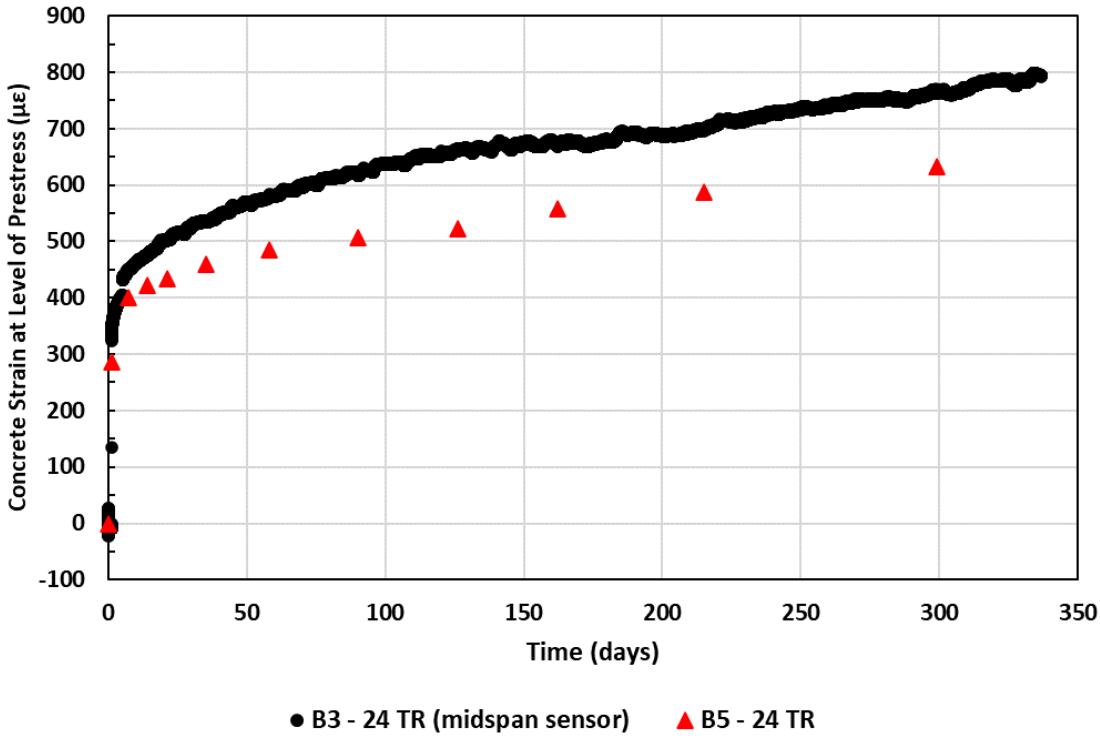

Figure 155: Midspan time-dependent strain comparison for 24 hour release beams

Figure 155 shows that both the elastic strain at prestress release and the strain due to time-dependent effects measured by the VWSG in B5-24TR were markedly lower than the same measurements for B3-24TR. The elastic strain measured at release for B3-24TR was about 15% higher than B5-24TR, and at around 160 days, the total strain measured for B3-24TR was around 20% higher than B5-24TR. Hypothetically, there should be a similar increase in strain due to summer temperatures for B5-24TR as that which was observed for B3-24TR. This increased strain rate would initiate earlier along the curve for B5-24TR because this beam was cast about 70 days after B3-24TR. Although it is more difficult to detect because of the discrete strain measurements, there is indeed a sort of "step" in the curve between about 120 and 160 days for B5-24TR. B5-24TR was cast on January 26, 2022 so that step in the curve corresponds to sometime between late May and early July 2022, which also coincides with the extremely hot ambient conditions noted for B3-24TR.

Figure 156 shows the non-prestressed companion mini-beam cast along with beam B3-24TR and instrumented with a single VWSG to measure shrinkage deformation and estimate the shrinkage portion of the prestress losses. Due to limited instrumentation, one companion beam was cast with a typical 24 hr release beam (B3-24TR) and one companion beam was cast with an early 3 hr release beam (B4-3TR). The companion beams were cast with the same concrete used in the batch for the full size beam, and the companion beams were cured and stored in the same conditions as the full size beams. The VWSG instruments for each companion beam were placed in the middle of the beam at the level of the lower reinforcement.



Figure 156: Non-prestressed companion beam for shrinkage measurements

The theoretical underpinning to this approach was that, to accurately replicate the degree of shrinkage that the full beam will experience, the V/SA ratio and the reinforcement ratio of the companion and the full specimen must match. Since the strands in the companion beam were not tensioned, no creep could occur, so the only time-dependent dimensional reduction apart from thermal effects would arise from restrained drying shrinkage. Since the strands in the companion beams were not tensioned like the full scale beams, the level of restraint may not be exactly proportional, but should be similar enough to accurately estimate shrinkage losses. The companion beams utilized two 0.52 in. strands and two No. 6 bars set at the same elevations as in the full beams, and two sheets of the same WWR were also included in the same orientation as in the full beams. The end plates shown in Figure 156 were left on the companion beams throughout the life of the tests so that their V/SA ratio would match the full beams as closely as

possible. The V/SA ratio of the full size beams was 2.07 overall, and the V/SA ratio was 2.11 if the surface area of the beam ends was neglected. This minor difference (less than 2%) is because the 20 ft length of the full size beams had a much greater V/SA ratio impact than the beam ends. For the 2 ft long companion beams, the V/SA ratio would have been around 1.8 overall, but by leaving the aforementioned end plates covering the companion beam ends, the effective V/SA ratio was 2.11 thereby closely matching the full size beams. Figure 157 shows the shrinkage strain that was measured for the companion mini beam cast with B3-24TR. Shrinkage is shown as a positive strain, and the zero point of the VWSG data was set as the time of casting the concrete.

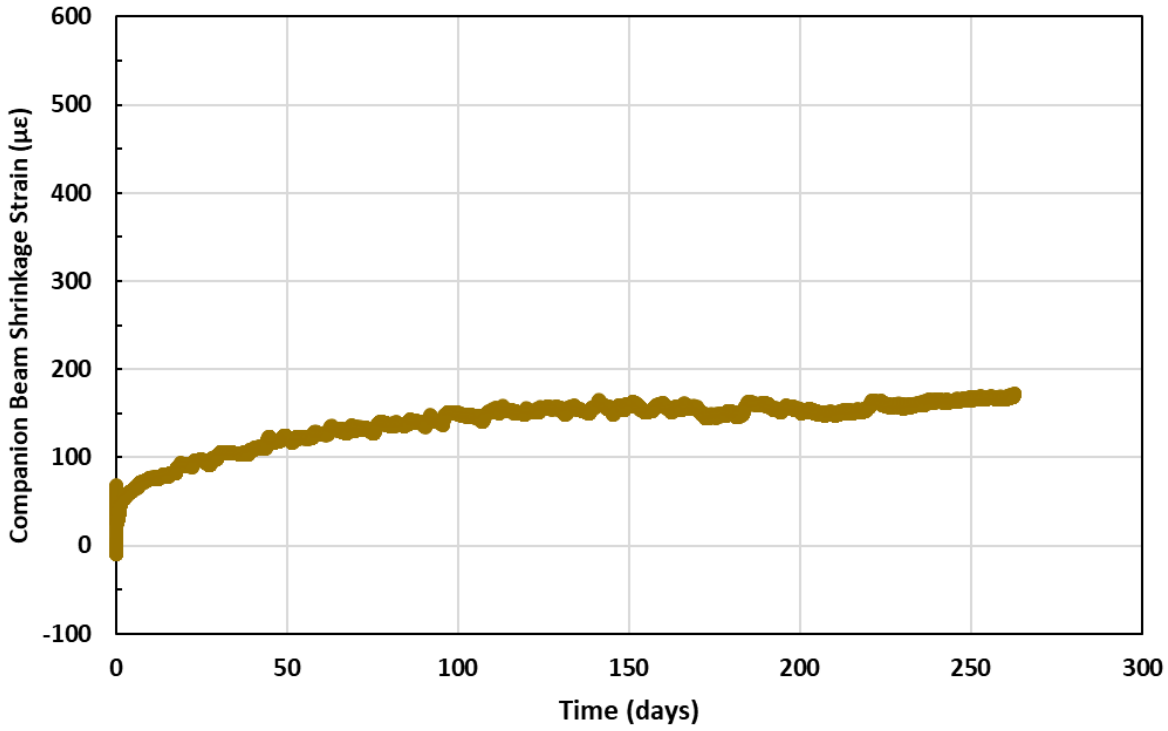

Figure 157: Shrinkage of non-prestressed companion beam for B3-24TR

Figure 157 shows that the companion beam exhibited about 170 με of net restrained shrinkage by an age of 260 days. If the total drying shrinkage is considered as measured from the

maximum expansion after casting, then this value would be around 180 με. Assuming that these shrinkage totals are proportional to the prestressed beam (which was the purpose of the companion beam), 170-180 με shortening would correspond to a prestress loss of 4.9-5.1 ksi. The time-dependent prestress loss totals are presented in Section 5.3, but for B3-24TR, average shrinkage deformation of 175 με would represent around 42% of the time-dependent deformation causing prestress loss and around 23% of the total deformation causing prestress loss (including elastic shortening effects).

5.1.2 Early (3 hour) Prestress Release

Beam B4-3TR was the designation for the early (3 hr) age prestress release beam with VWSG both in the end regions and at midspan. The VWSG in B4-3TR were connected to a data logger that collected strain measurements at specified intervals. Like B3-24TR, the measurement interval was set to 1 minute during casting, set, and prestress release and the interval was increased to 15 minutes and then 30 minutes for long-term monitoring. Figure 158 shows the strain data at midspan for B4-3TR for the first 7 days, so that key features related to early age effects can be highlighted.

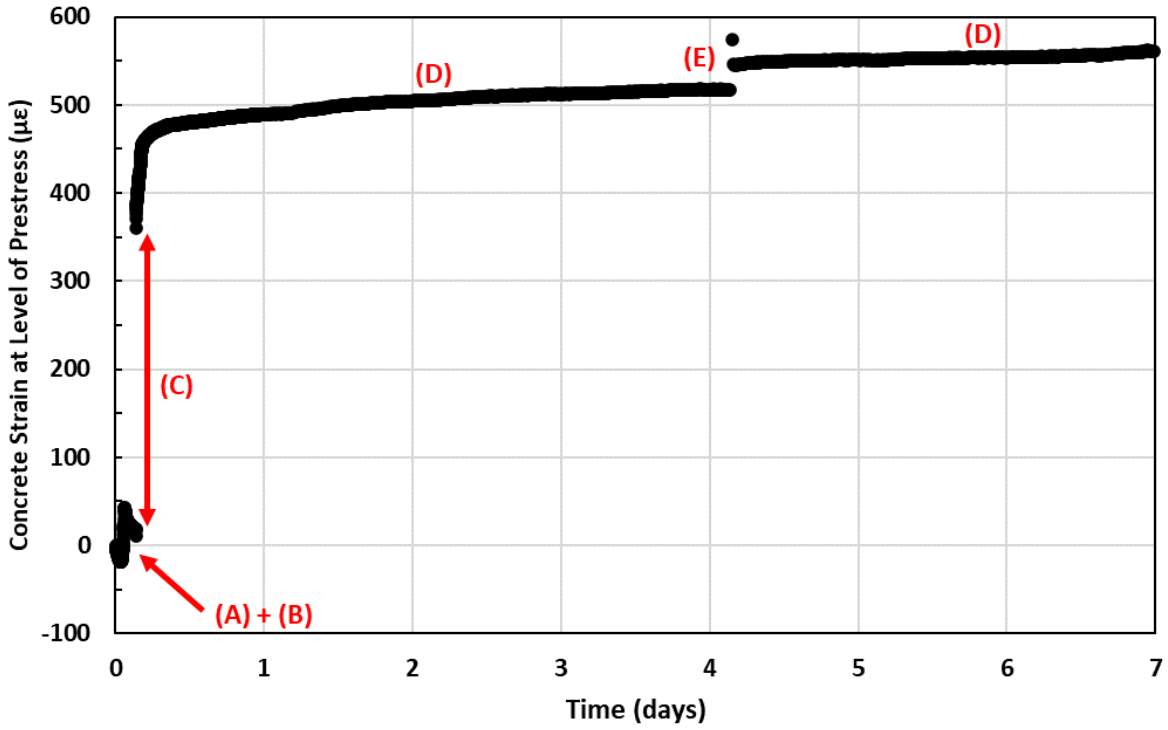

Figure 158: Early-age changes in midspan strain for B4-3TR: (A)+(B) casting, setting, and shrinkage/thermal strains; (C) elastic shortening at prestress release; (D) time-dependent deformation (primarily creep and shrinkage); and (E) moving beam from prestressing bed to long-term supports

In Figure 158, the (B) segment consisting of shrinkage and thermal strains after casting but prior to prestress release is much shorter than for B3-24TR because of the early prestress release time. Similarly to beam B3-24TR, segments (C) and (D) represent the elastic shortening and time-dependent strains respectively. It is interesting to note, however, that the shape of the curve immediately after prestress release for B4-3TR differs from B3-24TR. For beam B3-24TR with prestress release at 24 hr, the curve flattened out rapidly after prestress release (see Figure 153). For beam B4-3TR with early (3 hr) prestress release, however, Figure 158 shows that after the elastic shortening, the compressive strain continued to increase rapidly (evidenced by a nearly vertical curve) for a few hours, before beginning to flatten out. Just like for beam B3-24TR, a discontinuity in strain when the beam was moved to storage is clearly visible (marked

(E) in Figure 158), in this case early in day 4. The magnitude of this change in strain for beam B4-3TR is 28.6 με, very close to the change in strain at the same point for B3-24TR of 28.8 με. The span and support locations for beam B4-3TR were the same as for B3-24TR, so the theoretical change in strain was still 22.1 με, which differs from the measured value of 28.6 με by around 29%. The fact that two independently instrumented beams from separate mixes would register changes in service level strain to within a few tenths of a microstrain of one another speaks to the excellent performance of the VWSG. Secondarily, the general proximity of the measured change in strain due to beam self weight to the theoretical change in strain due to beam self weight lends increased confidence to the physical properties measured in this research, like the elastic modulus of the concrete, being representative of actual material behavior.

Figure 159 shows the strain data at midspan for beam B4-3TR, focusing on the long-term, time-dependent behavior with measurements out to around 315 days.

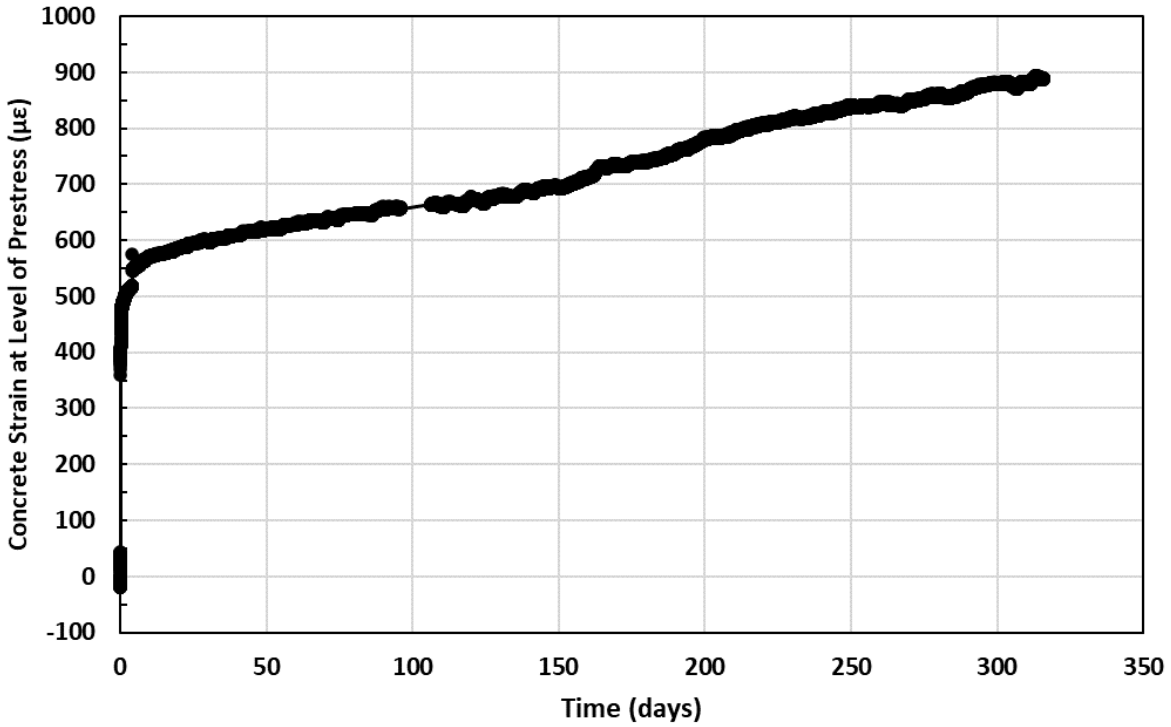

Figure 159: Time-dependent changes in strain at midspan for beam B4-3TR

The concrete strain in Figure 159 due to elastic effects, creep, and shrinkage (which cause the strands to shorten and leads to the loss in effective prestress) gradually increases after the beam was set on its supports at about 4 days of age. The strain rate remains mostly constant (linear trend) between about 50 and 150 days. Starting after 150-160 days, however, the compressive strain rate abruptly increases. A linear trend is maintained more or less, but with a steeper slope than previously observed. As mentioned for beam B3-24TR, this is most likely due to temperature effects; beam B4-3TR was cast on Dec. 9, 2021 so the 150-160 day (just over 5 month) mark was mid-May 2022. As stated previously, this time period marks the beginning of sustained hot weather in Oklahoma, and summer 2022 was a notably hot season. As explained before, it is hypothesized that as seasonal warming occurred throughout summer 2022, the

thermal expansion of the beams restrained by friction on the bearing pads resulted in a net increase in compressive strain at the level of the prestress force throughout the season.

Figure 160 shows the shows the long-term strain data at midspan for beam B4-3TR plotted with the same data for beam B11-3TR. Beam B11-3TR had only 1 gage at midspan, and was read intermittently with a discrete, single-channel reader instead of being connected to a continuous data logger.

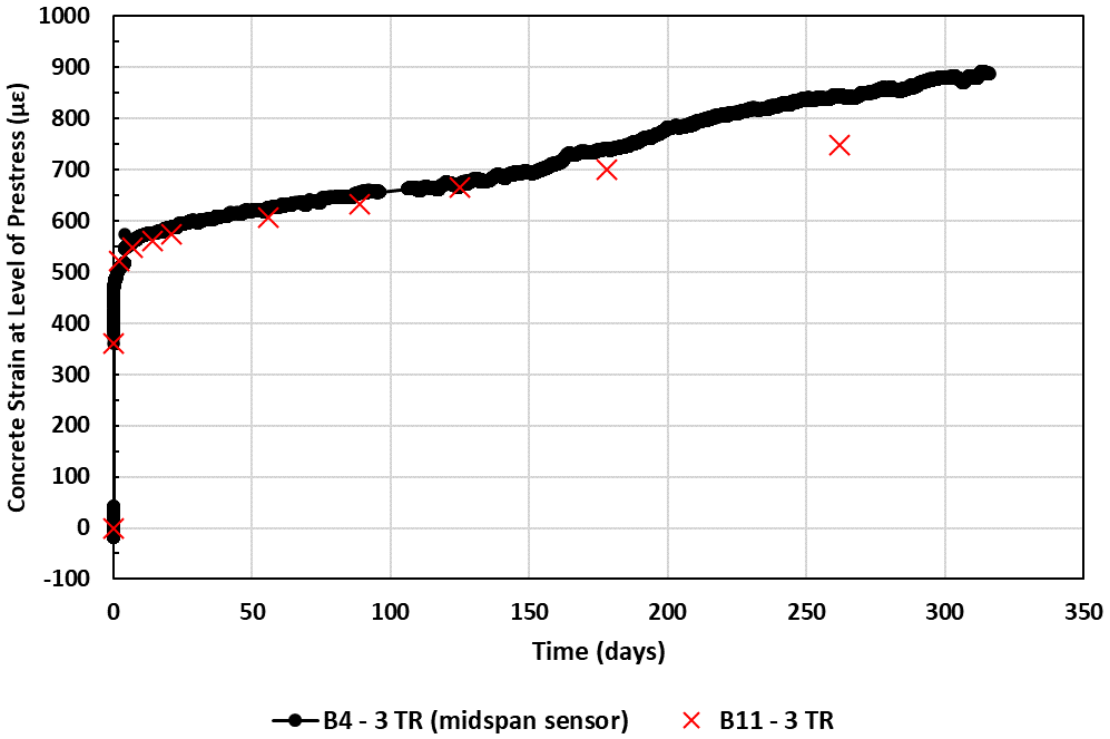

Figure 160: Midspan time-dependent strain comparison for 3 hour release beams

Figure 160 shows that both beams with an early prestress release at 3 hours showed similar elastic shortening and time-dependent strains, as the curves for the two beams overlay almost perfectly until around 6-9 months. The changes in elastic strain immediately after release varied by less than 2% between the two beams. At around 4 months, the total time-dependent

strains varied by less than 1% between the two beams. This variation increased to almost 13% by an age of about 260 days.

Figure 161 shows the shrinkage strains measured for the companion beam cast with B4-3TR.

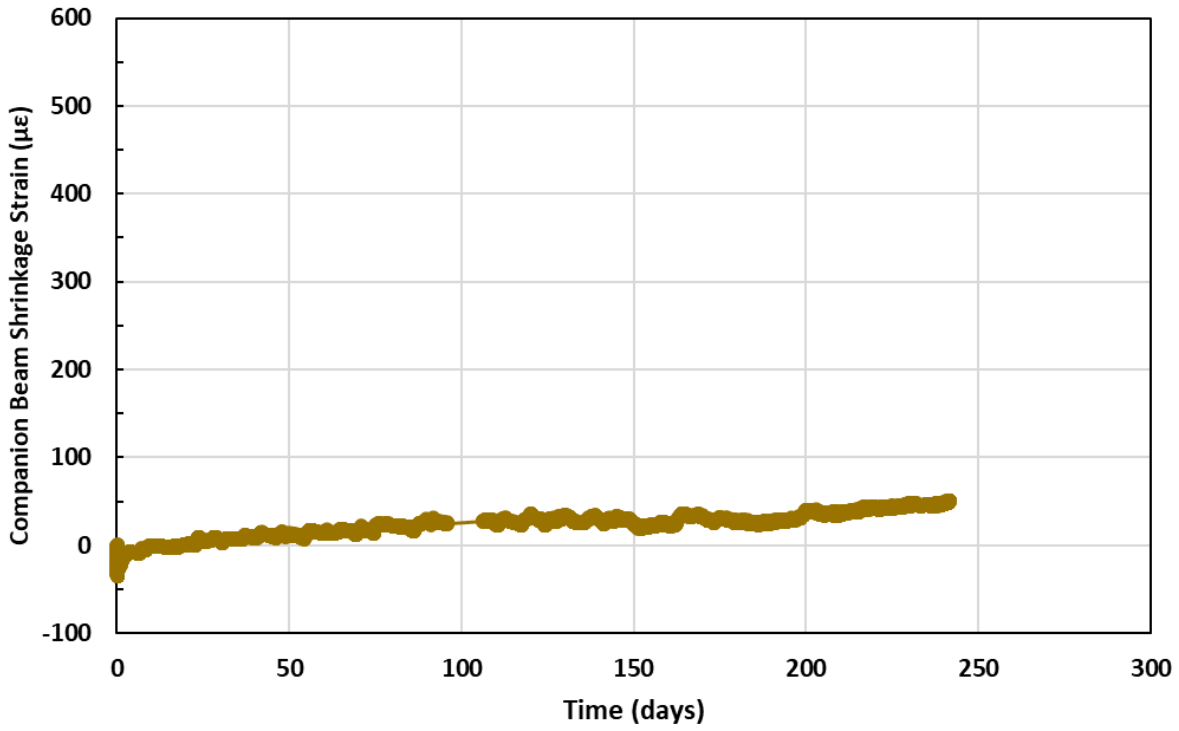

Figure 161: Shrinkage of non-prestressed companion beam for B4-3TR

Figure 161 shows that the companion beam exhibited about 50 με of net restrained shrinkage by an age of 240 days. If the total drying shrinkage is considered as measured from the maximum expansion after casting, then this value would be around 85 με. Assuming that these shrinkage totals are proportional to the prestressed beam (which was the purpose of the companion beam), 50-85 με shortening would correspond to a prestress loss of 1.4-2.4 ksi. The time-dependent prestress loss totals are presented in Section 5.3, but for B4-3TR, average shrinkage losses of about 68 με would represent around 15% of the time-dependent deformation

causing prestress loss and around 8% of the total deformation causing prestress loss (when including elastic shortening effects).

5.2 Elastic Shortening (ES)

Table 29 shows a comparison of the elastic shortening prestress losses measured for each beam using the VWSG and the theoretical elastic shortening losses. The theoretical ES values were computed according to fundamental mechanics by computing the net stress at the center of gravity of the prestressing strands due to the concentric and eccentric components of the prestress force as well as the beam's self-weight. That stress was converted to a strain using the concrete modulus of elasticity based upon the experimental measurements and best fit compressive strength correlation presented in Chapter 3 and Equation 5. Both the measured and the theoretical strains were converted to an equivalent prestress loss using the strand modulus supplied by the manufacturer. Transformed section properties were used for all computations. Although this computation is a fundamental application of engineering mechanics, the procedure stipulated by the AASHTO LRFD Specifications can be followed for explicit functional forms describing these steps. Note that this computation did not account for the changing prestress during elastic shortening; the calculation was treated as a single time step with the initial strand stress based on the load cell measurement immediately before prestress release.

Table 29: Measured and Theoretical Elastic Shortening Prestress Losses with Relative Difference

Release Time	Beam ID	Measured ES		Theoretical ES		% Diff's	
		με	ksi	με	ksi	-	Avg.
3 hr	B4 - 3 TR	353	10.1	392	11.2	10.9	6.6
	B11 - 3 TR	360	10.3	368	10.5	2.3	
24 hr	B3 - 24 TR	331	9.5	332	9.5	0.3	8.5
	B5 - 24 TR	286	8.2	334	9.6	16.6	

Figure 162 shows a graphical comparison of the measured and theoretical ES prestress losses.

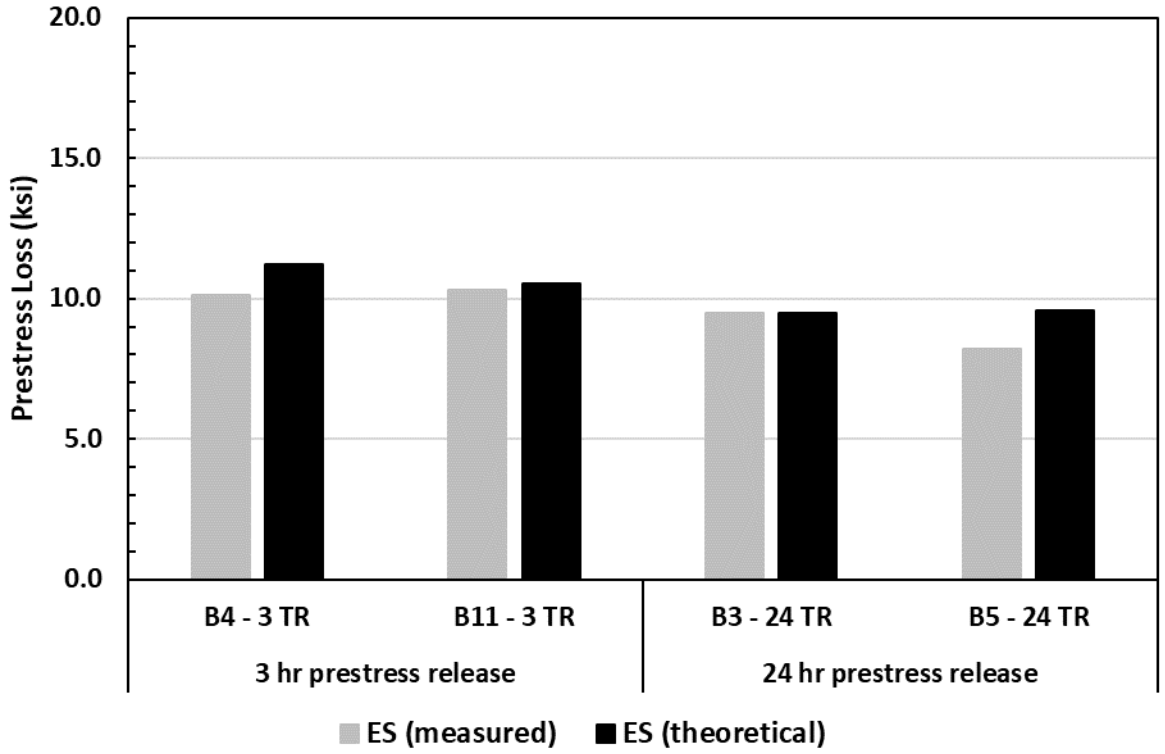

Figure 162: Comparison of measured and theoretical ES prestress loss values

Table 29 and Figure 162 show that, generally speaking, the measured ES losses agree closely with the calculated ES losses. Additionally, the elastic shortening of the 3 hour release

beams was slightly, but consistently, higher than that of the 24 hour release beams. This outcome is reasonable in light of the fact that the compressive strength at release and therefore the estimated elastic modulus for the 24 hour prestress release beams was higher than that of the 3 hour release beams. While both the measured and theoretical ES loss ranged from around 10.1-11.2 ksi for the 3 hour release beams, neither the actual nor the theoretical ES loss for the 24 hour release beams reached 10 ksi. The highest measured or estimated ES value for the 24 hour release beams was 9.6 ksi. It is possible that the theoretical ES values are higher than the measured ES values because the cross-section of the beam with the strands, top rebar, and continuous WWR has significant moment redistribution capacity and behaves with an even higher effective stiffness than the transformed section properties can account for.

5.3 Time-Dependent Losses

Figure 163 shows the time-dependent losses (consisting primarily of creep and shrinkage) for each of the 4 TR series beams which had at least 1 VWSG at midspan. The measured concrete strain data were temperature compensated, the elastic strain at prestress release was deducted, and the resulting strains were multiplied by the strand modulus (28,600 ksi) to obtain the observed decreases in strand stress shown in Figure 163.

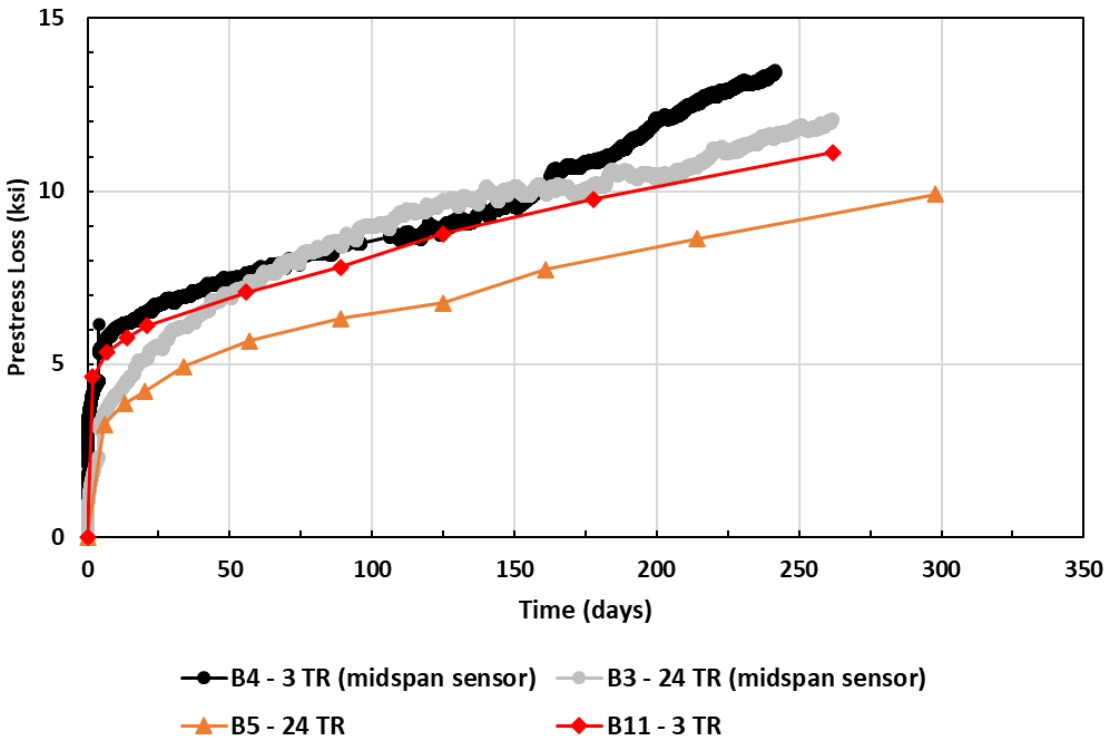

Figure 163: Time-dependent (primarily creep and shrinkage) losses for TR series prestressed beams

In Figure 163, the prestress losses for beams B3-24TR, B4-3TR, and B11-3TR are very close in magnitude to one another, with the results from beam B5-24TR noticeably lower. Similar to the observation made concerning the early age strain data with the ES shown, the time-dependent loss data in Figure 163 shows that a primary difference between the behavior of the early (3 hr) and typical (24 hr) prestress release is the shape of the loss curve, especially in the days immediately following prestress release. The strain curves for beams B3-24TR and B5-24TR roll over and flatten out comparatively soon after prestress release, while the strain curves for beams B4-3TR and B11-3TR retain a steep slope, rapidly accumulating losses for a few days after prestress release. However, after that point, the strain curves for the 3 hour release beams turn suddenly and then flatten out like those for the 24 hour release beams. In fact, the curves for beams B4-3TR and B11-3TR flatten out rapidly enough after their early steep segments that the

beam B3-24TR curve actually crosses both the B4-3TR and B11-3TR curves between 50 and 75 days. Additionally, apart from the suspected thermal effects observed for beam B4-3TR and the losses for beam B5-24TR being markedly lower than the others, it seems that the shape of the prestress loss curves may be a more significant difference between the time-dependent prestress losses for 3 hour versus 24 hour prestress release than the overall magnitude of the losses.

Figure 164 shows an itemized breakdown, estimating the contribution of each type of time-dependent effect to the long-term (240 day) prestress losses. As mentioned previously, non-prestressed companion beams used to estimate shrinkage losses were cast along with beams B3-24TR and B4-3TR. Beams B5-24TR and B11-3TR did not include shrinkage companions.

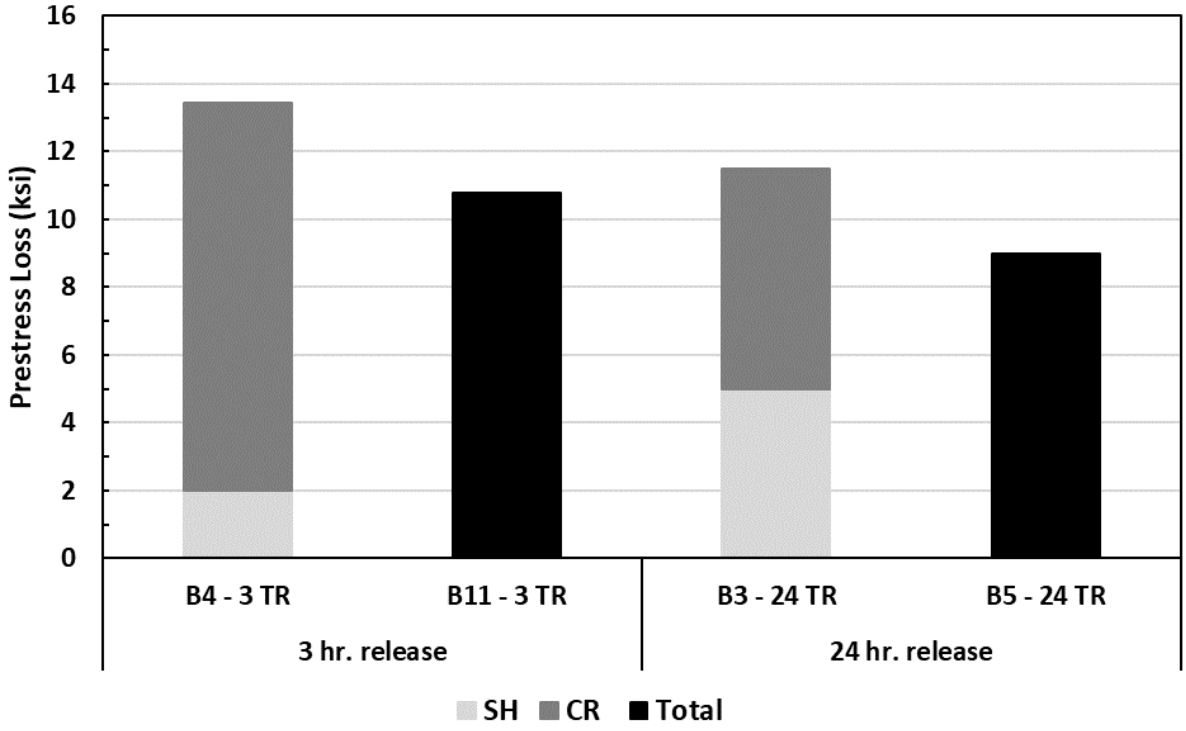

Figure 164: Itemized breakdown for sources of measured long-term (240 day) prestress losses

Figure 164 shows that, as stated previously, there is some substantial variation in the estimated contribution of shrinkage to the overall prestress losses starting from the time of

prestress release despite the companion beams being cast and cured in essentially identical environments. Correspondingly, this affects the estimated proportion of the losses accounted to creep and the latent effects of strand relaxation for beams B3-24TR and B4-3TR. In any case, the data from these tests indicate that the average contribution of shrinkage to the ultimate time-dependent prestress losses for the time periods examined should be less than half of the total.

Hypothetically, the shrinkage data from the companion beam to B4-3TR could have been used to estimate shrinkage losses for B11-3TR, and likewise for B3-24TR and B5-24TR. Or, the two companion beams could have been used together to estimate an average shrinkage value, and then the proportion of shrinkage losses for the two prestress release times could have been distinguished by zeroing the average shrinkage measurements to the appropriate release time. However, more in depth analysis concerning the proportion of shrinkage losses to the total would likely require more data and finer environmental control capacity.

5.4 Time-Step Integration Model for Prestress Losses

The approach used to develop a unique prestress loss estimation model for the RS-SCC was to pattern a time-step integration model after the procedure described in ACI 423.10R (ACI, 2016) in conjunction with the creep and shrinkage data gathered in the first phase of this research project. The quality of the results of the time-step integration model were analyzed by also utilizing other prestress loss prediction methods and determining which models yielded results closest to the experimentally measured values.

5.4.1 Model Development and Experimental Verification

5.4.1.1 Model Overview

A time-step integration model for prestress loss estimation functions on the basic principle that the driving force (the effective prestress) decreases with time. As a result, there is a compounding effect whereby the rate of shortening due to creep and strand relaxation decreases,

because the axial force is continually decreasing. A time-step integration model can yield accurate results, because instead of estimating the loss as a single value, a given time horizon is broken into many short discrete units. For each very short time step, the ending stress after the deduction of losses in that increment is used as the initial stress in the subsequent time step. This helps to account for the rate-dependency issue of the effective prestress force. The other key feature of a time-step integration model is the consideration of elastic rebound within each increment. When the prestress force is applied to the cross-section and the beam conforms due to incremental creep, shrinkage, or relaxation, the effective prestress decreases. This effect is accounted for by taking the difference in effective prestress within that increment and determining how much elastic rebound the beam would experience under the lower axial force. That elastic rebound is then deducted from the gross losses within that increment to determine the net loss for that increment before proceeding to the next time step.

5.4.1.2 Key Assumptions

Certain assumptions must be made in generating an effective time-step integration model that can impact the results of the analysis.

- Concrete elastic modulus (E_c): In time-step models, E_c can be taken as a constant value or as a function of time and the chosen assumption can greatly impact model results especially in the case of very early prestress release.
    - Constant and time-variant approaches for E_c were considered. Constant E_c approaches were found to aggravate consistent overestimation of time-dependent losses.

    - A piece-wise constant E_c assumption, taking a constant E_c from prestress release to 24 hours (unless release was at 24 hours), from 24 hours to 28 days, and from 28 days onward, was found to be suitable.
    - More complex time-variant approaches for E_c were considered irrational because elastic modulus testing was only performed at a few key time intervals, and functional forms for the variation between those times would be purely conjectural.
- Concrete creep increments: Depending on whether concrete maturity at prestress release or the applied stress level at prestress release is deemed more pertinent, there was a choice between 3 data sets from the creep testing with specimens loaded at 3 hours, 24 hours, and 28 days.
    - The ratio of the initially applied stress to the concrete compressive strength at the time of loading for the three creep testing ages were 0.74, 0.48, and 0.42 respectively.
    - The incremental creep data for the loading age that matched the prestress release age of the beam being modelled was used for analysis of the prestress losses measured in this research.
- Concrete shrinkage value: Since concrete shrinkage is assumed to be independent of stress levels declining with the effective prestress, the choice of incremental shrinkage data can strongly impact the model results.
    - In this study, incremental shrinkage data was available from creep companion cylinders with VWSG, ASTM C157 testing, or companion beams with VWSG.

- The data from the creep companion shrinkage cylinders with VWSG were chosen for the concrete shrinkage modelling because the time-steps matched the creep data, and the data was taken at finer increments than the ASTM C157 data.
- Using the data from the companion beams seemed to defeat the linear independence of the model because it would involve using elements of the data to be verified within the structure of the model itself.
- Incremental concrete shrinkage data was taken from the time of prestress release when the time-step model was applied, to account for the fact that drying or autogenous shrinkage which occurred between casting and prestress release would not contribute to prestress losses.

5.4.1.3 Key Equations

As stated previously, the RS-SCC time-step integration model followed a basic procedure described by ACI 423.10R (ACI, 2016). However, the description of this framework in ACI 423.10R is very generalized and a more specific explanation is provided here for the logical sequence that was used in this research.

At the beginning of each time step, the stress at the center of gravity of the prestressing strands, f_{cgs}, was computed using basic mechanics according to Equation 10:

$$f_{cgs} = \frac{P}{A} + \frac{Pey}{I} - \frac{M_D y}{I} \quad (10)$$

where P is the effective prestress force (kips), A is the area of the transformed section (in^2), I is the moment of inertia of the transformed section (in^4), e is the strand eccentricity (in.), y is the centroidal distance to the strand center of gravity (in.), and M_D is the self weight moment at the section of interest (kip-in). In this formulation, f_{cgs} was taken with compression positive in

ksi. The initial effective prestress force was computed using the calculated strand stress immediately after ES due to prestress release.

The creep coefficient increment, $\Delta\Phi_{cr}$ was computed for each time-step according to Equation 11:

$$\Delta\Phi_{cr} = \frac{\varepsilon_{cr}[j]}{\varepsilon_{cr}\,Ult} - \frac{\varepsilon_{cr}[i]}{\varepsilon_{cr}\,Ult} \tag{11}$$

where $\varepsilon_{cr}[i]$ and $\varepsilon_{cr}[j]$ are the VWSG measured, temperature compensated creep strains from subsequent time intervals, and ε_{cr} Ult is the VWSG measured, temperature compensated maximum creep strain (at whatever age for which prestress loss estimation is desired, but not exceeding the age at which the creep test specimens were unloaded).

The strain reduction in each increment due to creep, $\Delta\varepsilon_{cr}$ was computed by multiplying $\Delta\Phi_{cr}$ by the elastic strain at the strand center of gravity according to Equation 12:

$$\Delta\varepsilon_{cr} = \frac{f_{cgs}}{E_c}(\Delta\Phi_{cr}) \tag{12}$$

The total time-dependent loss in strand stress within each increment, Δf_i, was computed by adding the incremental shrinkage strain, $\Delta\varepsilon_{sh}$, to $\Delta\varepsilon_{cr}$ and multiplying by the strand modulus according to Equation 13:

$$\Delta f_i = (\Delta\varepsilon_{cr} + \Delta\varepsilon_{sh})E_{ps} \tag{13}$$

with E_{ps} and Δf_i in ksi. Then, Δf_i was subtracted from the strand stress at the beginning of each increment, to obtain the strand stress at the "middle" of that increment. Next, the elastic rebound of the cross-section was considered in order to determine the true reduction in stress for that increment. This was done by re-applying Equation 10 with the reduced prestress force

associated with the strand stress reduced by Δf_i in order to determine the change in stress at the center of gravity of the prestressing strands, Δf_{cgs}.

The strand stress rebound was computed according to Equation 14:

$$Rebound = \frac{\Delta f_{cgs}}{E_c}(E_{ps}) \quad (14)$$

with Δf_{cgs} and Rebound normally negative in ksi. Finally, the net prestress loss in each increment was computed according to Equation 15:

$$Net\ Loss = (\Delta f_i + Rebound) \quad (15)$$

The total time-dependent prestress loss at any desired time over which creep and shrinkage data was available was then the sum of the net losses in each time increment between immediately after prestress release and the final time in question.

5.4.1.4 Verification against Experimental Data

Figure 165 shows the time-dependent losses (consisting primarily of creep and shrinkage) for beams B3-24TR and B4-3TR plotted against the losses estimated with the time-step integration model developed from the creep and shrinkage data.

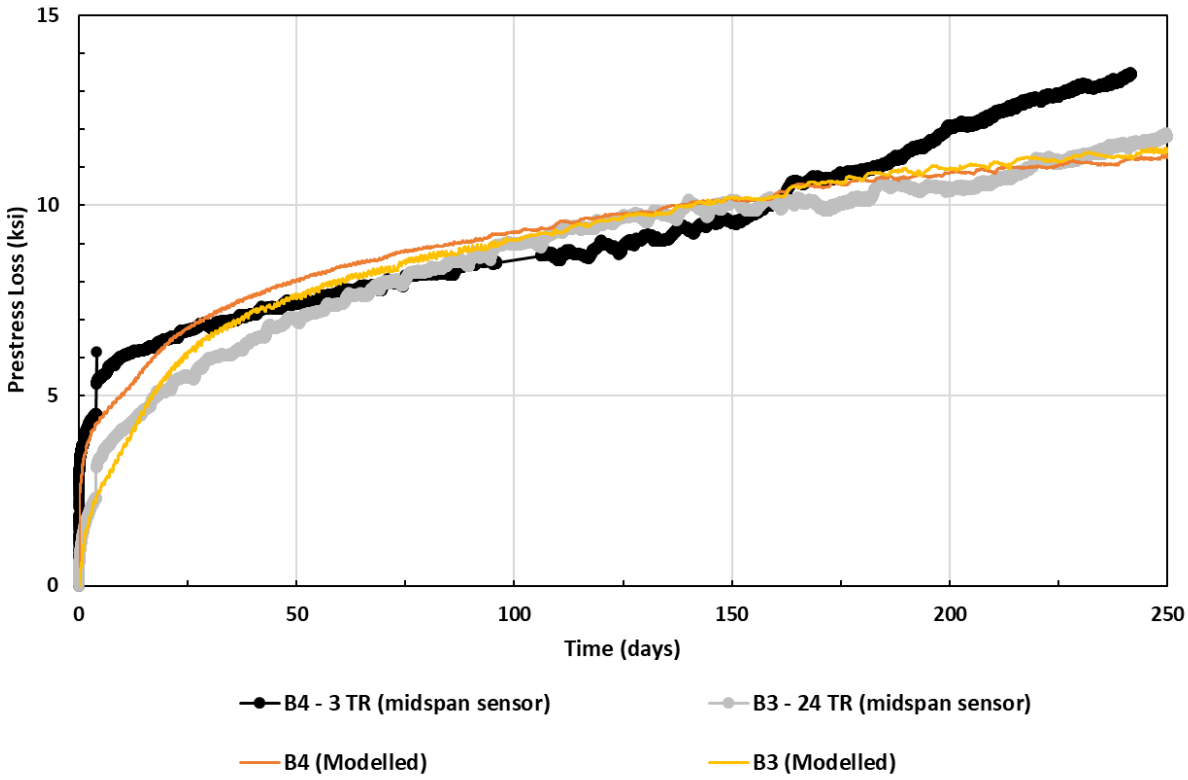

Figure 165: Comparison of measured time-dependent prestress losses with time-step integration model results

Note that in Figure 165, the modelled curves from the time-step integration model include the combined effects of creep and shrinkage but not strand relaxation. This is because measurement of strand relaxation data was beyond the scope of these experiments, and the incremental progression of strand relaxation would be co-dependent upon the relative changes in the other losses over time. Therefore, it would not be appropriate to include incremental relaxation losses in the modelled curves, especially because the measured values that are being compared to from the VWSG instrumentation also do not directly comprehend strand relaxation effects. Any relative error arising from the omission of relaxation effects from the model should be minimal since relaxation losses are minor compared to creep and shrinkage. Since the creep and shrinkage of RS-SCC are less than for conventional concrete, it is possible that the

proportion of loss due to relaxation effects could be slightly higher for RS-SCC than for conventional concrete. Further research is required to make a determination on this relationship more certain.

Figure 165 shows excellent agreement between both the magnitudes and the shapes of the experimentally measured and calculated time-dependent prestress loss curves. First of all, the magnitudes of the curves track closely over time, with significant departure occurring mainly in the summer months when the beams heated up. This departure would be expected because the time-step model employed was not equipped to consider ambient thermal influences. Second, the shapes of the experimental and calculated curves track together over time, except in the case of potential temperature effects. Both the experimental and calculated curves for beam B4-3TR (3 hour release) show the very steep, rapid increase in losses at early age, followed by a distinct flattening. In contrast, both the experimental and calculated curves for beam B3-24TR (24 hour release) roll over more quickly with less rapid early losses but show more losses over time and eventually catch up with or surpass the B4-3TR curves.

In order to gage the relative accuracy of the time-step integration model which was developed for the RS-SCC, the model outputs were compared to both the measured losses and an assortment of other prestress loss prediction models. The other models included the ACI (Zia et al., 1979) method, the AASHTO refined method (AASHTO LRFD 8th Edition, 2017), and a modification of the AASHTO refined method herein referred to as the "adjusted" AASHTO refined method. The ACI (Zia et al., 1979) method and the AASHTO refined method (AASHTO LRFD 8th Edition, 2017) were both applied as originally described in their respective originating literature, using the geometric values, modulus estimates, and creep/shrinkage models recommended by each method. The "adjusted" AASHTO refined method followed the

framework described in the AASHTO LRFD manual but utilized the creep and shrinkage values from the experiments in Chapter 3 directly, instead of applying the creep and shrinkage models recommended in the AASHTO LRFD manual. The AASHTO LRFD refined method was chosen for adjustment instead of the ACI (Zia et al., 1979) method, because the AASHTO LRFD refined method was better lent to parametric modifications for modern, high-strength concrete materials. The RS-SCC time-step integration model was applied as previously described in Section 5.4.1.

Figure 166 shows a comparison of these estimates for the modelled time-dependent losses and the measured time-dependent losses for beam B4-3TR (early, 3 hour prestress release).

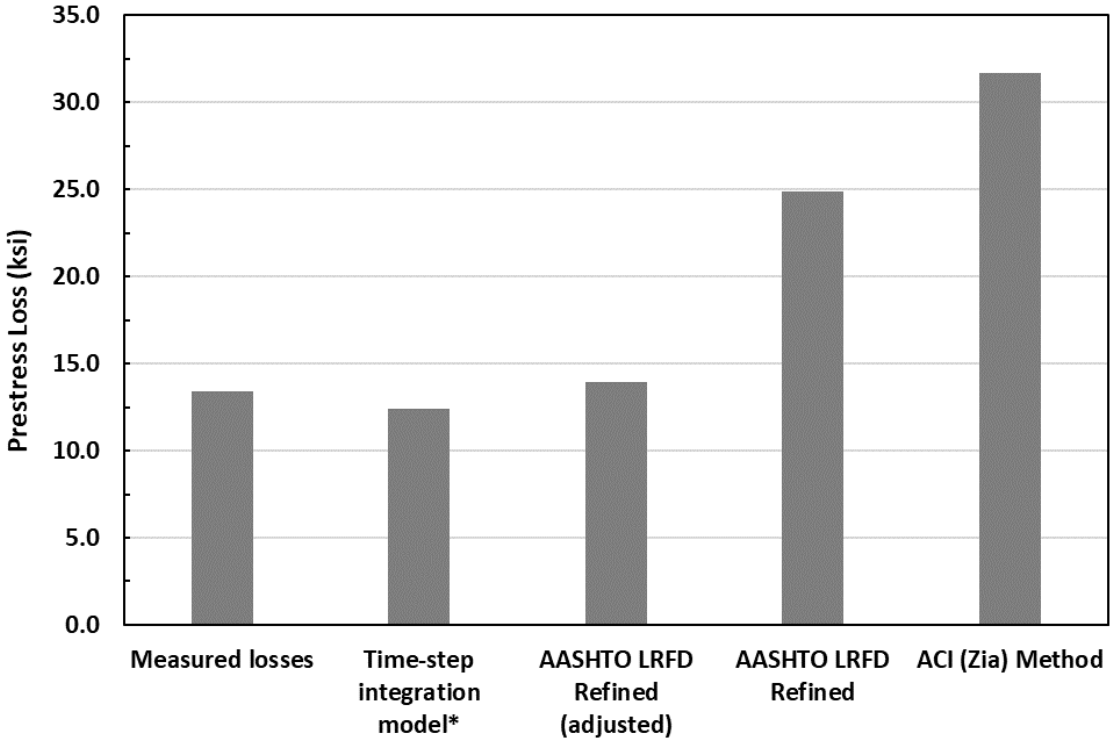

Figure 166: Comparison of long-term prestress loss estimation approaches for beam B4-3TR, 3 hour release (*Denotes 1.2 ksi lump sum addition for strand relaxation)

Figure 166 shows that applying the ACI (Zia et al., 1979) or AASHTO refined methods (AASHTO LRFD 8th Edition, 2017) as originally derived results in large error compared to the measured losses. The AASHTO refined method overpredicted the long-term losses by nearly 100% and the ACI (Zia et al., 1979) approach overpredicts by more than 100%.

Adjusting the AASHTO refined method by using the material properties measured for this particular BCSA cement concrete mix design proved to be a more accurate approach. This was accomplished by using the average 1 year creep coefficients and ultimate shrinkage strains measured in these experiments directly in the AASHTO refined method, instead of computing them with AASHTO's recommended equations. The AASHTO coefficient K_{id} was computed normally according to AASHTO Equation 5.9.3.4.2a-2, with the exception that the final creep coefficient used in this equation was taken directly from the creep testing data of Chapter 3 instead of being computed in accordance with AASHTO Equation 5.4.2.3.2-1 (AASHTO LRFD 8th Edition, 2017).

The last approach was the time-step integration model using the measured BCSA cement concrete material properties. The time-step model and the adjusted AASHTO refined method are clearly more accurate approaches for the BCSA cement concrete examined in this research, as shown in Figure 166. Both the time-step model and the adjusted AASHTO refined method predicted the losses to within 10% at 240 days, with the time-step model underpredicting by about 8% and the adjusted AASHTO refined method overpredicting by about 4%. Considering the naturally high degree of variability in prestress losses, this is a very strong level of agreement.

Figure 167 shows a comparison of estimates for the time-dependent losses with the measured losses for beam B3-24TR (typical, 24 hour prestress release).

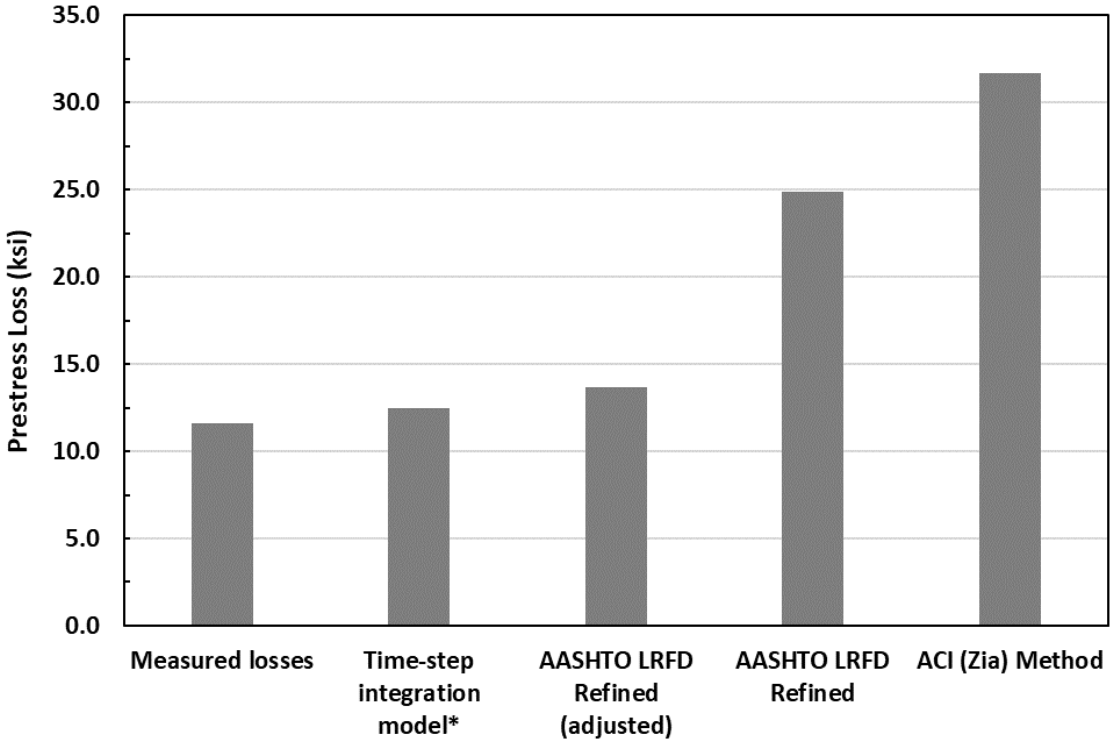

Figure 167: Comparison of long-term prestress loss estimation approaches for beam B3–24TR, 24 hour release (*Denotes 1.2 ksi lump sum addition for strand relaxation)

Figure 167 shows that similarly to B4-3TR with early prestress release, the conventional AASHTO refined method and ACI (Zia et al., 1979) methods produced poor predictions for this material, with both methods overpredicting the prestress losses by more than 100% in this case. In fact, the Zia method losses were nearly triple the measured losses for beam B3-24TR. Similarly to beam B4-3TR, the time-step model and the adjusted AASHTO refined method are significant improvements to the time-dependent prestress loss estimation for beam B3-24TR. The main change in the time-step model and the adjusted AASHTO refined methods to estimate the prestress losses for the different prestress release time of B3-24TR compared to B4-3TR was to replace the creep data based on the 3 hr loaded creep specimens with that of the 24 hr loaded creep specimens. For the time-step model, this included changing the entire creep response time history. For the adjusted AASHTO refined method, this meant changing the ultimate creep

coefficient to match that measured for the 24 hr loaded creep specimens. The measured time-dependent losses at 240 days for beam B3-24TR of 11.6 ksi are overpredicted by only 8% (12.5 ksi total) for the time-step model and 20% (14.0 ksi total) for the adjusted AASHTO refined method.

5.4.2 Model Validation with Data from Literature

In addition to verifying that the time-step model functioned correctly by analyzing its results relative to the actual prestress losses measured in this project, the model was validated by applying it to other projects in the literature where prestress losses were measured for BCSA cement concrete beams. Although these projects did not use identical mix designs, the common usage of BCSA cement concrete justifies investigating the robustness of the time-step model.

5.4.2.1 Bowser (2016)

The experimental setup, beam design, and testing protocol for this research are described in detail during the literature review of Chapter 2, but a few key details are repeated here for reference. The beam design utilized in this research was an 18 ft long eccentrically prestressed 6.5 in. x 12 in. cross section with two 0.60 in. strands 2 in. from the bottom. Mild steel reinforcement (two No. 6 bars) was used in the top of the section to resist tensile stresses at prestress release, and WWR shear reinforcement (W4) was used throughout the length of the section. Eight BCSA cement concrete beams were fabricated, and prestress was released for 4 beams at around 2 hours and prestress was released for the other 4 beams at around 24 hours. The 2 hr. prestress release concrete compressive strength averaged just over 3.6 ksi, while the 24 hr. prestress release concrete compressive strength averaged just over 4.4 ksi. Two 2 hr. prestress release beams and two 24 hr. prestress release beams were instrumented to measure prestress losses out to 28 days of age.

Figure 168 shows a comparison between the average time-dependent prestress losses measured for the four BCSA cement concrete beams at 28 days of age and three estimation techniques. The measured losses were based upon the strains from the embedded VWSG at midspan of the beam at the level of the prestressing strands at 28 days of age. The average measured prestress loss shown in Figure 168 represents the overall average of both the 2 hr. and 24 hr. prestress release beams taken together, because there was no significant difference in loss magnitude between the two groups.

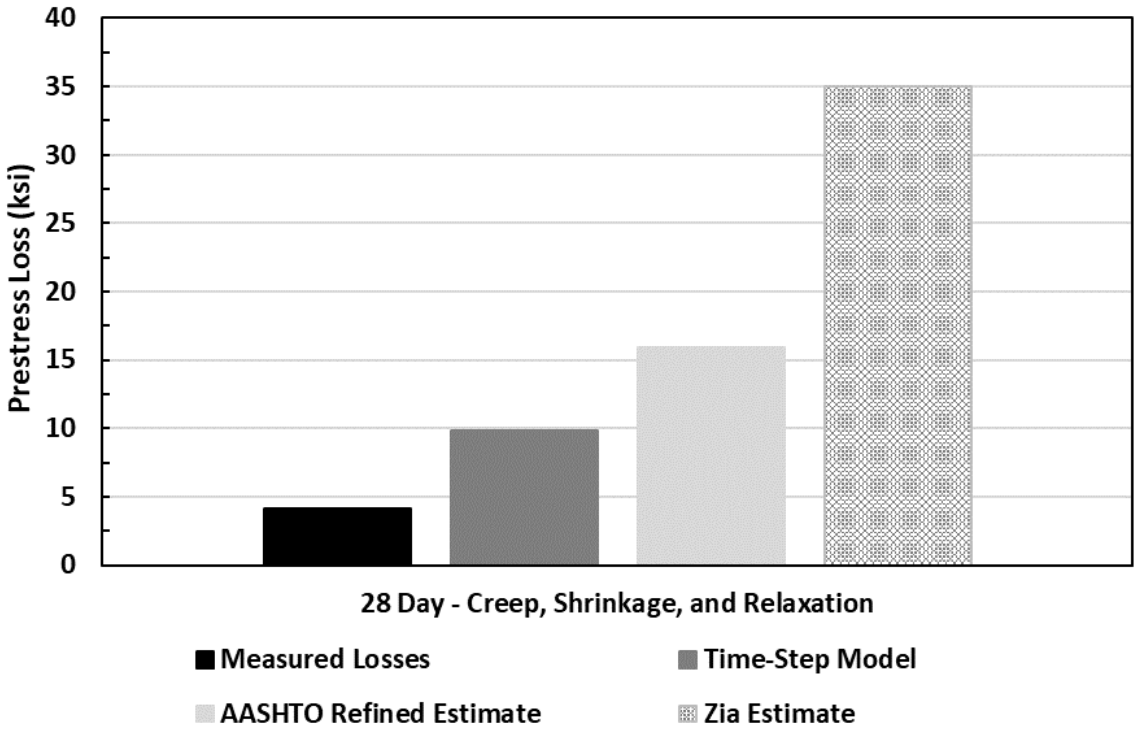

Figure 168: Validating time-step model with BCSA cement concrete prestress loss data from Bowser (2016) and comparing with existing AASHTO LRFD (7th edition) and ACI (Zia et al., 1979) models

Figure 168 shows that the AASHTO and Zia approaches (results computed by Bowser, 2016) significantly overestimated the actual measured prestress losses. Although this is an observation that has occurred consistently where prestressed BCSA cement concrete is

concerned, the significant difference in this particular case is partly due to the age of the concrete. In Bowser's work, prestress losses were only monitored out to 28 days, which is a shorter time period than the ACI and AASHTO methods are optimized for. The parameters of the beam design and concrete properties used by Bowser were used as inputs along with the creep and shrinkage data from this dissertation in the time-step prestress loss model and the 28-day losses were estimated. The time-step model gave a result of 9.8 ksi for the 28 day prestress losses caused by creep and shrinkage, which was a little over twice the measured value. Although the time-step approach results still have a significant disparity from the measured values in this particular case, its results are closer to the measured values than those from the other, existing estimation models. Also, although the VWSG method does not directly measure the losses caused by strand relaxation, strand relaxation has also been omitted from the modeled prestress loss so that the comparisons are as direct as possible.

There are likely several reasons for this imperfect agreement between modelled and measured prestress losses, even when using the time-step method equipped with creep and shrinkage data specifically for BCSA cement concrete. The primary difference is likely due to differences between the mix design used for Bowser's (2016) work and the mix design used in this dissertation. As previously noted, the mix design used in this dissertation was optimized for flowability, with much more fine aggregate than coarse aggregate (coarse to fine, C/F, aggregate ratio was around 0.53). In contrast, the mix design used in Bowser's work was more conventional in terms of aggregate proportions, with more coarse aggregate than fine (C/F aggregate ratio was around 1.3). Concrete paste is the primary contributor to creep if a sound, good quality coarse aggregate is used. Therefore, all else remaining equal, the BCSA cement concrete mix design tested in this dissertation would naturally lend itself to higher creep potential

(and therefore higher relative prestress losses) than the mix design used by Bowser because of the difference in coarse aggregate content. Another difference between Bowser's study and this research was the level of prestress. Although the beam geometry was extremely similar, Bowser utilized two 0.6 in. strands instead of two 0.52 in. strands. The difference in effective prestress force was comprehended in the time-step integration model and the other prestress loss estimates. It seems unlikely that this change explains the trend seen in Figure 168 however, because mechanistically, a higher prestress force would theoretically cause more creep and therefore relatively high measured prestress losses, instead of relatively low prestress losses. Just the same however, the difference in prestress force is important and should be noted.

5.4.2.2 Floyd and Ramseyer (2013)

The bulk of this study is discussed in the literature review, but a few key details are repeated here. The beam design utilized in this research was a 25 ft long concentrically prestressed 8 in. x 24 in. cross section with three 0.52 in. strands 2 in. from the bottom and three more 0.52 in. strands 2 in. from the top. There was no mild steel tensile or compressive reinforcement, and no shear reinforcement except for minimal bursting steel in the end regions. Four beams were fabricated, and prestress was released between about 1.5 – 2 hours with a concrete compressive strength between 3.8 - 4.5 ksi.

Figure 169 shows the average time-dependent prestress losses measured for the 4 beams studied in this project, compared to the ACI simplified (Zia et al., 1979) and AASHTO refined (AASHTO LRFD, 2017) methods as well as the time-step model using the material property data from Chapter 3. The measured losses were based upon the strains from the embedded VWSG at midspan of the beam at the level of the prestressing strands at around 3 years of age. The time-step integration and adjusted AASHTO LRFD refined models were based upon the creep data

from the specimens loaded at an age of 24 hours since the compressive stress at release for the beams in Floyd and Ramseyer's project were relatively low.

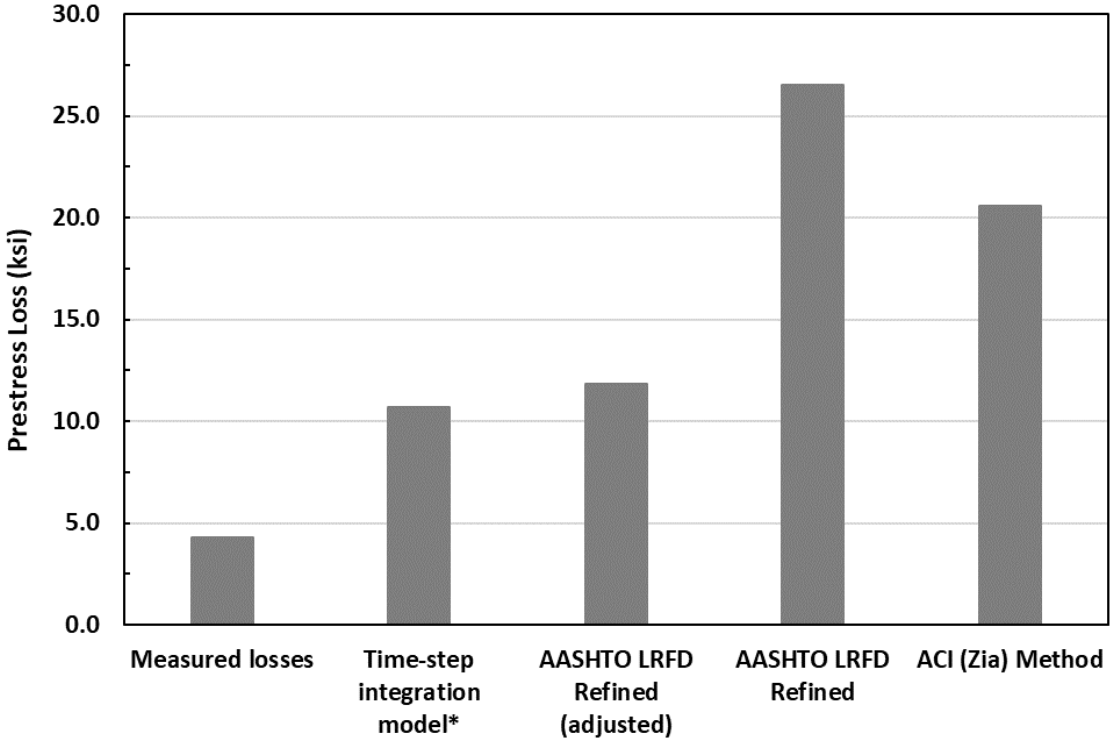

Figure 169: Average measured time-dependent prestress losses from Floyd and Ramseyer (2013) compared with multiple estimation techniques, using creep data loaded at 24 hrs under initial stress ratio of 0.48f'$_c$ for material models

Figure 169 shows that the ACI (Zia et al., 1979) and AASHTO refined methods significantly overpredicted the measured time-dependent prestress losses, as expected. The time-step model and the adjusted AASHTO refined method, with the ultimate creep coefficient and shrinkage strain substituted, have less relative error compared to the measured losses. Even still, the models tailored to BCSA cement concrete properties still produce values more than double the average measured prestress loss. There could be several reasons for this observation. First, like the Bowser (2016) data, the beams studied by Floyd and Ramseyer (2013) utilized a BCSA cement concrete mix design with more crushed limestone coarse aggregate than sand (coarse to

fine aggregate ratio of about 1.5). This difference could lead to significantly lower long-term prestress losses due to replacement of paste with a stiff, sound aggregate. Secondly, the beams studied by Floyd and Ramseyer (2013) utilized a concentric prestress layout. Without strand eccentricity, and with only 6 strands on the cross section, the compressive stress at release was low relative to the compressive strength of the concrete at release (stress ratio of 0.24, compared to max allowable limit of 0.70 per ACI 318). With such a relatively low initial stress applied to the cross section, combined with the mix design, it is reasonable that the observed prestress losses would have been low relative to even the time-step model approach.

Figure 170 shows the average time-dependent prestress losses measured for the 4 beams studied in this project, compared to the ACI and AASHTO methods as well as the time- step model based on the material property data from Chapter 3. In Figure 170, the estimates from the adjusted AASHTO refined estimate and the time-step model were based upon the creep data loaded at 28 days under a stress ratio of 0.40 instead of the earlier loaded creep specimens which were loaded at stress ratios closer to 0.50. The reason for this refinement was that, as mentioned previously, the stress ratio for the beams in this particular study were so low that the earlier loaded creep data was greatly overestimating the long-term prestress losses (see Figure 169). Even though the incremental creep coefficients in the time-step integration model are normalized by the elastic stress level on the beam cross-section at each time step, the model results are still highly dependent on the applied stress level at which the creep coefficients were measured, because creep is an inherently and significantly non-linear phenomenon. Usage of the 28 day loading creep coefficients was not applied for the integration time-step modelling in the verification modelling of Section 5.4.1.4 because significant overestimation of the prestress losses measured in the experiments of this research was not an issue.

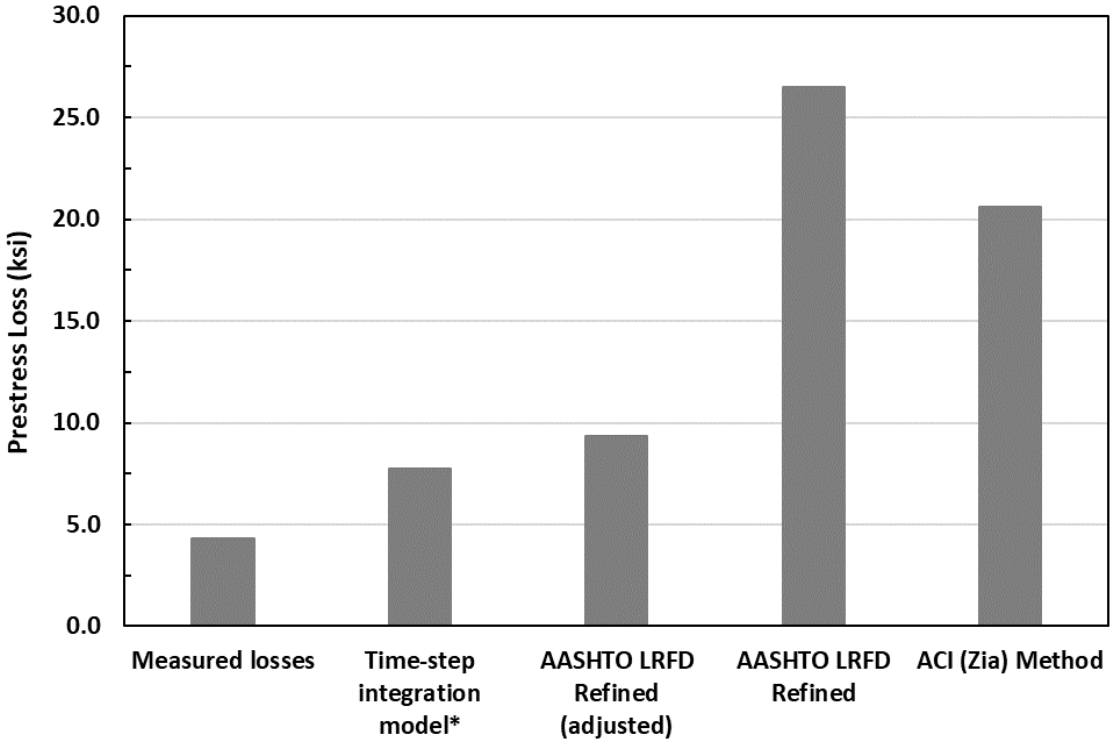

Figure 170: Average measured time-dependent prestress losses from Floyd and Ramseyer (2013) compared with multiple estimation techniques, using creep data loaded at 28 days under initial stress ratio of 0.40f'$_c$ for material models

Figure 170 shows that using the creep data loaded at 28 days in the material property inputs reduces the error relative to the measured values for both the time-step approach and the adjusted AASHTO refined approach.

Figure 171 shows the average time-dependent prestress losses measured for the 4 beams studied in this project, compared to the time-step model and the adjusted AASHTO refined approach using different creep coefficients. Creep data from the earlier loaded specimens (loaded at 24 hrs) and those loaded at 28 days are used in both models to compare the results and glean conclusions about how the applied stress level might affect the accuracy of the prestress loss estimates.

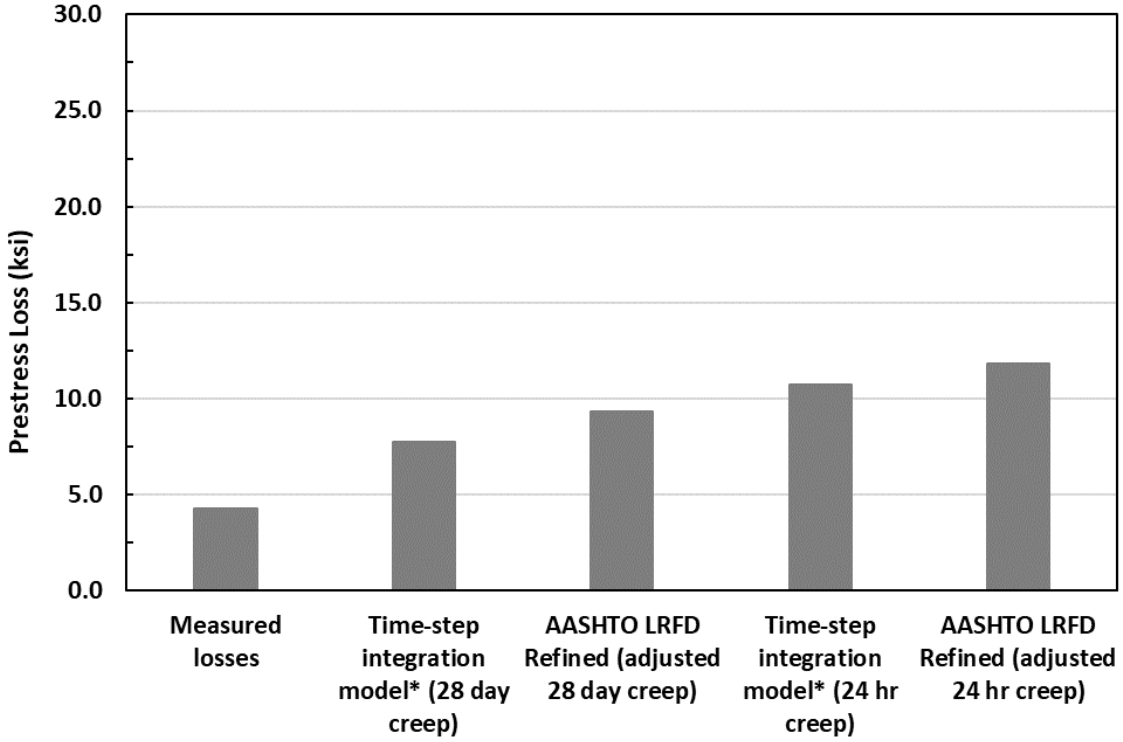

Figure 171: Average measured time-dependent prestress losses from Floyd and Ramseyer (2013) compared with time-step model and adjusted AASHTO refined method using creep data loaded at 28 days and at 24 hr age

Figure 171 shows that using the 28 day creep data which was loaded to $0.4f'_c$ as the input to the prestress loss model does indeed yield results that are closer to the average measured values. The comparison is still imperfect, which is expected due to the significant differences in mix design apart from the usage of the same type of BCSA cement. But the analysis further supports the observation that the time-step model is correctly capturing behavior, and that creep and shrinkage data that is more situation specific will yield progressively more accurate results.

5.5 Shrinkage and Creep Modelling for Prestress Loss Estimation

The time-step integration model presented in Section 5.4 delivered a more reasonable estimate for the prestress losses of RS-SCC prestressed beams compared to some existing, commonly utilized frameworks which were designed for PCC. However, in the model used for this research, incremental creep and shrinkage data was used which was gathered particularly for use in this model, and care was taken to make sure that the conditions under which the data was gathered would be as similar as possible. In practice, however, a practitioner will in all likelihood not have the luxury of situation-specific, incremental creep and shrinkage data ready to use in a time-step integration model tailored to their specific design criteria. And since measuring creep and shrinkage data can be such a difficult, expensive, and time-consuming process, it is important that design engineers have reasonably accurate mechanisms for modelling incremental creep and shrinkage values specifically for RS-SCC (and for BCSA cement concrete materials in general). This way, design engineers can use time-step integration models, or other approaches, with more correct material property input values in order to estimate prestress losses for RS-SCC/BCSA cement concrete more accurately than they could otherwise.

It is critical to note that the fundamental chemistry and physical microstructure of BCSA cements are significantly different from portland cements. Therefore, there is a strong case to be made that to model creep and shrinkage for BCSA cement concrete appropriately would require totally unique approaches compared to those designed for PCC. However, designing and calibrating holistic, comprehensive creep and shrinkage models for concrete materials requires very large amounts of data with significantly more parametric considerations than were possible within this scope, such as varying V/SA ratios, ambient curing temperatures (controlled), ambient curing humidity (controlled), w/cm ratio (and other mix design parameters), and

consideration of various mechanisms of volume change or dimensional instability (such as drying shrinkage, autogenous shrinkage, and carbonation shrinkage).

In this research multiple V/SA ratios were utilized, but ambient curing temperature and humidity could not be controlled for many of the larger scale specimens. And for the smaller scale specimens, temperature and humidity was held as constant as possible (outside of occasional air conditioning malfunctions) but was not parametrically varied to investigate higher or lower curing temperatures and humidity formally. In addition, the bulk of the material property and structural testing (outside of the test mixes) were performed for only one w/cm ratio and mix design. Finally, all shrinkage measurements were "gross" in nature, meaning that they represented a total shrinkage, and did not parse out the source of the shrinkage (drying, autogenous, or carbonation). For these reasons, it was determined that it was not appropriate to attempt to create totally unique creep and shrinkage models for BCSA cement concrete based only on the data gathered in these experiments. Instead, sections 5.5.1 and 5.5.2 investigate some existing shrinkage and creep estimation frameworks, explore how well suited they are for use with BCSA materials, and investigate how the models could be adjusted to make them most appropriate for BCSA materials.

As a final note, between this work and others, there is a growing pool of material property data available for BCSA cement concrete, both with regard to creep and shrinkage. Research projects overseen by Dr. Chris Ramseyer performed by D. Frank (2011), S. Shadrivan (2011), J. Roswurm (2018); Dr. Royce Floyd by S. Tanksley (2018); Afroughsabet (2019), and many others have expanded the state of the art knowledge in BCSA cement concrete to the point that a comprehensive research project on synthesizing these resources to formally approach creep and shrinkage modelling could easily spawn multiple theses or dissertations with especially

heavy emphases in statistical and analytical work. Although far beyond the scope of this research, such research projects are very much needed to further spur the development and applications of BCSA cement and would be accordingly positioned to make significant impact in concrete research and design literature.

5.5.1 Shrinkage Modelling

Four different shrinkage prediction models were compared to the experimental shrinkage measurements recorded for the ASTM C157 prisms from this research. The ASTM C157 prisms were chosen for the shrinkage modelling comparison because these specimens were stored in a small independent environmental chamber which held the ambient curing temperature and humidity much more constant than any of the other studied specimens which were stored elsewhere and had more variation in curing conditions. The shrinkage models chosen for comparison were the ACI 209 model (ACI 209, 2008), the AASHTO LRFD model (AASHTO LRFD 8th ed., 2017), the CEB MC90 model (after Muller and Hilsdorf, 1990), and the Bazant B3 model (Bazant and Baweja, 1995). Each of the 4 models shares the basic similarity of using some kind of total or ultimate shrinkage strain value which governs the maximum magnitude of the shrinkage accumulation, coupled with empirical or theoretical functional forms that dictate the accumulation rate of the shrinkage.

Figure 172 shows the results of each of these four shrinkage models plotted with time, compared to the actual shrinkage strains measured using the ASTM C157 specimens. Each of the four models was applied as described in their respective originating literature, using the basic geometric (V/SA = 0.66) and curing (RH = 50%) parameters of the ASTM C157 testing.

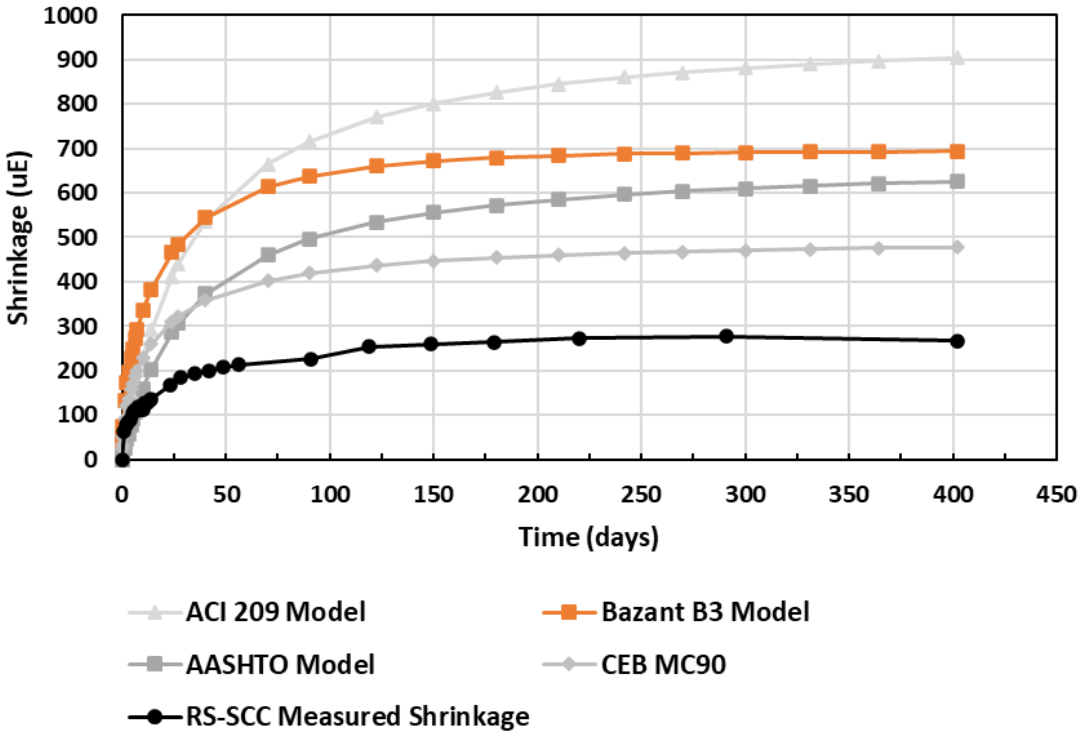

Figure 172: Comparison of measured RS-SCC shrinkage with modelled values for ASTM C157 testing without adjustment to models

Figure 172 shows that as might be expected, the four models which were originally calibrated for PCC and have not been adjusted for use here, do not correlate particularly well with the measured ASTM C157 shrinkage values for the RS-SCC. The measured shrinkage strain at just over 400 days was about 267 με, with the model estimates ranging from 478 με (CEB MC90) to 904 με (ACI 209) at the same time. This results in modelled shrinkage values at 400 days exceeding the measured shrinkage value by 180% to 340%.

In order to improve the agreement with experimental data, the models were modified to better reflect the RS-SCC behavior. This was done by directly replacing the ultimate shrinkage strain estimate of each method with the maximum experimentally measured shrinkage strain from the ASTM C157 test specimens. In this case, that value was 277 με at an age of about 290

days. Figure 173 shows the results of each of these four modified shrinkage models plotted with time, compared to the actual shrinkage strains measured using the ASTM C157 specimens.

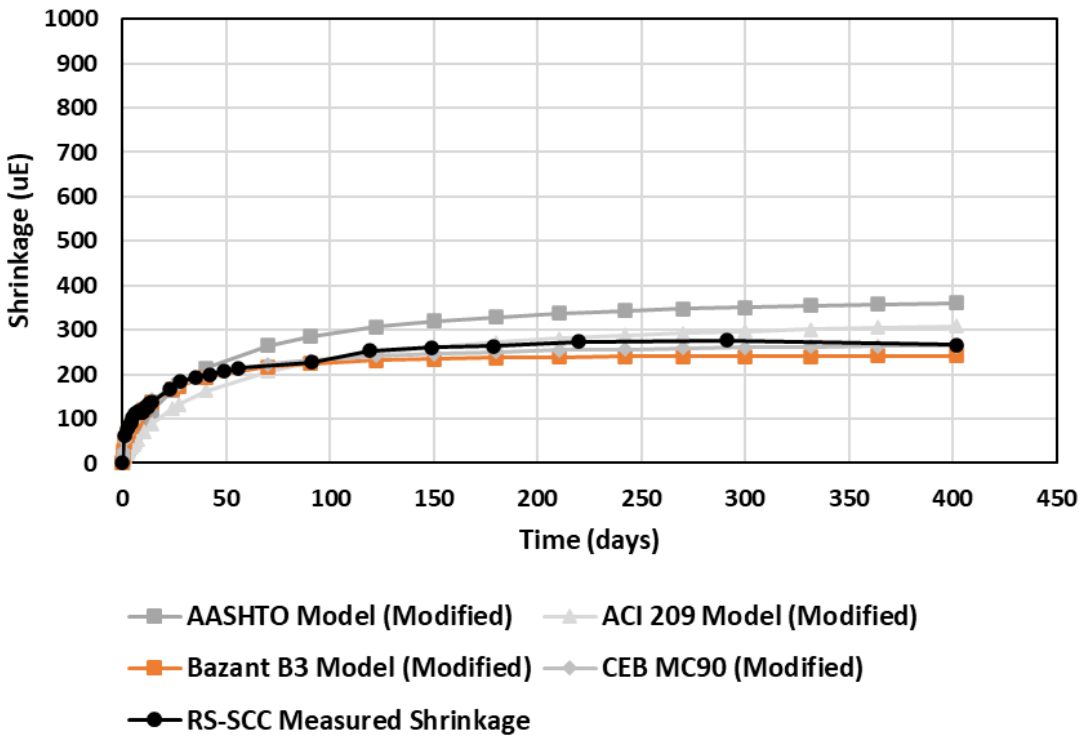

Figure 173: Comparison of measured RS-SCC shrinkage with modelled values for ASTM C157 testing with models adjusted for ultimate shrinkage strain of RS-SCC

Figure 173 shows that on average the model agreement is significantly improved by substituting the ultimate shrinkage strain used in each model with the measured ultimate shrinkage value from the ASTM C157 testing. The model estimates range from 241 με (Bazant B3) to 360 με (AASHTO) at 400 days, resulting in modelled shrinkage values varying from the measured shrinkage value by about 10% below to about 35% above the measured value of 267 με. In addition, the CEB MC90 error at 400 days was just over 1% and the ACI 209 error was just over 15%.

In order to determine which model most closely fit the experimental data, the sum of the root mean square (RMS) error was computed for each of the three closest models (Bazant B3, CEB MC90, and ACI 209). The RMS approach was an effective way of quantitatively gaging the proximity of the modelled curves to the measured curve across all time increments instead of computing a percent difference at a single discrete time increment. Although the ACI 209 model fell in closer proximity to the measured curve than the AASHTO model overall, it is clear graphically that the shape of the ACI 209 curve does not fit the experimental data particularly well. It is also evident graphically that the CEB MC90 and Bazant B3 models have shapes which more nearly track with the trajectory throughout both early and later time increments. The sum of the RMS error for the ACI 209, Bazant B3, and CEB MC90 models were 1317, 792, and 721 respectively (RMS error omitted for AASHTO model since it was visibly distant from other models). This reinforces the graphical observation that the CEB MC90 and Bazant B3 models fit the experimental data the best, with their total RMS error 40% - 45% lower than the next closest estimation, the ACI 209 model. All four models gave somewhat reasonable results, however, with the modified ultimate shrinkage value applied.

In summary, without creating a new RS-SCC shrinkage model or totally reconstructing an existing shrinkage model, a researcher or practitioner could easily use this approach to obtain reasonable incremental shrinkage data with time. Ultimate shrinkage values for BSCA cement concrete are available in this research, and in many other sources in the literature under various conditions. Or, if special conditions existed for a given BCSA cement concrete mix design or curing conditions, specimens could be cast for shrinkage measurements and monitored for an ample duration to estimate an ultimate shrinkage value. As is obvious from this data, a large majority of the shrinkage occurs within the first 56 days or so, and therefore it would not be

necessary to monitor for months or years if an approximate ultimate shrinkage value was required.

5.5.2 Creep Modelling

The ACI 209 and AASHTO LRFD prediction models were used to compare to the experimental creep measurements recorded by the VWSG equipped in the 6 in. x 12 in. cylinders from this research for each loading age studied (3 hours, 1 day, and 28 days). The ACI 209 method was applied according to its definition in ACI 209R-08 with all adjustment factors calculated and applied to the basic creep coefficient value of 2.35 for each loading age. Additionally, the ACI 209 method was modified for each loading age by replacing the adjustment factors and the basic creep value with the average maximum creep coefficient measured for each loading age. The AASHTO LRFD method was applied only as defined in the AASHTO LRFD code, partially because this method already accounted for compressive strength at loading as well as age related maturity development. The AASHTO LRFD method uses a default basic creep coefficient value of 1.9.

All model inputs utilized the V/SA ratio of the 6 in. x 12 in. cylinders with their ends covered (1.50) and an estimated curing RH of 50%. The environmental chamber where the creep specimens were cured was not capable of perfectly maintaining humidity control, so the RH fluctuated seasonally and with weather conditions. A RH value of 50%, however, is reasonable given the circumstances of the testing.

Figure 174 shows the results of each creep model result plotted with time, compared to the average creep coefficients measured over time for the specimens loaded at an age of 3 hours.

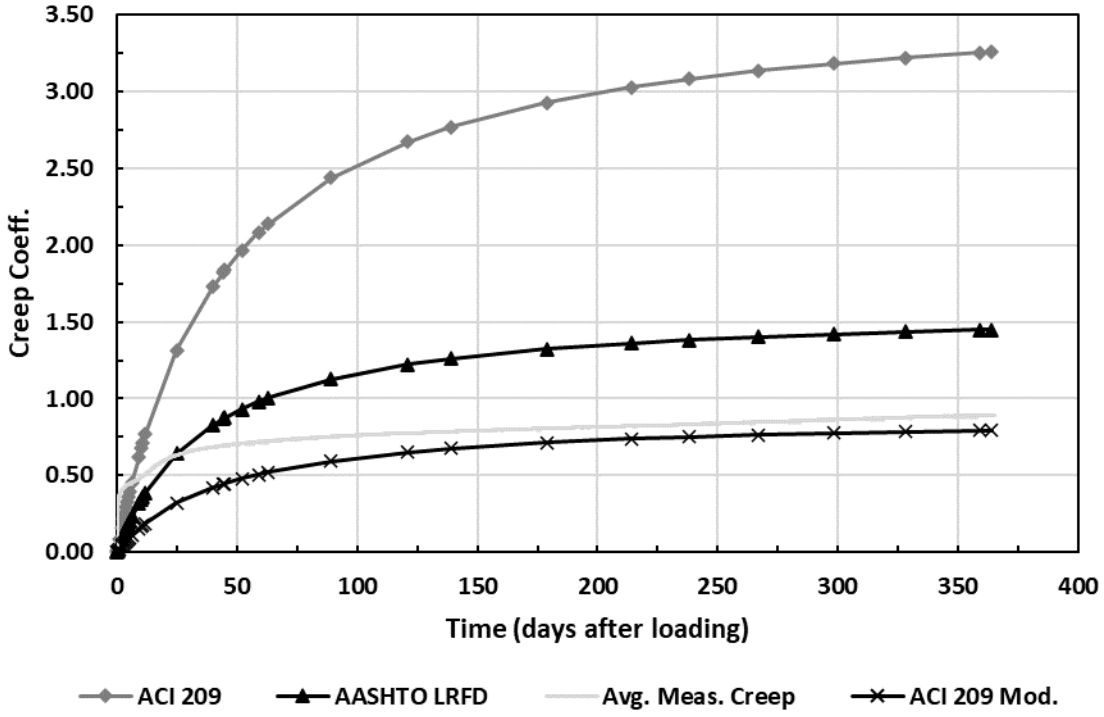

Figure 174: Comparison of measured RS-SCC creep with modelled values for creep specimens loaded at 3 hour age

Figure 174 shows that the ACI 209 model significantly overestimated creep across all time increments, culminating with a final creep coefficient of greater than 3. The modified ACI 209 model tracks much more closely with the measured data, especially at later ages (greater than 100 days or so) but it noticeably underestimates the early creep (within the first 50 days or so). The AASHTO LRFD model estimates early age creep more accurately than the modified ACI 209 model. However, at later ages (beyond 50-100 days), the AASHTO LRFD model begins to diverge and overestimates the ultimate creep by a wide margin.

Figure 175 shows the results of each creep model result plotted with time, compared to the average creep coefficients measured over time for the specimens loaded at an age of 1 day.

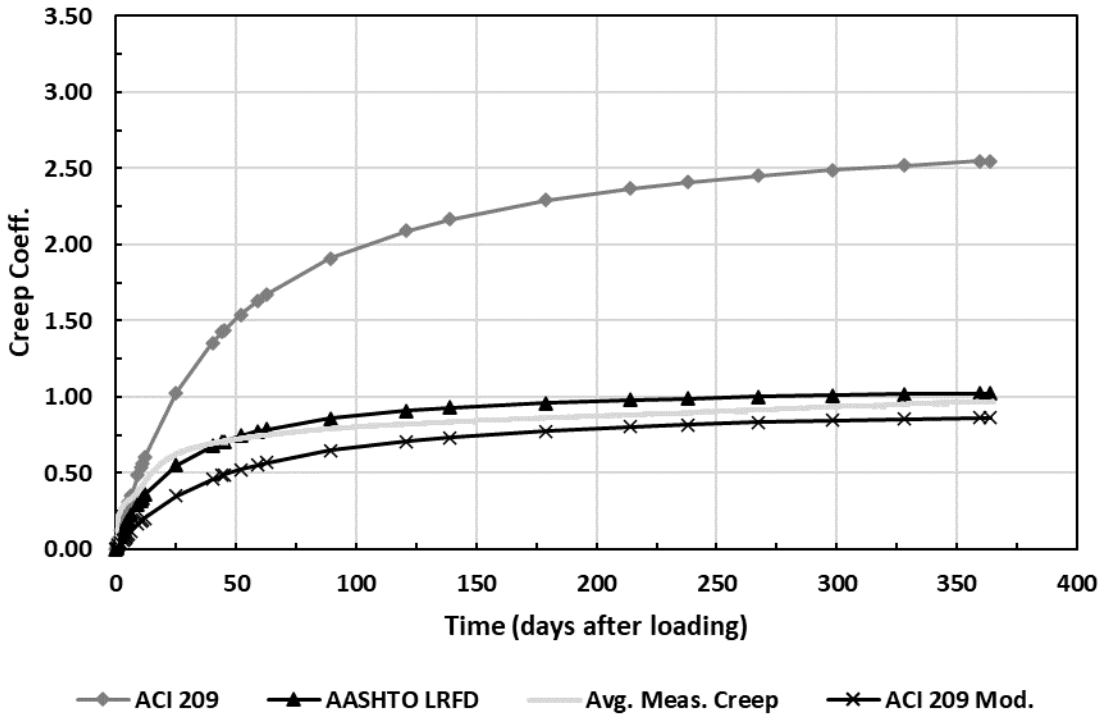

Figure 175: Comparison of measured RS-SCC creep with modelled values for creep specimens loaded at 1 day age

Figure 175 shows that the ACI 209 model still overestimated the measured creep across the entire timeframe. Similarly to the 3 hour creep models, the modified ACI 209 model gives a reasonable final creep estimate and tracks relatively close to the measured curve at later ages, but underpredicts the creep at earlier ages. The AASHTO LRFD model follows the measured creep curve very closely across all time increments for the 1 day loaded specimens.

Figure 176 shows the results of each creep model result plotted with time, compared to the average creep coefficients measured over time for the specimens loaded at an age of 28 days.

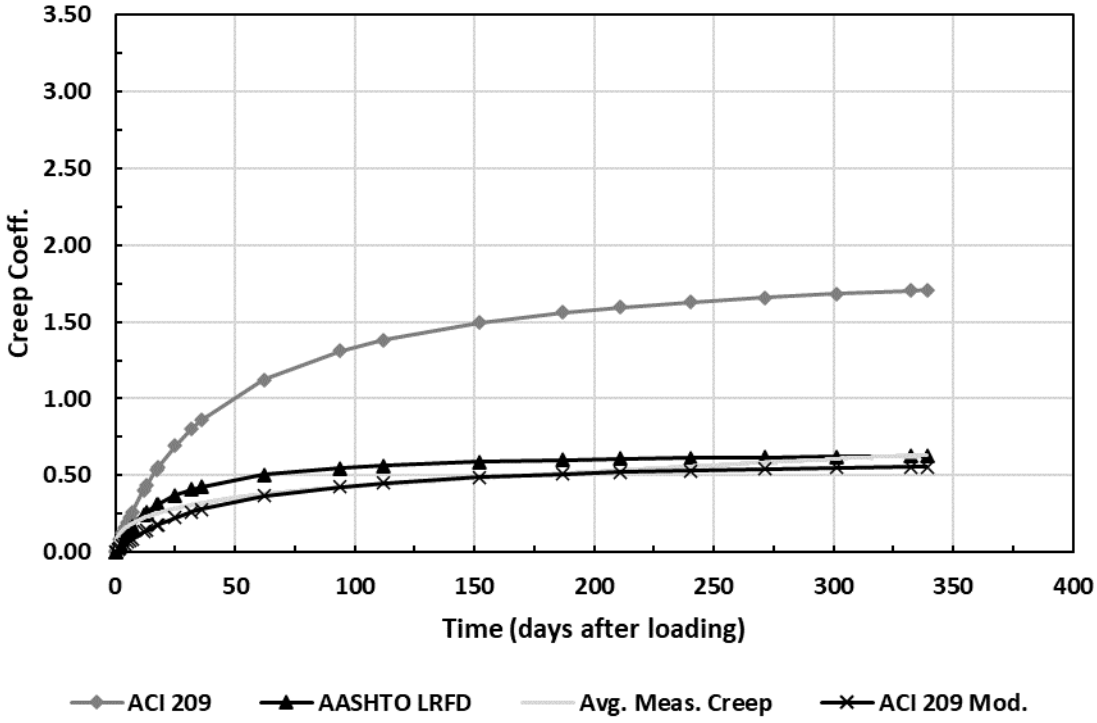

Figure 176: Comparison of measured RS-SCC creep with modelled values for creep specimens loaded at 28 day age

Note that in Figures 174 – 176, as the loading age increases from 3 hours, to 1 day, to 28 days, the magnitudes and the shapes of the modelled creep curves converge significantly towards the average measured creep curves. This is especially true for the AASHTO method and the modified ACI 209 method. The unmodified ACI 209 method is clearly not appropriate for estimating the RS-SCC creep behavior.

It is likely that the relative success of modifying the ACI 209 method is because this approach was originally derived on an empirical basis. Therefore, as Figures 174 – 176 show, it tends towards the ultimate measured compressive creep coefficient over time, even when the shape of the curve does not match measured values at earlier ages. As a result, the modified ACI 209 approach may yield somewhat reasonable incremental compressive creep coefficients

overall, but appears to generally underestimate, especially at earlier ages. If the model does not match the measured data even once the maximum creep potential has been adjusted, this might indicate that the functional form used by ACI 209 is not reflective of the RS-SCC material behavior.

Apart from the 3 hour loaded creep measurements, the AASHTO LRFD method appears to give a very reasonable approximation across all time increments. None of the three models seem to capture the unique behavior of the creep specimens loaded at an age of 3 hours. These specimens exhibit a rapid increase in creep for a week or so after loading, followed by a distinct flattening over which the continued creep rate is greatly reduced. This is very analogous to the strain behavior of beam B4 (shown in Figure 158) which experienced a 3 hour prestress release. Normally, when concrete is loaded to a high proportion of its compressive strength at a relatively early age, the ultimate creep potential (or total prestress losses) will be significantly increased. What appears to make RS-SCC unique compared to conventional concrete is that when RS-SCC is loaded at a very early age, the material is very compliant at first but in the long-term, the total creep (or prestress loss) potential does not seem to significantly increase. This may be due at least in part to highly accelerated maturation happening concurrently with the early compliance.

In summary, usage of the AASHTO LRFD method appears to be the preferred approach amongst those studied to estimate the RS-SCC creep when the concrete is loaded at 1 day or later. The modified ACI 209 approach will provide an estimate with limited accuracy (especially at early time increments) for any loading age, but it is quick and simple to perform. The unadjusted ACI 209 model is not recommended for use with BCSA cement concrete, because the basic creep coefficient used in this model appears to be inaccurate for this material. More modelling should be performed to study the phenomena involved with the RS-SCC creep

mechanisms at very early loading ages, since the creep models studied did not match the observed behavior particularly well for the 3 hour loading condition.

6. Conclusions and Recommendations

6.0 Introduction

The most significant conclusions from this research are summarized, starting with the materials testing, followed by the structural testing and the prestress loss analysis. An additional treatment is given to general conclusions, such as those relating to data acquisition and instrumentation. Finally, the dissertation is completed with a broad overview of future research topics identified during this research that would advance the state of the art in the understanding of BCSA cement concrete technology and applications.

6.1 Conclusions – Material Testing

The following summarizes the most salient conclusions derived from the data and analysis of Chapter 3 concerning the evaluation of the fresh and hardened material properties for the self-consolidating, rapid setting BCSA cement concrete mix design (RS-SCC) developed for and applied in this research.

- Mix proportions and mixing procedures were developed for rapid-setting BCSA cement that yield self-consolidating concrete with consistent fresh properties and very high early compressive strength.

- Extensive testing was conducted to balance the w/cm ratio, HRWRA dosage, and retarder dosage (granular citric acid) to achieve desired fresh and hardened properties.

- ASTM C403 testing and calorimetry testing was performed at a range of citric acid dosages and mix temperatures to develop a baseline understanding of how to extend workability/setting time and still reach very high early compressive strength targets.
    - This data is extremely dependent upon the specific mix design utilized and the conditions under which these particular data were gathered.
    - Great care should be exercised when extending these results to other situations involving BCSA cement concrete. They are intended as a guide or starting point.
    - The setting times estimated from calorimeter data showed strong intrinsic agreement with the ASTM C403 penetrometer data and showed common sense extrinsic agreement with CTS technical data.
    - In general, increasing citric acid dosages were adequate to extend the concrete setting time at elevated temperatures, while lower dosages were required at depressed temperatures. For moderate temperatures, a citric acid dosage of 0.1 – 0.25 lb/cwt was appropriate for this particular mix design.
- Modulus of Rupture (MOR) testing showed rapid early flexural strength gain.
    - Average MOR of the baseline RS-SCC mix design reached around 500 psi 3 hours after casting.
    - Maturity at early age was not problematic, as the normalized flexural strength relative to compressive strength at 3 hours was nearly the same or greater than at 28 days.

- It should be noted that varying mix parameters, such as coarse aggregate content, may result in MOR values differing from those described in this thesis.

- Modulus of Elasticity (MOE) testing showed consistent results with very high relative stiffness at early ages.

  - Average elastic modulus reached 3500 ksi in 3 hours; relative to compressive strength normalization, this value was higher than the MOE measured at 28 days and beyond.

  - The average elastic modulus reached nearly 4500 ksi at 56 days. The magnitude of MOE values measured across all ages were likely depressed somewhat because of the low coarse aggregate content in the mix design.

  - The elastic modulus was modelled with a linear correlation to the square root of the compressive strength. The model slope was 50,000 with f'_c in psi, and the model correlation coefficient was strong with an $R^2>0.99$.

  - An attempt to characterize the change in MOE with increased coarse aggregate failed due to moisture contamination of an improperly stored cement sack. This issue occurred only with 1 cement sack and affected no other tests in this project.

- Long-term creep and shrinkage testing was conducted to characterize the material behavior and assist in modeling prestress losses.

  - Shrinkage strains measured with VWSG were less than 200 με at 1 year, which is many times less than typical shrinkage for comparable high strength concrete.

- Ultimate creep coefficients at 1 year were less than 1.0 for all 3 loading ages and applied stress levels. Additionally, the results for each specimen within a loading group were very consistent.
    - The 28-day loading group at a stress level of $0.40f'_c$ (ASTM C512 compliant) had an average 1 year creep coefficient of only 0.56.
- The average elastic shortening of each group at loading was predicted very accurately (within < 10% on average) using the known applied stress and the model developed from the experimentally measured MOE.

6.2 Conclusions – Structural Testing

This section summarizes the conclusions concerning the data and analysis of Chapter 4 about the structural applications of the RS-SCC in this research. Note that for most of these results, the experimental outcomes are impacted to some degree by the prestressing strand quality. The 0.52 in. strand used in this research was qualified according to ASTM 1081 by previous OU researchers (Sadhasivam et al., 2017). If future researchers wish to compare to the results of this dissertation, it should be noted that using strand of lower or higher quality or surface condition would impact the results accordingly.

- Large block pullout tests (LBPT) were conducted in accordance with the protocol suggested by Logan (1997) to establish baseline strand bond characteristics and investigate maturity effects on strand bond.

- LBPT data showed rapid early bond strength gain, as the pullout capacity exceeded the recommended threshold for first slip capacity when the first strands were tested at 3 hours of age.

- The threshold for peak pullout capacity was not reached until between 1 day and 28 days, most likely because the compressive strength of the paste had to make significant gains to compensate for the type and proportion of coarse aggregate.
- At 1 year, the average pullout strength reached the full strength of the 0.52 in. strand (45 kips) and 4 out of 6 tested strands fractured during testing.

- Normalization of the pullout strengths by concrete compressive strength data showed that, in general, the maturity of the concrete at 3 hours did not materially hamper the strand bond compared to other testing ages.

- Ten 20 ft long prestressed RS-SCC beams were tested to ascertain the strand embedment required to achieve full development. Five were fabricated with prestress release at 3 hours, while five experienced prestress release at 24 hours. All ten were tested at around 28 days.

    - For the beams with both early (3 hr) and typical (24 hr) age prestress release, the measured development length was no more than 3.5 ft. For comparison, the ACI 318 and AASHTO LRFD equations estimated around 7.5 ft.

    - The true development lengths could be even shorter, because shear heavily influenced the failure modes at embedment lengths of 2.5 ft – 3 ft.

- Beams tested with strand embedment of 3.5 ft or greater failed in flexure, and strand slip either did not occur or was too minimal to materially impact the tested flexural capacity.

- The RS-SCC maturity at early prestress release did not appear to hamper strand bond or result in increased strand development length.

- Four prestressed beams were instrumented with VWSG, DEMEC gage points, and strand block clamps to estimate changes in transfer length from prestress release to long-term. In addition, all ten prestressed beams tested for development length were monitored for strand end-slip up until the week that they were tested.

  - The maximum transfer length estimate at prestress release was produced by the end-slip method for the 3 hour prestress release and was around 21 in. For comparison, ACI 318 (50 d_b) and AASHTO LRFD (60 d_b) estimates are 26.0 in. and 31.2 in. respectively.

  - The maximum transfer length estimate at prestress release for the 24 hour release beams was 13.4 in. and was also determined using the end-slip measurement approach.

  - Using the transfer length equation proposed by Ramirez and Russell (2008) for high-strength concrete predicted transfer lengths of 49db (25.5 in.) for the early (3 hour) release beams, and 40db (20.8 in.) for the typical (24 hour) release beams. These values somewhat more accurately reflect the observed transfer length measurements, because of the consideration of concrete compressive strength at

prestress release. This also indicates that strand bond parameters designed for high-strength concrete may be more appropriate for RS-SCC than other approaches.

- For a given transfer length measurement approach, the transfer length for the 24 hour prestress release was shorter than the transfer length for the 3 hour prestress release.

- The end-slip correlation method using $\alpha = 2.61$ consistently gave the highest transfer length estimates.

- The DEMEC baseline strain readings at prestress release for the 3 hour release beams were skewed due to thermal error caused by rapid cooling of the beams as the forms were stripped and the readings were taken.

    - The exact effects of this thermal error are difficult to quantify but the impacts were noted repeatedly in the DEMEC data.

- The measured transfer lengths increased marginally between prestress release and 56 days. The only exception was the DEMEC transfer lengths for the 3 hour release beams, which marginally decreased in the same time period.

- It is apparent that the transfer length was shorter in general for the beams which experienced prestress release at 24 hours compared to 3 hours. However, since the compressive strength at prestress release was significantly higher at 24 hours, it is not definite that this effect was entirely due to concrete maturity.

6.3 Conclusions – Prestress Losses

This section summarizes the conclusions concerning the data and analysis of Chapter 5 with respect to the measured prestress losses and how they compared both to existing estimation methods and to the time-step integration model which incorporated specific BCSA cement concrete material properties.

- Elastic shortening losses, as measured by VWSG at midspan in 4 separate beams, were closely predicted (average error <10%) using fundamental engineering mechanics (or the AASHTO LRFD approach) with transformed section properties and the elastic modulus estimate developed in Chapter 3.
    - Elastic shortening losses for the two beams with 3 hour prestress release were around 15% higher than those for the two beams with 24 hour prestress release, on average.
- The companion shrinkage beams showed strains indicating that shrinkage constituted around 15 – 42 % of the time-dependent prestress losses. The wide range was the result of one companion beam showing a significantly lower shrinkage strain (around 50% less) than the other.
- The AASHTO LRFD refined method and the ACI simplified (Zia et al.) method produced predictions of the long-term, time-dependent prestress losses that varied widely from the measured losses for the RS-SCC beams.
    - Both methods resulted in predicted time-dependent prestress loss totals that exceeded the observed losses by 186 – 274%.

- It is important to note that the overprediction of prestress losses noted with these approaches must be considered in the context of the specific parameters and time projections that they were designed for. For example, the ACI simplified (Zia et al., 1979) method considers total prestress losses, not prestress loss at a given time, "t".

- A time-step integration model for RS-SCC was developed which utilizes the creep and shrinkage data gathered from the material testing research phase (Chapter 3) along with a mechanistic framework outlined by ACI 423.10R.

  - This time-step model predicted the measured long-term prestress losses for both the 3 hour and 24 hour prestress release to within 10% (predicted 8% low for B4 – 3 TR and predicted 8% high for B3 – 24 TR).

  - In addition to reasonably predicting the long-term, time-dependent loss totals, the time-step model also generated prestress loss time-history curves that tracked closely with the measured prestress losses at any given concrete age.

  - The time-step model was externally validated by using it to predict the time-dependent prestress losses measured for BCSA cement concrete in the literature (Ramseyer and Floyd, 2013 and Bowser, 2016).

    - Although the time-step model overpredicted the measured losses, most likely because of key differences in mix design, it still resulted in better estimates than the other approaches.

- As a simplified alternative to a full time-step analysis, the AASHTO LRFD refined method was adjusted to utilize the ultimate shrinkage values and 1 year creep coefficients measured in these experiments, rather than the equations for these values recommended by AASHTO LRFD.
    - Compared to the normal AASHTO LRFD refined method or the ACI simplified method, this approach resulted in prestress loss estimates much closer to the measured values.
    - The so-called "adjusted" AASHTO refined approach overpredicted the long-term prestress loss for B4 – 3 TR by only 4% and for B3 – 24 TR by 20% (compare to 186% and 215% respectively without adjusting the AASHTO LRFD approach).
    - Adjusting the AASHTO LRFD refined method with appropriate creep and shrinkage values may be a convenient solution for practitioners not wishing to conduct a full time-step analysis.
        - The time-step analysis may be more appropriate given its fundamental mechanistic nature, and it should be chosen if the prestress loss at a given concrete age is desired, instead of a simple estimate of the total, ultimate prestress loss.
- Based upon the material property data and the prestress loss data gathered in this research, it can be concluded that the notably low prestress losses observed in this study and those from the literature (Ramseyer and Floyd, 2013 and Bowser, 2016) are due in large part to the high dimensional stability of BCSA cement concrete over time.

- The observed ultimate shrinkage values and creep coefficients were much lower than normal high strength concrete made with PC, and the modelled prestress losses matched those which were measured much more closely when these differences in material properties were comprehended.

6.4 Summary and General Conclusions

This section summarizes some general conclusions drawn from the research project as a whole, including observations regarding the performance of various data acquisition techniques and certain best practices that can be applied for future research opportunities.

- The vibrating wire strain gage (VWSG) system demonstrated outstanding performance throughout the project. The VWSG were a robust, simple, and accurate means of monitoring time-dependent strains.
    - Robust – all 33 gages not only survived installation and casting, but also functioned properly over the life of all experiments, a timeframe of 6 months to 1.5 years.
        - The VWSG strain data was almost completely seamless, except for a few days for beam B4-3TR when the logger briefly ran low on battery.
    - Simple – instrument and logger configuration, regular data downloads, and data reduction/temperature compensation were straightforward and well-documented in manufacturer literature.

- Accurate – VWSG used in this research had at least 1 με measurement accuracy and resulted in consistent measurements that correlated closely to calculated values for instantaneous and long-term changes in strain.

    - VWSG not only produced expected results for instantaneous shortening of both creep specimens and prestressed beams, but even detected and closely matched extremely small variations in strain due to changes in beam span configuration.

- DEMEC strain measurement techniques were viable but far more difficult and less accurate/repeatable compared to VWSG instrumentation.

    - When DEMEC points were glued on (as for the creep testing), there was gradual attrition over time as the glue failed and the points fell off.

        - For the creep specimen shrinkage companions, the points were lost soon enough that the DEMEC data was unusable.

        - For the creep data, there were enough specimens to maintain a running average, but the loss ratio for the DEMEC points still nearly reached 100% after a year of testing.

        - DEMEC strain gages are intended to be used in a horizontal orientation. Using the gage vertically for creep measurements is barely workable and requires extreme care by the operator. It can also lead to incidental

damage to the DEMEC gage because of excess stress on the spring system.

- With significant care by a single operator, the DEMEC strain measurements for the creep specimens were a useful “ballpark” check for the VWSG strains and did match the VWSG data reasonably well.

- When screw-type DEMEC points were used (as for the beam testing), the attrition rate was greatly reduced because the only points lost were a few which were damaged when forms were removed or when screws stripped during installation.

  - The trade-off for improved resilience with screw-type DEMEC points was reduced accuracy. These points were manufactured in-house at Fears Lab and therefore have more imperfections and variability in the tapping process.

- Thermal error was an unexpected issue for the DEMEC system, especially on the beam measurements.

  - Simply put, it is difficult to take so many measurements (56 per beam for example) quickly enough for the heat evolution and cooling of the specimens tested at early age not to noticeably skew the strain data.

  - Unlike the VWSG system, there is not currently a straightforward method to correct for DEMEC thermal error due to complex variations in heat loss along the span and cross-section.

- End-slip (strand drawn in) measurements were an easy approach for estimating transfer length but were highly variable in general.
    - The measurement variability combined with uncertainty concerning the "correct" bond stress distribution factor for a given situation mean that end-slip measurements and the resultant transfer length estimates should be viewed with an appropriate level of reservation.
    - It is the opinion of the author that these limitations indicate that end-slip measurements may be best suited to use as a quality assurance test with an upper bound bond factor to quickly, easily, and conservatively estimate transfer length.
- Minor transverse thermal cracking was noted on the tops of some of the first beams to be cast, because of cold ambient wintertime temperatures, coupled with rapid concrete heat evolution at early age.
    - This problem was easily resolved by layering burlap and plastic sheeting over the later beams. It is recommended that insulation be used, especially for large pours, to reduce this thermal gradient.
- It is critical that all cement (BCSA or otherwise) be stored with tremendous care to prevent premature moisture intrusion. All BCSA cement stored in drums with liners or sealed super sacks performed as expected. The only cement sack which was left unsealed due to miscommunication between the lab crew resulted in compromised concrete and useless data for a single batch.

6.5 Recommendations for Future Work

This section presents recommendations for future research projects that may greatly broaden and deepen the current understanding of BCSA cement concrete and increase its usefulness in the precast, prestressed concrete industry.

- More workability time and setting time testing in spaces with more sophisticated environmental/temperature control.
    - The testing in this research was limited because, although the initial materials and concrete temperatures could be controlled and the curing environment was consistent in a semi-adiabatic calorimeter, the ambient temperature during mixing could not be controlled.
    - Greater consistency could be achieved if the initial material temperatures, the ambient mixing temperature, and the curing temperatures could all match.
    - Another useful dataset would be workability/setting time when the materials and the concrete temperature were held constant, but the mixing and curing temperature varied, and vice-versa.
- For the sake of consistency, and to match the worst-case field scenario, all concrete in this research was cured in a dry condition, with no curing moisture beyond ambient humidity.
    - It is best practice, and completely realistic, to practice moist cure conditions, especially in a precast environment.

    - Future projects should investigate the impact of various curing regimes, including different moist cure durations, on properties like shrinkage, creep, and prestress loss. In principle, properly applied moist cure regimes would result in even better dimensional stability than the excellent properties observed in this study.

- Modulus of elasticity (MOE), creep, and prestress loss testing with a wider range of mix designs, especially including higher coarse to fine aggregate proportions.

    - The self-consolidating mix design used in this project was optimized for flowability and used a fine to coarse aggregate ratio of nearly 2:1.

    - This mix design met all targeted fresh and mechanical parameters and behaved excellently. The relatively low coarse aggregate content, however, likely resulted in comparatively depressed elastic modulus values and somewhat elevated creep and prestress loss measurements.
    - The material property and structural data should be expanded with future testing using various other w/cm ratios and paste contents, but especially with fine to coarse aggregate ratios closer to 1:1, for example.

- The structural testing should be expanded to more include more strand diameters, reinforcement configurations, beam geometries, and some larger-scale bridge girder sections.

    - The work done in this research and the previous literature on prestressed BCSA cement concrete was necessary to characterize fundamental structural responses of the material with straightforward geometries.

    - Moving forward, research on prestressed BCSA cement concrete must also focus on the material behavior under the many different scenarios that are used in the field, such as large-scale AASHTO girder shapes for example.

- On a practical basis, it is recommended that future research leverages VWSG instrumentation because of its robustness and accuracy.

    - DEMEC strain measurement is difficult, inaccurate, and logistically challenging compared to modern technology. Use of DEMEC strain measurement is recommended only as a compliment or check to more accurate approaches.

    - End-slip/strand draw in measurement is recommended as suitable for a quality assurance test in a precast concrete production environment, especially when complex instrumentation is infeasible. It is less useful as an index test in laboratory research.

- Some research in the literature has expressed concerns about durability issues like chloride ingress and carbonation in BCSA cement concrete and recommends polymer-based additives to reduce pore structure connectivity in this material.

    - Durability testing was beyond the scope of this research and mix designs including polymer-based additives were considered.

- Although concerns about chloride ingress and carbonation have been disputed by other researchers, polymer-based additives that reduce permeability are available from the manufacturer of domestically produced BCSA cements.

- If future stakeholders in academia or industry choose to use permeability reducing, polymer-based additives in prestressed BCSA cement concrete, some of the key material testing and structural testing performed in this research should be repeated to confirm that the polymer modified BCSA cement concrete behaves similarly from a structural perspective to the ordinary BCSA cement concrete.

References

American Association of State Highway and Transportation Officials (AASHTO), AASHTO LRFD Bridge Design Specifications, 8th Edition, Washington D.C., September 2017, Section 5.

ACI 209R-92, "Prediction of Creep, Shrinkage, and Temperature Effects in Concrete Structures," American Concrete Institute (ACI), Farmington Hills, MI, 1992 (Reapproved 2008).

ACI 209.2R-08, "Guide for Modeling and Calculating Shrinkage and Creep in Hardened Concrete," American Concrete Institute (ACI), Farmington Hills, MI, 2008.

ACI 318-14, "Building Code Requirements for Structural Concrete," American Concrete Institute (ACI), Farmington Hills, MI, 2014.

ACI 423.10R-16, "Guide to Estimating Prestress Loss," American Concrete Institute (ACI), Farmington Hills, MI, 2016.

Afroughsabet, V., Biolzi, L., and Cattaneo, S., Evaluation of Engineering Properties of Calcium Sulfoaluminate Cement-Based Concretes Reinforced with Different Types of Fibers. Materials, 12, 2151, 2019, pp. 1-18.

Alapati, P., Moradllo, M.K., Berke, N., Ley, T., and Kurtis, K.E., Designing Corrosion Resistant Systems with Alternative Cementitious Materials, *Cement*, Volume 8, June 2022, pp. 1-19.

Arezoumandi, M., Looney, K.B., and Volz, J.S., Bond Performance of Prestressing Strand in Self-Consolidating Concrete, Construction and Building Materials, 232, 2020, pp. 1-10.

ASTM A1081, “Standard Test Method for Evaluating Bond of Seven-Wire Steel Prestressing Strand,” ASTM International, West Conshohocken, PA.

ASTM C138, “Standard Test Method for Density (Unit Weight), Yield, and Air Content (Gravimetric) of Concrete,” ASTM International, West Conshohocken, PA.

ASTM C150, “Standard Specification for Portland Cement,” ASTM International, West Conshohocken, PA.

ASTM C157, “Standard Test Method for Length Change of Hardened Hydraulic-Cement Mortar and Concrete,” ASTM International, West Conshohocken, PA.

ASTM C1611, “Standard Test Method for Slump Flow of Self-Consolidating Concrete,” ASTM International, West Conshohocken, PA.

ASTM C231, “Standard Test Method for Air Content of Freshly Mixed Concrete by the Pressure Method,” ASTM International, West Conshohocken, PA.

ASTM C33, “Standard Specification for Concrete Aggregates,” ASTM International, West Conshohocken, PA.

ASTM C39, “Standard Test Method for Compressive Strength of Cylindrical Concrete Specimens,” ASTM International, West Conshohocken, PA.

ASTM C403, “Standard Test Method for Time of Setting of Concrete Mixtures by Penetration Resistance,” ASTM International, West Conshohocken, PA.

ASTM C469, “Standard Test Method for Static Modulus of Elasticity and Poisson’s Ratio of Concrete in Compression,” ASTM International, West Conshohocken, PA.

ASTM C512, “Standard Test Method for Creep of Concrete in Compression,” ASTM International, West Conshohocken, PA.

ASTM C78, “Standard Test Method for Flexural Strength of Concrete (Using Simple Beam with Third-Point Loading),” ASTM International, West Conshohocken, PA.

Bazant, Z.P. and Baweja, S. with RILEM TC 107, Creep and Shrinkage Prediction Model for Analysis and Design of Concrete Structures - Model B3. Materials and Structures, Vol. 28, 1995, pp. 357-365.

Bescher, E., Kim, J., Vallens, K., and Ramseyer, C., Low Carbon Footprint Pavement: History of Use, Performance and New Opportunities for Belitic Calcium Sulfoaluminate. Proceedings of the 13th International Symposium on Concrete Roads, Berlin, June 2018.

Bescher, E. and Ramseyer, C. Seattle-Tacoma Airport Concrete Rehabilitation Performance Review. TRB 93rd Annual Meeting, Washington D.C., April 2013.

Bescher, E., Rice, E.K., Ramseyer, C., and Roswurm, S.M., Sulfate Resistance of Calcium Sulphoaluminate Cement. Journal of Structural Integrity and Maintenance, Vol. 1, No. 3, September 2016, pp. 131-139.

Bescher, E., Stremfel, J., Ramseyer, C., and Rice, E.K., The Role of Calcium Sulfoaluminate in Concrete Sustainability. Twelfth International Conference on Recent Advances in Concrete Technology and Sustainability Issues, Prague, Czech Republic, October 30 – November 2, 2012.

Bodapati et al., Comparison of Initial and Long-Term Transfer Lengths Determined from Internal and External Concrete Strain Measurements. PCI/NBC, 2016.

Bowser, T.M., “Development Length of 0.6 in. Prestressing Strands in Precast, Prestressed Calcium Sulfoaluminate Cement Concrete,” Thesis, The University of Oklahoma, 2016.

Bowser, T.M., Murray, C.D., and Floyd, R.W., Bond Behavior of 0.6 in. (15.2 mm) Prestressing Strand in Belitic Calcium Sulfoaluminate (BCSA) Cement Concrete. ACI Structural Journal, V. 117, No. 1, January 2020, pp. 43-52.

Buckner, C.D., A Review of Strand Development Length for Pretensioned Concrete Members, PCI Journal, March-April 1995, pp. 84-105.

Bymaster, J.C., Dang, C.N., Floyd, R.W., and Hale, W.M., Prestress Losses in Pretensioned Concrete Beams Cast with Lightweight Self-Consolidating Concrete, Structures, 2, January 2015, pp. 50-57.

Chusid, M. 1,200-Foot Post-Tensioned Slab with Type K Cement Cleared for Take-off. PTI Journal, December 2006.

Cook, G., "Early Life Flexural Performance and Behavior of Reinforced BCSA Concrete Beams," Thesis, The University of Arkansas, 2018.

Crawford, Murphy, & Tilly, Inc. Constructability Report; Prestressed, Fibrous Concrete Pavement, Greater Rockford Airport, IL. U.S. Army Corps of Engineers and the U.S. DOT FAA, May 1995.

Dang, C.N., et. al., Analysis of Bond Stress Distribution for Prestressing Strand by Standard Test for Strand Bond. Engineering Structures, 2014, pp. 153-159.

Dang, C.N., et. al., A Correlation of Transfer Length and Strand End Slip. Proceedings of the 10th fib International PhD Symposium in Civil Engineering, Université Laval, Québec, Canada. July 21-23, 2014, pp. 535-540.

Dang, C.N., et. al., Correlation of Strand Surface Quality to Transfer Length. ACI Structural Journal, V. 111, No. 5, September-October 2014, pp. 1245-1252.

Dang, C.N., et. al., Determination of Bond Stress Distribution Coefficient by Maximum Likelihood Method. Journal of Structural Engineering, 2016.

Dang, C.N., et. al., Measured Development Lengths of 0.7 in. (17.8 mm) Strands for Pretensioned Beams. ACI Structural Journal, V. 113, No. 3, May June 2016, pp. 525-535.

Dang, C.N., et. al., Spacing Requirements of 0.7 in. (18 mm) Diameter Prestressing Strands. PCI Journal, January-February 2016, pp. 70-86.

de Bruyn, K., et. al., Pore Structure of Calcium Sulfoaluminate Paste and Durability of Concrete in Freeze –Thaw Environment. International Journal of Concrete Structures and Materials, Vol. 11, No. 1, March 2017, pp. 59-68.

Fimrite, P., "Work on I-280 in S.F. – Completed without a Hitch", San Francisco Chronicle – Article Reprint by CTS Cement Corp. September 2014.

Federal Highway Administration (FHWA), "Prestressing Strand for Pretension Applications – Development Length Revisited," FHWA Memorandum, October 26, 1988.

Federation International de la Precontrainte (FIP), "Test for the Determination of Tendon Transmission Length Under Static Conditions," FIP, 1982, Wexham Springs, U.K.

Floyd, R.W., Hale, W.M., and Howland, M.B., Evaluation of Strand Bond Equations for Prestressed Members Cast with Self-Consolidating Concrete, Engineering Structures, Vol. 33, July 2011, pp. 2879–2887.

Floyd, R.W., Hale, W.M., and Howland, M.B., Measured Transfer Length of 0.6 in. Prestressing Strands Cast in Lightweight Self-Consolidating Concrete, PCI Journal, May-June 2015, pp. 84-97.

Floyd, R.W., Pei, Jin-Song., Murray, C.D., Toshima, J., Ali, A., and Roswurm, S., "Development of Rating Tool for Prestressed Concrete Bridges Vulnerable to Shear," ODOT SP&R Item Number 2280, 2020, Oklahoma Department of Transportation, Oklahoma City, OK, pp. 128-129.

Floyd, R.W., Ruiz, E.D., Do, N.H., Staton, B.W., and Hale, W.M., Development Lengths of High-Strength Self-Consolidating Concrete Beams, PCI Journal, Winter 2011, pp. 36-53.

Floyd, R.W. and Soliman, M., "Application of Fiber Optic Sensors for Monitoring Prestressed Concrete Bridges," Report No. SPTC17.1-01A, 2018, Southern Plains Transportation Center, Norman, OK, pp. 1-24.

Frank, D., "The Effects of Temperature on Compressive Strength of Rapid Setting Concrete," Thesis, The University of Oklahoma, 2011.

Girgis, A.F. and Tuan, C.Y, Bond Strength of Self-Consolidating Concrete for Prestressed Concrete Applications, Nebraska Department of Roads Project Number SPR-P1(04) P571, University of Nebraska Lincoln, December 2004.

Hanson, N.W. and Kaar, P.H., Flexural Bond Tests of Pretensioned, Prestressed Beams. Journal of the American Concrete Institute, Vol. 30, No. 7, January 1959, pp. 783-802.

Hargis, C.W., Lothenbach, B.L., Muller, C.J., and Winnefeld, F., Carbonation of Calcium Sulfoaluminate Mortars. Cement and Concrete Composites, Vol. 80, March 2017, pp. 123-134.

Herrin, S. and Naughton, J. 10 Year Performance of Innovative Pavements, Greater Rockford Airport. Airfield Pavements Specialty Conference, September 2003.

Hicks, J.K., Caldarone, M.A., and Bescher, E., Opportunities from Alternative Cementitious Materials. Concrete International, April 2015, pp. 47-51.

Imbabi, M.S., Carrigan, C., and McKenna, S., Trends and Developments in Green Cement and Concrete Technology. International Journal of Sustainable Built Environment, 2012, pp. 194-216.

Janney, J.R., Nature of Bond in Pre-Tensioned Prestressed Concrete. ACI Journal, V. 50, No. 5, May 1954, pp. 717-736.

Khayat, K.H. and Mitchell, D., Self-Consolidating Concrete for Precast, Prestressed Concrete Bridge Elements. NCHRP Report 628 – Transportation Research Board, 2009.

Klein, A., Karby, T., and Polivka, M, Properties of an Expansive Cement for Chemical Prestressing. Journal of the American Concrete Institute, Vol. 58, No. 1, July 1961, pp. 59-82.

Kosmatka, S.H., Kerkhoff, B., and Panarese, W.C., "Design and Control of Concrete Mixtures," Portland Cement Association, 14th Edition, Skokie, Illinois, 2002.

Larson, K.H., “Evaluating the Time-Dependent Deformations and Bond Characteristics of a Self-Consolidating Concrete Mix and the Implication for Pretensioned Bridge Applications,” Dissertation, Kansas State University, 2006.

Ley, T., Synthesis of Rapid Setting Repair Materials. National Concrete Pavement Technology Center, Iowa State University - Technology Transfer Concrete Consortium (TTCC), February 2022.

Lin, T.Y and Klein, A., Chemical Prestressing of Concrete Elements using Expanding Cements. Journal of the American Concrete Institute, Vol. 60, No. 9, September 1963, pp. 1187-1218.

Logan, D.R., Acceptance Criteria for Bond Quality of Strand for Pretensioned Prestressed Concrete Applications, PCI Journal Special Report, March-April 1997, pp. 52-90.

Maggenti, R., Gomez, S., and Luena, R., Bridge Hinge Reconstruction in San Francisco - Accelerated Bridge Construction for Long Lasting Repairs on Aging Highways. Structure Magazine, January 2015, pp. 30-32.

Markosian, N., Tawadrous, R., Mastali, M., Thomas, R.J., and Maguire, M., Performance Evaluation of a Prestressed Belitic Calcium Sulfoaluminate Cement (BCSA) Concrete Bridge Girder. *Sustainability (MDPI)*, Vol. 13, No. 7875, September 2021, pp. 1 – 17. https://doi.org/10.3390/su13147875

Marti-Vargas, J.R., et al. Transfer and Development Lengths of Concentrically Prestressed Concrete. PCI Journal, September-October 2006a, pp. 74-85.

Marti-Vargas, J.R., et al. Test Method for Determination of the Transmission and Anchorage Lengths in Prestressed Reinforcement. Magazine of Concrete Research, Vol. 58, No. 1, February 2006b, pp. 21-29.

Marti-Vargas, J.R., et al. Reliability of Transfer Length Estimation from Strand End Slip. ACI Structural Journal, July-August 2007, pp. 487-494.

Moffatt, E.G. and Thomas, M.D.A., Durability of Rapid Strength Concrete Produced with Ettringite-Based Binders. ACI Materials Journal, V. 115, No. 1, January 2018, pp. 105-115.

Moustafa, S., Pull-Out Strength of Strand and Lifting Loops. Concrete Technology Associates Technical Bulletin, 1974.

Muller, H. S. and Hilsdorf, H. K. General Task Group 9, CEB *Comité Euro International du Béton*, 1990, pp. 201.

Murray, C.D., Floyd, R.W., and Ramseyer, C., Using Belitic Calcium Sulfoaluminate Cement for Precast, Prestressed Concrete Beams. PCI Journal, V. 64, No. 2, March-April 2019, pp. 55-67.

Naji, B., Ross, B. E., and Floyd, R. “Characterization of Bond-Loss Failures in Pretensioned Concrete Girders,” ASCE Journal of Bridge Engineering. Vol. 22, No. 4, 2017, DOI: 10.1061/(ASCE)BE.1943-5592.0001025.

Nawy, E.G., “Prestressed Concrete – A Fundamental Approach,” Prentice Hall, 5th Edition Update, Upper Saddle River, NJ, 2010.

Peterman, R.J., A Simple Quality Assurance Test for Strand Bond, PCI Journal, Spring 2009 (Revised May 2009) pp. 143-161.

Phillips, M.V., Ramey, G.E., Pittman, D.W. Bridge Deck Construction Using Type K Cement. Journal of Bridge Engineering, Vol. 2, No. 4, November 1997, pp. 176-182.

Precast/Prestressed Concrete Institute (PCI), “PCI Design Handbook – Precast and Prestressed Concrete,” 7th Edition, Chicago, IL, 2010, Chapter 5.

Ramirez-Garcia, A.T., et. al., Effect of Concrete Compressive Strength on Transfer Length, Structures, 2015, pp. 1-10.

Ramirez-Garcia, A.T., et. al., Influence of Concrete Strength on Development Length of Prestressed Concrete Members, Journal of Building Engineering, 2016, pp. 173-183.

Ramirez, J. and Russell, B., “Transfer, Development and Splice Length for Strand/Reinforcement in High-Strength Concrete.” National Cooperative Highway Research Program, Transportation Research Board, Washington, DC, 2008.

Ramseyer, C., and Perez, V., Highway Panel Replacement - CSA Concrete in California. National Conference on Preservation, Repair, and Rehabilitation of Concrete Pavements, St. Louis, Missouri., April 2009.

Richardson, D., Tung, Y., Tobias, D., Hindi, R. An Experimental Study of Bridge Deck Cracking using Type K-Cement. Construction and Building Materials, Vol. 52, February 2014, pp. 366-374.

Riding, K. A., Peterman, R. J., and Polydorou, T., “Establishment of Minimum Acceptance Criterion for Strand Bond as Measured by ASTM A1081,” PCI Journal, Vol. 61, No. 3, 2016, pp. 86-103.

Roswurm, J.S, “Influence of Retarders on Shrinkage and Compressive Strength in Rapid Set Concrete,” Thesis, The University of Oklahoma, 2018.

Roswurm, S.J, “Characterizing the Behavior of Concrete Cast with Type K Shrinkage Compensating Cement when Placed under Mechanical Restraint,” Thesis, The University of Oklahoma, 2018.

Roswurm, S.M, “Investigation of the Mechanical Behavior of Type K Shrinkage Compensating Concrete under Various Forms of Mechanical Restraint,” Thesis, The University of Oklahoma, 2013.

Russell, B.W. and Burns, N.H., Measurement of Transfer Lengths on Pretensioned Concrete Elements. Journal of Structural Engineering, May 1997, pp. 541-549.

Sadhasivam, K., Bella Canet, E., Wendling, A., and Floyd, R.W. Effect of Vertical Strand Location on Bond Performance of Prestressing Strands Cast in Lightweight Self-Consolidating

Concrete. Journal of Structural Integrity and Maintenance, Vol. 2, No. 1, 2017, pp. 39-47, DOI: 10.1080/24705314.2017.1280588.

Shadravan, S., "Dimensional Stability of Concrete Slabs on Grade," Dissertation, The University of Oklahoma, 2011.

Stumps, A., "Bond Stress Distribution of the Embedment Length of Prestressed Concrete Specimens," Honors Thesis, The University of Oklahoma, 2016.

Tabatabai, H. and Dickson, T.J., The History of the Prestressing Strand Development Length Equation, PCI Journal, November-December 1993, pp. 64-75.

Tadros, M.K., et. al., Prestress Losses in Pretensioned High-Strength Concrete Bridge Girders. NCHRP Report 496 – Transportation Research Board, 2003.

Tanksley, S.D, "Internal Curing of Calcium Sulfoaluminate Cement Concrete using Lightweight Aggregate," Thesis, The University of Oklahoma, 2018.

Thomas, R.J., Maguire, M., Sorenson, A.D., and Quezada, I., Calcium Sulfoaluminate Cement – Benefits and Applications. Concrete International, April 2018, pp. 65-69.

Wight, J.K., "Reinforced Concrete – Mechanics and Design," 7th Edition, Hoboken, NJ, 2016, Section 3-6.

Winnefeld, F., et al., Carbonation Resistance of Calcium Sulfoaluminate Cement Mortars. Conference Paper, Lausanne Switzerland, August 2018, pp. 243-246.

Zhao, W., et al. Development of a Laser-Speckle Imaging Device to Determine the Transfer Length in Pretensioned Concrete Members. PCI Journal, Winter 2012, pp. 135-143.

Zia, P., et. al., Estimating Prestress Losses. Concrete International, June 1979, pp. 32-38.

Appendix A: Heat Evolution Plots from Calorimetry

Note that in the calorimetry heat evolution plots, not every curve stops at the same time from casting. This is because multiple tests were being run in the calorimeter every day for this research, and usage of the calorimeter was being coordinated around other research projects as well. For every batch, however, it was ensured that the curve was allowed to run well past the peak temperature evolution, since the point of interest for setting time occurred before the temperature peak anyway.

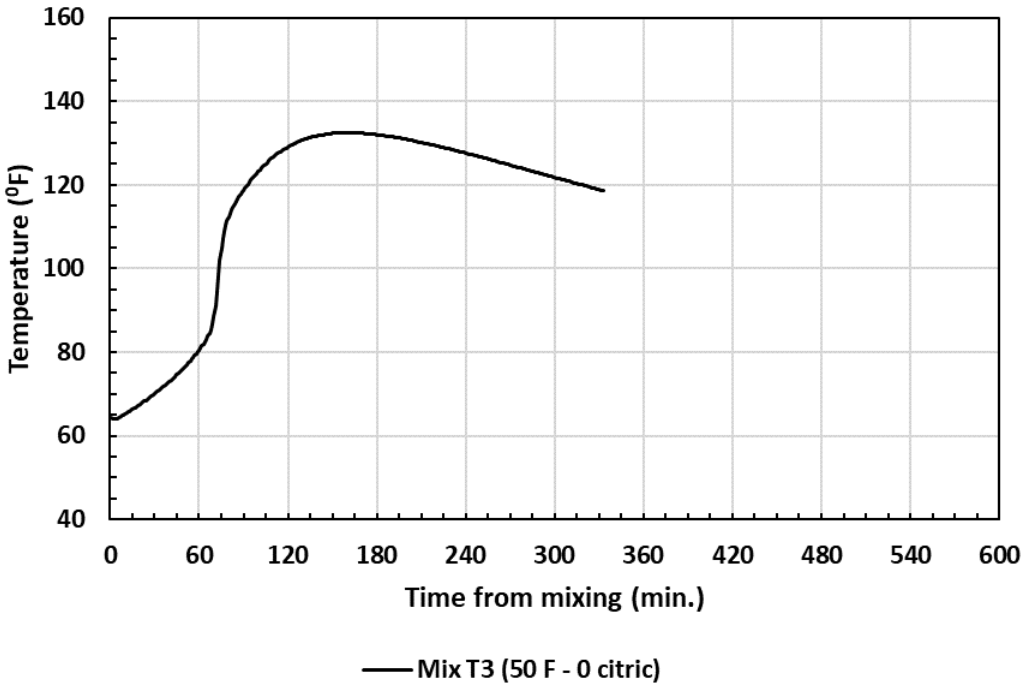

Figure 177: Calorimetry temperature curve for Mix T3, 50 ˚F, 0 lb/cwt citric acid

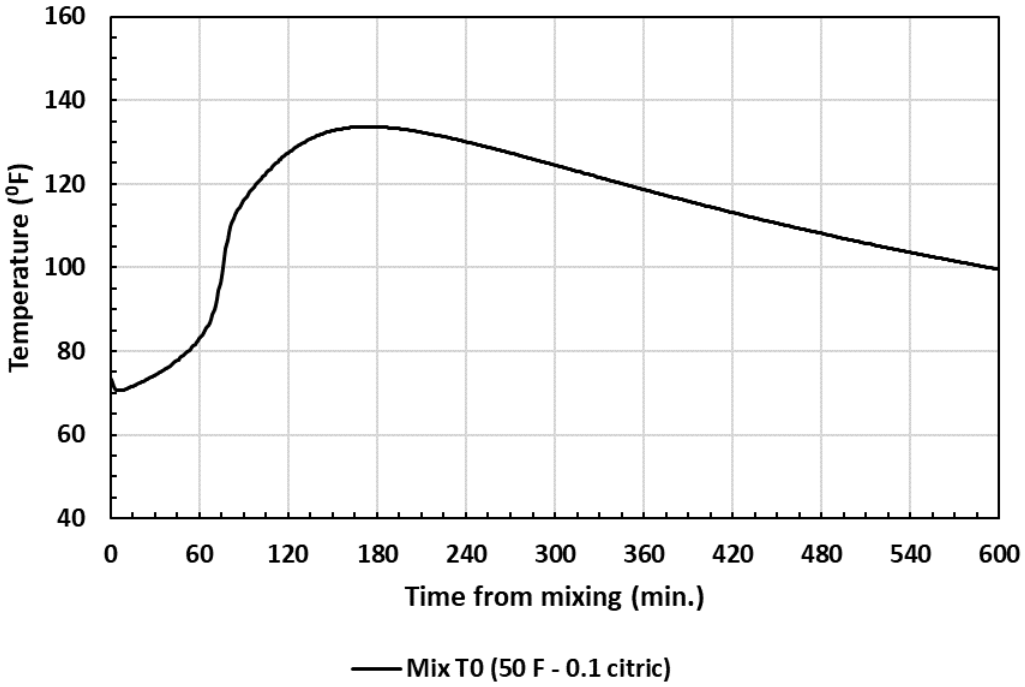

Figure 178: Calorimetry temperature curve for Mix T0, 50 ˚F, 0.1 lb/cwt citric acid

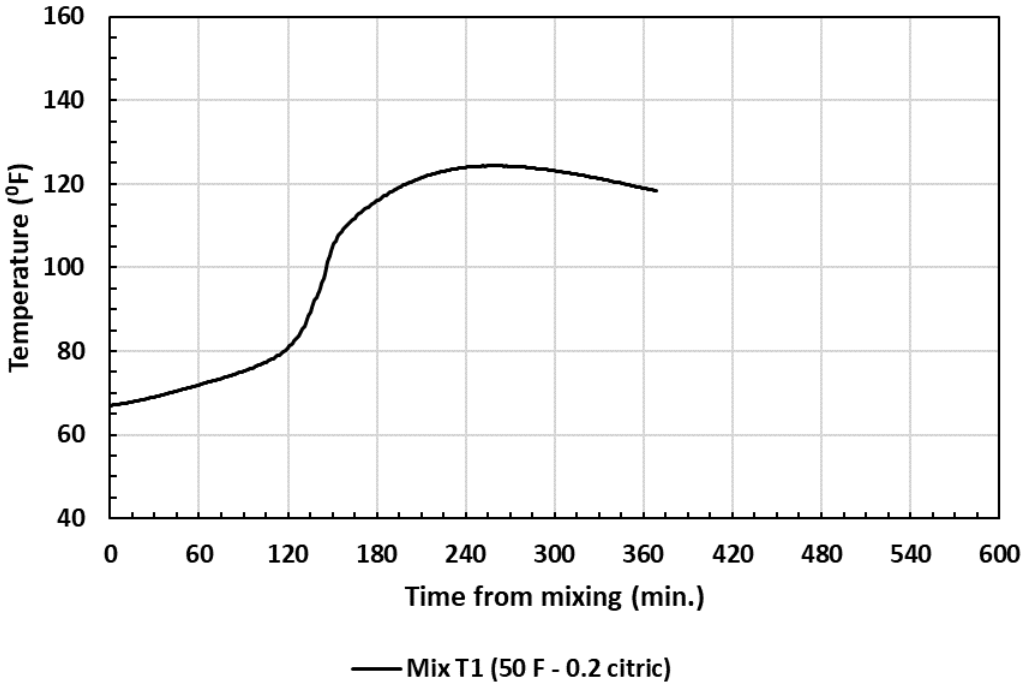

Figure 179: Calorimetry temperature curve for Mix T1, 50 ˚F, 0.2 lb/cwt citric acid

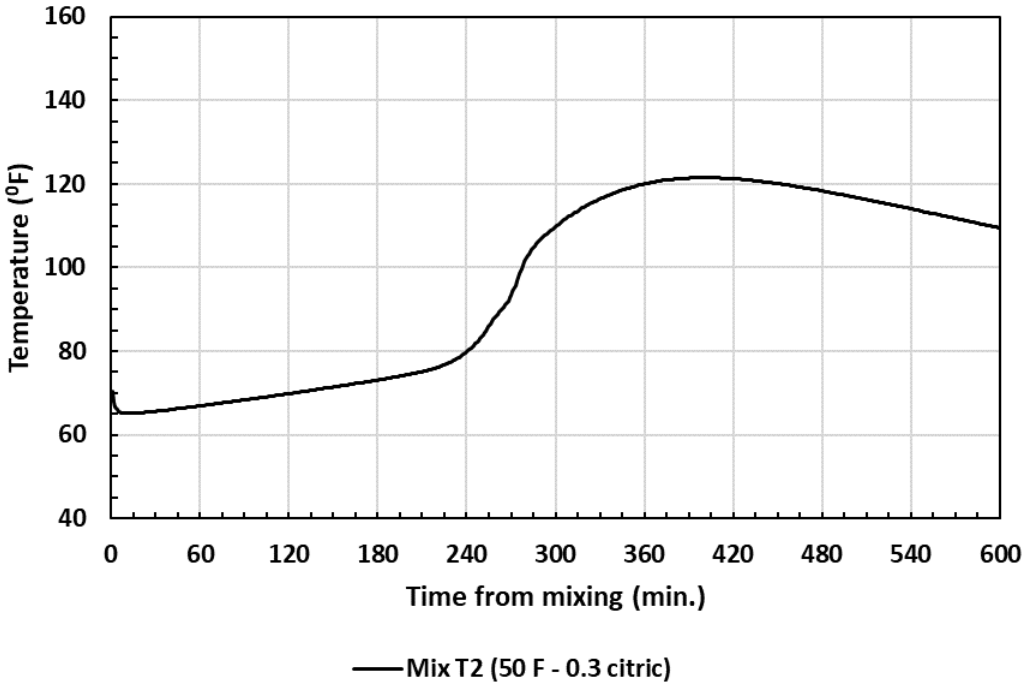

Figure 180: Calorimetry temperature curve for Mix T2, 50 ˚F, 0.3 lb/cwt citric acid

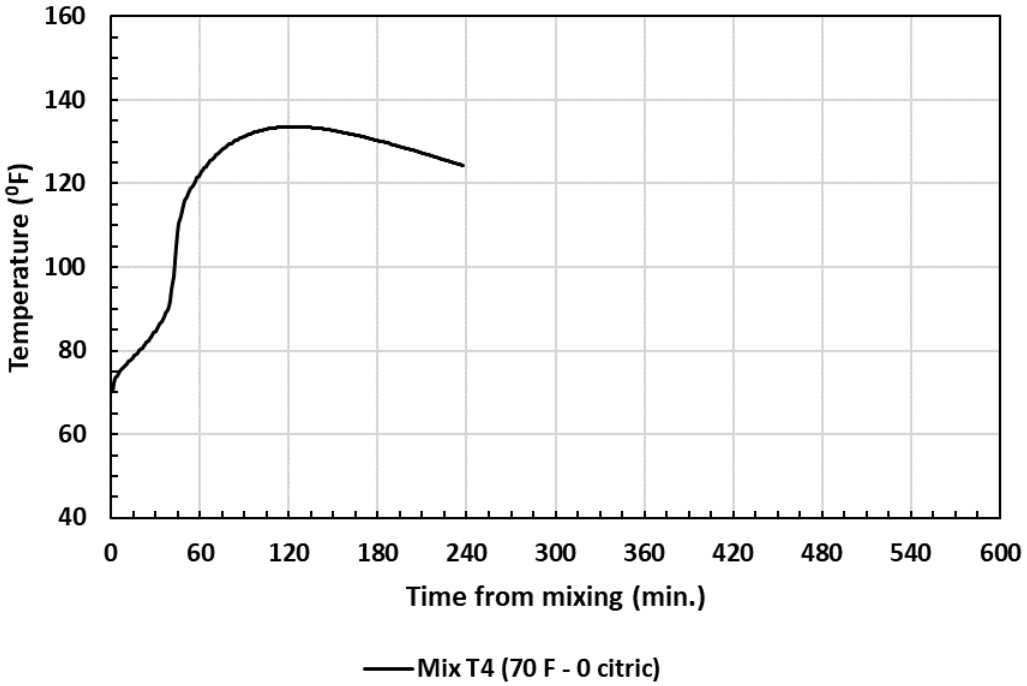

Figure 181: Calorimetry temperature curve for Mix T4, 70 ˚F, 0 lb/cwt citric acid

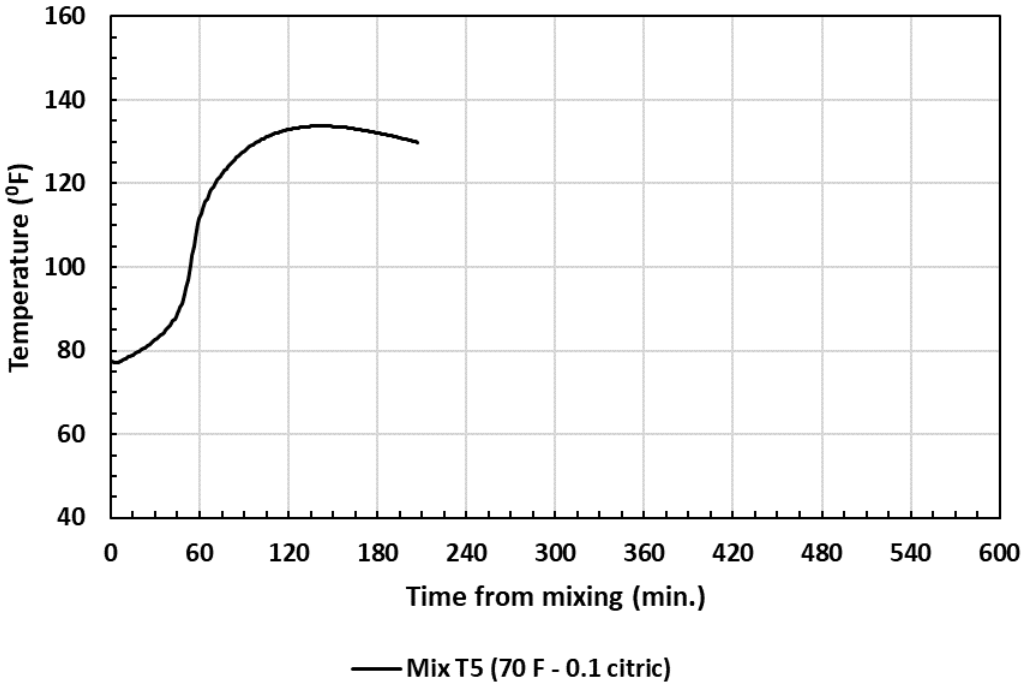

Figure 182: Calorimetry temperature curve for Mix T5, 70 ˚F, 0.1 lb/cwt citric acid

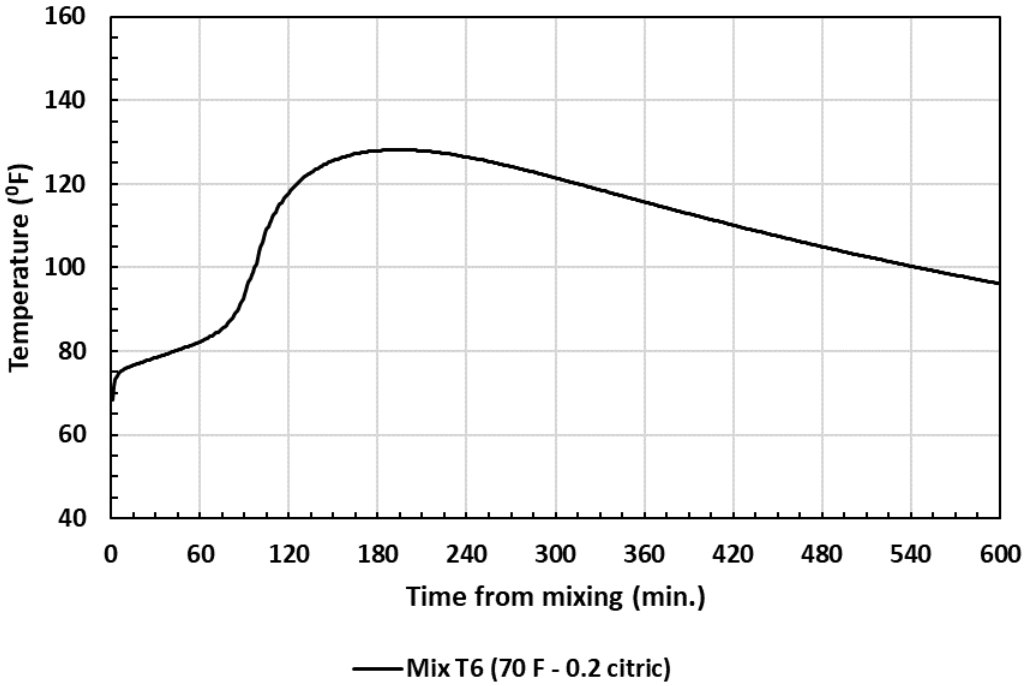

Figure 183: Calorimetry temperature curve for Mix T6, 70 ˚F, 0.2 lb/cwt citric acid

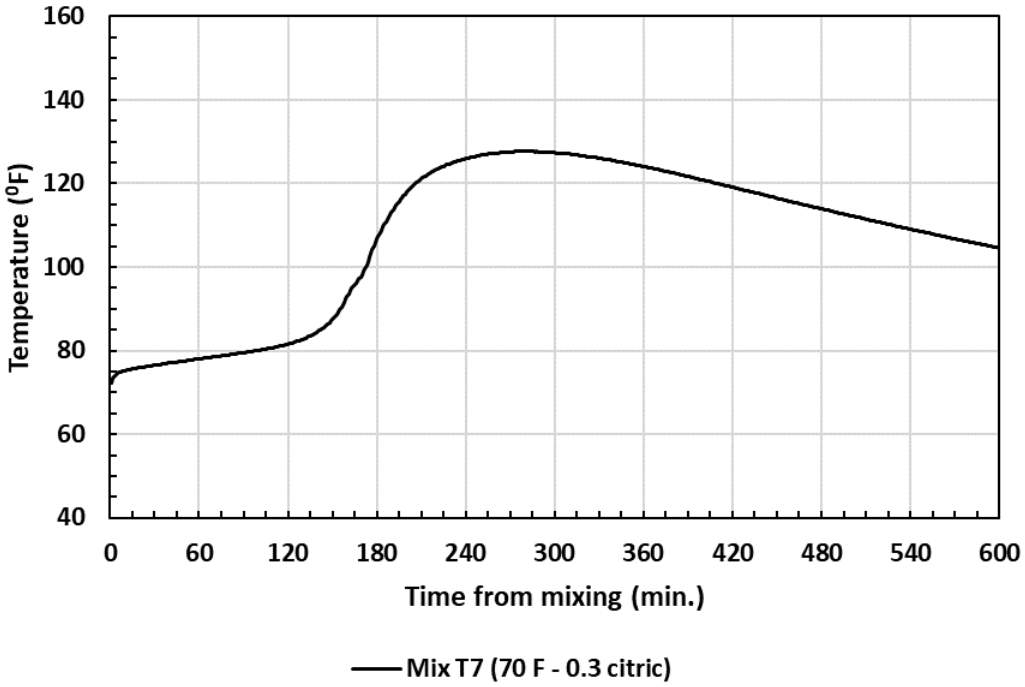

Figure 184: Calorimetry temperature curve for Mix T7, 70 ˚F, 0.3 lb/cwt citric acid

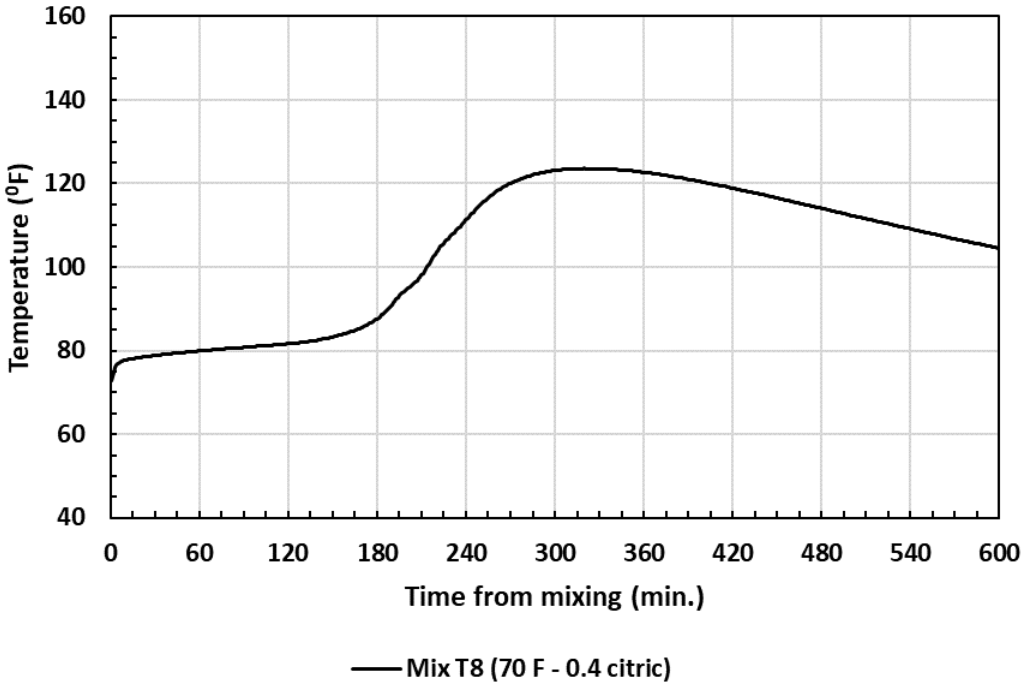

Figure 185: Calorimetry temperature curve for Mix T8, 70 ˚F, 0.4 lb/cwt citric acid

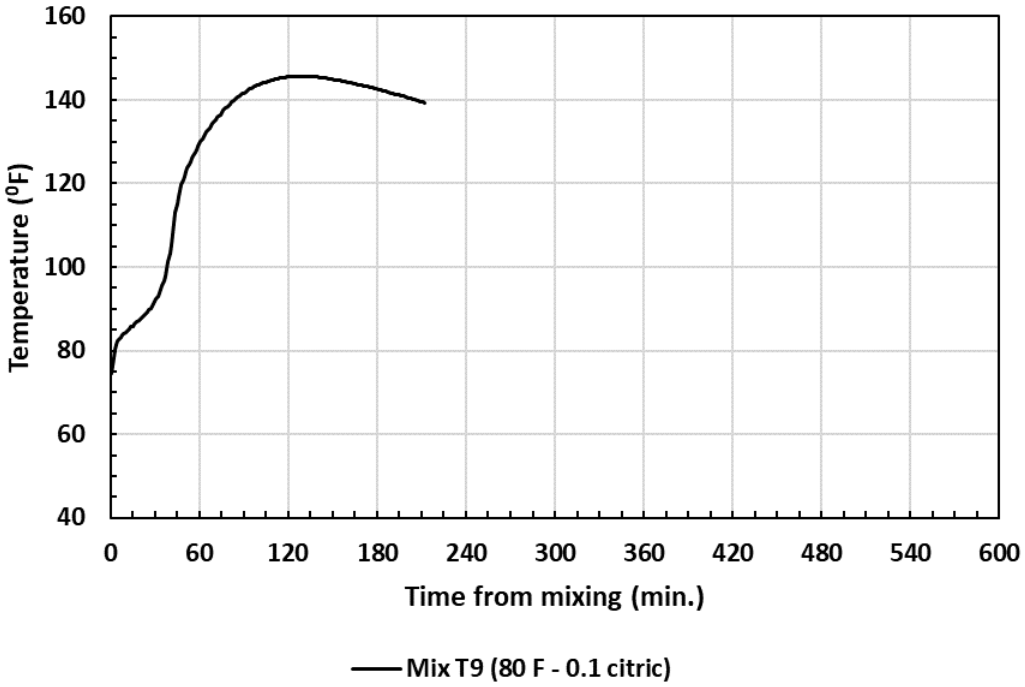

Figure 186: Calorimetry temperature curve for Mix T9, 80 ˚F, 0.1 lb/cwt citric acid

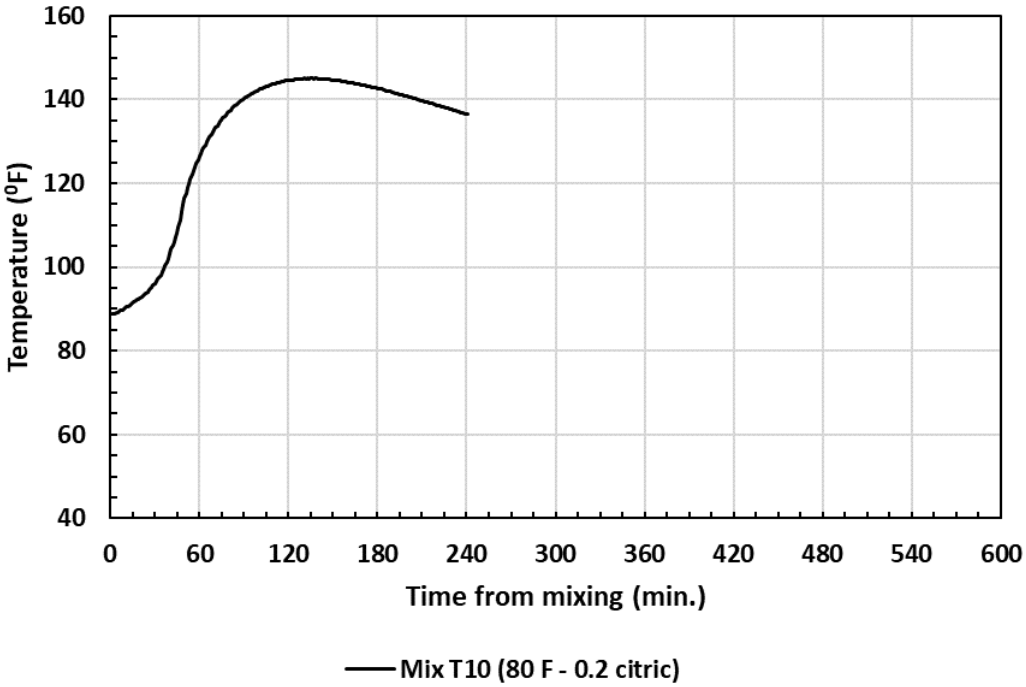

Figure 187: Calorimetry temperature curve for Mix T10, 80 ˚F, 0.2 lb/cwt citric acid

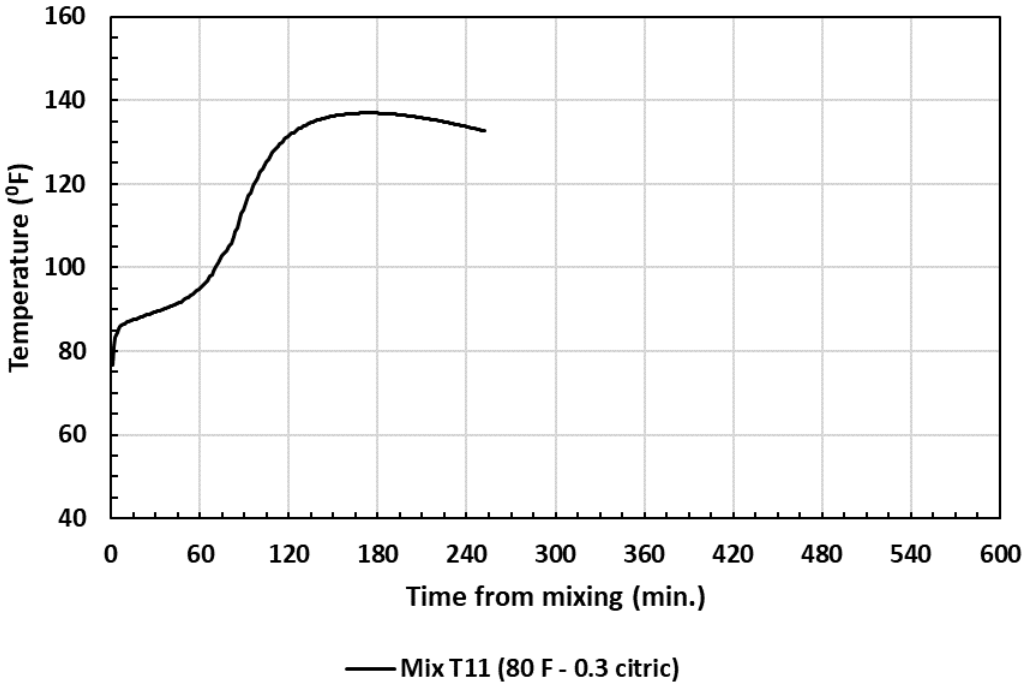

Figure 188: Calorimetry temperature curve for Mix T11, 80 ˚F, 0.3 lb/cwt citric acid

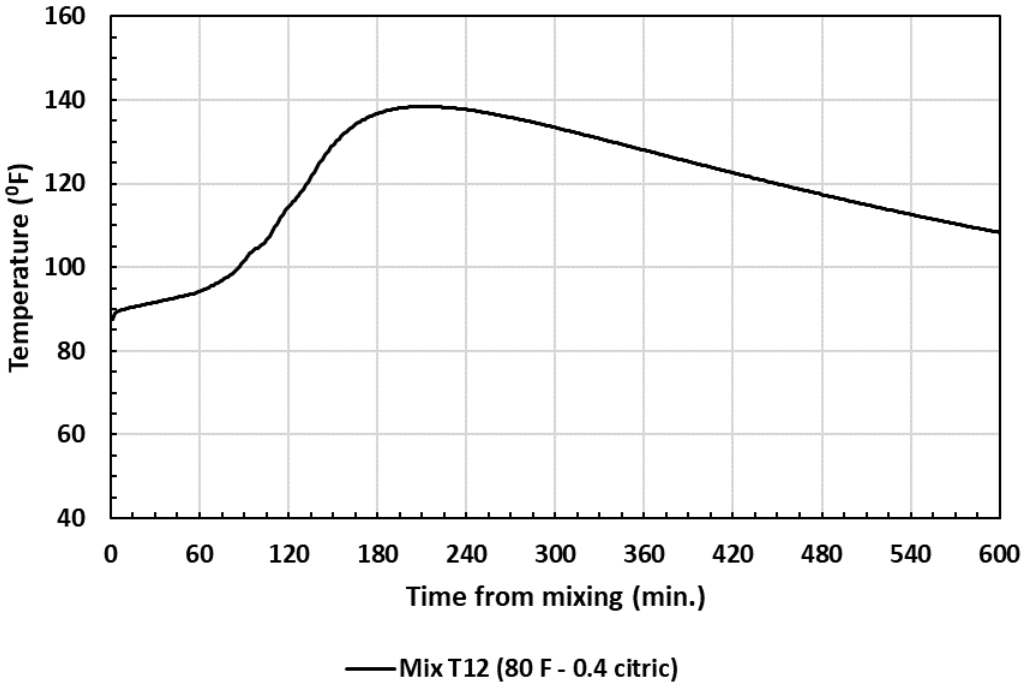

Figure 189: Calorimetry temperature curve for Mix T12, 80 ˚F, 0.4 lb/cwt citric acid

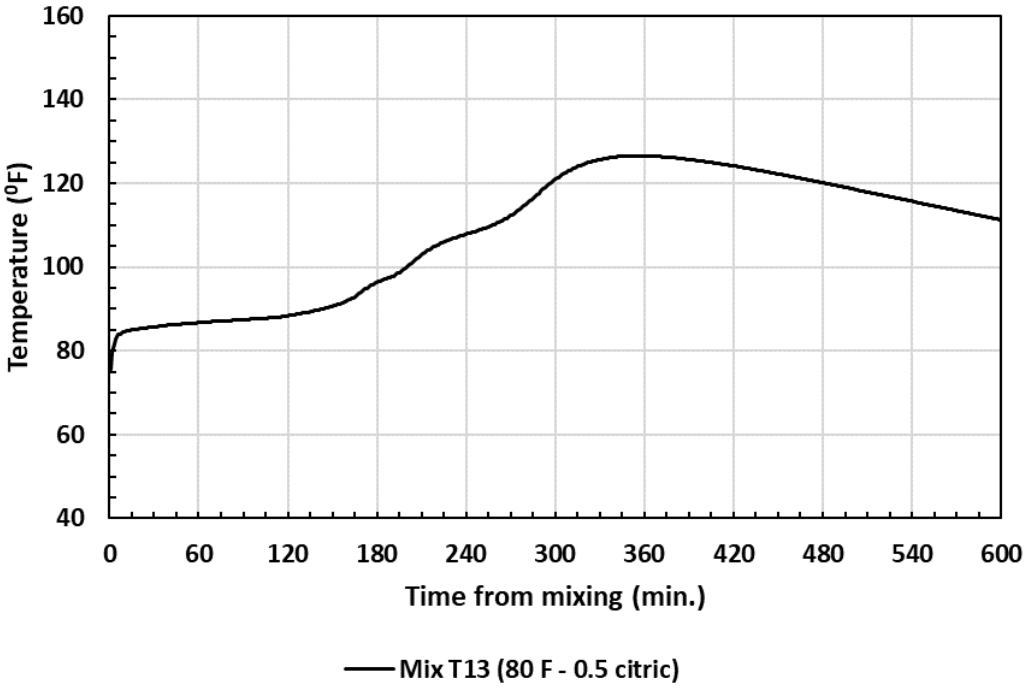

Figure 190: Calorimetry temperature curve for Mix T13, 80 ˚F, 0.5 lb/cwt citric acid

Appendix B: Mix Quantities and Fresh Concrete Data

Table 30: Mix Data for Beam B2 - Trial Pour

Rapid Set Test: **SCC Mix B2 (Trial 2)** 10/28/2021

w/cm =	0.34		Sand % water =	1.747	start	9:13 AM
PC =	0	type I	Rock % water =	0.326	batch	9:18 AM
RS =	752				stop	9:40 AM
Komp =	0					
FA =	150.4	0.200				

Sand SG=	2.63	SSD=	0.70	b/bo =	0.65	Fineness Modulus = 2.5
Rock SG=	2.68	SSD=	0.86	DRUW =	101.0	
H2O SG=	1.0					
C SG=	3.15					
RS SG=	2.88					
Komp SG	2.88					
FA SG=	2.58					

Theoretical	Weight	Volume
Portland Cement	0.0	0.00
Rapid Set Cement	752	4.18
Komponent	0	0.00
Fly Ash	150.4	0.93
Water	306.8	4.92
Rock	950.0	5.68
Air Entrapped 2%	0.0	0.54
DCI-chemical part	0.0	0.00
Sand	1763.2	10.74
Sum	3922.4	27

Coarse/Fines Ratio	
By Weight	0.54
By Volume	0.53

		1 yd	15	cu ft	
Portland Cement		0.0	0.00	lb	
Rapid Set Cement		752.0	417.78	lb	OLDER RS, from Ramseyer
Komponent		0.0	0.00	lb	
Fly Ash		150.4	83.56	lb	Class C Fly Ash (Red Rock, new)
Coarse Aggregate, ASTM #7		944.9	524.96	lb	(Dolese 5/8" #3 Cover)
Fine Aggregate, Dover Sand		1781.6	989.79	lb	
Water		293.2	162.89	lb	
Air Ent. Admixture	oz	0.0	0.00	ml	
Citric Acid Retarder	% of cement	0.22%	416.91	grams	
Glenium (HRWR)	oz/cwt	13.0	1929.13	ml	**2021 Glenium 7920 from Dolese*'
DCI (Accel w/ water)	oz	0.0	0.00	ml	

Concrete Temperature	- F
Air Temperature	61 F
Humidity	38%
Air Content	- %
Slump Flow	25.5-27"
Unit Weight Pot Empty	-
Unit Weight Pot Full	-

Expected Unit Wt		145.27
Measured	-	-
Difference	%	-

Table 31: Mix Data for Beam B3 – 24 Hour Transfer Length Testing

Rapid Set Test: **SCC Mix B3 - 24 TR** 11/18/2021

w/cm =	0.34		Sand % water =	2.004	start	10:01 AM
PC =	0	type I	Rock % water =	0.323	batch	10:05 AM
RS =	752				stop	10:40 AM
Komp =	0					
FA =	150.4	0.200				

Sand SG=	2.63	SSD=	0.70	b/bo =	0.65	Fineness Modulus = 2.5
Rock SG=	2.68	SSD=	0.86	DRUW =	101.0	
H2O SG=	1.0					
C SG=	3.15					
RS SG=	2.88					
Komp SG	2.88					
FA SG=	2.58					

Theoretical	Weight	Volume
Portland Cement	0.0	0.00
Rapid Set Cement	752	4.18
Komponent	0	0.00
Fly Ash	150.4	0.93
Water	306.8	4.92
Rock	950.0	5.68
Air Entrapped 2%	0.0	0.54
DCI-chemical part	0.0	0.00
Sand	1763.2	10.74
Sum	3922.4	27

Coarse/Fines Ratio	
By Weight	0.54
By Volume	0.53

		1 yd	15.5	cu ft	
Portland Cement		0.0	0.00	lb	
Rapid Set Cement		752.0	431.70	lb	NEW RS, July 2021
Komponent		0.0	0.00	lb	
Fly Ash		150.4	86.34	lb	Class C Fly Ash (Red Rock, new)
Coarse Aggregate, ASTM #7		944.9	542.44	lb	(Dolese 5/8" #3 Cover)
Fine Aggregate, Dover Sand		1786.2	1025.39	lb	
Water		288.6	165.68	lb	
Air Ent. Admixture	oz	0.0	0.00	ml	
Citric Acid Retarder	% of cement	0.22%	430.81	grams	
Glenium (HRWR)	oz/cwt	11.0	1686.75	ml	**2021 Glenium 7920 from Dolese**
DCI (Accel w/ water)	oz	0.0	0.00	ml	

Concrete Temperature	- F
Air Temperature	60 F
Humidity	10%
Air Content	- %
Slump Flow	28-29"
Unit Weight Pot Empty	-
Unit Weight Pot Full	-

Expected Unit Wt		145.27
Measured	-	-
Difference	%	-

Table 32: Mix Data for Beam B4 – 3 Hour Transfer Length Testing

Rapid Set Test: **SCC Mix B4 - 3 TR** 12/9/2021

w/cm =	0.34			Sand % water =	1.020	start	9:40 AM
PC =	0	type I		Rock % water =	0.228	batch	9:45 AM
RS =	752					stop	10:00 AM
Komp =	0						
FA =	150.4	0.200					

Sand SG=	2.63	SSD=	0.70	b/bo =	0.65	Fineness Modulus = 2.5
Rock SG=	2.68	SSD=	0.86	DRUW =	101.0	
H2O SG=	1.0					
C SG=	3.15					
RS SG=	2.88					
Komp SG	2.88					
FA SG=	2.58					

Theoretical	Weight	Volume		Coarse/Fines Ratio
Portland Cement	0.0	0.00	By Weight	0.54
Rapid Set Cement	752	4.18	By Volume	0.53
Komponent	0	0.00		
Fly Ash	150.4	0.93		
Water	306.8	4.92		
Rock	950.0	5.68		
Air Entrapped 2%	0.0	0.54		
DCI-chemical part	0.0	0.00		
Sand	1763.2	10.74		
Sum	3922.4	27		

		1 yd	16	cu ft	
Portland Cement		0.0	0.00	lb	
Rapid Set Cement		752.0	445.63	lb	NEW RS, July 2021
Komponent		0.0	0.00	lb	
Fly Ash		150.4	89.13	lb	Class C Fly Ash (Red Rock, new)
Coarse Aggregate, ASTM #7		944.0	559.41	lb	(Dolese 5/8" #3 Cover)
Fine Aggregate, Dover Sand		1768.8	1048.19	lb	
Water		307.1	181.99	lb	
Air Ent. Admixture	oz	0.0	0.00	ml	
Citric Acid Retarder	% of cement	0.12%	242.57	grams	
Glenium (HRWR)	oz/cwt	12.5	1978.60	ml	**2021 Glenium 7920 from Dolese**
DCI (Accel w/ water)	oz	0.0	0.00	ml	

Concrete Temperature	- F
Air Temperature	62.8 F
Humidity	35%
Air Content	- %
Slump Flow	31 "
Unit Weight Pot Empty	-
Unit Weight Pot Full	-

Expected Unit Wt		145.27
Measured	-	-
Difference	%	-

Table 33: Mix Data for Beam B5 – 24 Hour Transfer Length Testing

Rapid Set Test: **SCC Mix B5 - 24 TR** 1/26/2022

w/cm =	0.34		Sand % water =	2.836	start	8:53 AM
PC =	0	type I	Rock % water =	0.268	batch	8:58 AM
RS =	752				stop	9:15 AM
Komp =	0					
FA =	150.4	0.200				

Sand SG=	2.63	SSD=	0.70	b/bo =	0.65	Fineness Modulus = 2.5
Rock SG=	2.68	SSD=	0.86	DRUW =	101.0	
H2O SG=	1.0					
C SG=	3.15					
RS SG=	2.88					
Komp SG	2.88					
FA SG=	2.58					

Theoretical	Weight	Volume
Portland Cement	0.0	0.00
Rapid Set Cement	752	4.18
Komponent	0	0.00
Fly Ash	150.4	0.93
Water	306.8	4.92
Rock	950.0	5.68
Air Entrapped 2%	0.0	0.54
DCI-chemical part	0.0	0.00
Sand	1763.2	10.74
Sum	3922.4	27

Coarse/Fines Ratio	
By Weight	0.54
By Volume	0.53

		1 yd	15.5	cu ft	
Portland Cement		0.0	0.00	lb	
Rapid Set Cement		752.0	431.70	lb	NEW RS, July 2021
Komponent		0.0	0.00	lb	
Fly Ash		150.4	86.34	lb	Class C Fly Ash (Red Rock, new)
Coarse Aggregate, ASTM #7		944.4	542.14	lb	(Dolese 5/8" #3 Cover NEW 01/22)
Fine Aggregate, Dover Sand		1800.8	1033.80	lb	
Water		273.9	157.27	lb	
Air Ent. Admixture	oz	0.0	0.00	ml	
Citric Acid Retarder	% of cement	0.17%	332.90	grams	
Glenium (HRWR)	oz/cwt	11.0	1686.75	ml	**2021 Glenium 7920 from Dolese**
DCI (Accel w/ water)	oz	0.0	0.00	ml	

Concrete Temperature	62.5 F
Air Temperature	66.2 F
Humidity	10%
Air Content	- %
Slump Flow	30.5-31"
Unit Weight Pot Empty	-
Unit Weight Pot Full	-

Expected Unit Wt		145.27
Measured	-	-
Difference	%	-

Table 34: Mix Data for Beam B6 – 3 Hour Development Length Testing

Rapid Set Test: **SCC Mix B6 - 3 DV** 2/7/2022

w/cm =	0.34		Sand % water =	1.862	start	8:48 AM
PC =	0	type I	Rock % water =	0.327	batch	8:54 AM
RS =	752				stop	9:15 AM
Komp =	0					
FA =	150.4	0.200				

Sand SG=	2.63	SSD=	0.70	b/bo =	0.65	Fineness Modulus = 2.5
Rock SG=	2.68	SSD=	0.86	DRUW =	101.0	
H2O SG=	1.0					
C SG=	3.15					
RS SG=	2.88					
Komp SG	2.88					
FA SG=	2.58					

Theoretical	Weight	Volume
Portland Cement	0.0	0.00
Rapid Set Cement	752	4.18
Komponent	0	0.00
Fly Ash	150.4	0.93
Water	306.8	4.92
Rock	950.0	5.68
Air Entrapped 2%	0.0	0.54
DCI-chemical part	0.0	0.00
Sand	1763.2	10.74
Sum	3922.4	27

Coarse/Fines Ratio	
By Weight	0.54
By Volume	0.53

		1 yd	15.5	cu ft	
Portland Cement		0.0	0.00	lb	
Rapid Set Cement		752.0	431.70	lb	NEW RS, July 2021
Komponent		0.0	0.00	lb	
Fly Ash		150.4	86.34	lb	Class C Fly Ash (Red Rock, new)
Coarse Aggregate, ASTM #7		944.9	542.46	lb	(Dolese 5/8" #3 Cover NEW 01/22)
Fine Aggregate, Dover Sand		1783.7	1023.95	lb	
Water		291.1	167.13	lb	
Air Ent. Admixture	oz	0.0	0.00	ml	
Citric Acid Retarder	% of cement	0.12%	234.98	grams	
Glenium (HRWR)	oz/cwt	10.0	1533.41	ml	**2021 Glenium 7920 from Dolese**
DCI (Accel w/ water)	oz	0.0	0.00	ml	

Concrete Temperature	- F
Air Temperature	67.5 F
Humidity	27%
Air Content	- %
Slump Flow	31-34 "
Unit Weight Pot Empty	-
Unit Weight Pot Full	-

Expected Unit Wt		145.27
Measured	-	-
Difference	%	-

Table 35: Mix Data for Beam B7 – 3 Hour Development Length Testing

Rapid Set Test: **SCC Mix B7 - 3 DV** 2/11/2022

w/cm =	0.34		Sand % water =	2.682	start	8:57 AM
PC =	0	type I	Rock % water =	0.347	batch	9:02 AM
RS =	752				stop	9:20 AM
Komp =	0					
FA =	150.4	0.200				

Sand SG=	2.63	SSD=	0.70	b/bo =	0.65	Fineness Modulus = 2.5
Rock SG=	2.68	SSD=	0.86	DRUW =	101.0	
H2O SG=	1.0					
C SG=	3.15					
RS SG=	2.88					
Komp SG	2.88					
FA SG=	2.58					

Theoretical	Weight	Volume
Portland Cement	0.0	0.00
Rapid Set Cement	752	4.18
Komponent	0	0.00
Fly Ash	150.4	0.93
Water	306.8	4.92
Rock	950.0	5.68
Air Entrapped 2%	0.0	0.54
DCI-chemical part	0.0	0.00
Sand	1763.2	10.74
Sum	3922.4	27

Coarse/Fines Ratio	
By Weight	0.54
By Volume	0.53

		1 yd	15.5	cu ft	
Portland Cement		0.0	0.00	lb	
Rapid Set Cement		752.0	431.70	lb	NEW RS, July 2021
Komponent		0.0	0.00	lb	
Fly Ash		150.4	86.34	lb	Class C Fly Ash (Red Rock, new)
Coarse Aggregate, ASTM #7		945.1	542.57	lb	(Dolese 5/8" #3 Cover NEW 01/22)
Fine Aggregate, Dover Sand		1798.1	1032.25	lb	
Water		276.0	158.46	lb	
Air Ent. Admixture	oz	0.0	0.00	ml	
Citric Acid Retarder	% of cement	0.12%	234.98	grams	
Glenium (HRWR)	oz/cwt	10.0	1533.41	ml	**2021 Glenium 7920 from Dolese**
DCI (Accel w/ water)	oz	0.0	0.00	ml	

Concrete Temperature	68 F
Air Temperature	71 F
Humidity	25%
Air Content	- %
Slump Flow	27-28.5"
Unit Weight Pot Empty	-
Unit Weight Pot Full	-

Expected Unit Wt		145.27
Measured	-	-
Difference	%	-

Table 36: Mix Data for Beam B8 – 3 Hour Development Length Testing

Rapid Set Test: **SCC Mix B8 - 3 DV** 2/15/2022

w/cm =	0.34		Sand % water =	1.672	start	10:51 AM
PC =	0	type I	Rock % water =	0.139	batch	10:57 AM
RS =	752				stop	11:15 AM
Komp =	0					
FA =	150.4	0.200				

Sand SG=	2.63	SSD=	0.70	b/bo =	0.65	Fineness Modulus = 2.5
Rock SG=	2.68	SSD=	0.86	DRUW =	101.0	
H2O SG=	1.0					
C SG=	3.15					
RS SG=	2.88					
Komp SG	2.88					
FA SG=	2.58					

Theoretical	Weight	Volume
Portland Cement	0.0	0.00
Rapid Set Cement	752	4.18
Komponent	0	0.00
Fly Ash	150.4	0.93
Water	306.8	4.92
Rock	950.0	5.68
Air Entrapped 2%	0.0	0.54
DCI-chemical part	0.0	0.00
Sand	1763.2	10.74
Sum	3922.4	27

Coarse/Fines Ratio	
By Weight	0.54
By Volume	0.53

		1 yd	15.5	cu ft	
Portland Cement		0.0	0.00	lb	
Rapid Set Cement		752.0	431.70	lb	NEW RS, July 2021
Komponent		0.0	0.00	lb	
Fly Ash		150.4	86.34	lb	Class C Fly Ash (Red Rock, new)
Coarse Aggregate, ASTM #7		943.1	541.44	lb	(Dolese 5/8" #3 Cover NEW 01/22)
Fine Aggregate, Dover Sand		1780.3	1022.03	lb	
Water		296.3	170.10	lb	
Air Ent. Admixture	oz	0.0	0.00	ml	
Citric Acid Retarder	% of cement	0.14%	274.15	grams	
Glenium (HRWR)	oz/cwt	10.0	1533.41	ml	**2021 Glenium 7920 from Dolese**
DCI (Accel w/ water)	oz	0.0	0.00	ml	

Concrete Temperature	70.7 F
Air Temperature	70.5 F
Humidity	31%
Air Content	- %
Slump Flow	31.25 "
Unit Weight Pot Empty	-
Unit Weight Pot Full	-

Expected Unit Wt		145.27
Measured	-	-
Difference	%	-

Table 37: Mix Data for Beam B9 – 3 Hour Development Length Testing

Rapid Set Test: **SCC Mix B9 - 3 DV** 2/18/2022

w/cm =	0.34			Sand % water =	1.972	start	8:45 AM
PC =	0	type I		Rock % water =	0.142	batch	8:51 AM
RS =	752					stop	9:20 AM
Komp =	0						
FA =	150.4	0.200					

Sand SG=	2.63	SSD=	0.70	b/bo =	0.65	Fineness Modulus = 2.5
Rock SG=	2.68	SSD=	0.86	DRUW =	101.0	
H2O SG=	1.0					
C SG=	3.15					
RS SG=	2.88					
Komp SG	2.88					
FA SG=	2.58					

Theoretical	Weight	Volume
Portland Cement	0.0	0.00
Rapid Set Cement	752	4.18
Komponent	0	0.00
Fly Ash	150.4	0.93
Water	306.8	4.92
Rock	950.0	5.68
Air Entrapped 2%	0.0	0.54
DCI-chemical part	0.0	0.00
Sand	1763.2	10.74
Sum	3922.4	27

Coarse/Fines Ratio	
By Weight	0.54
By Volume	0.53

		1 yd	15.5	cu ft	
Portland Cement		0.0	0.00	lb	
Rapid Set Cement		752.0	431.70	lb	NEW RS, July 2021
Komponent		0.0	0.00	lb	
Fly Ash		150.4	86.34	lb	Class C Fly Ash (Red Rock, new)
Coarse Aggregate, ASTM #7		943.2	541.45	lb	(Dolese 5/8" #3 Cover NEW 01/22)
Fine Aggregate, Dover Sand		1785.6	1025.07	lb	
Water		290.9	166.98	lb	
Air Ent. Admixture	oz	0.0	0.00	ml	
Citric Acid Retarder	% of cement	0.13%	254.57	grams	
Glenium (HRWR)	oz/cwt	10.0	1533.41	ml	**2021 Glenium 7920 from Dolese**
DCI (Accel w/ water)	oz	0.0	0.00	ml	

Concrete Temperature	60 F	Expected Unit Wt		145.27
Air Temperature	64.2 F	Measured	-	-
Humidity	17%	Difference	%	-
Air Content	- %			
Slump Flow	37 "	(29.5" 10 min. later)		
Unit Weight Pot Empty	-			
Unit Weight Pot Full	-			

Table 38: Mix Data for Beam B10 – 3 Hour Development Length Testing

Rapid Set Test: **SCC Mix B10 - 3 DV** 2/22/2022

w/cm =	0.34		Sand % water =	2.407	start	11:18 AM
PC =	0	type I	Rock % water =	0.219	batch	11:23 AM
RS =	752				stop	11:45 AM
Komp =	0					
FA =	150.4	0.200				

Sand SG=	2.63	SSD=	0.70	b/bo =	0.65	Fineness Modulus = 2.5
Rock SG=	2.68	SSD=	0.86	DRUW =	101.0	
H2O SG=	1.0					
C SG=	3.15					
RS SG=	2.88					
Komp SG	2.88					
FA SG=	2.58					

Theoretical	Weight	Volume
Portland Cement	0.0	0.00
Rapid Set Cement	752	4.18
Komponent	0	0.00
Fly Ash	150.4	0.93
Water	306.8	4.92
Rock	950.0	5.68
Air Entrapped 2%	0.0	0.54
DCI-chemical part	0.0	0.00
Sand	1763.2	10.74
Sum	3922.4	27

Coarse/Fines Ratio	
By Weight	0.54
By Volume	0.53

		1 yd	15.5	cu ft	
Portland Cement		0.0	0.00	lb	
Rapid Set Cement		752.0	431.70	lb	NEW RS, July 2021
Komponent		0.0	0.00	lb	
Fly Ash		150.4	86.34	lb	Class C Fly Ash (Red Rock, new)
Coarse Aggregate, ASTM #7		943.9	541.88	lb	(Dolese 5/8" #3 Cover NEW 01/22)
Fine Aggregate, Dover Sand		1793.3	1029.47	lb	
Water		282.3	162.03	lb	
Air Ent. Admixture	oz	0.0	0.00	ml	
Citric Acid Retarder	% of cement	0.11%	215.40	grams	
Glenium (HRWR)	oz/cwt	9.0	1380.07	ml	**2021 Glenium 7920 from Dolese**
DCI (Accel w/ water)	oz	0.0	0.00	ml	

Concrete Temperature	- F
Air Temperature	65 F
Humidity	10%
Air Content	- %
Slump Flow	30 "
Unit Weight Pot Empty	-
Unit Weight Pot Full	-

Expected Unit Wt		145.27
Measured	-	-
Difference	%	-

Table 39: Mix Data for Beam B11 – 3 Hour Transfer Length Testing

Rapid Set Test: **SCC Mix B11 - 3 TR** 3/4/2022

w/cm =	0.34		Sand % water =	2.320	start	9:49 AM
PC =	0	type I	Rock % water =	0.579	batch	9:55 AM
RS =	752				stop	10:10 AM
Komp =	0					
FA =	150.4	0.200				

Sand SG=	2.63	SSD=	0.70	b/bo =	0.65	Fineness Modulus = 2.5
Rock SG=	2.68	SSD=	0.86	DRUW =	101.0	
H2O SG=	1.0					
C SG=	3.15					
RS SG=	2.88					
Komp SG	2.88					
FA SG=	2.58					

Theoretical	Weight	Volume
Portland Cement	0.0	0.00
Rapid Set Cement	752	4.18
Komponent	0	0.00
Fly Ash	150.4	0.93
Water	306.8	4.92
Rock	950.0	5.68
Air Entrapped 2%	0.0	0.54
DCI-chemical part	0.0	0.00
Sand	1763.2	10.74
Sum	3922.4	27

Coarse/Fines Ratio	
By Weight	0.54
By Volume	0.53

		1 yd	15.5	cu ft	
Portland Cement		0.0	0.00	lb	
Rapid Set Cement		752.0	431.70	lb	NEW RS, July 2021
Komponent		0.0	0.00	lb	
Fly Ash		150.4	86.34	lb	Class C Fly Ash (Red Rock, new)
Coarse Aggregate, ASTM #7		947.3	543.84	lb	(Dolese 5/8" #3 Cover NEW 01/22)
Fine Aggregate, Dover Sand		1791.7	1028.59	lb	
Water		280.4	161.00	lb	
Air Ent. Admixture	oz	0.0	0.00	ml	
Citric Acid Retarder	% of cement	0.15%	293.73	grams	
Glenium (HRWR)	oz/cwt	11.5	1763.42	ml	**2021 Glenium 7920 from Dolese**
DCI (Accel w/ water)	oz	0.0	0.00	ml	

Concrete Temperature	70.5 F
Air Temperature	67 F
Humidity	38%
Air Content	- %
Slump Flow	30-31 "
Unit Weight Pot Empty	-
Unit Weight Pot Full	-

Expected Unit Wt		145.27
Measured	-	-
Difference	%	-

Table 40: Mix Data for Beam B12 – 24 Hour Development Length Testing

Rapid Set Test: **SCC Mix B12 - 24 DV** 3/9/2022

w/cm =	0.34		Sand % water =	1.626	start	8:49 AM
PC =	0	type I	Rock % water =	0.368	batch	8:55 AM
RS =	752				stop	9:11 AM
Komp =	0					
FA =	150.4	0.200				

Sand SG=	2.63	SSD=	0.70	b/bo =	0.65	Fineness Modulus = 2.5
Rock SG=	2.68	SSD=	0.86	DRUW =	101.0	
H2O SG=	1.0					
C SG=	3.15					
RS SG=	2.88					
Komp SG	2.88					
FA SG=	2.58					

Theoretical	Weight	Volume
Portland Cement	0.0	0.00
Rapid Set Cement	752	4.18
Komponent	0	0.00
Fly Ash	150.4	0.93
Water	306.8	4.92
Rock	950.0	5.68
Air Entrapped 2%	0.0	0.54
DCI-chemical part	0.0	0.00
Sand	1763.2	10.74
Sum	3922.4	27

Coarse/Fines Ratio	
By Weight	0.54
By Volume	0.53

		1 yd	15.5	cu ft	
Portland Cement		0.0	0.00	lb	
Rapid Set Cement		752.0	431.70	lb	NEW RS, July 2021
Komponent		0.0	0.00	lb	
Fly Ash		150.4	86.34	lb	Class C Fly Ash (Red Rock, new)
Coarse Aggregate, ASTM #7		945.3	542.69	lb	(Dolese 5/8" #3 Cover NEW 01/22)
Fine Aggregate, Dover Sand		1779.5	1021.56	lb	
Water		295.0	169.34	lb	
Air Ent. Admixture	oz	0.0	0.00	ml	
Citric Acid Retarder	% of cement	0.15%	293.73	grams	
Glenium (HRWR)	oz/cwt	8.0	1226.73	ml	**2021 Glenium 7920 from Dolese**
DCI (Accel w/ water)	oz	0.0	0.00	ml	

Concrete Temperature	62 F
Air Temperature	61.2 F
Humidity	27%
Air Content	- %
Slump Flow	28 "
Unit Weight Pot Empty	-
Unit Weight Pot Full	-

Expected Unit Wt		145.27
Measured	-	-
Difference	%	-

Table 41: Mix Data for Beam B13 – 24 Hour Development Length Testing

Rapid Set Test: **SCC Mix B13 - 24 DV** 3/11/2022

w/cm =	0.34		Sand % water =	1.412	start	8:03 AM
PC =	0	type I	Rock % water =	0.211	batch	8:09 AM
RS =	752				stop	8:18 AM
Komp =	0					
FA =	150.4	0.200				

Sand SG=	2.63	SSD=	0.70	b/bo =	0.65	Fineness Modulus = 2.5
Rock SG=	2.68	SSD=	0.86	DRUW =	101.0	
H2O SG=	1.0					
C SG=	3.15					
RS SG=	2.88					
Komp SG	2.88					
FA SG=	2.58					

Theoretical	Weight	Volume
Portland Cement	0.0	0.00
Rapid Set Cement	752	4.18
Komponent	0	0.00
Fly Ash	150.4	0.93
Water	306.8	4.92
Rock	950.0	5.68
Air Entrapped 2%	0.0	0.54
DCI-chemical part	0.0	0.00
Sand	1763.2	10.74
Sum	3922.4	27

Coarse/Fines Ratio	
By Weight	0.54
By Volume	0.53

		1 yd	15.5	cu ft	
Portland Cement		0.0	0.00	lb	
Rapid Set Cement		752.0	431.70	lb	NEW RS, July 2021
Komponent		0.0	0.00	lb	
Fly Ash		150.4	86.34	lb	Class C Fly Ash (Red Rock, new)
Coarse Aggregate, ASTM #7		943.8	541.83	lb	(Dolese 5/8" #3 Cover NEW 01/22)
Fine Aggregate, Dover Sand		1775.7	1019.39	lb	
Water		300.3	172.39	lb	
Air Ent. Admixture	oz	0.0	0.00	ml	
Citric Acid Retarder	% of cement	0.15%	293.73	grams	
Glenium (HRWR)	oz/cwt	8.0	1226.73	ml	**2021 Glenium 7920 from Dolese**
DCI (Accel w/ water)	oz	0.0	0.00	ml	

Concrete Temperature	64 F
Air Temperature	64.4 F
Humidity	10%
Air Content	- %
Slump Flow	30 "
Unit Weight Pot Empty	-
Unit Weight Pot Full	-

Expected Unit Wt		145.27
Measured	-	-
Difference	%	-

Table 42: Mix Data for Beam B14 – 24 Hour Development Length Testing

Rapid Set Test: **SCC Mix B14 - 24 DV** 3/18/2022

w/cm =	0.34		Sand % water =	1.059	start	11:10 AM
PC =	0	type I	Rock % water =	0.435	batch	11:16 AM
RS =	752				stop	11:45 AM
Komp =	0					
FA =	150.4	0.200				

Sand SG=	2.63	SSD=	0.70	b/bo =	0.65	Fineness Modulus = 2.5
Rock SG=	2.68	SSD=	0.86	DRUW =	101.0	
H2O SG=	1.0					
C SG=	3.15					
RS SG=	2.88					
Komp SG	2.88					
FA SG=	2.58					

Theoretical	Weight	Volume
Portland Cement	0.0	0.00
Rapid Set Cement	752	4.18
Komponent	0	0.00
Fly Ash	150.4	0.93
Water	306.8	4.92
Rock	950.0	5.68
Air Entrapped 2%	0.0	0.54
DCI-chemical part	0.0	0.00
Sand	1763.2	10.74
Sum	3922.4	27

Coarse/Fines Ratio	
By Weight	0.54
By Volume	0.53

		1 yd	15.5	cu ft	
Portland Cement		0.0	0.00	lb	
Rapid Set Cement		752.0	431.70	lb	NEW RS, July 2021
Komponent		0.0	0.00	lb	
Fly Ash		150.4	86.34	lb	Class C Fly Ash (Red Rock, new)
Coarse Aggregate, ASTM #7		946.0	543.05	lb	(Dolese 5/8" #3 Cover NEW 01/22)
Fine Aggregate, Dover Sand		1769.5	1015.82	lb	
Water		304.5	174.79	lb	
Air Ent. Admixture	oz	0.0	0.00	ml	
Citric Acid Retarder	% of cement	0.18%	352.48	grams	
Glenium (HRWR)	oz/cwt	8.0	1226.73	ml	**2021 Glenium 7920 from Dolese**
DCI (Accel w/ water)	oz	0.0	0.00	ml	

Concrete Temperature	64 F
Air Temperature	67 F
Humidity	34%
Air Content	- %
Slump Flow	23 "
Unit Weight Pot Empty	-
Unit Weight Pot Full	-

Expected Unit Wt		145.27
Measured	-	-
Difference	%	-

Table 43: Mix Data for Beam B15 – 24 Hour Development Length Testing

Rapid Set Test: **SCC Mix B15 - 24 DV** 3/22/2022

w/cm =	0.34		Sand % water =	2.148	start	12:26 PM
PC =	0	type I	Rock % water =	0.324	batch	12:32 PM
RS =	752				stop	12:50 PM
Komp =	0					
FA =	150.4	0.200				

Sand SG=	2.63	SSD=	0.70	b/bo =	0.65	Fineness Modulus = 2.5
Rock SG=	2.68	SSD=	0.86	DRUW =	101.0	
H2O SG=	1.0					
C SG=	3.15					
RS SG=	2.88					
Komp SG	2.88					
FA SG=	2.58					

Theoretical	Weight	Volume
Portland Cement	0.0	0.00
Rapid Set Cement	752	4.18
Komponent	0	0.00
Fly Ash	150.4	0.93
Water	306.8	4.92
Rock	950.0	5.68
Air Entrapped 2%	0.0	0.54
DCI-chemical part	0.0	0.00
Sand	1763.2	10.74
Sum	3922.4	27

Coarse/Fines Ratio

By Weight	0.54
By Volume	0.53

		1 yd	15.5	cu ft	
Portland Cement		0.0	0.00	lb	
Rapid Set Cement		752.0	431.70	lb	NEW RS, July 2021
Komponent		0.0	0.00	lb	
Fly Ash		150.4	86.34	lb	Class C Fly Ash (Red Rock, new)
Coarse Aggregate, ASTM #7		944.9	542.45	lb	(Dolese 5/8" #3 Cover NEW 01/22)
Fine Aggregate, Dover Sand		1788.7	1026.84	lb	
Water		286.0	164.18	lb	
Air Ent. Admixture	oz	0.0	0.00	ml	
Citric Acid Retarder	% of cement	0.20%	391.64	grams	
Glenium (HRWR)	oz/cwt	8.0	1226.73	ml	**2021 Glenium 7920 from Dolese**
DCI (Accel w/ water)	oz	0.0	0.00	ml	

Concrete Temperature	68 F
Air Temperature	70 F
Humidity	35%
Air Content	- %
Slump Flow	25 "
Unit Weight Pot Empty	-
Unit Weight Pot Full	-

Expected Unit Wt		145.27
Measured	-	-
Difference	%	-

Table 44: Mix Data for Beam B16 – 24 Hour Development Length Testing

Rapid Set Test: **SCC Mix B16 - 24 DV** 3/24/2022

w/cm =	0.34		Sand % water =	4.559	start	11:40 AM
PC =	0	type I	Rock % water =	1.786	batch	11:46 AM
RS =	752				stop	12:00 PM
Komp =	0					
FA =	150.4	0.200				

Sand SG=	2.63	SSD=	0.70	b/bo =	0.65	Fineness Modulus = 2.5
Rock SG=	2.68	SSD=	0.86	DRUW =	101.0	
H2O SG=	1.0					
C SG=	3.15					
RS SG=	2.88					
Komp SG	2.88					
FA SG=	2.58					

Theoretical	Weight	Volume
Portland Cement	0.0	0.00
Rapid Set Cement	752	4.18
Komponent	0	0.00
Fly Ash	150.4	0.93
Water	306.8	4.92
Rock	950.0	5.68
Air Entrapped 2%	0.0	0.54
DCI-chemical part	0.0	0.00
Sand	1763.2	10.74
Sum	3922.4	27

Coarse/Fines Ratio	
By Weight	0.54
By Volume	0.53

		1 yd	15.5	cu ft	
Portland Cement		0.0	0.00	lb	
Rapid Set Cement		752.0	431.70	lb	NEW RS, July 2021
Komponent		0.0	0.00	lb	
Fly Ash		150.4	86.34	lb	Class C Fly Ash (Red Rock, new)
Coarse Aggregate, ASTM #7		958.8	550.42	lb	(Dolese 5/8" #3 Cover NEW 01/22)
Fine Aggregate, Dover Sand		1831.2	1051.25	lb	
Water		227.3	130.47	lb	
Air Ent. Admixture	oz	0.0	0.00	ml	
Citric Acid Retarder	% of cement	0.20%	391.64	grams	
Glenium (HRWR)	oz/cwt	10.5	1610.08	ml	**2021 Glenium 7920 from Dolese**
DCI (Accel w/ water)	oz	0.0	0.00	ml	

Concrete Temperature	68 F
Air Temperature	67 F
Humidity	10%
Air Content	2.7 %
Slump Flow	29.25"
Unit Weight Pot Empty	7.76
Unit Weight Pot Full	43.4

Expected Unit Wt		145.27
Measured	35.64	142.56
Difference	%	1.87

Appendix C: Detailed Pretensioning Records

Note that f_{si} denotes the initial strand stress, immediately prior to prestress release, as measured by the load cell between the strand chuck and live end abutment bulkhead. Note also that the theoretical elongation is constituted solely by elastic deformation and does not attempt to account for chuck slip or strand curvature.

Table 45: Prestress Data for Beam B2 - Trial Pour

Prestress Record			
Date:	10/27/2021		
Beam Index:	B2 - Trial		
Elongation			
Load (lb.)	Stress (ksi)	Ruler (in.)	Δ (in.)
0	0	12-1/4	-
34,375	206.2	16	3.75
Theoretical Elongation (in.) ≈			3
Chuck Slip			
Chuck	Initial (in.)	Tensioned (in.)	Slip (in.)
DE	32/64	21/64	0.17
DW	30/64	19/64	0.17
LE	34/64	20/64	0.22
LW	32/64	20/64	0.19
Average Chuck Slip (in.) =			0.188
Prestress Release			
Time (hrs.)	Load (lb.)	f_{si} (ksi)	f'_{ci} (psi)
3.5	31,964	191.7	4322

Table 46: Prestress Data for Beam B4 – 3TR

Prestress Record			
Date:	12/9/2021		
Beam Index:	B4 - 3TR		
Elongation			
Load (lb.)	Stress (ksi)	Ruler (in.)	Δ (in.)
0	0	12-1/4	-
34,484	206.9	16-3/16	3.938
Theoretical Elongation (in.) ≈			3
Chuck Slip			
Chuck	Initial (in.)	Tensioned (in.)	Slip (in.)
DE	30/64	17/64	0.20
DW	30/64	17/64	0.20
LE	32/64	19/64	0.20
LW	32/64	19/64	0.20
Average Chuck Slip (in.) =			0.203
Prestress Release			
Time (hrs.)	Load (lb.)	f_{si} (ksi)	f'_{ci} (psi)
3.67	32,055	192.3	5597

Table 47: Prestress Data for Beam B6 – 3DV

Prestress Record			
Date:	2/7/2022		
Beam Index:	B6 - 3DV		
Elongation			
Load (lb.)	Stress (ksi)	Ruler (in.)	Δ (in.)
0	0	12-1/4	-
34,411	206.4	16-1/16	3.813
Theoretical Elongation (in.) ≈			3
Chuck Slip			
Chuck	Initial (in.)	Tensioned (in.)	Slip (in.)
DE	28/64	16/64	0.19
DW	32/64	21/64	0.17
LE	31/64	20/64	0.17
LW	32/64	21/64	0.17
Average Chuck Slip (in.) =			0.176
Prestress Release			
Time (hrs.)	Load (lb.)	f_{si} (ksi)	f'_{ci} (psi)
3.17	31,950	191.7	4899

Table 48: Prestress Data for Beam B7 – 3DV

Prestress Record			
Date:	2/11/2022		
Beam Index:	B7 - 3DV		
Elongation			
Load (lb.)	Stress (ksi)	Ruler (in.)	Δ (in.)
0	0	12-1/4	-
34,417	206.5	16	3.75
Theoretical Elongation (in.) ≈			3
Chuck Slip			
Chuck	Initial (in.)	Tensioned (in.)	Slip (in.)
DE	26/64	14/64	0.19
DW	24/64	13/64	0.17
LE	28/64	16/64	0.19
LW	29/64	17/64	0.19
Average Chuck Slip (in.) =			0.184
Prestress Release			
Time (hrs.)	Load (lb.)	f_{si} (ksi)	f'_{ci} (psi)
3.25	31,849	191.1	5941

Table 49: Prestress Data for Beam B8 – 3DV

Prestress Record			
Date:	2/15/2022		
Beam Index:	B8 - 3DV		
Elongation			
Load (lb.)	Stress (ksi)	Ruler (in.)	Δ (in.)
0	0	12-5/16	-
34,392	206.3	16	3.688
Theoretical Elongation (in.) ≈			3
Chuck Slip			
Chuck	Initial (in.)	Tensioned (in.)	Slip (in.)
DE	34/64	21/64	0.20
DW	31/64	20/64	0.17
LE	27/64	16/64	0.17
LW	31/64	19/64	0.19
Average Chuck Slip (in.) =			0.184
Prestress Release			
Time (hrs.)	Load (lb.)	f_{si} (ksi)	f'_{ci} (psi)
3.25	31,811	190.8	4732

Table 50: Prestress Data for Beam B9 – 3DV

Prestress Record			
Date:	2/18/2022		
Beam Index:	B9 - 3DV		
Elongation			
Load (lb.)	Stress (ksi)	Ruler (in.)	Δ (in.)
0	0	12-1/4	-
34,413	206.4	16-1/8	3.875
Theoretical Elongation (in.) ≈			3
Chuck Slip			
Chuck	Initial (in.)	Tensioned (in.)	Slip (in.)
DE	27/64	14/64	0.20
DW	27/64	15/64	0.19
LE	28/64	15/64	0.20
LW	33/64	20/64	0.20
Average Chuck Slip (in.) =			0.199
Prestress Release			
Time (hrs.)	Load (lb.)	f_{si} (ksi)	f'_{ci} (psi)
3.5	32,022	192.1	5152

Table 51: Prestress Data for Beam B10 – 3DV

Prestress Record			
Date:	2/22/2022		
Beam Index:	B10 - 3DV		
Elongation			
Load (lb.)	Stress (ksi)	Ruler (in.)	Δ (in.)
0	0	12-1/4	-
34,398	206.3	16-1/16	3.813
Theoretical Elongation (in.) ≈			3
Chuck Slip			
Chuck	Initial (in.)	Tensioned (in.)	Slip (in.)
DE	27/64	15/64	0.19
DW	29/64	17/64	0.19
LE	31/64	19/64	0.19
LW	29/64	17/64	0.19
Average Chuck Slip (in.) =			0.188
Prestress Release			
Time (hrs.)	Load (lb.)	f_{si} (ksi)	f'_{ci} (psi)
3.0	31,900	191.4	5740

Table 52: Prestress Data for Beam B11 – 3TR

Prestress Record			
Date:	3/4/2022		
Beam Index:	B11 - 3TR		
Elongation			
Load (lb.)	Stress (ksi)	Ruler (in.)	Δ (in.)
0	0	12-1/4	-
34,265	205.5	16-3/16	3.938
Theoretical Elongation (in.) ≈			3
Chuck Slip			
Chuck	Initial (in.)	Tensioned (in.)	Slip (in.)
DE	32/64	17/64	0.23
DW	33/64	18/64	0.23
LE	31/64	17/64	0.22
LW	30/64	17/64	0.20
Average Chuck Slip (in.) =			0.223
Prestress Release			
Time (hrs.)	Load (lb.)	f_{si} (ksi)	f'_{ci} (psi)
2.83	32,197	193.1	6457

Table 53: Prestress Data for Beam B3 – 24TR

Prestress Record			
Date:	11/18/2021		
Beam Index:	B3 - 24TR		
Elongation			
Load (lb.)	Stress (ksi)	Ruler (in.)	Δ (in.)
0	0	12-1/4	-
34,397	206.3	16-1/8	3.875
Theoretical Elongation (in.) ≈			3
Chuck Slip			
Chuck	Initial (in.)	Tensioned (in.)	Slip (in.)
DE	32/64	21/64	0.17
DW	32/64	21/64	0.17
LE	35/64	22/64	0.20
LW	34/64	20/64	0.22
Average Chuck Slip (in.) =			0.191
Prestress Release			
Time (hrs.)	Load (lb.)	f_{si} (ksi)	f'_{ci} (psi)
25	33,308	199.8	9086

Table 54: Prestress Data for Beam B5 – 24TR

Prestress Record			
Date:	1/26/2022		
Beam Index:	B5 - 24TR		
Elongation			
Load (lb.)	Stress (ksi)	Ruler (in.)	Δ (in.)
0	0	12-1/2	-
34,717	208.3	16-3/8	3.875
Theoretical Elongation (in.) ≈			3
Chuck Slip			
Chuck	Initial (in.)	Tensioned (in.)	Slip (in.)
DE	24/64	12/64	0.19
DW	31/64	19/64	0.19
LE	30/64	16/64	0.22
LW	31/64	19/64	0.19
Average Chuck Slip (in.) =			0.195
Prestress Release			
Time (hrs.)	Load (lb.)	f_{si} (ksi)	f'_{ci} (psi)
24	33,523	201.1	9132

Table 55: Prestress Data for Beam B12 – 24DV

Prestress Record			
Date:	3/9/2022		
Beam Index:	B12 - 24DV		
Elongation			
Load (lb.)	Stress (ksi)	Ruler (in.)	Δ (in.)
0	0	12-1/4	-
34,449	206.7	16-1/4	4.0
Theoretical Elongation (in.) ≈			3
Chuck Slip			
Chuck	Initial (in.)	Tensioned (in.)	Slip (in.)
DE	32/64	20/64	0.19
DW	32/64	20/64	0.19
LE	31/64	18/64	0.20
LW	33/64	21/64	0.19
Average Chuck Slip (in.) =			0.191
Prestress Release			
Time (hrs.)	Load (lb.)	f_{si} (ksi)	f'_{ci} (psi)
24	32,943	197.6	9129

Table 56: Prestress Data for Beam B13 – 24DV

Prestress Record			
Date:	3/11/2022		
Beam Index:	B13 - 24DV		
Elongation			
Load (lb.)	Stress (ksi)	Ruler (in.)	Δ (in.)
0	0	12-1/4	-
34,420	206.5	16-1/8	3.875
Theoretical Elongation (in.) ≈			3
Chuck Slip			
Chuck	Initial (in.)	Tensioned (in.)	Slip (in.)
DE	30/64	18/64	0.19
DW	31/64	20/64	0.17
LE	32/64	19/64	0.20
LW	30/64	19/64	0.17
Average Chuck Slip (in.) =			0.184
Prestress Release			
Time (hrs.)	Load (lb.)	f_{si} (ksi)	f'_{ci} (psi)
24	33,001	198.0	8875

Table 57: Prestress Data for Beam B14 – 24DV

Prestress Record			
Date:	3/18/2022		
Beam Index:	B14 - 24DV		
Elongation			
Load (lb.)	Stress (ksi)	Ruler (in.)	Δ (in.)
0	0	12-1/4	-
34,468	206.8	16	3.75
Theoretical Elongation (in.) ≈			3
Chuck Slip			
Chuck	Initial (in.)	Tensioned (in.)	Slip (in.)
DE	31/64	20/64	0.17
DW	33/64	22/64	0.17
LE	31/64	19/64	0.19
LW	31/64	20/64	0.17
Average Chuck Slip (in.) =			0.176
Prestress Release			
Time (hrs.)	Load (lb.)	f_{si} (ksi)	f'_{ci} (psi)
24.5	33,052	198.3	8342

Table 58: Prestress Data for Beam B15 – 24DV

Prestress Record			
Date:	3/22/2022		
Beam Index:	B15 - 24DV		
Elongation			
Load (lb.)	Stress (ksi)	Ruler (in.)	Δ (in.)
0	0	12-1/4	-
34,374	206.2	16-1/16	3.813
Theoretical Elongation (in.) ≈			3
Chuck Slip			
Chuck	Initial (in.)	Tensioned (in.)	Slip (in.)
DE	31/64	18/64	0.20
DW	29/64	17/64	0.19
LE	31/64	18/64	0.20
LW	30/64	19/64	0.17
Average Chuck Slip (in.) =			0.191
Prestress Release			
Time (hrs.)	Load (lb.)	f_{si} (ksi)	f'_{ci} (psi)
24	33,435	200.6	9255

Table 59: Prestress Data for Beam B16 – 24DV

Prestress Record			
Date:	3/24/2022		
Beam Index:	B16 - 24DV		
Elongation			
Load (lb.)	Stress (ksi)	Ruler (in.)	Δ (in.)
0	0	12-1/4	-
34,382	206.3	16-1/8	3.875
Theoretical Elongation (in.) ≈			3
Chuck Slip			
Chuck	Initial (in.)	Tensioned (in.)	Slip (in.)
DE	31/64	19/64	0.19
DW	30/64	20/64	0.16
LE	30/64	18/64	0.19
LW	32/64	20/64	0.19
Average Chuck Slip (in.) =			0.180
Prestress Release			
Time (hrs.)	Load (lb.)	f_{si} (ksi)	f'_{ci} (psi)
24	33,305	199.8	9872